The controlled hydro/solvothermal synthesis of ceria-based materials

By

Alexander James Aiken Dunn

Thesis submitted for the degree of

Doctor of Philosophy in Chemistry

Department of Chemistry, University of Warwick

September 2018

Acknowledgements

Firstly, I would like to extend sincerest thanks to Professor Richard I. Walton, for providing me with the opportunity to be a member of his group for the past four years. His immeasurable guidance, patience and support throughout the years, it has been greatly appreciated.

I would also like to thank Janet Fisher and David Thompsett for their invaluable input and supervision of the course of my PhD. To Janet also, for her aid in running the TPR, BET and Raman measurements and for generally looking after me every time I had to take a trip down to the Johnson Matthey Technology centre. The past and presents members of the Walton group for being a constant source of help and for accompanying me on my multiple 24/7 beamline experiments. I thank Professor Gopinathan Sankar and Glen Smales for providing the use of the hydrothermal cell used for the in situ XANES measurements, and their endeavours throughout the preparation of and during the beamtime.

I thank Reza Kashtiban for providing all the TEM images and their respective elemental analysis. Dr. Helen Y. Playford for performing the XRF measurements. Dan cook and Thomas chamberlain for their help operating the porosimeter. Maria Vlachou for collecting and her help in interpreting the NMR spectra presented herein.

The time and hard work of the beamline scientists Paul Thompson, Oxana Magdysyuk, Stefan Michalik, Diego Gianolio and Giannantonio Cibin providing their expertise and advice on the use of the beamlines for out which the experiments would not be possible.

Last, but by no means least I would like to thank my family and friends for being there for me and providing their support.

Contents

Declaration

This thesis submitted to the University of Warwick is in support of my application for the degree of Doctor of Philosophy in Chemistry. It has been composed by me and has not been submitted for a degree at any other institution.

Abstract

This thesis reports on the one-pot hydro/solvothermal synthesis of a range of mixed metal cerium oxides with potential catalysis applications. The produced materials were characterised using a wide range of techniques to understand the synthesis-dependent variations in crystallite size, morphology, surface absorbed species and redox properties.

The hydrothermal synthesis of bismuth-substituted cerium dioxide is reported. The choice of starting reagents in the hydrothermal reaction was found to affect the crystallite sizes of the resulting $Ce_{0.5}Bi_{0.5}O_{2-\delta}$ samples. The $Ce_{0.5}Bi_{0.5}O_{2-\delta}$ samples with the lower crystallite size and hence larger surface areas were derived from the use of $Ce(NH_4)_2(NO_3)_6$ as the cerium source. In situ X-ray diffraction and X-ray absorption experiments indicate that the cubic structure of $Ce_{0.5}Bi_{0.5}O_{2-\delta}$ is formed via formation of poorly ordered CeO_2 followed by the reduction of bismuth and/or to the crystallisation of α-Bi_2O_3 from the bismuth starting reagents prior to its inclusion into CeO_2.

The solvothermal reaction of $CeCl_3$ with $LnCl_3$ (Ln = La, Pr, Gd and Tb) in polyethylene glycol at 240 °C yields a range of previously unreported $Ce_{1-x}Ln_x(OH)_2Cl$ samples with a unusual morphology. Barring lanthanum, up to approximately 50% lanthanide-substitution was achieved. Contrarily, the series of $Ce_{1-x}Ln_x(OH)CO_3$ materials prepared via the use of nitrate precursors achieved only 20% lanthanide-substitution. The thermal decomposition of the lanthanide-substituted cerium precursors produces materials that adopt the fluorite type unit cell and retain their unique crystal morphology. X-ray absorption near-edge structure spectra recorded at the Pr and Tb K-edges indicates the existence of both in two oxidation states, Tb^{3+}/Tb^{4+} and Pr^{3+}/Pr^{4+}. The results deduced from XANES spectra of the mixed oxides agree with the calculated lattice parameters refined from the X-ray diffraction patterns. The incorporation of lanthanide cations improves the reducibility of ceria as measured by H_2-temperature programmed reduction.

Three methods using alkoxide starting reagents have successfully been able to synthesise the ordered k-$Ce_2Zr_2O_8$ phase. Powder X-ray diffraction shows that the cationic ordering can be achieved at temperatures as low as 1000 °C without the use

of reducing gases. A study of both the local environment and structure of the zirconium substituted ceria samples reveals that the solvothermal method of synthesis produces materials that contain a larger quantity of Ce^{3+}.

1. Introduction

1.1 Cerium dioxide (Ceria, CeO_2)

CeO_2 is widely known for its catalytic properties due to the fact that is susceptible to reduction by either reducing gases such as carbon monoxide or just by heating in air. This occurs by firstly reacting with the oxygen atoms on the surface layer of CeO_2 to produce oxygen vacancies in the CeO_2 lattice and carbon dioxide. The oxygen deficient CeO_2 can be then efficiently replenished under sufficient oxidising conditions. [1]

$$CeO_2 + \delta CO \rightarrow CeO_{2-\delta} + \delta CO_2$$

$$CeO_{2-\delta} + \frac{1}{2}\delta O_2 \rightarrow CeO_2$$

The redox cycle of inter-converting between the +4 and +3 oxidation states of cerium in the above equation is limited by δ, which is defined as the oxygen storage capacity (OSC). For heterogeneous catalytic applications being able to increase the surface area and hence enabling easier reduction of CeO_2 is a desired attribute. In order to maximise this attribute and the OSC of CeO_2 the majority of the research conducted in this area has focused on substituting cerium with other cations with the aspiration to either establish active sites for absorption and subsequent catalysis or create lattice distortions in order to increase oxygen vacancies and ion mobility.

1.1.1 Properties and uses

CeO_2 exists in the cubic fluorite type of structure (CaF_2) with space group $Fm\bar{3}m$, which is a face-centred cubic unit cell (a = 5.4112 Å). [2] The structure consists of an array of cerium cations co-ordinated by eight nearest-neighbour oxygen anions, while each oxygen is co-ordinated by four nearest-neighbour cerium cations (Figure 1). CeO_2 is pale yellow in colour, presumably due to the $Ce^{4+} \rightarrow O^{2-}$ charge transfer. [3]

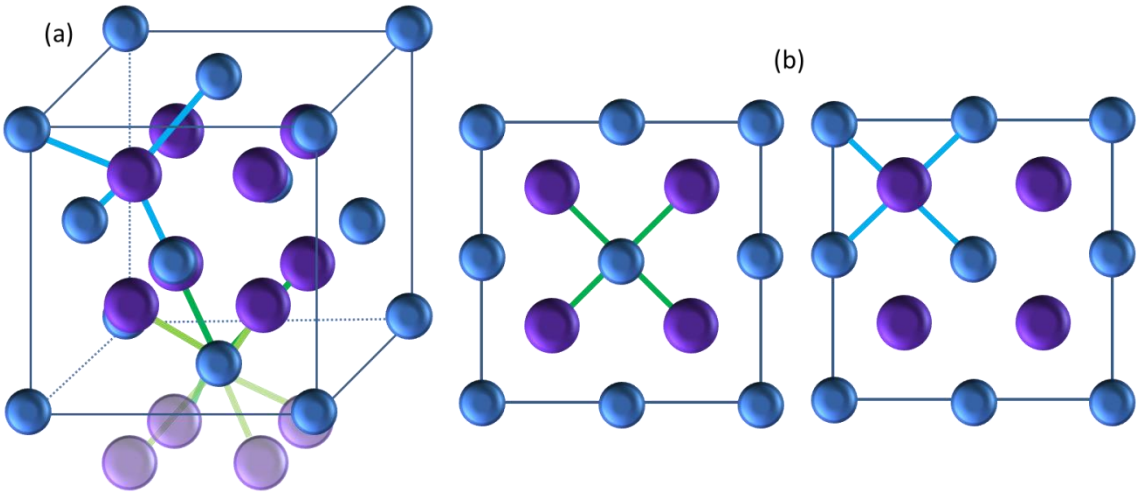

Figure 1: a) A CeO_2 unit with cerium atoms in blue and oxygen atoms in purple b) Two views along the surface of the unit cell. (Green lines depict the cerium co-ordination and blue lines the oxygen co-ordination).

Stoichiometric CeO_2 is an insulator, and its electronic structure is characterised as a fully occupied O 2p and empty 4f and 5d states. [4] At elevated temperatures and in an O_2-deficient atmosphere, CeO_2 is susceptible to reduction to give non-stoichiometric $CeO_{2-\delta}$ ($0 < \delta \leq 0.5$) which has a dark blue, virtually black colour. [5] Under extreme reducing conditions CeO_2, converts to the sesquioxide Ce_2O_3 (space group: $P\bar{3}m1$). [6] The formation of oxygen vacancies is a consequence of decreasing O^{2-}, to maintain the charge balance two reduced Ce^{3+} species are formed. This partially reduced phase contains a distribution of Ce^{3+} and Ce^{4+} centres that can readily interconvert, by the oxidation and reduction of the Ce 4f levels. This affects the electronic conduction of CeO_2, which has been attributed to the formation of small polarons that diffuse via a hopping mechanism between the Ce^{3+} and Ce^{4+} valence states. [7] The alteration of $CeO_{2-\delta}$ valence and defect structure is dynamic and depends on variations in temperature, oxygen partial pressure, surface stresses, electrical field and substitution with other cations and so on. [8-10] The non-stoichiometry of ceria originates from the fact that cerium can readily change its oxidation state. The oxidation of cerium however, is much faster than the reduction therefore a lot of research has focused on promoting its reducibility.

The presence or lack of lattice oxygen is therefore presumably responsible for the useful catalytic properties of ceria. These unique properties have led CeO_2 to be used in several applications such as, UV-protecting agents, [11-13] as anti-corrosion protection for metals and alloys, [14-16] as an anode material for lithium ion batteries, [17] water-gas shift reaction, [18-19] as a catalyst for diesel soot combustion, [20-21]

water-splitting (H_2 generation), [22] solar cells [23] and various biological applications. [24]

1.1.2 Synthesis techniques

The chemical methods of synthesis play a vital role in the discovery and in the design of novel materials. Inorganic solids have been prepared in the past years using a wide array of synthetic conditions. Solid-state synthesis often edging towards the extreme, such as high temperatures and pressures, as well as oxygen partial pressures have been employed for metal oxide synthesis. These methods tend to produce the most thermodynamically stable materials but lack the ability to possess more control over the particle size and morphology. The extreme conditions used in solid-state methods are also not normally necessary, so the present trend has focused on getting better control of the structure, stoichiometry, and purity through more refined methods. Low temperature chemical routes such as solution-based methods make use of simple chemical reactions such as, condensation, hydrolysis, dehydration and chemical reduction. Many of the materials prepared by these methods are metastable and contain some degree of disorder and/or defects, which are favoured for applicability in a wide range of commercial devices. The materials can be engineered to have different, sizes, shapes and surface characteristics, which are highly tuneable properties owing to the large variety of controllable synthetic parameters.

In this chapter a few of the frequently used synthetic techniques are addressed in more detail below.

1.1.2.1 Solid-state methods

The most common and oldest method of preparing metal oxides is by the solid-state method. This method involves grinding reagents (generally oxides, oxalates, carbonates or other suitable metal containing compounds) and then heating the mixture to a desired temperature. The entire reaction progresses by a phase boundary reaction at the interface between the reagents and subsequently by ion diffusion. As the reaction advances the diffusion paths increase and the reaction rate decrease. Therefore, it is often necessary to perform several intermittent grinding and re-heating cycles to speed up the reaction and to obtain a phase pure product. The advantages of using this method is that the desired compositional ratio of the product will usually be known and the conditions for the synthesis are straightforward. Since

usually the method involves the use of extreme temperatures the products typically very crystalline, which makes product identification simple.

However, the solid-state method also has its limitations, periodic X-ray diffraction data and other measurement techniques are required to determine if the reaction has reached completion. Therefore, achieving a phase pure product is basically trial and error, to which some mixtures are commonly unable to be separated or contain local inhomogeneity. This method is also only suitable for when the product is the most thermodynamically stable phase. Frequently the products formed also have a low surface area which limits the number of applications the materials are suitable for. Despite of these drawbacks, the solid-state method has been successfully used to synthesise a wide range of solid materials. For example, $La_{1-x}Sr_xGa_{1-y}Mg_yO_{3-\delta}$ can be synthesised either by using a conventional furnace at 1550 °C [25] or by a CO_2 laser [26] which is a modification on the solid-state method to aid in overcoming some of its limitations. By reducing the time, energy and the inhomogeneity of the desired product. Hence, improving the materials suitability as a potential electrolyte for SOFCs.

1.1.2.2 Sol-gel methods

The sol-gel method is a well-established approach for the synthesis of inorganic oxides. The formation of the metal oxide via this approach involves several different consecutive steps. The first involves forming a dispersion of colloidal powders within a solution (the sol). This sol then becomes a 'gel' through simultaneous hydrolysis and polycondensation of the organometallic precursors (generally metal acetates, nitrates or metal alkoxides etc). The formed gel is an interconnected three-dimensional network of oxide- or alcohol-bridged metal ions within a liquid medium. The third step involves the water and/or other volatile liquids being removed from the gel network, either by thermal evaporation or extracted under supercritical conditions. The choice of this drying process in some cases has a direct result on the pore radii as well as the structure of the product. As when the pore liquid is removed, it induces capillary stresses on the gel which results in either a close resemblance or a collapsed version of the original gel network. The former being known as an aerogel which is recovered by evacuation and the latter as an xerogel by evaporation. These reactions typically occur at room temperature, so an

optional final step is a further heat treatment to a higher temperature (≥ 300 °C) to forge a more crystalline product. The beneficial features of the sol-gel method are better homogeneity compared to the traditional solid-state method, lower reaction temperature, better size and morphology control. The tunability of the final products are significant due to the wealth of variable parameters being precursor structure and concentration, pH, agitation, as well as the use of aqueous or non-aqueous solvents. The synthetic procedure can also be modified to include the use of chelating agents, one such example being the Pechini method. The synthetic process for the Pechini method involves introducing the metal salts into a solution such as citric acid and ethylene glycol. [27] This method is based on the fact that the organic acid can form stable chelates with multiple cations. [28] Upon heating in the presence of the alcohol a polycondensation reaction occurs resulting in the formation of an amorphous product. Further heating to a higher temperature results in the thermal decomposition of the organic ligands to form the nanocrystalline products. [29]

1.1.2.3 Hydrothermal and solvothermal methods

The hydrothermal or solvothermal methods are one of the most common and effective synthetic routes to synthesise inorganic materials with a variety of morphologies. The hydrothermal synthesis method is described as a chemical reaction that occurs in an aqueous solution that is heated in a closed system above ambient temperature and pressure (typically > 100 °C and 1 atm). [30] Under such conditions an autogenous pressure is created internally due to the vapour pressure of the water, contrary to an external one being applied. Hydrothermal processing allows many inorganic materials to be prepared at temperatures substantially below those required by solid-state methods. The hydrothermal method relies on generating "gel precursors" which involves the complexing of metal salts in basic solutions, which are stirred at room temperature in a Teflon liner. The Teflon containers are then transferred and sealed into metal autoclaves and placed into an oven and heated for a period, after which, the mixture is filtered and dried to recover the crystalline material. During this process the applied conditions facilitate the dissolution of the metal salts and the products are then formed by crystallisation. The advantages of utilising aqueous solvents are that it aids in the dissolution of the reagents and improves ion migration which affords higher homogeneity. The modification of the

thermodynamic variables or the solvent used alters the crystallisation process which enables for the control of the resulting particles morphology and size. [31]

However, there is no requirement for the reaction solvent to be an aqueous solution, non-aqueous solvents have also been used and these types of reactions are termed solvothermal. [32-34] Solvothermal synthesis is similar to the hydrothermal method but uses organic solvents (such as, ethanol, toluene, chloroform, etc), this allows for the use of precursors or allows for the formation of products that would otherwise be unstable in water. The use of a non-aqueous media in solvothermal reactions induces low solubility of inorganics, due to its low dielectric constant that would otherwise display low solubilities under ambient conditions. Above the supercritical temperature of the solvent, the solvent exhibits the characteristics of both a liquid and of a gas. The properties of the solvent, such as dielectric constant and density, change dramatically under supercritical conditions as a function of temperature and pressure. Adjusting these parameters allows for control over the particle size, morphology and microstructure of the obtained products. Most reactions, however, simply take advantage of the increased solubility and reactivity of the metal salts at elevated temperatures without bringing the solvent to its critical point. As lower temperature reactions are less energy intensive and incur lower production cost for commercial applications.

In the case of sol-gel methods, which also have the advantage of lower reaction temperatures subsequent annealing is required to produce a more crystalline product unlike with the hydrothermal methods. The disadvantages of using hydrothermal methods is that it utilises a closed system which limits the amount of analytical information that can be obtained about the formation of the crystals and the mechanisms involved. Overall this synthetic technique affords a simple one-step synthetic route that is particularly well known for its capability to synthesise a diverse range of phase pure single and multi-component oxide materials.

1.2 Doping of cerium dioxide

CeO_2 has the capacity to integrate an extensive range of dopant ions, whilst retaining the fluorite structure. These systems have a long history of investigations as potential materials for both catalyst supports and as the active catalyst. Limited research has been conducted on introducing anions into the ceria lattice. The research that has,

focused on replacing the oxygen in ceria for fluoride anions [35] and others on doping nitrogen into the structure. [36-37] However, most of the conducted research into ceria has focused on the substitution of Ce for other cations, to form either ternary or higher oxides.

Among the aliovalent cations that have been substituted into ceria, the divalent alkali earth metal Ca, is a competitive candidate for use as an electrolyte in SOFCs because of its high ionic conductivity at the intermediate temperature region (300-500 °C). [38-40] $Ce_{1-x}Ca_xO_{2-\delta}$ demonstrates two essential commercial advantages, a lower production cost and being less of an environmental concern. These attributes have also led to them being a promising candidate for UV-protection materials in sunscreens [41] and have been prepared by simple co-precipitation methods. [42-43]

Comprehensive reviews on transition metal substituted ceria have been conducted as ceria is almost able to incorporate every single one of them to some degree. For example, the substitution of Ce^{4+} with the considerably smaller Ti^{4+} cations (0.97 and 0.74 Å, respectively) of the form $Ce_{1-x}Ti_xO_{2-\delta}$ still retains the fluorite structure up to a value of x = 0.5. EXAFS studies on these materials has revealed two distinct Ti – O bond lengths, resulting in a two difference types of oxygen, one set more strongly bound than the other. The weaker bound oxygens being responsible for the improved catalytic performance of these mixed oxides. [44] As a catalyst these materials were studied for a variety of potential applications such as wet air oxidation, [45] NO removal, [46-48] and low-temperature CO oxidation. [49] Solid solutions of $Ce_{1-x}Y_xO_{2-\delta}$ can be synthesised over the whole range of compositions ($0 \leq x \leq 1$). The ionic radius of Y^{3+} (1.019 Å) is very similar to that of Ce^{4+}, thus facilitating easy dissolution into the ceria lattice. Closely related to the fluorite structure, Y_2O_3 adopts the C-type structure (space group: $Ia\bar{3}$), when the compositional range exceeds x = 0.5 the materials exhibit this structure. Combining Rietveld and Pair distribution function (PDF) analyses of neutron and X-ray powder diffraction data suggests that at low dopant concentrations Y_2O_3 exists as domains within the CeO_2 matrix. For the inverse the model is reversed CeO_2 domains reside within Y_2O_3. [50-51] The lower valency of Y leads to the formation of oxygen vacancies, this and the non-random distribution of cations results in excellent ionic conductivity at low dopant concentrations. These attributes have led to extensive research in these materials for applications as electrolytes in SOFCs. [52]

$Ce_{0.67}Cr_{0.33}O_{2.11}$ was initially synthesised via a hydrothermal reaction using diethylenetriamine (DETA) as the solvent. [53] The oxidation states of Cr were investigated by XPS which revealed that the substituted Cr has a mixed valence state Cr^{4+}/Cr^{6+} in a 2:1 ratio, respectively. The mixed oxidation states of Cr in the ceria lattice creates distortions, permitting extra oxygen to occupy interstitial sites. These factors were to be found to improve the oxygen release/ storage properties of the ceria making it markedly active for low temperature water splitting. [54] However, the viability of these materials for commercial applications is a concern due to the toxicity of Cr^{6+}. Mn-substituted ceria has been shown to have exceptional catalytic performance for oxidation reactions, diesel soot, [55-57] chlorobenzene, [58] phenol, [59] hexane, [60] as well as selective catalytic reduction of NO with NH_3 at low temperature. [61-62] Cu-containing CeO_2 material have acquired considerable attention in the fields of energy and environmental applications due to their unique physiochemical characteristics. [63-65] In situ XANES combined with diffuse reflectance infrared Fourier transform spectroscopy (DRIFTS) was used recently to identify the local structure of a 5% loaded CuO/CeO_2 catalyst under reduction by CO. The study was able to determine under increasing temperature a transformation of the Cu oxidation state on the surface occurred, shifting gradually from Cu^{2+} to Cu^{+} and finally Cu^{0}. However, it was determined that only the Ce^{4+}/Ce^{3+} and Cu^{2+}/Cu^{+} species participates in the redox mechanism of CO oxidation over Cu^{0}. [66]

Most of the research into the addition of precious metals have focused on loading small quantities ($\leq$ 5 mol%, due to the considerable expense of these materials) of the metal on the surface via typically a wet impregnation method. [67-70] The addition of the precious metals notably enhances the lower temperature reducibility of the materials, by creating oxygen vacancies and active centres that act as adsorption sites. [71-72] So predominantly the research has focused on reducing the quantity of precious metal whilst retaining its improved catalytic performance. Studies have shown that for Pt/CeO_2 the different morphologies of CeO_2 affects the concentration of oxygen vacancies and the metal-support interaction between the Pt species and CeO_2, in turn affecting the catalytic performance for CO oxidation. [73-74] The solid solution form of $Ce_{1-x}M_xO_{2-\delta}$ (M = Pd, Pt, Ru, Rh) shows favourable hydrocarbon and CO oxidation as well as NO reduction activity compared to the dispersion of the precious metals on the surface. [75-76] Recently, $Ce_{0.99}Rh_{0.01}O_{2-\delta}$ has been synthesised

by a co-precipitation method which exhibits a high potential for use as an active material to convert H_2O and CO_2 directly into organic fuels. [77] Sonochemical synthesis of $Ce_{1-x}M_xO_{2-\delta}$ (M = Pt or Pd, $0 \leq x \leq 0.1$) has been shown to be an effective catalyst for methanol oxidation. [78] Hydrothermal synthesis of $Ce_{0.95}Ru_{0.05}O_{2-\delta}$ showed improved activity for the water-gas shift reaction at low temperature. [79]

Post-transition metal substitution into ceria has also been investigated showing high levels of incorporation for the metals that can be incorporated by a variety of synthetic techniques. For instance, a range of preparative techniques have been used to synthesise $Ce_{1-x}Sn_xO_{2-\delta}$ using electrospinning, [80] co-precipitation, [81] solution combustion [82] and hydrothermal methods. [83] Sn-substituted ceria has exhibited improved CO conversion [84] as well as selective catalytic reduction of NO_x by NH_3. [85] These materials have the additional benefit of possessing a high tolerance towards H_2O and H_2S, which is a very promising attribute for the latter type of emissions.

Lanthanoid inclusion into the ceria lattice has been studied extensively, due to their ionic radii being similar to that of Ce^{4+} as well as being able to occupy eight-coordinate sites. For example, ceria doped with lower valent cations such as Gd form highly oxygen deficient materials that exhibit high oxygen ion conductivities at elevated temperatures and have been previously studied for their application in SOFCs. [86-89] Lanthanum substituted ceria is also considered a high-k gate dielectric material for use in microelectronic devices. [90] Lanthanoids with aliovalency such as praseodymium and terbium (Pr^{3+}/Pr^{4+} and Tb^{3+}/Tb^{4+}) reaction higher oxygen ion mobility and the substitution of cerium with either cation, increases the number of redox sites on the surface, and hence creates more oxygen vacancies. These beneficial effects have led to the potential use of $Ce_{1-x}Pr_xO_{2-\delta}$ as catalysts for diesel soot combustion. [91-94] The substitution of Pr into ceria has also shown to increase the dispersion of other metals loaded on to the surface, such as Pd. The increased metal catalyst dispersion as well as the increased lower temperature reduction of the materials has produced materials which have improved catalytic activity for the water gas shift reaction. [95] The inclusion of Tb into ceria has shown to be an interesting material in research areas such as air separation, due to its high O_2/N_2 selectivity. The increased oxygen uptake has shown to increase upon increasing Tb

content. [96] Other rare-earth cations like Yb, Tm and Ho have been incorporated into ceria and have been shown to cause electronic interactions, due to spin-orbit coupling and the degeneracy of the 4f levels. The ability to absorb light in the infrared region, results in the excitation of electrons to the higher 4f energy levels. The resulting reversion of these electrons to the ground state generates emissions in the green and red regions of the electromagnetic spectrum. These attributes have led to these materials being used in energy conversion devices such as in solar cells. [97] A huge range of approaches have been utilised to synthesise $Ce_{1-x}Sm_xO_{2-\delta}$ such as polymer pyrolysis, [98] pulsed laser deposition, [99] ultrasonic spray deposition, [100] hydrothermal synthesis, [101] solid-state ceramic method, [102] and co-precipitation. [103] Samarium modified ceria has been described as a potential catalyst for selective oxidation of methane, [104] electrolyte in SOFCs, [105] and electro-oxidation catalyst, [101] due to a high oxygen mobility.

1.2.1 Cerium bismuth oxides

Cerium bismuth oxides have previously been studied as they present enhanced properties in contrast to pure ceria such as an increased number of oxygen vacancies. The introduction of bismuth (Bi^{3+}) into the structure also creates an unsymmetrical distortion due to the presence of a lone pair of electrons, this distortion improves ion migration. The attributes of this oxide, for example have led to research for its use as an oxidation catalyst for hydrogen combustion. $Ce_{0.9}Bi_{0.1}O_2$ has been reported to have both a higher activity and selectivity towards hydrogen combustion in comparison to other conventional catalysts. [106] Other research has reported that these advantages make $Ce_{0.8}Bi_{0.2}O_2$ useful for solar energy conversion as a photo/ thermo-catalyst as it couples both ionic and electronic conductivity at a low temperature (20-80 °C). [107] Cerium-bismuth oxides have previously been successfully synthesised from several different starting reagents and various synthetic routes have also been developed to produce these cerium-bismuth oxide materials ($Ce_{1-x}Bi_xO_{2-\delta}$) such as hydrothermal synthesis, [107-109] chemical precipitation (Pechini method) [110-111] and self-propagating room temperature. [112-113]

1.2.2 Cerium hydroxides

Cerium carbonate hydroxide is known to have either hexagonal ($P\bar{6}2c$) or orthorhombic (Pnma) structure and both have been studied and employed due to

their electronic [114] and optical properties. [115] Novel synthetic routes have been developed to synthesise cerium carbonate hydroxides with different morphologies. Among these reports, shape-controlled synthesis has been achieved via sonochemical [116] and hydrothermal [117] methods producing varied structural morphologies. A wide range of different crystal morphologies have been reported in the literature and a few examples include dendrite, [118] flower-like, [119-120] nanorod [121] and shuttle morphologies. [122] More recent applications of this material are as an electrode material for lithium ion (Li-O_2) batteries [123] as it is claimed to have electrochemical reversibility. Cerium carbonate hydroxide has also been used for synthesising ceria while retaining the unusual morphologies through thermal decomposition.

1.2.3 Cerium zirconium oxides

One of the major applications of cerium zirconium oxides is in three-way catalysts (TWC). [124-125] The most well-known problem involved with using ceria as an automotive exhaust catalyst is the sintering of the ceria particles at high temperatures and after progressive aging. This sintering process is strongly correlated to the redox properties of ceria. [126] The incorporation of zirconium into the ceria lattice stabilises the structure and improves the thermal properties and longevity of the catalysts. The insertion of a smaller sized ion as zirconium also improves the oxygen storage capacity (OSC) of ceria. The size difference creates a higher degree of structural disorder, with oxygen atoms positioned at weaker bonding distances, [127] thus increasing the reducibility of Ce^{4+} and hence the mobility of the oxygen anions within the lattice. Numerous protocols for synthesising $Ce_{1-x}Zr_xO_{2-\delta}$ have been prepared such as, co-precipitation, [128-129] sol-gel [130] and hydrothermal methods. [131] The oxygen storage capacity of $Ce_{0.5}Zr_{0.5}O_{2-\delta}$ can be enhanced by reducing the material under a flow of H_2 at high temperatures (≥1000 °C) to form a pyrochlore phase ($Ce_2Zr_2O_{7+\delta}$, space group: $Fd\bar{3}m$). Performing a mild re-oxidation (≥500 °C) of this material under atmospheric conditions produces a kappa phase ($Ce_2Zr_2O_8$, space group: $P2_13$). This phase contains a higher degree of cationic ordering and allows for the formation of weakly bound oxygen atoms (1/8 of the oxygen anions can be readily removed).

1.2.4 Cerium aluminium oxides

$Ce_{1-x}Al_xO_{2-\delta}$ has been reported to have been successfully synthesised using $CeCl_3$ and $AlCl_3$ as starting reagents via the combination of chemical precipitation and

annealing at 900 °C. One article reports up to x = 0.15 aluminium. [133] Other literature has reported that cerium aluminium oxide has been synthesised by combustion synthesis and investigation as a new cathode material for lithium ion (Li-O_2) batteries. Aluminium content of up to x = 0.2, has been reported to give a higher surface area and porous morphology for improved discharge capacity. [134] The crystal structure of these produced materials is still under debate however as conflicting information is provided about the lattice parameters in relation to CeO_2, either due to synthetic route or other unknown factors. One report suggests the lattice parameter increases due to oxygen ion vacancies and on the other hand that it contracts due to the small ionic radii of aluminium. [133-134]

1.3 Aims of the PhD study

- To develop a broader understanding of the formation mechanisms involved during the synthesis of inorganic oxide materials, to lead to being able to control mixed metal oxide materials morphology, particle size and crystal structure.
- Initially the simple system of cerium-bismuth oxide will be investigated, and the knowledge gained will later be integrated into developing the understanding of more complex systems, with the eventual intent of producing new target materials.
- To synthesise pure materials with well-defined crystal structures via different synthetic routes and combinations of starting materials.
- The synthesised materials will be analysed using various diffraction and spectroscopic techniques to determine the crystal structures and morphologies of each of the materials prepared by different synthetic methods.
- To test catalytic properties of materials in collaboration with Johnson Matthey for applications such as water-gas shift catalysis and automotive three-way catalysis.

References

1. A. Trovarello. (1996). Catalytic properties of Ceria and CeO_2- containing materials. *Catalysis Reviews: Science and Engineering*. 38 (4), p439-520.
2. E.A. Kummerle and G. Heger. (1999). The Structures of C–$Ce_2O_{3+\delta}$, Ce_7O_{12}, and $Ce_{11}O_{20}$. *Journal of Solid State Chemistry*. 147 (2), p485-500.

3. M. Mogensen, N.M. Sammes and G.A. Tompsett. (2000). Physical, chemical and electrochemical properties of pure and doped ceria. *Solid State Ionics*. 129 (1-4), p63-94.
4. A.M. Boring and J.H. Wood. (1983). The electronic structure of CeO_2 and PrO_2. *Solid State Communications*. 47 (4), p227-232.
5. Y. Yuan, D. Hao-Hong, L. Le-Le, S. Ling-Dong, Z. Ya-Wen and Y. Chun-Hua. (2005). Controlled synthesis and assembly of ceria-based nanomaterials. *Journal of Colloid and Interface Science*. 335, p151-167.
6. M. Gasgnier, G. Schiffmacher, P. Caro and L. Eyring. (1986). The formation of rare earth oxides far from equilibrium. *Journal of the Less-Common Metals*. 116 (1), p31-42.
7. J.J. Plata, A.M. Marquez and J.F. Sanz. (2013). Electron Mobility via Polaron Hopping in Bulk Ceria: A First Principles Study. *The Journal of Physical Chemistry C*. 117, p14502-14509.
8. M.V. Ganduglia-Pirovano, A. Hofmann and J. Sauer. (2007). Oxygen vacancies in transition metal and rare earth oxides: Current state of understanding and remaining challenges. *Surface Science Reports*. 62 (6), p219-270.
9. E. Mamontov and T. Egami. (2000). Lattice Defects and Oxygen Storage Capacity of Nanocrystalline Ceria and Ceria-Zirconia. *Journal of Physical Chemistry B*. 104, p11110-11116.
10. N.A.M. Fadzil, M.H.A. Rahim and G.P. Maniam. (2018). Brief review of ceria and modified ceria: synthesis and application. *Materials Research Express*. 5, p85019-85036.
11. T. Masui, K. Fujiwara, K. Machida and G. Adachi. (1997). Characterization of Cerium (IV) Oxide Ultrafine Particles Prepared Using Reversed Micelles. *Chemistry of Materials*. 9, p2197-2204.
12. S. Tsunekawa, R. Sahara, Y. Kawazoe and A. Kasuya. (2000). Origin of the Blue Shift in Ultraviolet Absorption Spectra of Nanocrystalline CeO_{2-x} Particles. *Materials Transactions*. 41 (8), p1104-1107.
13. M. Yamashita, K. Kameyama and S. Yabe. (2002). Synthesis and microstructure of calcia doped ceria as UV filters. *Journal of Materials Science*. 37, p683-687.
14. D. Ghosh, A.K. Shukla and S.K. Mitra. (2013). Effect of ceria coating on corrosion behaviour of low alloy steel. *Surface Engineering*. 29 (8), p584-587.
15. A.S. Hamdy. (2006). Advanced nano-particles anti-corrosion ceria-based sol gel coatings for aluminium alloys. *Materials Letters*. 60, p2633-2637.
16. X. Zhong, Q. Li, J. Hu and Y. Lu. (2008). Characterization and corrosion studies of ceria thin film based on fluorinated AZ91D magnesium alloy. *Corrosion Science*. 50, p2304-2309.
17. F. Zhou, X. Ni, Y. Zhang and H. Zheng. (2007). Size-controlled synthesis and electrochemical characterization of spherical CeO_2 crystallites. *Journal of Colloid and Interface Science*. 307, p135-138.
18. S. Hilaire, X. Wang, T. Luo, R.J. Gorte and J. Wagner. (2001). A comparative study of water-gas-shift reaction over ceria supported metallic catalysts. *Applied Catalysis A: General*. 215, p271-278.
19. R.J. Gorte and S. Zhao. (2005). Studies of the water-gas-shift reaction with ceria-supported precious metals. *Catalysis Today*. 104 (1), p18-24.
20. P.A. Kumar, M.D. Tanwar, S. Bensaid, N. Russo and D. Fino. (2012). Soot combustion improvement in diesel particulate filters catalyzed with ceria nanofibers. *Chemical Engineering Journal*. 207-208, p258-266.
21. P. Palmisano, N. Russo, P. Fino, D. Fino and C. Badini. (2006). High catalytic activity of SCS-synthesized ceria towards diesel soot combustion. *Applied Catalysis B: Environmental*. 69, p85-92.
22. S. Abanades and G. Flamant. (2006). Thermochemical hydrogen production from a two-step solar-driven water-splitting cycle based on cerium oxides. *Solar Energy*. 80 (12), p1611-1623.
23. A. Corma, P. Atienzar, H. Garcia and J. Chane-Ching. (2004). Hierarchically mesostructured doped CeO_2 with potential for solar-cell use. *Nature Materials*. 3, p394-397.
24. A. Xu and X. Qu. (2014). Cerium oxide nanoparticle: a remarkably versatile rare earth nanomaterial for biological applications. *Nature Materials.* 6, p90-106.

25. E. Gomes, F.M.B. Marques and F.M. Figueiredo. (2008). Microstructural effects on the electrical properties of grain boundary Fe-doped LSGM. *Solid State Ionics*. 179, p1325-1328.
26. Z. Zhang, E.J. Liang and X.H. Zhang. (2010). Rapid synthesis of $La_{0.9}Sr_{0.1}Ga_{0.8}Mg_{0.2}O_{3-\delta}$ electrolyte by a CO_2 laser and its electric properties for intermediate temperature solid state oxide full cells. *Journal of Power Sources*. 195 (19), p6758-6763.
27. L. Bourja, B. Bakiz, A. Benlhachemi, M. Ezahri, S. Villain and J.R. Gavarri. (2010). Synthesis and characterization of nanosized $Ce_{1-x}Bi_xO_{2-\delta}$ solid solutions for catalytic applications. *Journal of Taibah University for Science*. 4, p1-8.
28. A.M. Huizar-Felix, T. Hernandez, S. de la Parra, J. Ibarra and B. Kharisov. (2012). Sol–gel based Pechini method synthesis and characterization of $Sm_{1-x}Ca_xFeO_3$ perovskite $0.1 \leq x \leq 0.5$. *Powder Technology*. 229, p290-293.
29. L. Zhi-Cheng, Z. Hong and B. Bergman. (2008). Synthesis and characterization of nanostructured Bi_2O_3-doped cerium oxides fabricated by PVA polymerization process. *Ceramics International*. 34 (8), p1949-1953.
30. R.E. Riman, W.L. Suchanek and M.M. Lencka. (2002). Hydrothermal crystallization of ceramics. *Annales de Chimie Science des Matériaux*. 27 (6), p15-36.
31. W.L. Suchanek and R.E. Riman. (2006). Hydrothermal Synthesis of Advanced Ceramic Powders. *Advances in Science and Technology*. 45, p184-193.
32. D.R. Modeshia and R.I. Walton. (2010). Solvothermal synthesis of perovskites and pyrochlores: crystallisation of functional oxides under mild conditions. *Chemical Society Reviews*. 39, p4303-4325.
33. G. Demazeau. (2010). Solvothermal Processes: Definition, Key Factors Governing the Involved Chemical Reactions and New Trends. *Naturforschung*. 65 (b), p999-1006.
34. M. Niederberger, G. Garnweitner, J. Ba, J. Polleux and N. Pinna. (2007). Nonaqueous synthesis, assembly and formation mechanisms of metal oxide nanocrystals. *International Journal of Nanotechnology*. 4 (3), p263-281.
35. S. Ahmad, K. Gopalaiah, S.N. Chandrudu and R. Nagarajan. (2014). Anion (Fluoride)-Doped Ceria Nanocrystals: Synthesis, Characterization, and Its Catalytic Application to Oxidative Coupling of Benzylamines. *Inorganic Chemistry*. 53 (4), p2030-2039.
36. A.B. Jorge, J. Fraxedas, A. Cantarero, A.J. Williams, J. Rodgers, J.P. Attfield and A. Fuertes. (2008). Nitrogen Doping of Ceria. *Chemistry of Materials*. 20 (5), p1682-1684.
37. Y. Xu and R. Li. (2018). Wet-chemical synthesis and characterization of nitrogen-doped CeO_2 powders for oxygen storage capacity. *Applied Surface Science*. 455, p997-1004.
38. V. Thangadurai and P. Kopp. (2007). Chemical synthesis of Ca-doped CeO_2—Intermediate temperature oxide ion electrolytes. *Journal of Power Sources*. 168 (1), p178-183.
39. M. Yan, T. Mori, F. Ye, D.R. Ou, J. Zou and J. Drennan. (2008). Effects of dopant concentration and calcination temperature on the microstructure of Ca-doped ceria nanopowders. *Journal of the European Ceramic Society*. 28 (14), p2709-2716.
40. M. Yan, T. Mori, J. Zou and J. Drennan. (2009). Effect of Grain Growth on Densification and Conductivity of Ca-Doped CeO_2 Electrolyte. *Journal of the American Ceramic Society*. 92 (11), p2745-2750.
41. L. Truffault, T. Minh-Tri, T. Devers, K. Konstantinov, V. Harel, C. Simmonard, C. Andreazza, I.P. Nevirkovets, A. Pineau, O. Veron and J-P. Blondeau. (2010). Application of nanostructured Ca doped CeO_2 for ultraviolet filtration. *Materials Research Bulletin*. 45 (5), p527-535.
42. S. Carolis, J.L. Pascual and L.G.M. Pettersson. (1999). Structure and Electronic Properties of Ca-Doped CeO_2 and Implications on Catalytic Activity: An Experimental and Theoretical Study. *Journal of Physical Chemistry. B*. 103, p7627-7636.
43. M. Yan, T. Mori, J. Zou, H. Huang and J. Drennan. (2010). Microstructures and mechanical properties of $Ce_{1-x}Ca_xO_{2-y}$ ($x = 0.05, 0.1, 0.2$) with different sintering temperatures. *Journal of the European Ceramic Society*. 30 (3), p669-675.
44. G. Dutta, U.V. Waghmare, T. Baidya, M.S. Hedge, K.R. Priolkar and P.R. Sarode. (2006). Origin of Enhanced Reducibility/Oxygen Storage Capacity of $Ce_{1-x}Ti_xO_2$ Compared to CeO_2 or TiO_2. *Chemistry of Materials*. 18 (14), p3249-3256.
45. S. Yang, W. Zhu, Z. Jiang, Z. Chen and J. Wang. (2006). The surface properties and the activities in catalytic wet air oxidation over CeO_2–TiO_2 catalysts. *Applied Surface Science*. 252, p8499-8505.

46. W. Xu, Y. Yu, C. Zhang and H. He. (2008). Selective catalytic reduction of NO by NH_3 over a Ce/TiO_2 catalyst. *Catalysis Communications*. 9, p1453-1457.
47. X. Gao, Y. Jiang, Y. Zhong, Z. Luo and K. Cen. (2010). The activity and characterization of CeO_2-TiO_2 catalysts prepared by the sol–gel method for selective catalytic reduction of NO with NH_3. *Journal of Hazardous Materials*. 174 (1-3), p734-739.
48. P. Li, Y. Xin, Q. Li, Z. Wang, Z. Zhang and L. Zheng. (2012). Ce−Ti Amorphous Oxides for Selective Catalytic Reduction of NO with NH_3: Confirmation of Ce−O−Ti Active Sites. *Environmental Science and Technology*. 46, p9600-9605.
49. Z. Zhi-Qiang, M. Meng, G. Li-Hong and Z. Yu-Qing. (2009). Synthesis and characterization of $CuO/Ce_{1-x}Ti_xO_2$ catalysts used for low-temperature CO oxidation. *Journal of Hazardous Materials.* 163, p835-842.
50. M. Coduri, M. Scavini, M. Allieta, M. Brunelli and C. Ferrero. (2013). Defect Structure of Y-Doped Ceria on Different Length Scales. *Chemistry of Materials*. 25, p4278-4289.
51. M. Burbano, S.T. Norberg, S. Hull, S.G. Eriksson, D. Marrocchelli, P.A. Madden and G.W. Watson. (2012). Oxygen Vacancy Ordering and the Conductivity Maximum in Y_2O_3-Doped CeO_2. *Chemistry of Materials*. 24, p222-229.
52. J.V. Herle, T. Horita, T. Kawada, N. Sakai, H. Yokokawa and M. Dokiya. (1996). Sintering behaviour and ionic conductivity of yttria-doped ceria. *Journal of the European Ceramic Society*. 16 (9), p961-973.
53. P. Singh, M.S. Hedge and J. Gopalakrishnan. (2008). $Ce_{2/3}Cr_{1/3}O_{2+y}$: A New Oxygen Storage Material Based on the Fluorite Structure. *Chemistry of Materials*. 20, p7268-7273.
54. P. Singh and M.S. Hedge. (2010). $Ce_{0.67}Cr_{0.33}O_{2.11}$: A New Low-Temperature O_2 Evolution Material and H_2 Generation Catalyst by Thermochemical Splitting of Water. *Chemistry of Materials*. 22, p762-768.
55. P. Venkataswamy, D. Jampaiah, K.N. Rao and B.M. Reddy. (2014). Nanostructured $Ce_{0.7}Mn_{0.3}O_{2-\delta}$ and $Ce_{0.7}Fe_{0.3}O_{2-\delta}$ solid solutions for diesel soot oxidation. *Applied Catalysis A: General*. 488, p1-10.
56. W. Shan, N. Ma, J. Yang, X. Dong, C. Liu and L. Wei. (2010). Catalytic oxidation of soot particulates over MnO_x-CeO_2 oxides prepared by complexation-combustion method. *Journal of Natural Gas Chemistry*. 19, p86-92.
57. S. Liu, X. Wu, D. Weng and R. Ran. (2015). Ceria-based catalysts for soot oxidation: a review. *Journal of Rare Earths*. 33 (6), p567-590.
58. W. Xingyi, K. Qian and L. Dao. (2009). Catalytic combustion of chlorobenzene over MnO_x–CeO_2 mixed oxide catalysts. *Applied Catalysis B: Environmental*. 86 (3-4), p166-175.
59. H. Chen, A. Sayari, A. Adnot and F. Larachi. (2001). Composition–activity effects of Mn–Ce–O composites on phenol catalytic wet oxidation. *Applied Catalysis B: Environmental*. 32 (3), p195-204.
60. G. Picasso, M. Gutierrez, M.P. Pina and J. Herguido. (2007). Preparation and characterization of Ce-Zr and Ce-Mn based oxides for n-hexane combustion: Application to catalytic membrane reactors. *Chemical Engineering Journal*. 126 (2-3), p119-130.
61. G. Qi, R.T. Yang and R. Chang. (2004). MnO_x-CeO_2 mixed oxides prepared by co-precipitation for selective catalytic reduction of NO with NH_3 at low temperatures. *Applied Catalysis B: Environmental*. 51 (2), p93-106.
62. M. Machida, D. Kurogi and T. Kijima. (2003). NO_x storage and reduction characteristics of Pd/MnO_x–CeO_2 at low temperature. *Catalysis Today*. 84, p201-207.
63. R. Dziembaj, M. Molenda, M.M. Zaitz, L. Chmielarz and K. Furczon. (2013). Correlation of electrical properties of nanometric copper-doped ceria materials ($Ce_{1-x}Cu_xO_{2-\delta}$) with their catalytic activity in incineration of VOCs. *Solid State Ionics*. 251, p18-22.
64. J. Melnik, X.Z. Fu, J.L. Luo, A.R. Sanger, K.T. Chuang and Q.M. Yang. (2010). Ceria and copper/ceria functional coatings for electrochemical applications: Materials preparation and characterization. *Journal of Power Sources*. 195, p2189-2195.
65. S. Li, N. Wang, Y. Yue, G. Wang, Z. Zu and Y. Zhang. (2015). Copper doped ceria porous nanostructures towards a highly efficient bifunctional catalyst for carbon monoxide and nitric oxide elimination. *Chemical Science*. 6 (4), p2495-2500.
66. S. Yao, K. Mudiyanselage, W. Xu, A.C. Johnston-Peck, J.C. Hanson, T. Wu, D. Stacchiola, J.A. Rodriguez, H. Zhao, K.A. Beyer, K.W. Chapman, P.J. Chupas, A. Martinez-Arias, R.

Si, T.B. Bolin, W. Liu and S.D. Senanayake. (2014). Unravelling the Dynamic Nature of a CuO/CeO_2 Catalyst for CO Oxidation in Operando: A Combined Study of XANES (Fluorescence) and DRIFTS. *American Chemical Society Catalysis.* 4, p1650-1661.

67. M. Itoh, M. Saito, M. Takehara, K. Motoki, J. Iwamoto and K. Machida. (2009). Influence of supported-metal characteristics on deNO_x catalytic activity over Pt/CeO_2. *Journal of Molecular Catalysis A: Chemical*. 304 (1-2), p159-165.
68. S. Hinokuma, H. Fujii, Y. Katsuhara, K. Ikeue and M. Machida. (2014). Effect of thermal ageing on the structure and catalytic activity of Pd/CeO_2 prepared using arc-plasma process. *Catalysis Science and Technology*. 4 (9), p2990-2996.
69. N. Barrabes, K. Fottinger, A. Dafinov, F. Medina, G. Rupprechter, J. Llorca and J.E. Sueiras. (2009). Study of Pt–CeO_2 interaction and the effect in the selective hydrodechlorination of trichloroethylene. *Applied Catalysis B: Environmental*. 87 (1-2), p84-91.
70. X. Hong and Y. Sun. (2016). Effect of Preparation Methods on the Performance of Pt/CeO_2 Catalysts for the Catalytic Oxidation of Carbon Monoxide. *Catalysis Letters*. 146, p2001-2008.
71. D.O. Scanlon, B.J. Morgan and G.W. Watson. (2011). The origin of the enhanced oxygen storage capacity of $Ce_{1-x}(Pd/Pt)_xO_2$. *Journal of Physical Chemistry*. 13, p4279-4284.
72. P. Bera and M.S. Hegde. (2015). Noble metal ions in CeO_2 and TiO_2: synthesis, structure and catalytic properties. *Royal Society of Chemistry Advances*. 5, p94949-94979.
73. Y. Gao, W. Wang, S. Chang and W. Huang. (2013). Morphology Effect of CeO_2 Support in the Preparation, Metal–Support Interaction, and Catalytic Performance of Pt/CeO_2 Catalysts. *ChemCatChem*. 5, p3610-3620.
74. P. Bera, K.C. Patil, V. Jayaram, G.N. Subbanna and M.S. Hedge. (2000). Ionic Dispersion of Pt and Pd on CeO_2 by Combustion Method: Effect of Metal–Ceria Interaction on Catalytic Activities for NO Reduction and CO and Hydrocarbon Oxidation. *Journal of Catalysis*. 196, p293-301.
75. K.R. Priolkar, P. Bera, P.R. Sarode, M.S. Hedge, S. Emura, R. Kumashiro and N.P. Lalla. (2002). Formation of $Ce_{1-x}Pd_xO_{2-\delta}$ Solid Solution in Combustion-Synthesized Pd/CeO_2 Catalyst: XRD, XPS, and EXAFS Investigation. *Chemistry of Materials*. 14, p2120-2128.
76. M.S. Hedge and P. Bera. (2015). Noble metal ion substituted CeO_2 catalysts: Electronic interaction between noble metal ions and CeO_2 lattice. *Catalysis Today*. 253, p40-50.
77. F. Lin, A. Wokaun and I. Alxneit. (2015). Rh-doped ceria: solar organics from H_2O, CO_2 and sunlight? *Energy Procedia*. 69, p1790-1799.
78. P. Singh and M.S. Hedge. (2010). Sonochemical Synthesis of Thermally Stable Hierarchical $Ce_{1-x}M_xO_{2-\delta}$ (M = Pt or Pd, $0 \leq x \leq 0.10$) Nanocrystallites: Redox Properties and Methanol Electro-Oxidation Activity. *Crystal Growth and Design*. 10 (7), p2995-3004.
79. P. Singh, N. Mahadevaiah, S.K. Parida and M.S. Hedge. (2011). Ru^{4+} ion in CeO_2 ($Ce_{0.95}Ru_{0.05}O_{2-\delta}$): A non-deactivating, non-platinum catalyst for water gas shift reaction. *Journal of Chemical Sciences*. 123 (5), p577-592.
80. W. Qin, L. Xu, J. Song, R. Xing and H. Song. (2013). Highly enhanced gas sensing properties of porous SnO_2–CeO_2 composite nanofibers prepared by electrospinning. *Sensors and Actuators B: Chemical*. 185, p231-237.
81. H. Chang, J. Li, X. Chen, L. Ma, S. Yang, J.W. Schwank and J. Hao. (2012). Effect of Sn on MnO_x–CeO_2 catalyst for SCR of NO_x by ammonia: Enhancement of activity and remarkable resistance to SO_2. *Catalysis Communications*. 27, p54-57.
82. A. Gupta, M.S. Hedge, K.R. Priolkar, U.V. Waghmare, P.R. Sarode and S. Emura. (2009). Structural Investigation of Activated Lattice Oxygen in $Ce_{1-x}Sn_xO_2$ and $Ce_{1-x-y}Sn_xPd_yO_{2-\delta}$ by EXAFS and DFT calculation. *Chemistry of Materials*. 21, p5836-5847.
83. G. Xiao, S. Li, H. Li and L. Chen. (2009). Synthesis of doped ceria with mesoporous flower-like morphology and its catalytic performance for CO oxidation. *Microporous and Mesoporous Materials*. 120 (3), p426-431.
84. R. Sasikala, N.M. Gupta and S.K. Kulshreshtha. (2001). Temperature-programmed reduction and CO oxidation studies over Ce–Sn mixed oxides. *Catalysis Letters*. 71 (1-2), p69-73.
85. Z. Liu, X. Feng, Z. Zhou, Y. Feng and J. Li. (2018). Ce-Sn binary oxide catalyst for the selective catalytic reduction of NO_x by NH_3. *Applied Surface Science*. 428, p526-533.

86. K.C. Anjaneya, G.P. Nayaka, J. Manjanna, G. Govindaraj and K.N. Ganesha. (2013). Preparation and characterization of $Ce_{1-x}Gd_xO_{2-\delta}$ (x = 0.1–0.3) as solid electrolyte for intermediate temperature SOFC. *Journal of Alloys and Compounds*. 578, p53-59.
87. B. Rambabu, S. Ghosh and H. Jena. (2006). Novel wet-chemical synthesis and characterization of nanocrystalline CeO_2 and $Ce_{0.8}Gd_{0.2}O_{1.9}$ as solid electrolyte for intermediate temperature solid oxide fuel cell (IT-SOFC) applications. *Journal of Materials Science*. 41, p7530-7536.
88. J.M. Im, H.J. You, Y.S. Yoon and D.W. Shin. (2008). Synthesis of nano-crystalline $Gd_{0.1}Ce_{0.9}O_{2-x}$ for IT-SOFC by aerosol flame deposition. *Ceramics International*. 34 (4), p877-881.
89. T. Mori, R. Buchanan, D.R. Ou, F. Ye, T. Kobayashi, J.D. Kim, J. Zou and J. Drennan. (2008). Design of nanostructured ceria-based solid electrolytes for development of IT-SOFC. *Journal of Solid State Electrochemistry*. 12, p841-849.
90. M.J. Kishor Kumar and J.T. Kalathi. (2018). Low-temperature sonochemical synthesis of high dielectric Lanthanum doped Cerium oxide nanopowder. *Journal of Alloys and Compounds*. 748, p348-354.
91. N. Guillen-Hurtado, A. Garcia-Garcia and A. Bueno-Lopez. (2015). Active oxygen by Ce–Pr mixed oxide nanoparticles outperform diesel soot combustion Pt catalysts. *Applied Catalysis B: Environmental*. 174-175, p60-66.
92. V. Rico-Perez, E. Aneggi, A. Bueno-Lopez and A. Trovarelli. (2016). Synergic effect of $Cu/Ce_{0.5}Pr_{0.5}O_{2-\delta}$ and $Ce_{0.5}Pr_{0.5}O_{2-\delta}$ in soot combustion. *Applied Catalysis B: Environmental*. 197, p95-104.
93. K. Harada, T. Oishi, S. Hamamoto and T. Ishihara. (2014). Lattice Oxygen Activity in Pr- and La-Doped CeO_2 for Low-Temperature Soot Oxidation. *Journal of Physical Chemistry C*. 118 (1), p559-568.
94. K. Krishna, A. Bueno-Lopez, M. Makkee and J.A. Moulijn. (2007). Potential rare-earth modified CeO_2 catalysts for soot oxidation. *Topics in Catalysis*. 42-43, p221-228.
95. K.C. Chanapattharapol, S. Krachuamram, A. Makdee, P. Unwiset and S. Srikwanjai. (2017). Preparation and characterization of $Ce_{1-x}Pr_xO_2$ supports and their catalytic activities. *Journal of Rare Earths*. 35 (12), p1197-1205.
96. A.M. D'Angelo and A.L. Chaffee. (2017). Oxygen uptake, selectivity and reversibility of Tb–CeO_2 mixed oxides for air separation. *Adsorption*. 23 (4), p465-475.
97. L.G.A. Carvalho, L.A. Rocha, J.M.M. Buarque, R.R. Goncalves, C.S. Nascimento, M.A. Schiavon, S.J.L. Ribeiro and J.L. Ferrari. (2015). Color tunability in green, red and infra-red upconversion emission in $Tm^{3+}/Yb^{3+}/Ho^{3+}$ co-doped CeO_2 with potential application for improvement of efficiency in solar cells. *Journal of Luminescence*. 159, p223-228.
98. E. Swatsitang, S. Phokha, S. Hunpratub and S. Maensiri. (2016). Characterization of Sm-doped CeO_2 nanoparticles and their magnetic properties. *Physica B: Condensed Matter*. 485, p14-20.
99. M. Balestrieri, S. Colis, M. Gallart, G. Schmerber, P. Bazylewski, G.S. Chang, M. Ziegler, P. Gilliot, A. Slaoui and A. Dinia. (2016). Photon management properties of rare-earth (Nd,Yb,Sm)-doped CeO_2 films prepared by pulsed laser deposition. *Physical Chemistry Chemical Physics*. 18 (4), p2527-2534.
100. A.A. Ibrahim, A.Y. Ilyushechkin and I.E. Agranovski. (2014). Oriented Sm-doped CeO_2 thin films on biaxially textured Ni-W substrate produced by ultrasonic spray deposition. *Materials Letters*. 136, p435-437.
101. M.K. Chinnu, K.V. Anand, R.M. Kumar, T. Alagesan and R. Jayavel. (2013). Synthesis and enhanced electrochemical properties of Sm:CeO_2 nanostructure by hydrothermal route. *Materials Letters*. 113, p170-173.
102. P.S. Anjana, T. Joseph and M.T. Sebastian. (2010). Microwave dielectric properties of $_{(1-x)}CeO_{2-x}RE_2O_3$ (RE = La, Nd, Sm, Eu, Gd, Dy, Er, Tm, Yb and Y) ($0 \leq x \leq 1$) ceramics. *Journal of Alloys and Compounds*. 490 (1-2), p208-213.
103. Y. Xin, Y. Qi, X. Ma, Z. Wang, Z. Zhang and S. Zhang. (2010). Rare-earth (Nd, Sm, Eu, Gd and Y) enhanced CeO_2 solid solution nanorods prepared by co-precipitation without surfactants. *Materials Letters*. 64 (23), p2659-2662.

104. V.A. Sadykov, T.G. Kuznetsova, G.M. Alikina, Y.V. Frolova, A.I. Lukashevich, Y.V. Potapova, V.S. Muzykantov, V.A. Rogov, V.V. Kriventsov, D.I. Kochubei, E.M. Moroz, D.I. Zyuzin, V.I. Zaikovskii, V.N. Kolomiichuk, E.A. Paukshtis, E.B. Burgina, V.V. Zyryanov, N.F. Uvarov, S. Neophytides and E. Kemnitz. (2004). Ceria-based fluorite-like oxide solid solutions as catalysts of methane selective oxidation into syngas by the lattice oxygen: synthesis, characterization and performance. *Catalysis Today*. 93-95, p45-53.
105. T. Mori, J. Drennan, J.H. Lee, J.G. Li and T. Ikegami. (2002). Oxide ionic conductivity and microstructures of Sm- or La-doped CeO_2-based systems. *Solid State Ionics*. 154-155, p461-466.
106. J. Beckers, A.F. Lee and G. Rothenberg. (2009). Bismuth-Doped Ceria, $Ce_{0.90}Bi_{0.10}O_2$: A Selective and Stable Catalyst for Clean Hydrogen Combustion. *Advanced Synthesis and Catalysis*. 351, p1557-1566.
107. D. Jiang, W. Wang, E. Gao, L. Zhang and S. Sun. (2013). Bismuth-Induced Integration of Solar Energy Conversion with Synergistic Low-Temperature Catalysis in $Ce_{1-x}Bi_xO_{2-\delta}$ Nanorods. *Physical Chemistry*. 117, p24242-24249.
108. G. Li, Y. Mao, L. Li, S. Feng, M. Wang and X. Yao. (1999). Solid Solubility and Transport Properties of Nanocrystalline $(CeO_2)_{1-x}(BiO_{1.5})_x$ by Hydrothermal Conditions. *Chemistry of Materials*. 11 (5), p1259-1266.
109. K. Sardar, H.Y. Playford, R.J. Darton, E.R. Barney, A.C. Hannon, D. Thompsett, J. Fisher, R.J. Kashtiban, J. Sloan, S. Ramos, G. Cibin and R.I. Walton. (2010). Nanocrystalline Cerium-Bismuth Oxides: Synthesis, Structural Characterization, and Redox Properties. *Chemistry of Materials*. 22, p6191-6201.
110. H. Zhao, S. Feng and W. Xu. (2000). A soft chemistry route for the synthesis of nano solid electrolytes $Ce_{1-x}Bi_xO_{2-x/2}$. *Materials Research Bulletin*. 35 (14-15), p2379-2386.
111. L. Bourja, B. Bakiz, A. Benlhachemi, M. Ezahri, S. Villain and J.R. Gavarri. (2010). Synthesis and characterization of nanosized $Ce_{1-x}Bi_xO_{2-\delta}$ solid solutions for catalytic applications. *Journal of Taibah University for Science*. 4, p1-8.
112. M. Prekajski, M. Stojmenovic, A. Radojkovic, G. Brankovic, H. Oraon, R. Subasri and B. Matovic. (2014). Sintering and electrical properties of $Ce_{1-x}Bi_xO_{2-\delta}$ solid solution. *Journal of Alloys and Compounds*. 617, p563-568.
113. M. Prekajski, Z. Dohcevic-Mitrovic, M. Radovic, B. Babic, J. Pantic, A. Kremenovic and B. Matovic. (2012). Nanocrystaline solid solution CeO_2–Bi_2O_3. *European Ceramic Society*. 32 (9), p1983-1987.
114. F. Zhou, X. Zhao, H. Xu and C. Yuan. (2007). CeO_2 Spherical Crystallites: Synthesis, Formation Mechanism, Size Control, and Electrochemical Property Study. *The Journal of Physical Chemistry C*. 111, p1651-1657.
115. C.R. Li, M.Y. Cui, Q.T. Sun, W.J. Dong, Y.Y. Zheng, K. Tsukamoto, B.Y. Chen and W.H. Tang. (2010). Nanostructures and optical properties of hydrothermal synthesized $CeOHCO_3$ and calcined CeO_2 with PVP assistance. *Journal of Alloys and Compounds*. 504 (2), p498-502.
116. K. Li and P. Zhao. (2009). Synthesis and characterization of $CeCO_3OH$ one-dimensional quadrangular prisms by a simple method. *Materials Letters*. 63, p2013-2015.
117. L. Chung-Hsin and W. Hsien-Cheng. (2002). Formation and microstructural variation of cerium carbonate hydroxide prepared by the hydrothermal process. *Materials Science and Engineering: B*. 90 (1-2), p138-141.
118. G. Kun, Z. Yi-Yang, T. Da-Qing, T. Li, W. Zhao-Hui and W. Xiao-Zu. (2014). Hydrothermal synthesis of single-crystal $CeCO_3OH$ and their thermal conversion to CeO_2. *Chinese Chemical Letters*. 25 (2), p383-386.
119. Z. Guo, F. Du and Z. Cui. (2009). Hydrothermal synthesis of single-crystalline $CeCO_3OH$ flower-like nanostructures and their thermal conversion to CeO_2. *Materials Chemistry and Physics*. 113, p53-56.
120. N. Sabari Arul, D. Mangalaraj and T. Whan Kim. (2013). Photocatalytic degradation mechanisms of self-assembled rose-flower-like CeO_2 hierarchical nanostructures. *Applied Physics Letters*. 102, p223115-223119.
121. Z. Guo, F. Du and Z. Cui. (2007). Synthesis and characterization of bundle-like structures consisting of single crystal $Ce(OH)CO_3$ nanorods. *Materials letters*. 61, p694-696.

122. Z. Guo, F. Du, G. Li and Z. Cui. (2008). Synthesis of Single-crystalline $CeCO_3OH$ with Shuttle Morphology and Their Thermal Conversion to CeO_2. *Crystal Growth and Design*. 8 (8), p2674-2677.
123. F. Hrizi, H. Dhaouadi and F. Touati. (2014). Cerium carbonate hydroxide and ceria micro/nanostructures: Synthesis, characterization and electrochemical properties of $CeCO_3OH$. *Ceramics International*. 40 (A), p25-30.
124. J.R. Gonzalez-Velasco, M.A. Gutierrez-Ortiz, J.L. Marc, J.A. Botas, M.P. Gonzalez-Marcos and G. Blanchard. (1999). Contribution of cerium/zirconium mixed oxides to the activity of a new generation of TWC. *Applied Catalysis B*. 22, p167-178.
125. J.R. Gonzalez-Velasco, M.A. Gutierrez-Ortiz, J.L. Marc, J.A. Botas, M.P. Gonzalez-Marcos and G. Blanchard. (2000). Effects of redox thermal treatments and feedstream composition on the activity of Ce/Zr mixed oxides for TWC applications. *Applied Catalysis B*. 25 (1), p19-29.
126. S.J. Schmieg and D.N. Belton. (1995). Effect of hydrothermal aging on oxygen storage/release and activity in a commercial automotive catalyst. *Applied Catalysis B*. 6, p127-144.
127. A.E. Nelson and K.H. Schulz. (2003). Surface chemistry and microstructural analysis of $Ce_xZr_{1-x}O_{2-y}$ model catalyst surfaces. *Applied Surface Science*. 210, p206-221.
128. C. Bozo, F. Gaillard and N. Guilhaume. (2001). Characterisation of ceria–zirconia solid solutions after hydrothermal ageing. *Applied Catalysis A*. 220, p69-77.
129. L. Zhu, J. Yu and X. Wang. (2007). Oxidation treatment of diesel soot particulate on $Ce_xZr_{1-x}O_2$. *Journal of Hazardous Materials*. 140 (1-2), p205-210.
130. S. Letichevsky, C.A. Tellez, R.R. Avillez, M.I.P. Silva, M.A. Fraga and L.G. Appel. (2005). Obtaining CeO_2–ZrO_2 mixed oxides by coprecipitation: role of preparation conditions. *Applied Catalysis B*. 58 (3-4), p203-210.
131. M. Alifanti, B. Baps, N. Blangenois, J. Naud, P. Grange and B. Delmon. (2003). Characterization of CeO_2-ZrO_2 Mixed Oxides. Comparison of the Citrate and Sol-Gel Preparation Methods. *Chemistry of Materials*. 15, p395-403.
132. R. Si, Y.W. Zhang S.J. Li, B.X. Lin and C.H. Yan. (2004). Urea-Based Hydrothermally Derived Homogeneous Nanostructured $Ce_{1-x}Zr_xO_2$ (x = 0-0.8) Solid Solutions: A Strong Correlation between Oxygen Storage Capacity and Lattice Strain. *Journal of Physical Chemistry B*. 108 (33), p12481-12488.
133. T. Dhannia, S. Jayalekshmi, M.C. Santhosh Kumar, T. Prasado Rao and A. Chandra Bose. (2009). Effect of aluminium doping and annealing on structural and optical properties of cerium oxide nanocrystals. *Journal of Physics and Chemistry of Solids*. 70 (11), p1443-1447.
134. R.S. Kalubarme and C. Park. (2012). Al-doped Ceria: A New Cathode Catalyst for LiO_2. *The Chemical society of Japan*. 41, p612-613.

2. Experimental

2.1 Crystal systems and unit cells

Crystals are regular-shaped solid particles that are derived from a three-dimensional arrangement of atoms. These arrangements are composed of basic repeat units, singularly known as a *unit cell*. By defining the different shapes and symmetries of the unit cell as well as the locations and the identities of the atoms within it, enables an easy method to both categorise and compare different crystal systems. As most importantly, regardless of its physical size the entire crystal can be reconstructed by simple translations of this unit cell in any direction. Six scalar quantities are used to define the dimensions and geometries of the unit cell: (*a*, *b* and *c*) represent each edge of the unit cell and (α, β and γ) represent the angles between them. Together these scalar quantities with the simple translational symmetry give rise to seven different crystal classes as shown in Figure 2. The positions of the atoms within these unit cells are described by fractional co-ordinates (*x*, *y* and *z*) with respect to a point of origin.

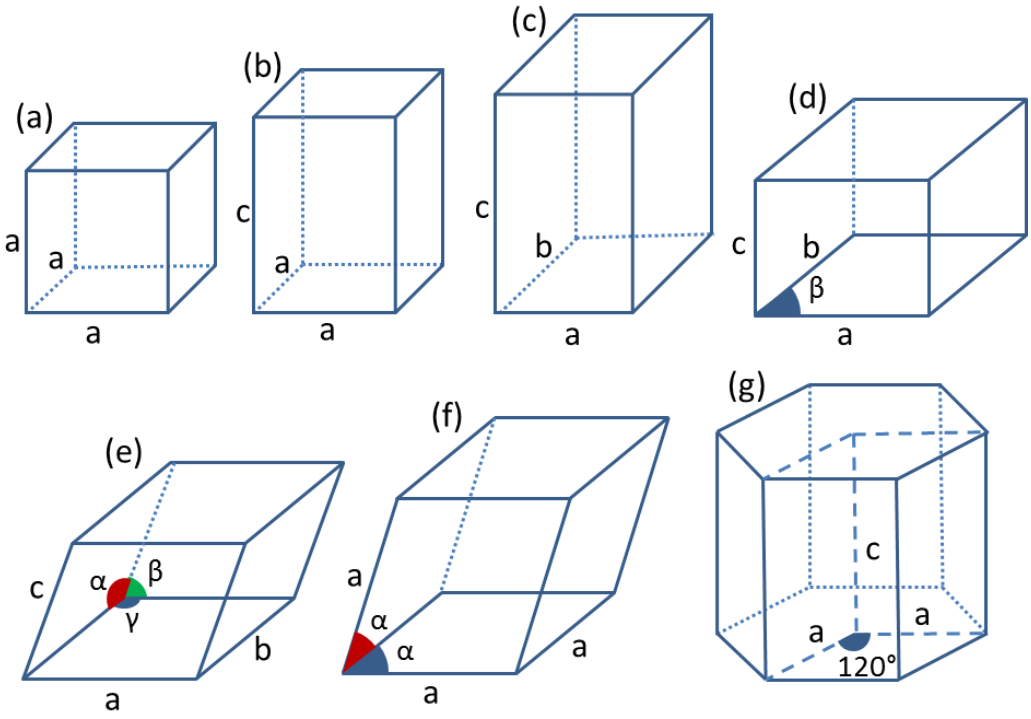

Figure 2: Unit cells of the seven crystal systems: (a) Cubic, (b) Tetragonal, (c) Orthorhombic, (d) Monoclinic, (e) Triclinic, (f) Trigonal and (g) Hexagonal.

2.2 Lattice and Bravais lattice

A *lattice* is defined as a regular array of equivalent points, termed *lattice points*. The unit cells are constructed by linking these lattice points in three dimensional space. The lattice provides no information about the positions of the atoms, only the translational symmetry. A lattice can be one of four unique possibilities, either primitive, body-centred, face-centred or base centred denoted as P, I, F and C respectively. A primitive cell contains lattice points in only the corners. A body-centred lattice contains an additional lattice point in the centre of the cell. A face-centred lattice contains lattice points centred on each of the faces. A base-centred lattice contains points that are on an opposite pair of faces. These four possibilities as shown in Figure 3 can be combined with the seven crystal systems to form what is known as *Bravais lattices* which define all possible crystal variations.

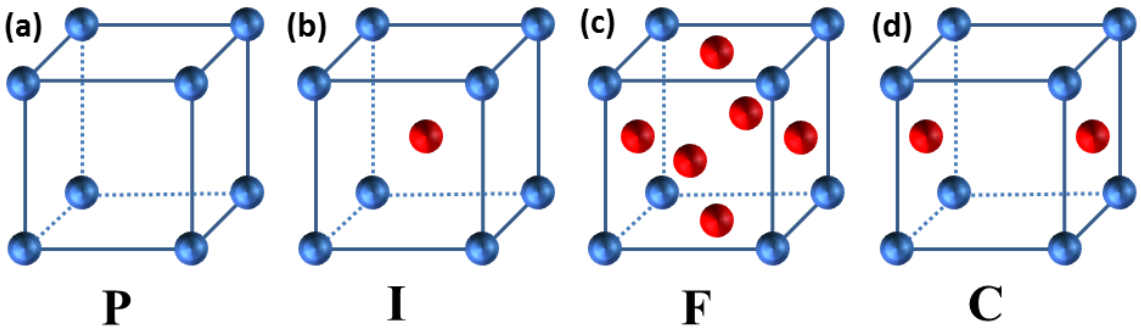

Figure 3: Bravais lattices for the cubic unit cell: (a) P- Primitive, (b) I - Body centred, (c) F- Face-centred and (d) C-Base-centred.

Additionally, however, not all of the four lattices can be combined with each of the seven different crystal systems to give rise to a unique Bravais lattice. As some would violate symmetry requirements, hence there are fourteen different types of Bravais lattice as shown in Table 1.

Table 1: The seven crystal systems and their respective parameters and Bravais lattices.

Crystal system	Unit cell parameters	Bravais lattices	Example
Cubic	$a=b=c$, $\alpha=\beta=\gamma=90°$	P, I, F	NaCl
Tetragonal	$a=b\neq c$, $\alpha=\beta=\gamma=90°$	P, I	TiO_2
Orthorhombic	$a\neq b\neq c$, $\alpha=\beta=\gamma=90°$	P, I, F, C	$MgSO_4$
Hexagonal	$a=b\neq c$, $\alpha=\beta=90°$, $\gamma=120°$	P	ZnO
Trigonal (a)	$a=b=c$, $\alpha=\beta=\gamma\neq90°$	P	$CaMg(CO_3)_2$
Trigonal (b)	$a=b\neq c$, $\alpha=\beta=90°$, $\gamma=120°$	P	$Ir_4(CO)_{12}$
Monoclinic (a)	$a\neq b\neq c$, $\alpha=\gamma=90°$, $\beta\neq90°$	P, C	KYb_2F_7
Monoclinic (b)	$a\neq b\neq c$, $\alpha=\beta=90°$, $\gamma\neq90°$	P, C	Gd_2Cl_3
Triclinic	$a\neq b\neq c$, $\alpha\neq\beta\neq\gamma\neq90°$	P	$K_2Cr_2O_7$

2.3 Miller Indices and lattice planes

Repeat translations of the unit cells form an equally spaced array of lattice points. Connecting these lattice points with imaginary lines in two dimensional space forms parallel sets of lines known as lattice planes. For three dimensional structures these lines are known as lattice planes which are described by integer values, (h, k and l), called Miller indices. The Miller indices (hkl) refer to the intersection of the plane on the three axes of the unit cell (a, b and c) from a defined origin. The points of intersection occur at fractional intercepts along each edge and hence are given by reciprocals of the Miller indices $(1/h, 1/k \text{ and } 1/l)$. The perpendicular distances separating these parallel lattice planes are known as the d-spacing, denoted as d_{hkl}. The Bragg peaks in an X-ray diffraction pattern can be indexed by relating these distances to the Miller indices by an equation specific to each individual crystal system. For simple cubic systems the equation is given below:

$$\frac{1}{d_{hkl}^2} = \frac{h^2+k^2+l^2}{a^2}$$

2.4 X-ray analysis

2.4.1 Powder X-ray Diffraction (XRD)

Powder X-ray diffraction (XRD) is a useful technique to analyse the structure of crystalline solids and is able to provide information about both the size of the unit cell and its symmetry. The X-rays interact with the electron cloud surrounding atoms as they are of an appropriate wavelength to be diffracted by the crystal lattice. Bragg's law describes this diffraction in terms of reflections of the X-rays from a parallel set of lattice planes. Bragg's Law states that a parallel beam of monochromatic X-rays directed at the surface of a crystal with an incident angle, θ, will be reflected with the same angle of scattering as shown in Figure 4. If the d-spacing, d, between the crystal planes is equal to an integer number, n, of the wavelength, λ, then constructive interference will occur.

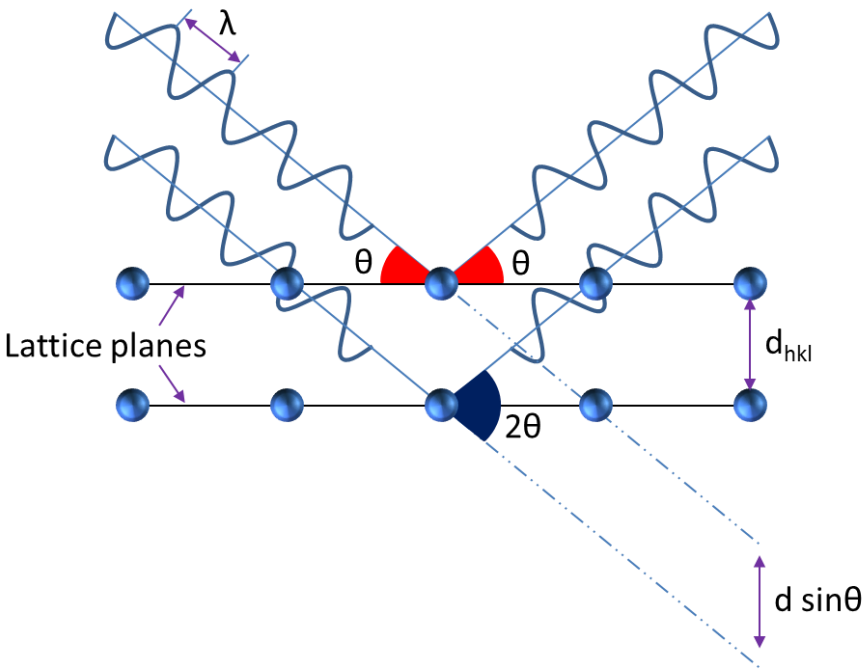

Figure 4: Pictorial derivation of Bragg's Law.

Bragg equation:

$$n\lambda = 2dsin\theta$$

Symbol	Definition
n	An integer
λ	X-ray wavelength
d	d-spacing
θ	Bragg angle

Grinding a crystal sample into a fine powder produces a large number of small crystallites with a vast range of random orientations. Subjecting this powder to a monochromatic beam of X-rays will cause diffraction to occur from the different symmetry planes within, that have the desired orientation to fulfil the Bragg equation. By vary both the angle of incident beam and the position of the detector it is possible to produce a diffraction pattern by plotting the counts of the detected X-rays as a function of the scattering angle (2θ).

2.4.2 Powder X-ray diffraction (XRD) experiment

A Bruker D5000 powder X-ray diffractometer equipped with a standard Bragg-brentano reflection geometry was used to characterise the majority of the prepared samples. The diffractometer also employs a Cu K_α radiation (λ_1 = 1.5405 Å, λ_2 = 1.5418 Å) source. A typical scan short scan range was between 10 – 60° with at step size of 0.02° and a time per step of 1.3 seconds. All of the samples were rotated

during the measurements at 1 rpm to reduce effects of preferred orientation from the powder. The typical long range scans covered 10 – 120° with at step size of 0.02° and a time per step of 11 seconds.

The samples were transferred into circularly indented aluminium sample holder and pressed down by a glass slide. The diffractometer is tuned to reduce the aluminium Bragg peaks attributed to the sample holder.

2.4.3 High resolution powder XRD experiment

High resolution powder XRD data was collected using a PANalytical X'Pert Pro MRD powder X-ray diffractometer equipped with a Johansson monochromator to produce monochromatic Cu $K_{\alpha 1}$ radiation (λ = 1.5406 Å). A typical scan was measured over an angle range of 10 – 80° and had a step size of 0.0131° and a time per step of 10 s.

2.4.4 In situ heating powder XRD

A Bruker D8 Advance powder diffractometer was used to collect in situ heating powder XRD under flow of air. Samples were loaded onto a ceramic sample holder and held within an Anton Paar XRK 900 reaction chamber. Each individual scan was measured over an angle range of 10 – 60° and had a step size of 0.0081° and a time per step of 0.45 s. The data was collected at 30 °C and ramped at 10 °C intervals to 800 °C at a heating ramp rate of 0.2 $°Cs^{-1}$. A dwell time of 300 s was inserted before each scan was measured in order for the temperature to stabilise.

2.4.5 Profile refinement

The collected XRD patterns of the materials were refined using the Le Bail method. This was achieved by inputting the raw data and the appropriate space group in to GSAS, a parameter refinement software. The software enabled for the determination of both the lattice parameters and for the full width half –maximum (FWHM) for each of the Bragg peaks in the pattern.

2.4.6 Scherrer equation

From the calculated FWHM, the crystallite sizes of each of the samples were estimated using the Scherrer equation. As the size of the crystals have a direct correlation with the widths of the Bragg peaks within a diffraction pattern.

Scherrer equation:

$$\tau = \frac{K\lambda}{\beta cos\theta}$$

Symbol	Definition
τ	Crystallite size (Å)
β	Line broadening (FWHM)
θ	Bragg angle
λ	X-ray wavelength (Å)
K	Shape factor

2.4.7 Williamson-Hall plot analysis

Another method employed to aid with the estimation of the particle sizes of the produced materials is the Williamson-Hall plot analysis. [1-2] The method relies on the general principle that not only does the width of the Bragg peaks broaden due to the size of the crystallites but also that there is a strain component. The principle is that these two factors vary very differently with respect to the Bragg angle. The equation below enables a quick estimation of both of these parameters simultaneously, by plotting Bcosθ as a function of sinθ. The gradient of slope being the strain component (Cε) and the y-intercept as the Kλ/L expression, shown below.

$$B cos\theta = C\varepsilon sin\theta + \frac{K\lambda}{L}$$

$$y = mx + c$$

Symbol	Definition
B	Line broadening (FWHM)
θ	Bragg angle
Cε	Strain component
K	Shape factor
λ	X-ray wavelength (Å)
L	Crystallite size (Å)

2.4.8 X-ray absorption near-edge structure (XANES)

X-ray absorption near-edge structure (XANES) is an X-ray absorption technique that provides both structural and electronic information about the bulk of a given sample. XANES is an element specific technique that involves scanning a range of energies to measure the absorption co-efficient at each step. Quantitatively it describes the difference in X-ray intensity between the incident and the transmitted as shown in the equation below. The absorption process involves atoms absorbing the incident X-ray beam at certain energies through the photo-electric effect. The general principle is that the core level electrons (such as the 1s or 2p levels) absorb the energy of the incident X-ray beam and subsequently eject an electron, known as a *photo-electron*. Leaving the atom in an excited state with an empty electronic level, termed a *core hole*. Any excess absorbed energy is transferred to the ejected photo-electrons, which propagate out of the atom. The scattering photo-electrons propagate out as a

spherical wave that interacts with surrounding atoms, by scattering back to the absorbing atom. This produces an interference pattern as the back-scattering electron interfere with the photo-electrons radiating from the absorbing atom. XANES focuses on the near-edge structure of this inference pattern, that is to say up to about 200 eV either side of the edge position ('white line'). The edge position refers to the sharp absorption increase produced as the energy of the X-ray approaches the binding energy of core level electrons. As the energy required to eject the photo-electrons initially must be of greater energy for the particular element under analysis, which is the reason for the technique being element specific. The near-edge region is directly influenced by the nature of the chemical environment surrounding the absorbing atom. The position of the edge in particular being dependant on the oxidation state and molecular symmetry of the site, with the position shifting to higher energy with an increased oxidation state. Comparing the shifts measured to a set of known standard samples allows for the determination of the ratio of oxidation states within mixed oxides.

$$I_t(E) = I_0(E)e^{-\mu(E)t}$$

$$\mu(E) = \frac{1}{t}\ln(^{I_0}/_{I_t})$$

Symbol	Definition
I_t	Transmitted X-ray intensity
I_0	Incident X-ray intensity
μ	Absorption coefficient
t	Sample thickness

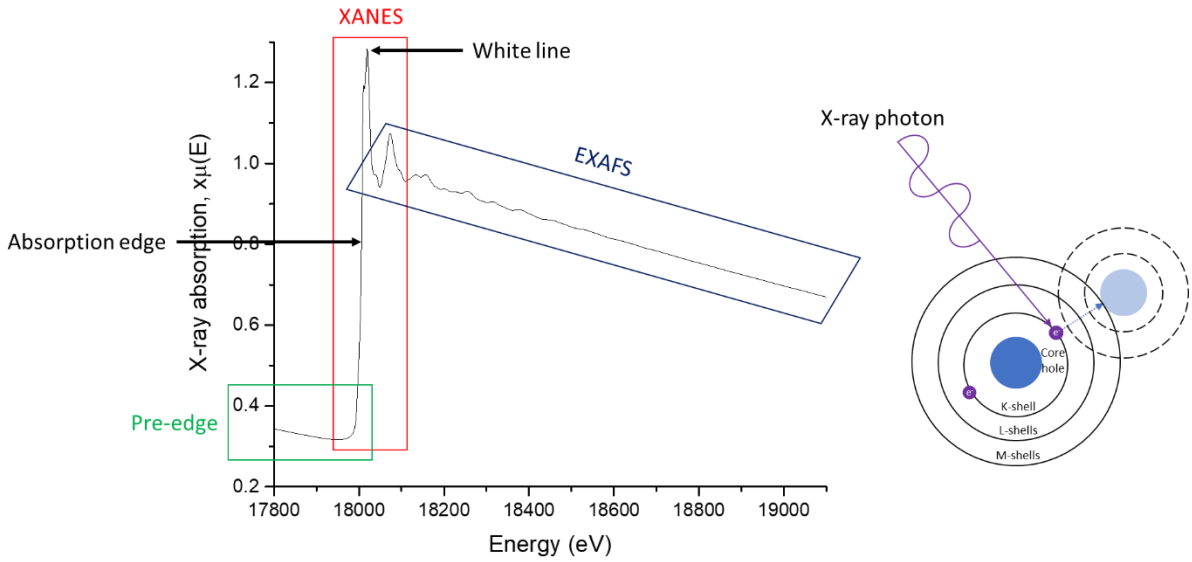

Figure 5: An X-ray absorption spectrum split into the difference regions of interest.

2.5 General characterisation techniques

2.5.1 Thermal gravimetric analysis (TGA)

Thermal analysis was performed to determine the mass loss of the starting reagents and the mixed-metal oxides as a function of temperature, providing information about the decomposition of the materials and the quantification of the water content. A Mettler Toledo TGA/DSC 1 STAR^e System was used to implement the analysis and the data was processed using the supplied STAR^e version 12.1 software.

Small quantities of sample (5-10 mg) were transferred into an alumina crucible (70 μL) and placed on the instrument for analysis. The samples were analysed under flow of nitrogen gas (100 cm^3 min^{-1}) using the following heating profile: 30 °C to 1000 °C at 5 °C min^{-1}.

2.5.2 Scanning electron microscopy (SEM)

A Zeiss Supra 55-VP field emission scanning electron microscope (FE-SEM) was used to study the topography and the morphology of the prepared materials. The modes of detection that were used to capture the micrographs were InLens (backscattered electrons) and secondary electrons. The applied accelerating voltages were within the range of 5-10 kV at an aperture size of around 10 μm. SmartSEM software was used to capture and process images.

Energy dispersive X-ray analysis (EDXA) was used to determine approximate metal ratios of the samples by selectively analysing multiple areas (approx. 6) to infer homogeneity. Genesis Software was used to collect and quantify the data and process the information into EDXA spectrums. The results in this thesis correspond to the average atomic percentage of the elements identified in the EDXA spectrum.

Aluminium circular SEM stubs (12.5 mm, diameter) were covered by adhesive conductive carbon tape. The powdered samples were transferred on to individual SEM stubs. The stubs were placed within a carbon evaporator to coat the sample with carbon particles to reduce charging.

2.5.3 Transmission electron microscopy (TEM)

Transmission electron micrographs were collected by Reza J. Kashtiban, using a JEOL ARM200F TEM operating at 200 kV.

2.5.4 Raman spectroscopy

Room temperature Raman spectra were acquired using a Renishaw inVia reflex Raman microscope equipped with a HeNe laser with wavelength 633 nm and Renishaw charged-coupled device (CCD) detector. The Raman spectra were recorded using the equipped x50 objective lens and acquisition times were 15 mins for 6 repetitions.

2.5.5 Infra-red spectroscopy

Infra-red spectra were recorded using a Bruker Alpha FT-IR spectrometer equipped with a single reflection platinum attenuated total reflection sampling module. The spectra were measured across 400 – 4000 cm^{-1} and was used to determine the presence of water, hydroxide or any organic components.

2.5.6 X-ray photoelectron spectroscopy (XPS)

XPS was performed using a Kratos AXIS Ultra DLD equipped with a monochromatic Al K_α source ($h\nu$ = 1486.6 eV). XPS measurements were carried out in an ultra-high vacuum (UHV) system with a base pressure of 5×10^{-11} mbar. The measurements were conducted at room temperature and the photo-electrons being detected at a 90° with respect to the surface. The data was analysed using the CasaXPS package, using Shirley-type backgrounds and Voigt (mixed Gaussian-Lorentzian) line shapes. The samples were mounted on carbon tape attached to an aluminium sample holder.

2.5.7 Solid state nuclear magnetic resonance (solid state NMR)

Solid state ^{27}Al MAS-NMR was performed by Maria Vlachou at the University of Warwick.

2.5.8 Brunauer-Emmett-Teller (BET)

Surface area measurements were calculated from N_2-adsorption isotherms, through which the number of N_2 molecules absorbed onto the surface of the particle is correlated to the total surface area of the material. The BET measurements were collected using a Micrometrics Tristar 3000 porosimeter at Johnson Matthey Technology Centre. The samples (0.1 – 0.3 g) were first measured out into a bulb-shaped glass sample tube, weighed, and dried under a stream of N_2 at 150 °C for 24 hours. After this period, the tubes were re-weighed and then attached to the porosimeter and known amounts of N_2 was introduced at cryogenic temperatures up

to the saturation pressure. The porosimeter measures the pressure and the total adsorbed N_2 is calculated.

2.5.9 Inductively coupled plasma – optical emission spectroscopy (ICP-OES)

The detector measures the intensity of light emitted from a flame, produced by the atomizer. In this case the atomizer is an ICP torch, which generates plasma. The plasma is generated by passing a time-varying electric current (radio frequency) through an induction coil. Argon gas is used as a fuel source and as the gas flow through the coil this induces azimuthal electric currents, to generate plasma which is overall neutrally charged. However, a large proportion of the atoms are ionised by the high temperatures that are generated. This enables the atomiser to convert the components of a sample to atoms or ions by removing their outer electrons. This process excites a fraction of these species to a higher electronic state which subsequently emit light which can be measured. The wavelength of light transmitted is specific of the elements within the sample, quantitative analysis of the sample can be achieved because the intensity of the detected light is proportional to the abundance of the element. Assays were conducted by MEDAC Ltd, using a Varian Vista MPX ICP-OES system equipped with a CCD detector.

2.5.10 Temperature-programmed reduction/oxidation (TPR/TPO)

Temperature-programmed reduction/oxidation profiles were measured using apparatus stationed at JMTC. Temperature programmed reduction flows a gas mixture of 10% H_2/N_2 over a sample which is heated at a constant rate (10 °C min^{-1}) and a decline in the concentration of H_2 is characteristic of the sample undergoing reduction. The thermal conductivity of the H_2 gas was measured before and after passing contact with the sample, the difference in recorded conductivities (mV) corresponds to the amount of H_2 consumed by the sample. Accurate quantification of the H_2 consumption was achieved by injecting a known quantity (1 ml) of N_2 gas into the H_2/N_2 gas stream before the execution of the experiment. The injection decreases the H_2 concentration in the gas stream creating a calibration peak for comparison to the measured values during the experiment. A water trap is inserted in the system after the gas flows over the sample in order to absorb the H_2O formed by H_2 oxidation. Quantification of the gas consumption was performed by the integration of the peaks in the TPR/TPO profiles using a software program

developed by JMTC. Temperature-programmed oxidation profiles were measured under similar conditions to the TPR apart from using a 10% O_2/He gas mixture.

A quartz glass tube was sealed at one end with quartz wool and a quantity of sample (190-210 mg) was transferred into the centre of the tube and sealed again at the other end for analysis. The complete sample preparation is pictured in Figure 6.

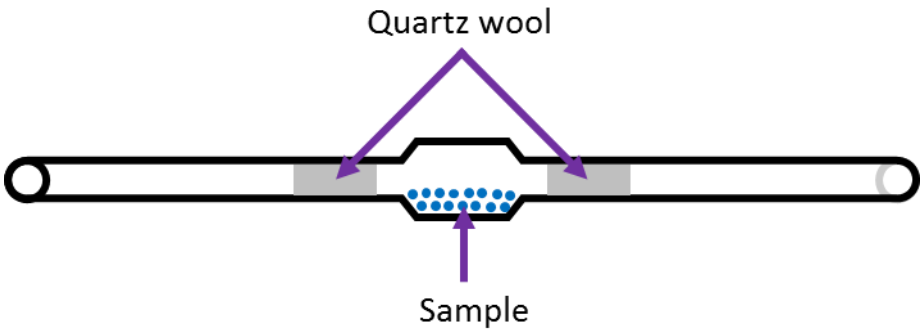

Figure 6: Sample preparation for TPR/TPO analysis.

References

1. T. Ungar and A. Borbely. (1996). The effect of dislocation contrast on X-ray line broadening: A new approach to line profile analysis. *Applied Physics Letters*. 69 (21), p3173-3175.
2. T. Ungar, S. Ott, P.G. Sanders, A. Borbely and J.R. Weertman. (1998). Dislocations, grain size and planar faults in nanostructured copper determined by high resolution X-ray diffraction and a new procedure of peak profile analysis. *Acta Materialia*. 46 (10), p3693-3699.

3. Understanding the crystallisation mechanisms involved in the synthesis of cerium bismuth oxides

3.1 Introduction

This chapter focuses on the hydrothermal synthesis of $Ce_{0.5}Bi_{0.5}O_{2-\delta}$ via the use of four different combinations of starting reagents. The structural characterisations of these oxides were undertaken to determine any differences between them from the use of metal salts with varying oxidation states. As established, hydrothermal synthesis is a closed system reaction, so the formation mechanisms involved in the synthesis of mixed metal oxides are still somewhat of an enigma. [1] Typically, the formation of mixed metal oxides via hydrothermal synthesis is a trial and error-based procedure, involving quenching the reactions after different applied temperatures and times in order to optimise reaction conditions. Trying to elucidate the growth and crystallisation of the target materials via this methodology may provide some insights, however, quenching the reactions may influence the reaction mechanisms, pathways or the products/intermediates obtained. Therefore, the design of novel reaction vessels and the configuration of time-resolved XRD experiments are beneficial, since they can provide a direct insight into the mechanisms involved in the hydrothermal reaction, in situ. Understanding this will yield the ability to optimise synthetic routes as well as provide for opportunity to tailor desirable properties. Therefore, in this study the application of in situ hydrothermal XANES and XRD measurements were undertaken to develop a more in depth understanding of how the series of cerium bismuth oxides are formed.

3.2 Synthesis

3.2.1 Hydrothermal synthesis of $Ce_{0.5}Bi_{0.5}O_{2-\delta}$ and CeO_2 standards

Cerium nitrate hexahydrate ($Ce(NO_3)_3 \cdot 6H_2O$, 2 mmol) and bismuth nitrate pentahydrate ($Bi(NO_3)_3 \cdot 5H_2O$, 2 mmol) were ground individually using a pestle and mortar and weighed using an analytical balance. Both precursors were ground with a pestle and mortar and measured using an analytical balance and transferred into a Teflon autoclave liner (20 ml). Sodium hydroxide (10 M, 8 ml) was measured and was transferred into the Teflon liner. A magnetic stirrer was placed inside the liner, which was covered with a lid and placed on a stirring plate and was left to stir for a period of 3 hours. This was followed by sealing the Teflon liner in a steel

autoclave and transferring it into a pre-heated oven set at 240 °C for 96 hours. The mixture was filtered using a Büchner funnel and flask under vacuum pump suction. The solid was placed within a drying oven (70 °C) overnight and ground in a pestle and mortar prior to analysis. This sample is referred to in the text as Ce^{3+}/Bi^{3+}.

The procedure above was repeated using the following combination of reagents:

Reagents	**Abbreviation**
Cerium nitrate ($Ce(NO_3)_3 \cdot 6H_2O$, 2 mmol) and sodium bismuthate ($NaBiO_3$, 2 mmol)	Ce^{3+}/Bi^{5+}
Ammonium cerium nitrate ($Ce(NH_4)_2(NO_3)_6$, 2 mmol) and bismuth nitrate pentahydrate ($Bi(NO_3)_3 \cdot 5H_2O$, 2 mmol)	Ce^{4+}/Bi^{3+}
Ammonium cerium nitrate ($Ce(NH_4)_2(NO_3)_6$, 2 mmol) and sodium bismuthate ($NaBiO_3$, 2 mmol)	Ce^{4+}/Bi^{5+}
Cerium nitrate ($Ce(NO_3)_3 \cdot 6H_2O$, 4 mmol)	$CeO_2 – Ce(NO_3)_3$
Ammonium cerium nitrate ($Ce(NH_4)_2(NO_3)_6$, 4 mmol)	$CeO_2 – Ce(NH_4)_2(NO_3)_6$
Cerium chloride ($CeCl_3 \cdot 7H_2O$, 4 mmol)	$CeO_2 – CeCl_3$
Cerium sulfate ($Ce(SO_4)_2$, 4 mmol)	$CeO_2 – Ce(SO_4)_2$

3.2.2 In situ XANES measurements of the hydrothermal reactions at the Ce and Bi L_{III}-edges

The in situ XANES measurements were measured on the XMaS beamline at the European synchrotron radiation facility (ESRF), Grenoble, France. Ce L_{III}-edge XANES and Bi L_{III}-edge XANES were measured. The beam size was 80 µm in diameter and the detector used was a 49 mm^2 Vortex silicon drift diode at a distance from sample to detector equal to 183 mm.

3.2.2.1 Ce L_{III}-edge method and set-up

Cerium nitrate hexahydrate ($Ce(NO_3)_3 \cdot 6H_2O$, 2 mmol) and sodium bismuthate ($NaBiO_3 \cdot 2H_2O$, 2 mmol) were ground individually using a pestle and mortar and weighed using an analytical balance. The powders were combined and were ground again together for a few minutes. The powder was transferred into a glass vial (20 ml) and shaken. An aliquot of this powder was transferred into the X-ray hydrothermal reaction cell until it was just below the maximum capacity. Using a

glass pipette 6- 7 drops of sodium hydroxide solution (10 M) was transferred into the cell. The cell (Figure 7) was sealed between two Kapton windows and transferred into the furnace for analysis.

3.2.2.2 Bi L_{III}-edge method and set-up

The same synthesis method used in section 3.2.2.1 was applied, however a Teflon disc with a 1 mm diameter hole in the middle was used in combination with a mica window (25 µm). The mica windows couldn't be used for the Ce L_{III}-edge as mica contains Ti which absorbs in the same region.

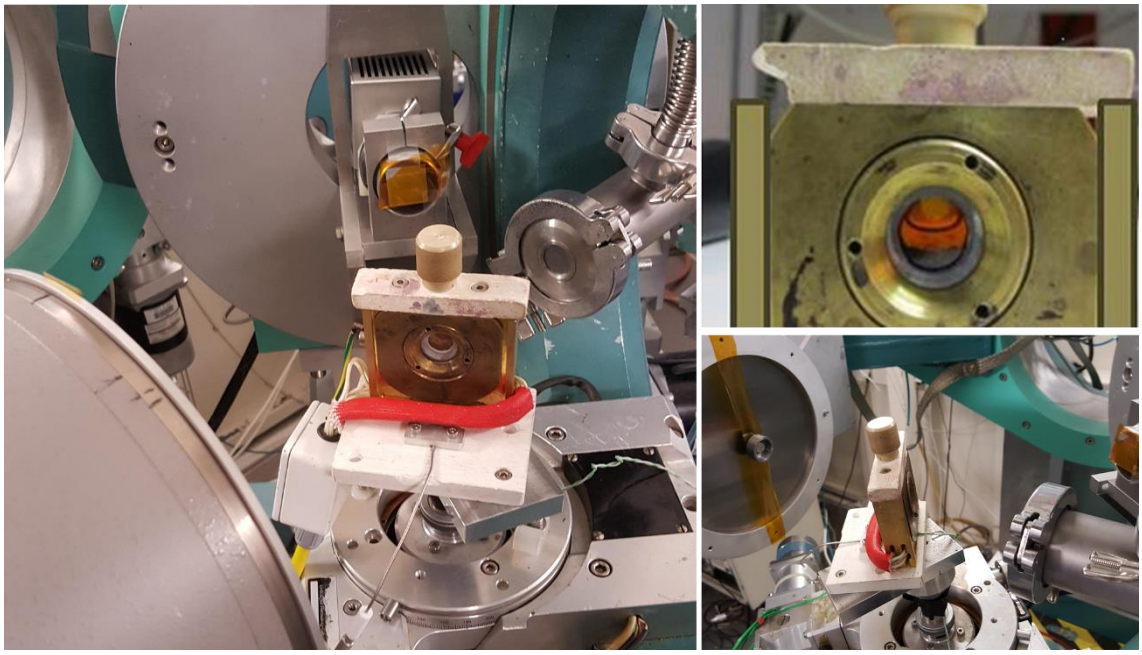

Figure 7: Picture of the hydrothermal reaction cell and set-up used for the in situ XANES measurements.

3.2.3 Time-resolved in situ X-ray diffraction measurements of the hydrothermal reactions to form $Ce_{0.5}Bi_{0.5}O_{2-\delta}$

The time-resolved diffraction measurements were performed on beamline I12 at the Diamond Light Source, UK. The hydrothermal reactions were implemented using a Teflon lined steel autoclave coupled with a furnace named ODSIC. [2] Two thermocouples were attached to the outside of the steel autoclave to control and measure the applied temperature via a PID controller. The ODISC cell is comprised of infra-red lamps which are used to heat the autoclave to high temperatures quickly. The X-rays had an energy of 80.306 keV (λ = 0.155 Å) in order to penetrate the stainless-steel autoclave and the diffraction patterns were accumulated in 4 second acquisitions. The diffraction patterns were normalised and analysed using the

DAWNDiamond software. In a typical reaction, 2 mmol of each reagent were ground together and placed within the Teflon liner before a NaOH solution was added (8 ml, 10 M).

3.3 Powder XRD analysis

The powder XRD patterns of $Ce_{0.5}Bi_{0.5}O_{2-\delta}$ and CeO_2 standards can be indexed and profile fitted to a cubic fluorite cell (space group: $Fm\bar{3}m$). For the $Ce_{0.5}Bi_{0.5}O_{2-\delta}$ samples, the lattice expansion is consistent with the larger atomic ionic radius of Bi^{3+} compared to that of Ce^{4+} (eight co-ordinate Bi^{3+} and Ce^{4+} have respective ionic radii of 1.17 and 0.97 Å). A linear relationship between the unit cell length and composition in correspondence with Vegard's law is shown in Figure 8. This figure shows the results from this study compared against literature values, revealing that as the bismuth content is increased there is a positive linear correlation with the lattice parameter. The produced materials lattice parameters agree with the literature values suggesting accurate target doping was achieved, apart from the Ce^{4+}/Bi^{5+} sample which suggests that less bismuth substitution has occurred. The crystallite sizes for all samples were estimated using the Scherrer equation and the Williamson-Hall method (Table 2). Notably NIST-CeO_2 is the one sample that has a slightly negative strain component (Cε) which is physically meaningless. The negative gradient encountered indicates that the Williamson-Hall method is not suitable for accounting for the combined contributions of crystallite size and strain to the powder XRD line broadening. [1] The comparison of the CeO_2 samples synthesised from different starting reagents shows that the lattice parameter is similar for each material, however each has varying crystallite sizes. For the $Ce_{0.5}Bi_{0.5}O_{2-\delta}$ samples, the crystallographic strain components determined from the Williamson-Hall analysis, increases upon the incorporation of bismuth in comparison to CeO_2. This is due to the substitution of Ce^{4+} by Bi^{3+} which has a larger ionic radius creating lattice distortion and hence inducing strain effects. The $Ce_{0.5}Bi_{0.5}O_{2-\delta}$ samples formed from the use of the Ce^{3+} starting reagents synthesise the products with the higher crystallite sizes. Conversely the Ce^{4+} reagents form products with lower crystallite sizes, and hence higher surface areas. The calculated crystallographic strain effects relating to these materials is also greater than for the material synthesised from the Ce^{3+} reagents.

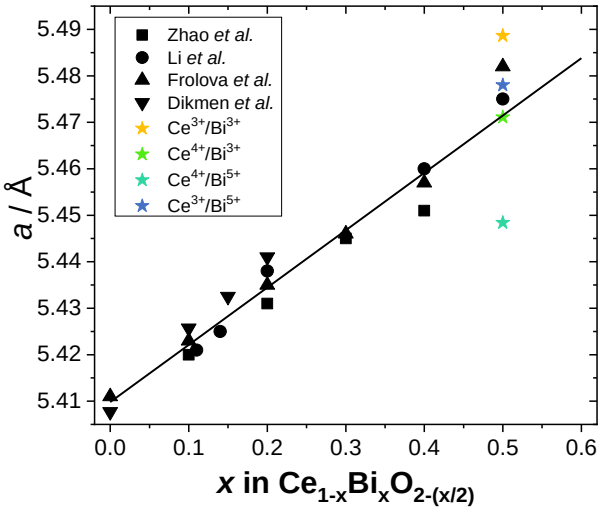

Figure 8: A comparison figure of the lattice parameters as a function of bismuth content in $Ce_{1-x}Bi_xO_{2-\delta}$, collated from literature values and the results from this study. [4-7]

Table 2: Results of Le Bail fitting to powder XRD data of $Ce_{0.5}Bi_{0.5}O_{2-\delta}$ and the surface area measurements determined by BET. Additionally, a set of ceria samples were synthesised (an exception being NIST-CeO_2, which is a purchased standard) and added for comparison. [a] Crystallite size calculated using the Scherrer equation via Eq.(2.4.6), and [b] Strain (Cε) and crystallite size (L) calculated using the Williamson-Hall analysis method via Eq.(2.4.7).

Product	*a* (Å)	[a]Crystallite size (Å)	[b]$C\varepsilon$	[b]L (Å)	BET (m^2g^{-1})
Ce^{3+}/Bi^{3+}	5.48865 (14)	216 (31)	0.00439 (3)	351	10
Ce^{4+}/Bi^{3+}	5.4711 (4)	44 (3)	0.0108 (3)	55	83
Ce^{4+}/Bi^{5+}	5.4484 (5)	35 (5)	0.0251 (9)	55	96
Ce^{3+}/Bi^{5+}	5.47908 (17)	146 (1)	0.00033 (5)	148	47
NIST – CeO_2	5.41044 (18)	894 (41)	-0.00025 (8)	815	2
CeO_2 – $Ce(NO_3)_3$	5.41356 (27)	704 (41)	0.00017 (8)	737	8
CeO_2 – $Ce(NH_4)_2(NO_3)_6$	5.40737 (16)	188 (11)	0.0019 (2)	221	37
CeO_2 – $CeCl_3$	5.41057 (7)	341 (15)	0.00072 (14)	385	4.3
CeO_2 – $Ce(SO_4)_2$	5.40955 (16)	154 (9)	0.0018 (4)	175	48.5

The conventional approach of optimising hydrothermally synthesised materials is to adjust the synthetic parameters. Therefore $Ce_{0.5}Bi_{0.5}O_{2-\delta}$ materials were synthesised at various temperatures and times using hydrothermal synthesis between $Ce(NO_3)_3$ and $Bi(NO_3)_3$ as shown in Figure 9.

After 3 hours of stirring in NaOH at room temperature, it can be observed that there are no Bragg peaks associated with the starting reagents. However it can be observed that the $Bi(NO_3)_3$ has converted to α-Bi_2O_3 in solution. As the hydrothermal reaction is extended to higher temperature and longer reaction times, the Bragg peaks attributed to α-Bi_2O_3 progressively becomes less intense as the bismuth is incorporated in to the $Ce_{1-x}Bi_xO_{2-\delta}$ lattice. The bismuth incorporation appears to have reached completion after 18 hours at 175 °C. After which it can also observed that the X-ray diffraction peaks become sharper as the reaction time and temperature increases.

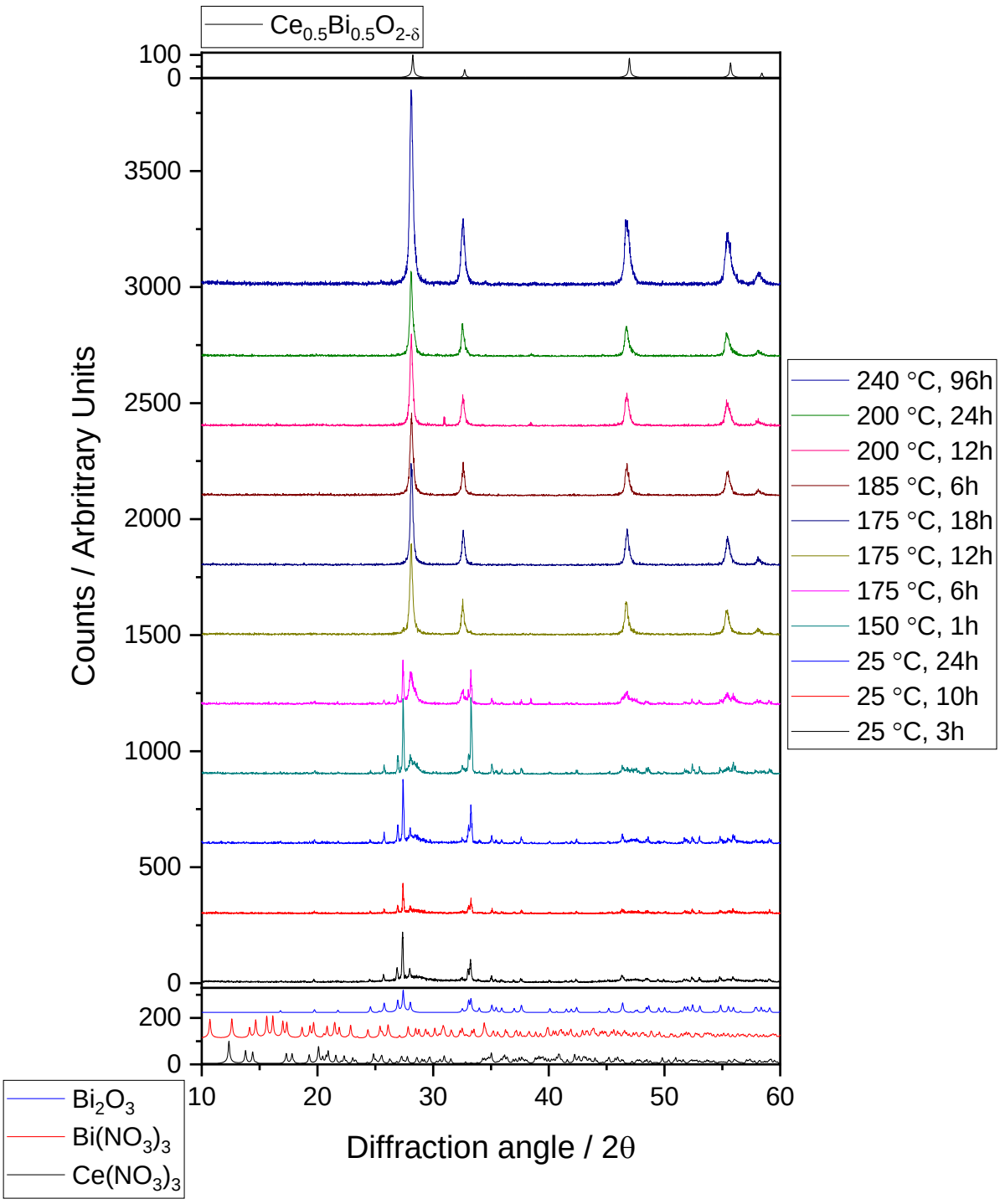

Figure 9: Ex situ powder XRD patterns of the hydrothermal reaction between $Ce(NO_3)_3$ and $Bi(NO_3)_3$ quenched at different reaction temperatures and times. [8-11]

The ex situ study of the Ce^{4+}/Bi^{3+} hydrothermal reaction (Figure 10) shows that after filtering the reaction mixture under room temperature conditions, CeO_2 and α-Bi_2O_3 crystallise out at reaction times of ≥ 3 hours. Longer reaction times result in the formation of the $Ce_{0.5}Bi_{0.5}O_{2-\delta}$ phase even under room temperature conditions which is presumably due to the starting reagents having the same oxidation state as the

products. Therefore, heating the solid solutions is not a key aspect in the formation of this $Ce_{0.5}Bi_{0.5}O_{2-\delta}$ however as mentioned it does influence other characteristics, such as crystallite size.

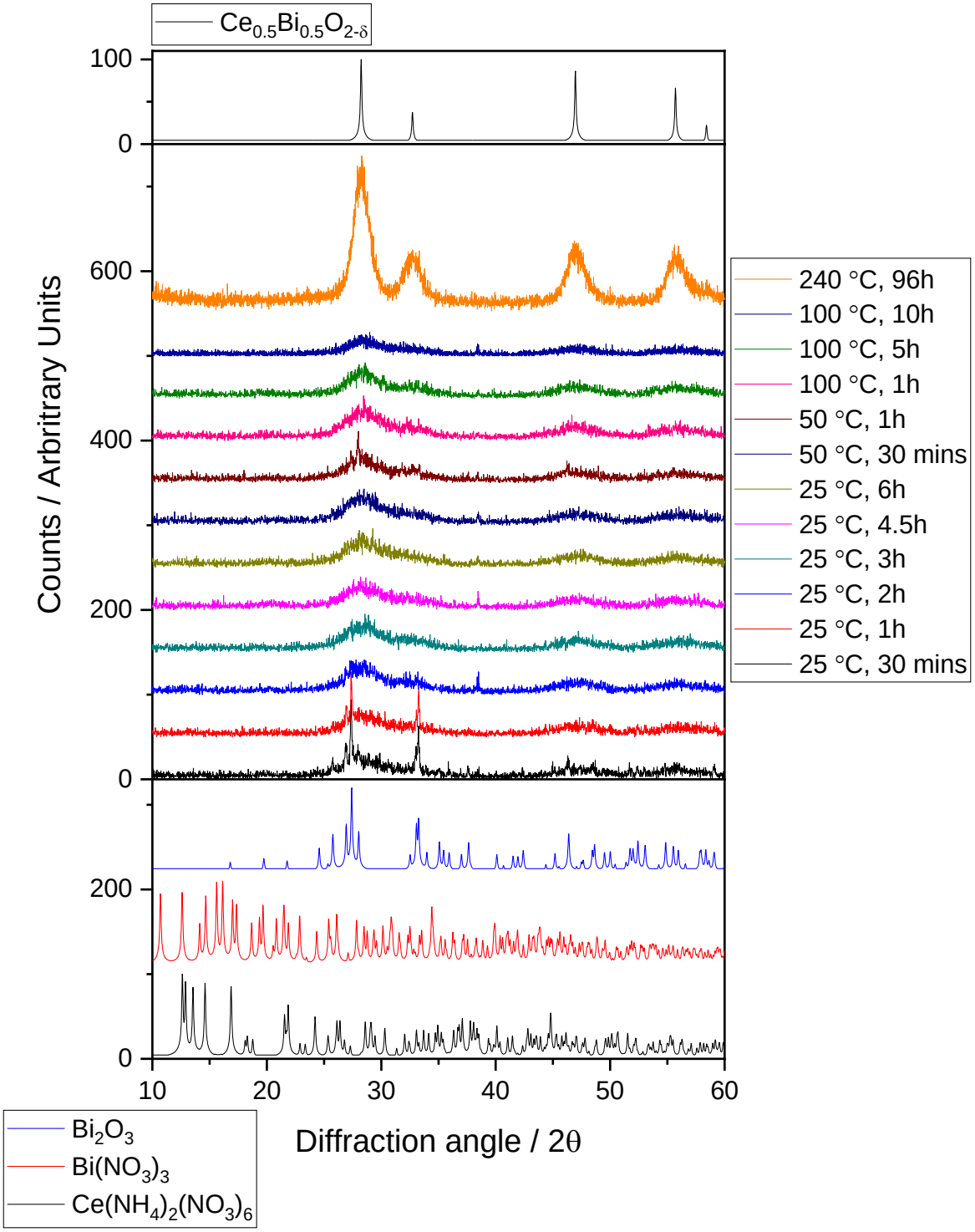

Figure 10: Ex situ powder XRD patterns of the hydrothermal reaction between $Ce(NH_4)_2(NO_3)_6$ and $Bi(NO_3)_3$ quenched at different reaction temperatures and times. [8-10,12]

The ex situ study of the Ce^{3+}/Bi^{5+} hydrothermal reaction (Figure 11) shows that unlike the Ce^{3+}/Bi^{3+} reaction, there are Bragg peaks attributed to both of the starting reagents ($NaBiO_3$ and $Ce(NO_3)_3$). The $NaBiO_3$ however goes through the same intermediate phase transformation as $Bi(NO_3)_3$ before incorporation in to $Ce_{1-x}Bi_xO_{2-\delta}$ lattice. The $NaBiO_3$ is reduced to α-Bi_2O_3 and this is clearly seen in the reaction quenched after 6 hours at 100 °C. Again, it can also be observed that the X-ray diffraction peaks associated with the $Ce_{0.5}Bi_{0.5}O_{2-\delta}$ phase become sharper as the reaction time and temperature increases.

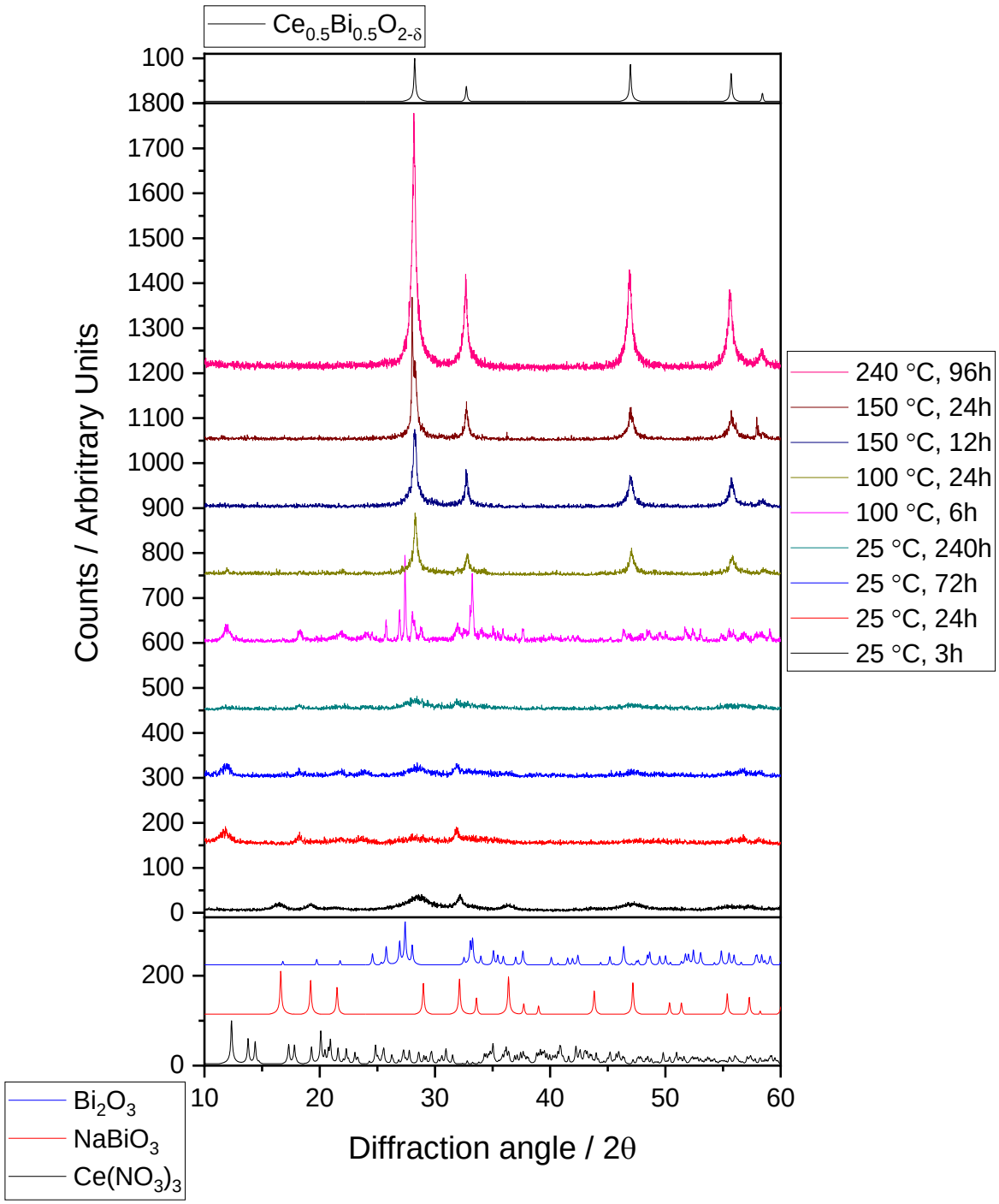

Figure 11: Ex situ powder XRD patterns of the hydrothermal reaction between $Ce(NO_3)_3$ and $NaBiO_3$ quenched at different reaction temperatures and times. [8,9,11,13]

The ex situ study of the Ce^{4+}/Bi^{5+} hydrothermal reaction (Figure 12) shows that like the Ce^{3+}/Bi^{5+} reaction, there are Bragg peaks attributed to both of the starting reagents ($NaBiO_3$ and $Ce(NH_4)_2(NO_3)_6$).

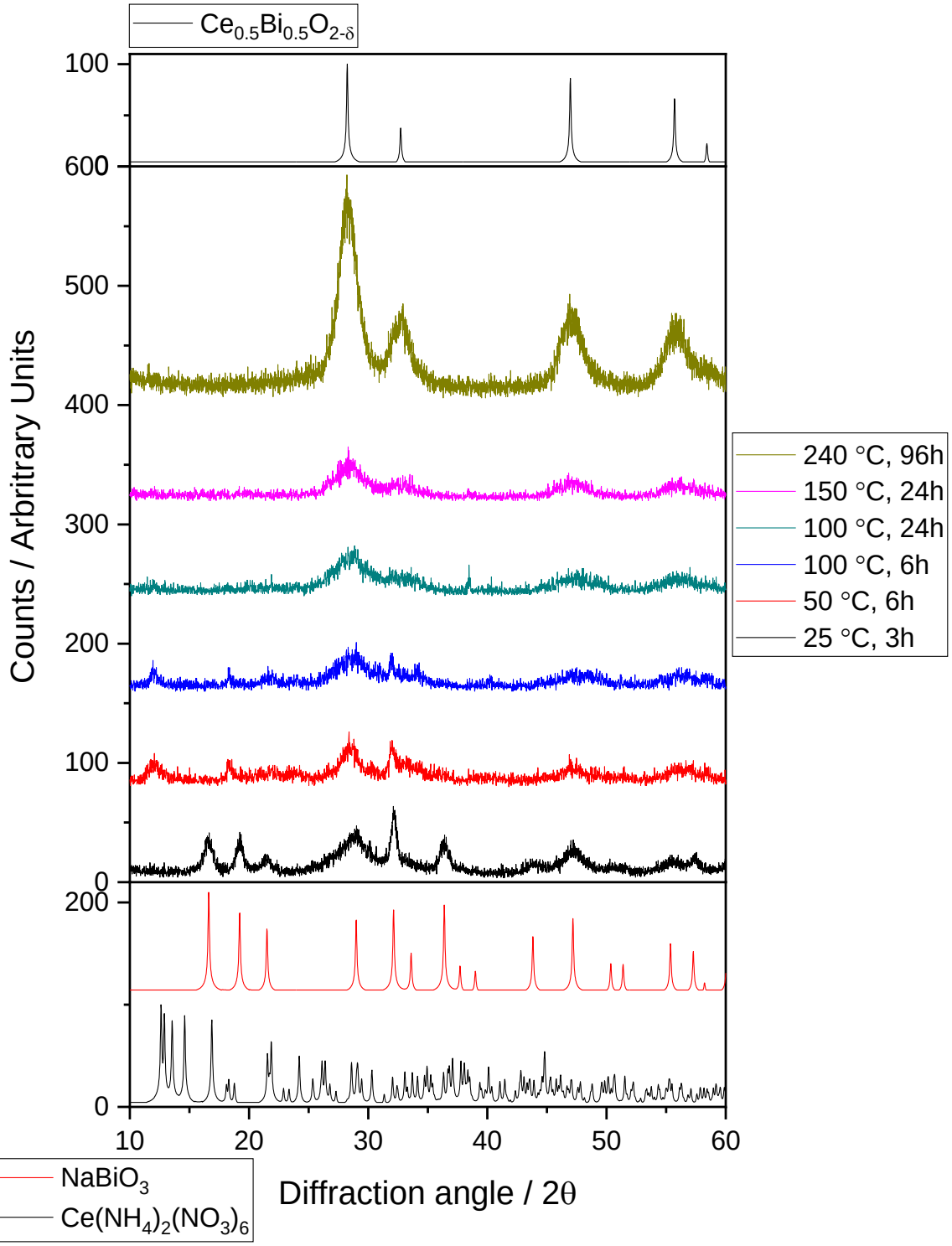

Figure 12: Ex situ powder XRD patterns of the hydrothermal reaction between $Ce(NH_4)_2(NO_3)_6$ and $NaBiO_3$ quenched at different reaction temperatures and times. [8,9,12,13]

3.4 Further characterisation

From the TGA-MS results in Figures 12-15, it is observed that the two products formed from the Ce^{4+} reagents show a greater mass loss of water and other small

quantities of absorbed nitrates. The presence of residual nitrates is not surprising, as the synthesis procedure involves the use of metal nitrates as starting materials.

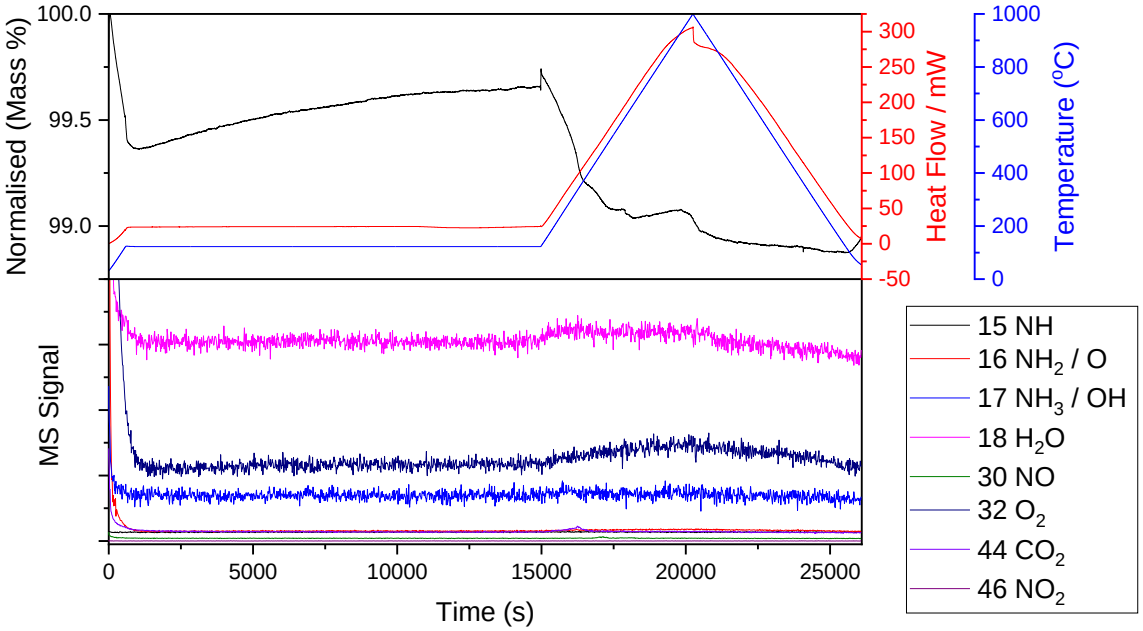

Figure 12: TGA-MS of the $Ce_{0.5}Bi_{0.5}O_{2-\delta}$ samples synthesised from the Ce^{3+}/Bi^{3+} hydrothermal reaction. Performed under flow of Ar.

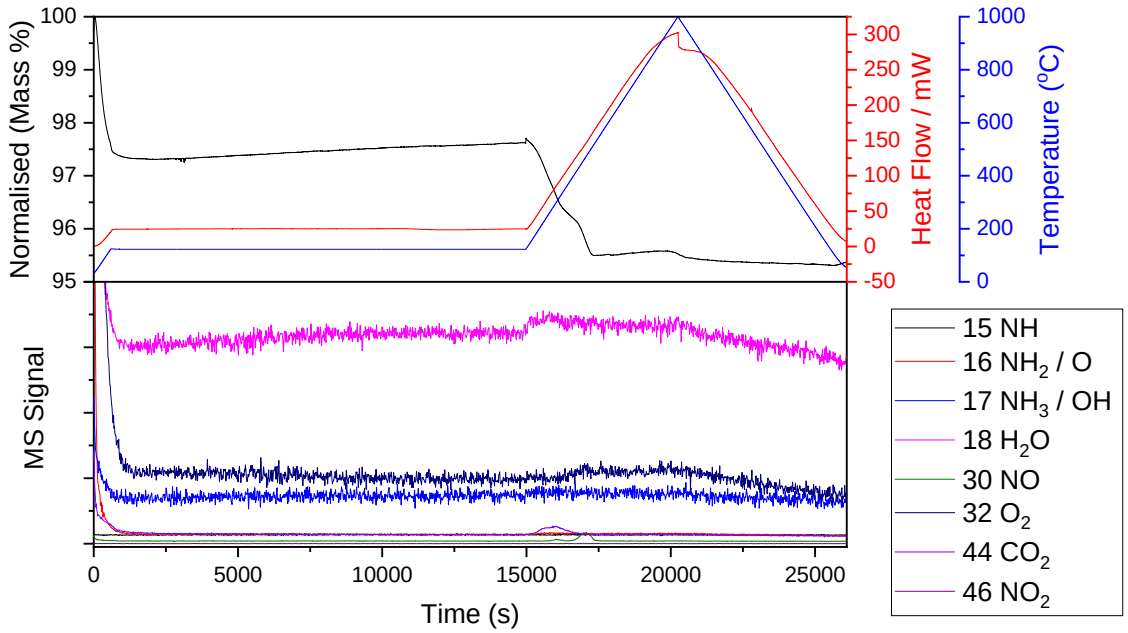

Figure 13: TGA-MS of the $Ce_{0.5}Bi_{0.5}O_{2-\delta}$ samples synthesised from the Ce^{4+}/Bi^{3+} hydrothermal reaction. Performed under flow of Ar.

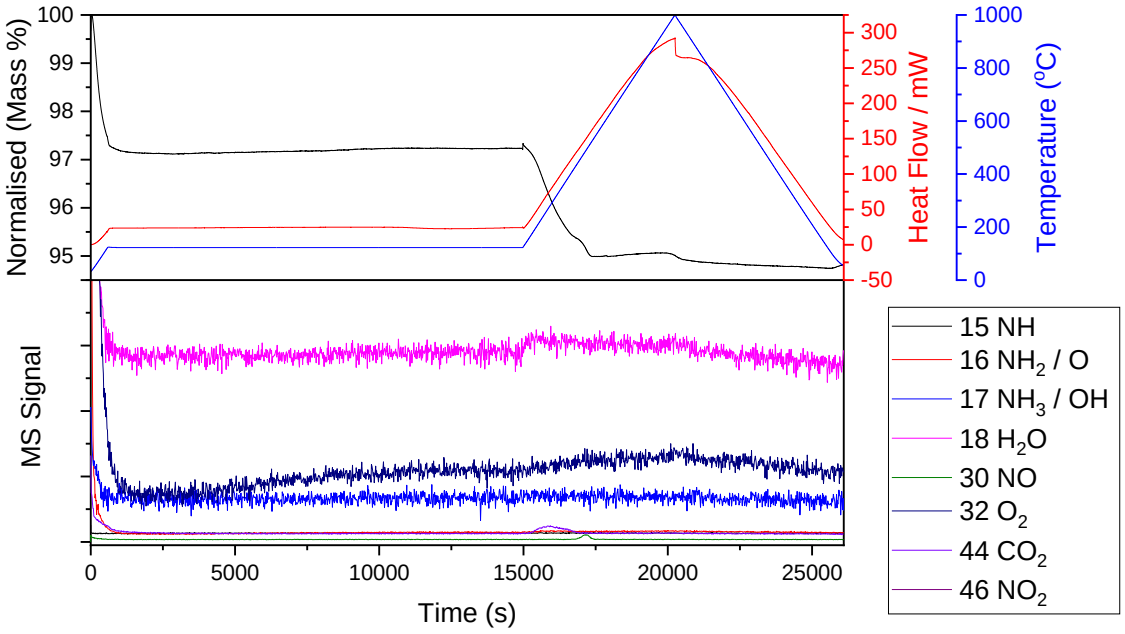

Figure 2: TGA-MS of the $Ce_{0.5}Bi_{0.5}O_{2-\delta}$ samples synthesised from the Ce^{4+}/Bi^{5+} hydrothermal reaction. Performed under flow of Ar.

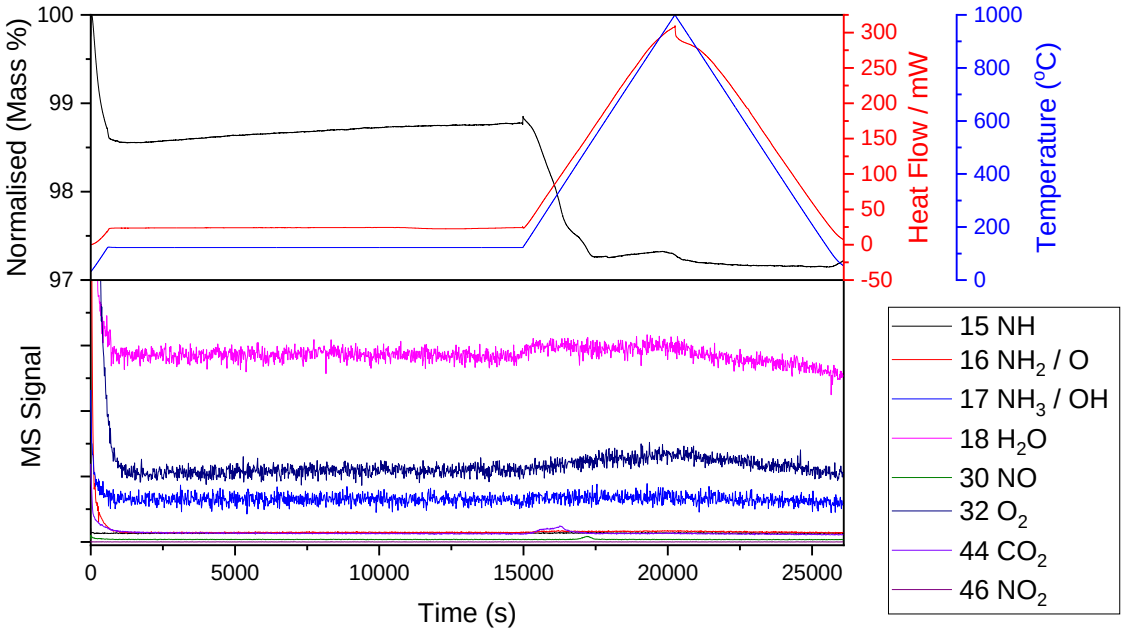

Figure 3: TGA-MS of the $Ce_{0.5}Bi_{0.5}O_{2-\delta}$ samples synthesised from the Ce^{3+}/Bi^{5+} hydrothermal reaction. Performed under flow of Ar.

To further characterise the final products obtained from the hydrothermal reactions, SEM and TEM was carried out to investigate the microstructure and morphology of the samples. The TEM images (Figure 16) were selected as being representative of each of the samples. It was found that the morphology and size of the products are

sensitive to their respective reaction conditions. From the TEM images it can be observed that all four samples are composed of aggregated and uniform nanocrystals with crystallite sizes of 10s of nm. The selected area electron diffraction (SAED) patterns (Figure 16) show varying degrees of crystallinity consistent with the powder XRD. Because of the high energy of the electron beam, there is a higher tendency for Bi segregation at domain. Energy-dispersive X-ray analysis (EDXA) was conducted to determine the composition of the materials. In comparison between EDXA measurements performed using TEM and SEM (Table 3), the SEM results show close agreement across all samples except the Ce^{3+}/Bi^{5+} sample which on average appears to be more Ce-rich. The standard deviation for this sample measurement is also quite large suggesting inhomogeneity on the micron scale. The TEM EDXA results look at the elemental composition on a more local scale, however the TEM results suggest that both samples starting from $NaBiO_3$, contains more Bi. Semi-quantitative chemical analysis on the samples was performed by XRF (Table 3), which revealed a fairly similar nominal composition for all four $Ce_{0.5}Bi_{0.5}O_{2-\delta}$ with the samples being slightly Bi-rich. Bulk compositional analysis was achieved on the samples by utilising ICP-OES (Table 3). ICP-OES elemental analysis shows the measured Ce:Bi ratio in the samples is very similar to the intended target ratio. There is an insignificant quantity of sodium present which can be assumed to be residue of NaOH on the surface not removed by washing with hot water. Na-substitution is not expected as it is not necessary to balance the charge.

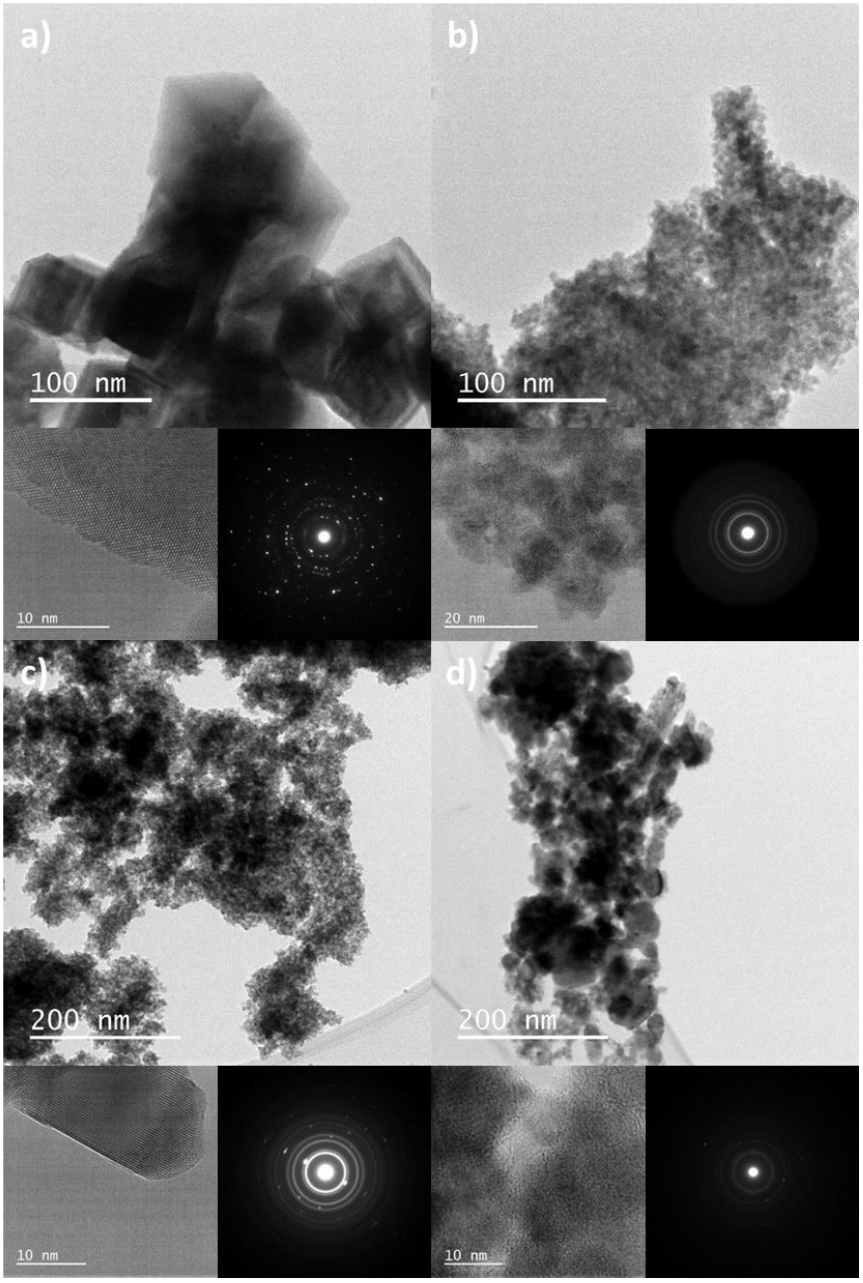

Figure 16: High-resolution transmission electron micrographs and corresponding selected area of diffraction patterns of fluorite-like $Ce_{0.5}Bi_{0.5}O_{2-\delta}$ samples a) Ce^{3+}/Bi^{3+}, b) Ce^{4+}/Bi^{3+}, c) Ce^{4+}/Bi^{5+} and d) Ce^{3+}/Bi^{5+}.

Table 3: Compositional information determined elemental analysis of the four $Ce_{0.5}Bi_{0.5}O_{2-\delta}$ samples.

EDXA	SEM			TEM			XRF		ICP-OES
Sample	Weight %			Atomic %			Bi	Ce	Formula
	Bi (M)	Ce (L)	STDEV	Bi	Ce	STDEV			
Ce^{3+}/Bi^{3+}	50.9	49.1	1.6	49.5	50.5	12.4	46.6	53.4	$Na_{0.13}Bi_{0.5}Ce_{0.5}O_x$
Ce^{4+}/Bi^{3+}	53.3	47.7	2.5	54.1	45.9	7.2	45.5	54.6	$Na_{0.01}Bi_{0.5}Ce_{0.5}O_x$
Ce^{4+}/Bi^{5+}	54.2	45.8	1.3	72.1	25.9	25.9	44.1	55.9	$Na_{0.01}Bi_{0.5}Ce_{0.46}O_x$
Ce^{3+}/Bi^{5+}	36.5	63.5	16.3	77.0	23.0	27.0	47.3	52.8	$Na_{0.02}Bi_{0.5}Ce_{0.47}O_x$

To study the surface features of the samples and to attempt to correlate them with the influence of the choice of precursors used for their characterisation was accomplished by XPS. Figure 17 shows a typical Ce $3d_{3/2,5/2}$ spectrum for the $Ce_{0.5}Bi_{0.5}O_{2-\delta}$ samples which consists of two multiplets (u and v). These multiplets correlate to the spin-orbit split $3d_{3/2}$ and $3d_{5/2}$ core holes. The spin-orbit splitting is approximately 18.6 eV, and each spin-orbit component is comprised of five peaks

(v^{III}-v^{0} and u^{III}-u^{0}). The Ce^{3+} surface percentages (Table 4) measured are quite similar for all four samples, ranging in a narrow interval of values between 29.17 – 32.83 %. The presence of Ce^{3+} cations in the samples can be attributed to the reduction of the Ce^{4+} in the samples due to the ultra-high vacuum in combination with the X-ray irradiation during XPS measurements. The effect of this therefore means the obtained Ce^{3+} percentages are higher than their realistic values.

The Bi 4f energy region of the same samples (Figure 18) shows a representative Bi $4f_{7/2,5/2}$ spectrum for the $Ce_{0.5}Bi_{0.5}O_{2-\delta}$ samples which consists of two singlets. The binding energy positions for the Bi $4f_{7/2}$ (157.7 eV) and Bi $4f_{5/2}$ (164.0 eV) spin states have a spin-orbit splitting of about 6.3 eV. There is no observed asymmetry of the peaks either at the lower or higher binding energy sides, which can be assigned to the presence of Bi^{5+} or Bi metal. The calculated percentage Bi^{3+} contents are indistinguishable between each of the four samples, even for the sample prepared using $NaBiO_3$ all the Bi has been reduced to Bi^{3+}.

Table 5 summarises the overall XPS compositional results which are in close agreement with all four of the samples, approximately 60% Bi to 40% Ce. However, they're above the target stoichiometric chemical composition, suggesting that there is a greater percentage of bismuth situated on the surface of the samples.

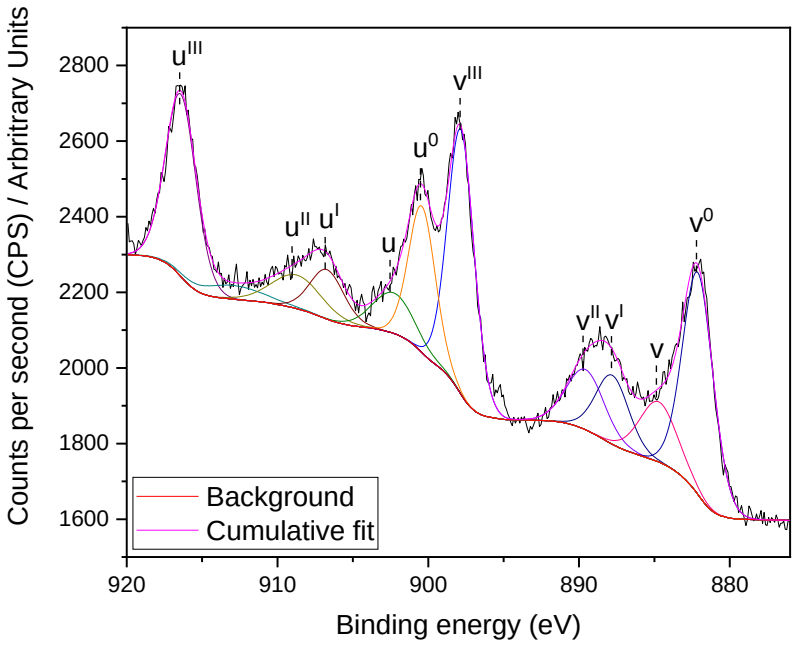

Figure 17: Al K_α excited Ce $3d_{3/2,5/2}$ XPS spectrum collected for a typical $Ce_{0.5}Bi_{0.5}O_{2-\delta}$ sample.

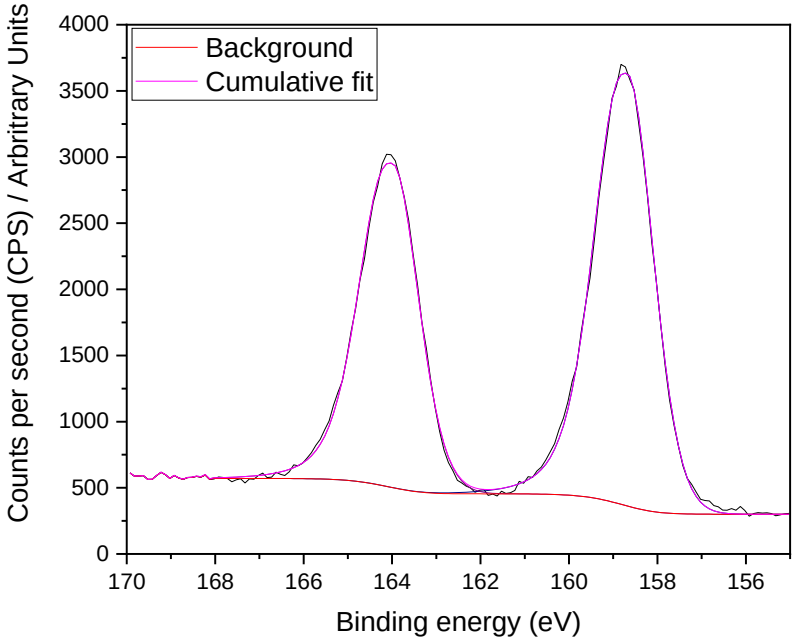

Figure 4: Al K_α excited Bi $4f_{7/2,5/2}$ XPS spectrum collected for a typical $Ce_{0.5}Bi_{0.5}O_{2-\delta}$ sample.

Table 4: Cerium and bismuth oxidation state data from surface analysis by XPS calculated from the Ce $3d_{3/2,5/2}$ and Bi $4f_{7/2,5/2}$ respectively.

Sample	Percentage Ce (III) (%)	Percentage Bi (III) (%)
NIST - CeO_2	31.7	N/A
$CeAlO_3$	67.7	N/A
CeO_2 - $Ce(NO_3)_3$	29.4	N/A
CeO_2 - $Ce(NH_4)_2(NO_3)_6$	32.1	N/A
CeO_2 - $Ce(SO_4)_2$	31.1	N/A
CeO_2 - $CeCl_3$	32.8	N/A
Ce^{3+}/Bi^{3+}	30.2	49.0
Ce^{4+}/Bi^{3+}	30.0	49.0
Ce^{4+}/Bi^{5+}	30.2	49.0
Ce^{3+}/Bi^{5+}	29.2	49.0

Table 5: Surface composition data from surface analysis by XPS of the four $Ce_{0.5}Bi_{0.5}O_{2-\delta}$ samples.

Sample	Bi (%)	Ce (%)
Ce^{3+}/Bi^{3+}	60.8	39.2
Ce^{4+}/Bi^{3+}	58.8	41.2
Ce^{4+}/Bi^{5+}	57.8	42.2
Ce^{3+}/Bi^{5+}	61.4	38.6

3.5 In-situ hydrothermal X-ray absorption spectroscopy (XAS)

3.5.1 Ce L_{III}-edge XANES of the final products

Ce L_{III}-edge XANES of $Ce_{0.5}Bi_{0.5}O_{2-\delta}$ (Figure 19) shows the near edge regions for each reaction overlapping, suggesting each sample contains an equal ratio of Ce^{3+}/Ce^{4+}. The edge positions of all four cases remains close to the observed position of NIST-CeO_2 spectra indicating that near complete conversion to Ce^{4+} has occurred.

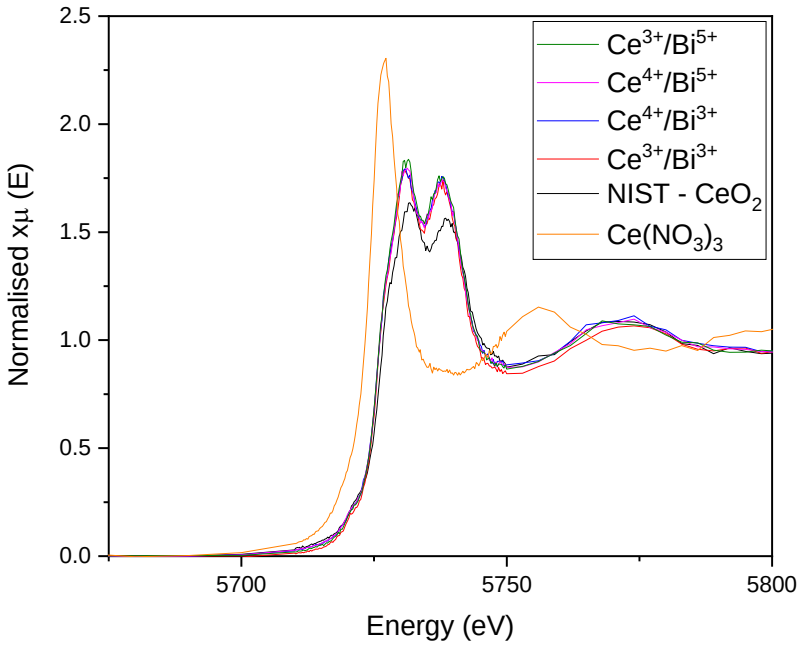

Figure 19: Normalised Ce L_{III}-edge XANES spectra of $Ce_{0.5}Bi_{0.5}O_{2-\delta}$ prepared using the four different sets of reagents, compared against reference compounds with known Ce oxidation states ($Ce(NO_3)_3$ and NIST-CeO_2).

3.5.2 In situ Ce L_{III}-edge XANES of the hydrothermal reaction

XANES data recorded *in situ* during room temperature and hydrothermal synthesis (Figure 20) were successful in monitoring the change in oxidation state ($Ce^{3+} \rightarrow Ce^{4+}$) between the starting reagent and the final product, as shown by the formation of the characteristic peak for Ce^{4+} at ~5738 eV which is due to the $2p_{3/2} \rightarrow (4f^0)5d$ transition. The slight shoulder at ~5730 eV suggests that there might be some residual Ce in the +3 oxidation state, which is generally the case for small particles of CeO_2. [1] Even at room temperature in the absence of $NaBiO_3$ the Ce^{3+} is oxidised, which suggests that oxygen in the air or dissolved in water is enough to oxidise the cerium.

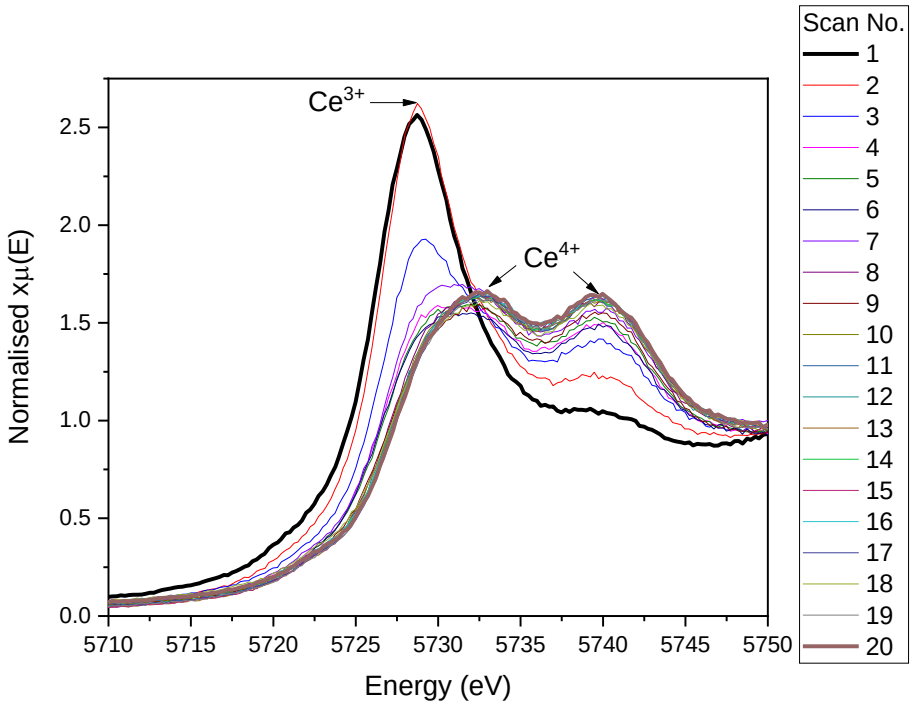

Figure 5: Normalised In-situ XANES spectra of $Ce(NO_3)_3$ control reaction measured at room temperature repeatedly (Scan No.) in sodium hydroxide (10 M).

Comparison of the two in situ room temperature and hydrothermal reactions (Figure 21) shows that addition of bismuth into the reaction may have induced some redox potential, promoting the oxidation of cerium. The application of a higher temperature as expected increases the oxidation of cerium to the +4 oxidation state.

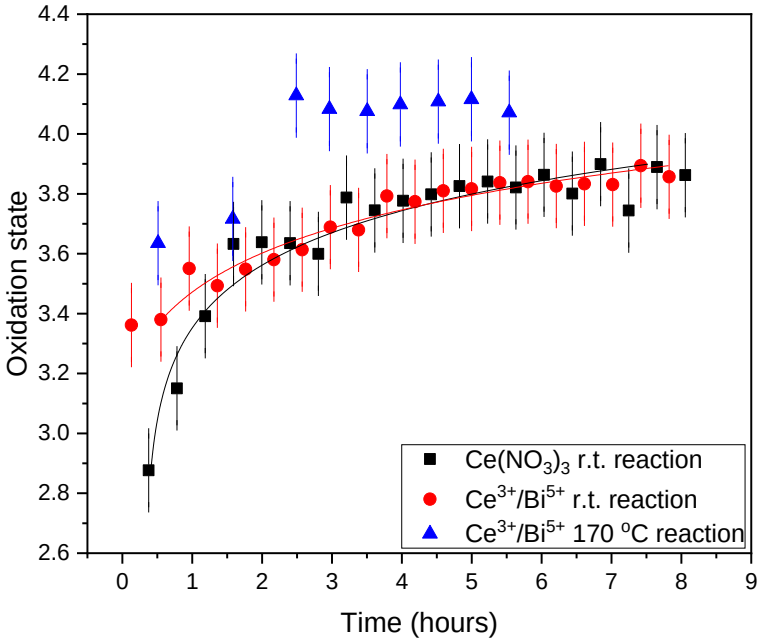

Figure 21: A plot of time as a function of oxidation state, extracted from a linear fit of the Ce reference compounds, to estimate the observed oxidation state changes during the measured reactions.

3.5.3 Bi L_{III}-edge XANES of the final products

Since Bi^{5+} starting reagents were used in the synthesis of the materials it was important to the oxidation state of bismuth in the final products. Bi L_{III}-edge XANES of the four $Ce_{0.5}Bi_{0.5}O_{2-\delta}$ samples (Figure 22) show the near edge regions for each reaction overlapping, suggesting each sample contains an equal Bi^{3+}/Bi^{5+} ratio. The edge positions of all four cases remains close to the observed position of the α-Bi_2O_3 spectra indicating that near complete conversion to Bi^{3+} has occurred.

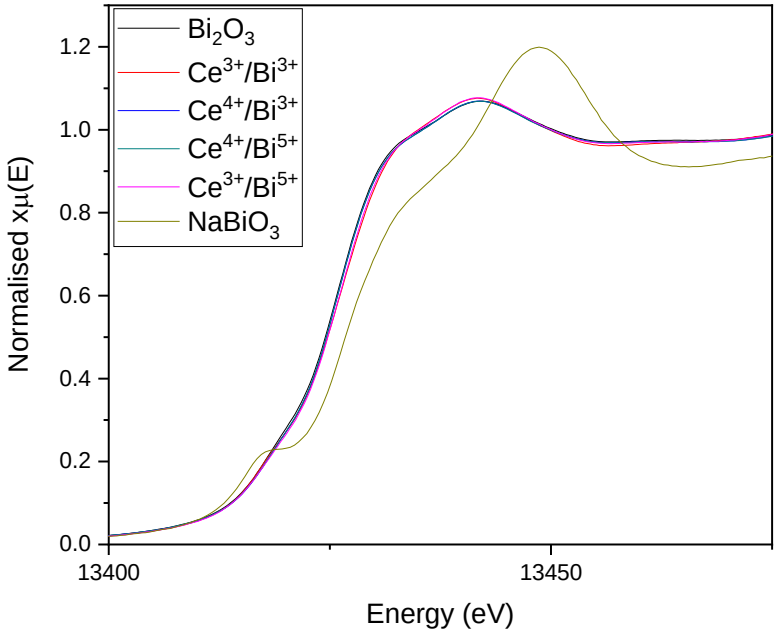

Figure 22: Normalised Bi L_{III}-edge XANES spectra of $Ce_{0.5}Bi_{0.5}O_{2-\delta}$ prepared using the four different sets of reagents, compared against reference compounds with known Bi oxidation states (Bi_2O_3 and $NaBiO_3$).

3.5.4 In situ Bi L_{III}-edge XANES of the hydrothermal reaction

Bi L_{III}-edge XANES data recorded in situ, during the hydrothermal reaction of Ce^{3+}/Bi^{5+} at 170 °C (Figure 23) were partially able to monitor the reduction of Bi^{5+} to Bi^{3+} between the starting reagent and the final products. The first being the pre-edge feature in $NaBiO_3$ (Bi^{5+}) which is assigned to the $2p_{3/2} \rightarrow 6s$ transition, as the reaction advances the peak becomes progressively less prominent as the 6s orbital is filled in Bi^{3+}. The second being the shift in white line position to lower energy.

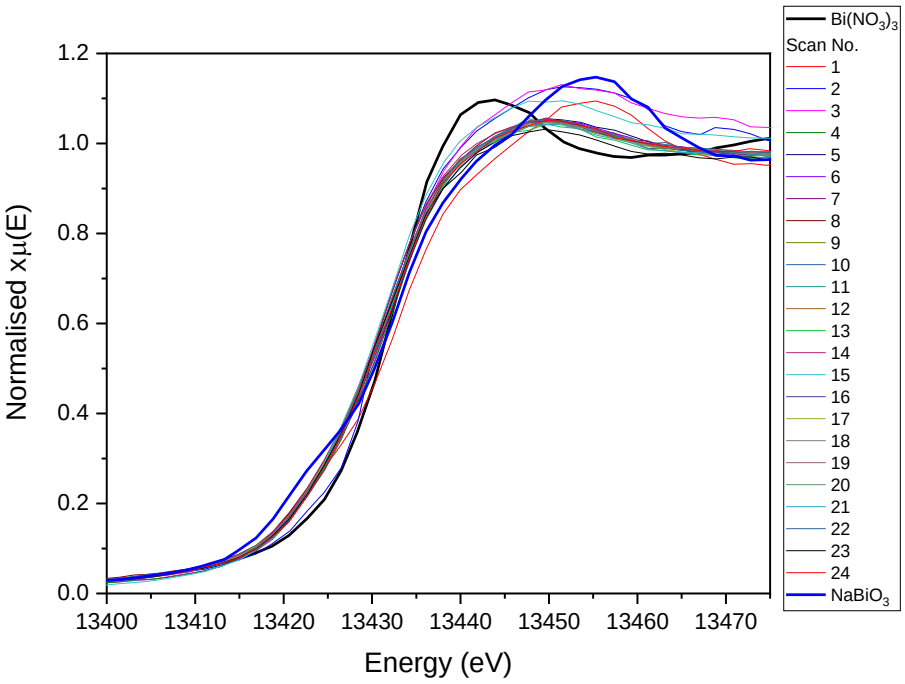

Figure 6: Normalised In situ Bi L_{III}-edge XANES spectra of the hydrothermal reaction between $Ce(NO_3)_3$ and $NaBiO_3$, measured at 170 °C in sodium hydroxide (10 M).

Bi L_{III}-edge XANES of the in situ reaction (Figure 24) between $Ce(NO_3)_3$ and $NaBiO_3$ at 170 °C, shows that conversion from Bi^{5+} to Bi^{3+} isn't observed after 11 hours of reaction. The conversion has only reached approximately half Bi^{5+} reduction, compared to the ex-situ samples measured previously (Figure 22). Comparing these results with the in-situ data at the Ce L_{III}-edge shows that the cerium has been oxidised prior to the bismuth this is not unexpected since Ce^{3+} is oxidised just in air.

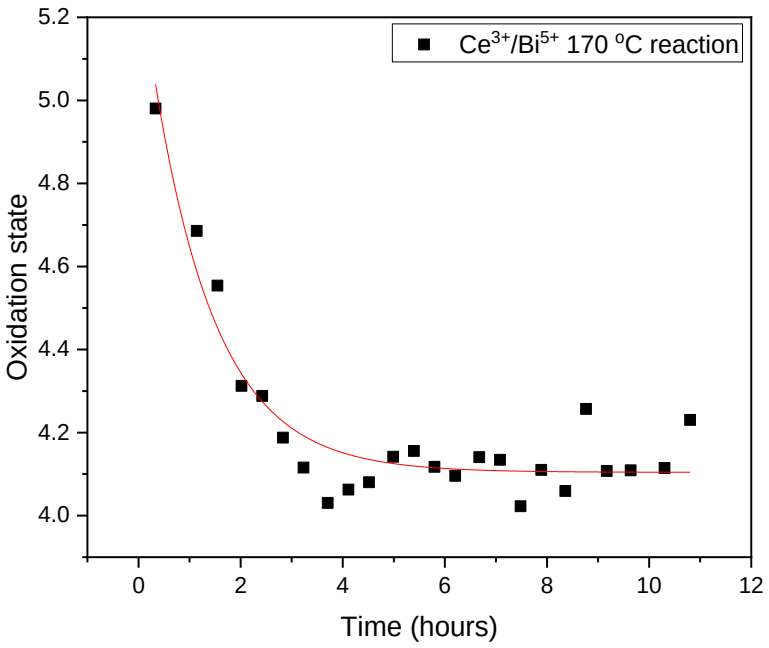

Figure 7: A plot of time as a function of oxidation state, extracted from a linear fit of the Bi reference compounds, to estimate the observed oxidation state changes during the measured reaction.

3.6 Two-step crystallisation model

The results of the in situ XANES measurement led to the proposal of a two-step model which involves the formation of CeO_2 before the incorporation of bismuth into the structure. Therefore, test reactions were performed to identify if bismuth could be incorporated after the formation of CeO_2, has already occurred. Two sets of reactions were performed the first entailed stirring the $Ce(NO_3)_3$ in NaOH at room temperature before the addition of $NaBiO_3$, and comparing this with $Ce(NO_3)_3$ and adding the two reagents simultaneously (Figure 25). The second set is repeating these reactions and transferring them into an autoclave for a hydrothermal reaction at 170 °C (Figure 26). Figure 25 shows that poorly crystalline CeO_2 does form at room temperature, before the addition of $NaBiO_3$. The calculated lattice parameters for addition of $NaBiO_3$ after forming CeO_2 shows no differentiation from the $Ce_{0.5}Bi_{0.5}O_{2-\delta}$ sample synthesised from the simultaneous addition of the two reagents (Table 6). Hydrothermally synthesising CeO_2 before the addition of $NaBiO_3$ creates a crystalline CeO_2 which can't incorporate bismuth after the reaction.

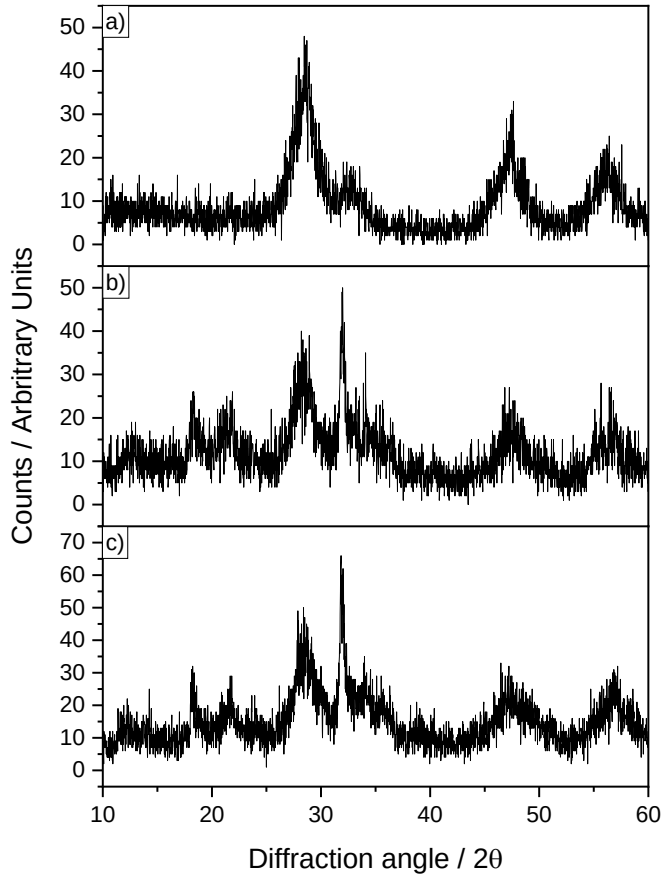

Figure 8: Powder XRD patterns of the room temperature reaction of a) $Ce(NO_3)_3$ in NaOH (10 M), b) $Ce(NO_3)_3$ and $NaBiO_3$ in NaOH (10 M) and c) Stirring the $Ce(NO_3)_3$ in NaOH (10 M) for 4 hours prior to the addition of $NaBiO_3$.

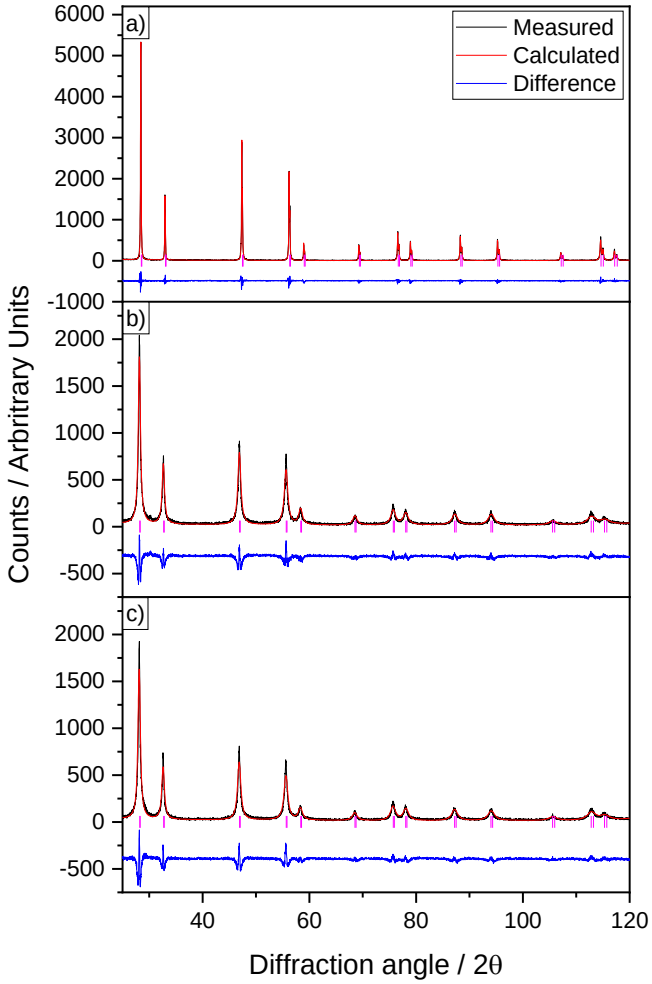

Figure 9: Powder XRD patterns of the hydrothermal reactions (at 170 °C, 24h) of a) $Ce(NO_3)_3$ in NaOH (10 M), b) $Ce(NO_3)_3$ and $NaBiO_3$ in NaOH (10 M) and c) Stirring the $Ce(NO_3)_3$ in NaOH (10 M) for 4 hours prior to the addition of $NaBiO_3$.

Table 6: Calculated lattice parameters from the Le Bail fitting to powder XRD data shown in Figure 26.

Samples	*a* (Å)
CeO_2	5.41435 (2)
$Ce(NO_3)_3$ + $NaBiO_3$	5.4710 (17)
$Ce(NO_3)_3$ stirred 4 h + $NaBiO_3$	5.47099 (17)

3.7 In situ X-ray diffraction of the hydrothermal reaction

The in situ X-ray diffraction measurements were conducted using an Oxford-Diamond in situ cell (ODISC), the setup involves the use of a PTFE-lined steel autoclave as with laboratory based experiments. The main difference, between the two is that typically the stirring of the reaction reagents in solution occurs prior to the heating of the autoclave, whereas here it was applied simultaneously to keep the solid in the beam. The experimental peak profiles observed during these

hydrothermal reactions are a convolution of both instrumental and sample profile components. The former relating to scatter from the cell walls, optics and so forth of the instrumentation and the latter originating from microstructural effects of the materials under investigation. A key consideration in any structural analysis based on an XRD peak profile is to determine and de-convolute the contributions attributed to each of these two components. As shown in Figure 27 the diffraction pattern of the final product re-suspended in NaOH is dominated by the Bragg reflections which arise from the stainless steel autoclave, PTFE liner and the Kapton windows of the ODISC cell.

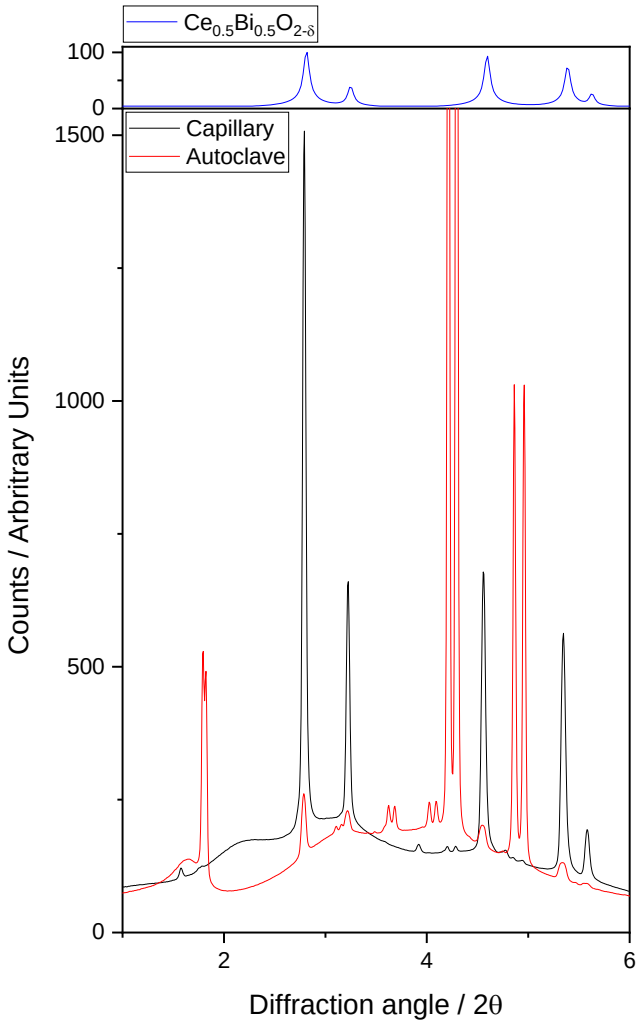

Figure 10: Comparison of $Ce_{0.5}Bi_{0.5}O_{2-\delta}$ (made from Ce^{3+}/Bi^{3+}) sample placed in a capillary and the same sample suspended in NaOH within the stainless-steel autoclave. Both measurements were recorded with the samples contained within the ODISC cell. [8]

Incorporation of Bi^{3+} cations into the fluorite structure and the growth of $Ce_{0.5}Bi_{0.5}O_{2-\delta}$ were studied using in situ powder X-ray diffraction. The in situ experiments revealed that the fluorite structure is formed as $Ce_{1-x}Bi_xO_{2-\delta}$ ($x \geq 0.5$) in

the early stages of the reaction. The Ce^{3+}/Bi^{3+} reaction (Figure 28) corroborates the results obtained from the ex situ syntheses, with the formation of α-Bi_2O_3 before incorporation into the fluorite structure. The Bragg peaks attributed to $Ce(NO_3)_3$ also dissipate swiftly, prior to α-Bi_2O_3. The in situ diffraction measurements give an insight into the crystallite growth but not the initial stages of the reaction, as it takes some time for solution to reach the optimal temperature for the material to be within the path of the beam.

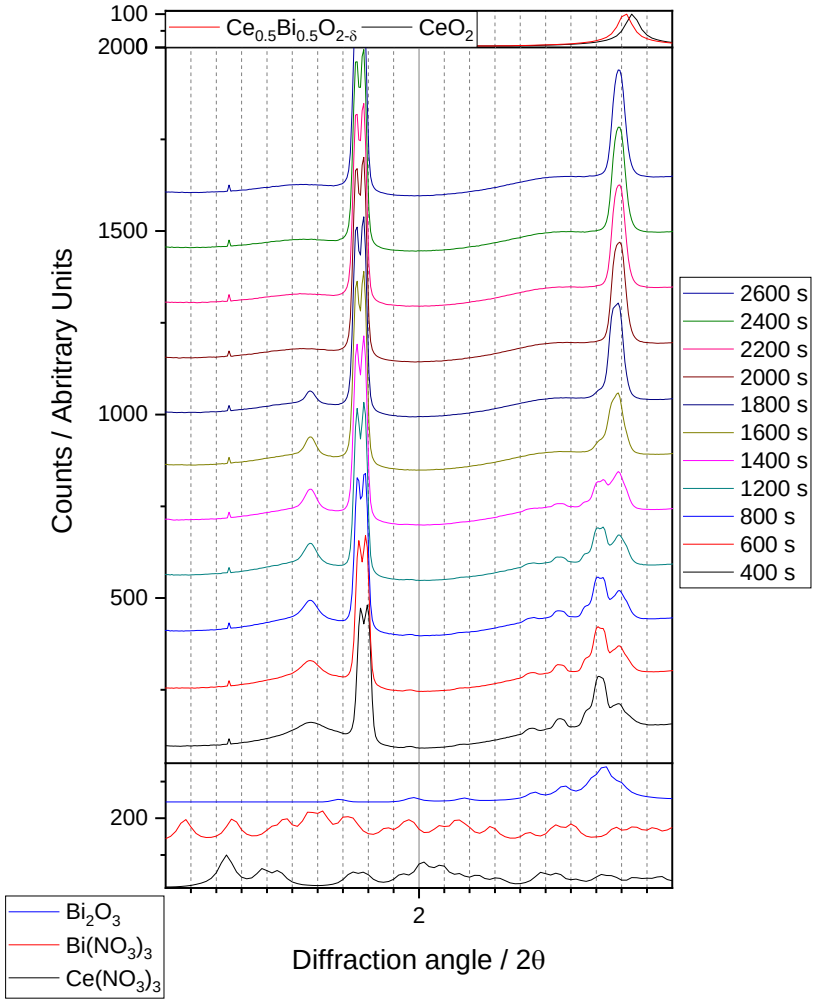

Figure 11: In situ Bragg reflections collected during the hydrothermal synthesis of $Ce_{0.5}Bi_{0.5}O_{2-\delta}$ for the reaction between $Ce(NO_3)_3$ and $Bi(NO_3)_3$ for different times at 200 °C. The results are compared against reference literature spectra for the starting reagents, intermediate phases and products. [8-11,14]

The evolution of lattice parameter as a function of time was determined by the sequential profile refinements of the diffraction patterns. The refined cubic unit cell length, a, of the (1,1,1) peak as a function of reaction time begins at a = 5.482 Å which gradually increases for the next 15 minutes, before a sudden significant unit cell expansion to 5.526 Å, and a decline to 5.508 Å. The fractional progress of α-

Bi_2O_3 and $Ce_{0.5}Bi_{0.5}O_{2-\delta}$ as a function of time for the Ce^{3+}/Bi^{3+} reaction shows an increasing fraction of the cerium bismuth oxide with a corresponding simultaneous decrease in the bismuth oxide fraction as the reaction time progresses. Contrary to the ex situ powder XRD patterns the Bragg peaks attributed to α-Bi_2O_3 are no longer visible after the reaction time exceeds approximately 30 minutes. The evolution of Scherrer crystallites sizes, calculated from the refined peak profiles are shown in Figure 29. The evolution of crystallite size has an inverse trend to the lattice parameter, starting from 170 Å, decreasing in size and finally becoming larger again to 158 Å.

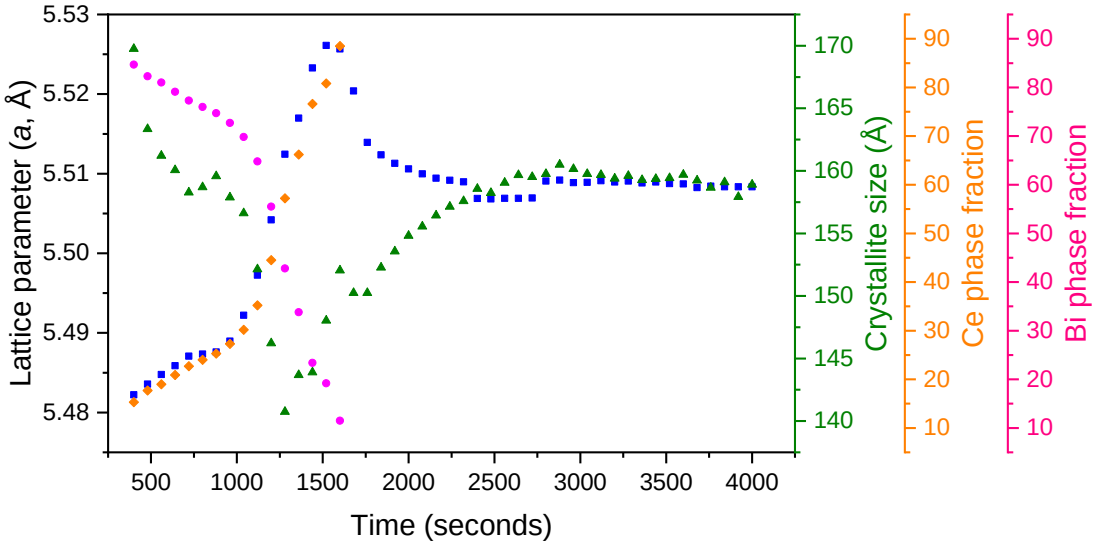

Figure 129: Results of the profile refinements for the in situ diffraction data of the Ce^{3+}/Bi^{3+} hydrothermal reaction. The lattice parameter was calculated from the (1,1,1) peak of $Ce_{1-x}Bi_xO_{2-\delta}$. The crystallite size was estimated from the same peak using the Scherrer equation.

Contrary to the in situ Ce^{3+}/Bi^{3+} diffraction data the Bragg reflections attributed to $Ce(NO_3)_3$ are present within the patterns for the Ce^{4+}/Bi^{5+} reaction (Figure 30). Again, this agrees with the diffraction patterns of the quenched reactions for the same reagents. The Bragg peaks associated with the presence of $NaBiO_3$, subsequently disappear after $Ce(NO_3)_3$ at approximately 1400 s. Additionally, because of the insufficient resolution and due to the background intensity the initial reaction mechanisms again aren't observed.

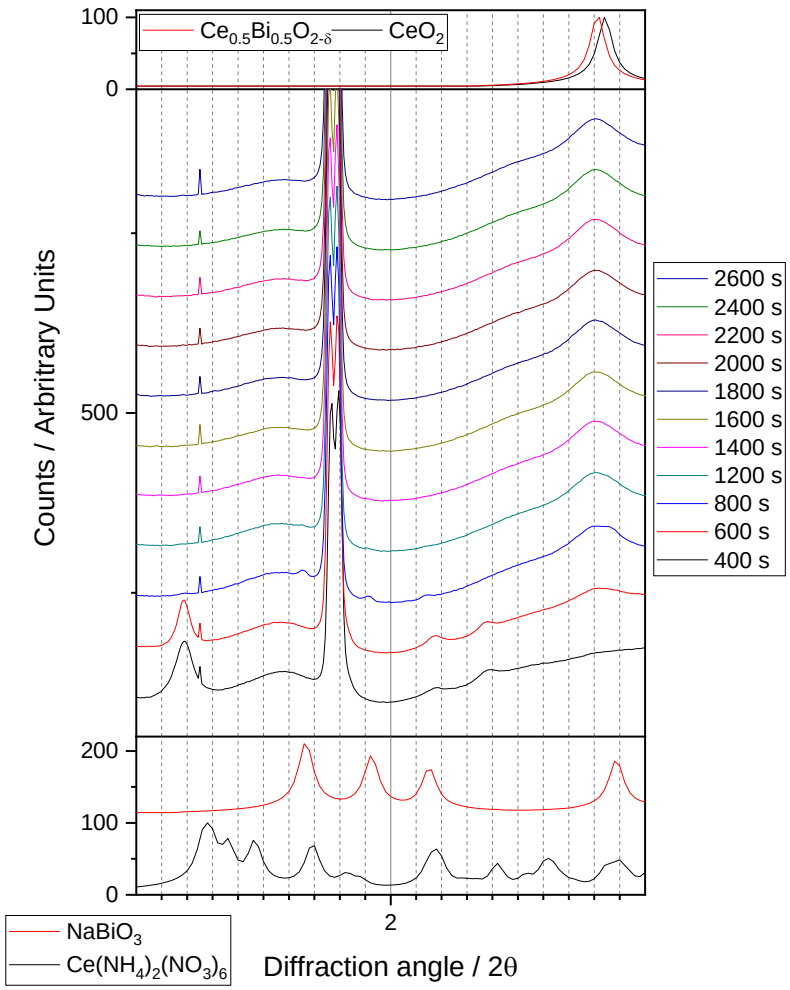

Figure 30: In situ Bragg reflections collected during the hydrothermal synthesis of $Ce_{0.5}Bi_{0.5}O_{2-\delta}$ for the reaction between $Ce(NH_4)_2(NO_3)_6$ and $NaBiO_3$ for different times at 200 °C. The results are compared against reference literature spectra for the starting reagents, intermediate phases and products. [8,12-14]

The in situ diffraction data for the Ce^{3+}/Bi^{5+} hydrothermal reaction (Figure 31) as for the Ce^{4+}/Bi^{5+} reaction, contains peaks associated with both of the starting reagents. Showing little differentiation between the results observed in the ex situ powder patterns of the equivalent reaction. The Bragg peaks attributed to the presence of $NaBiO_3$, subsequently disappear after $Ce(NO_3)_3$ at approximately 1800 s. Furthermore, because of the insufficient resolution the observation of α-Bi_2O_3 isn't very prominent but still observable.

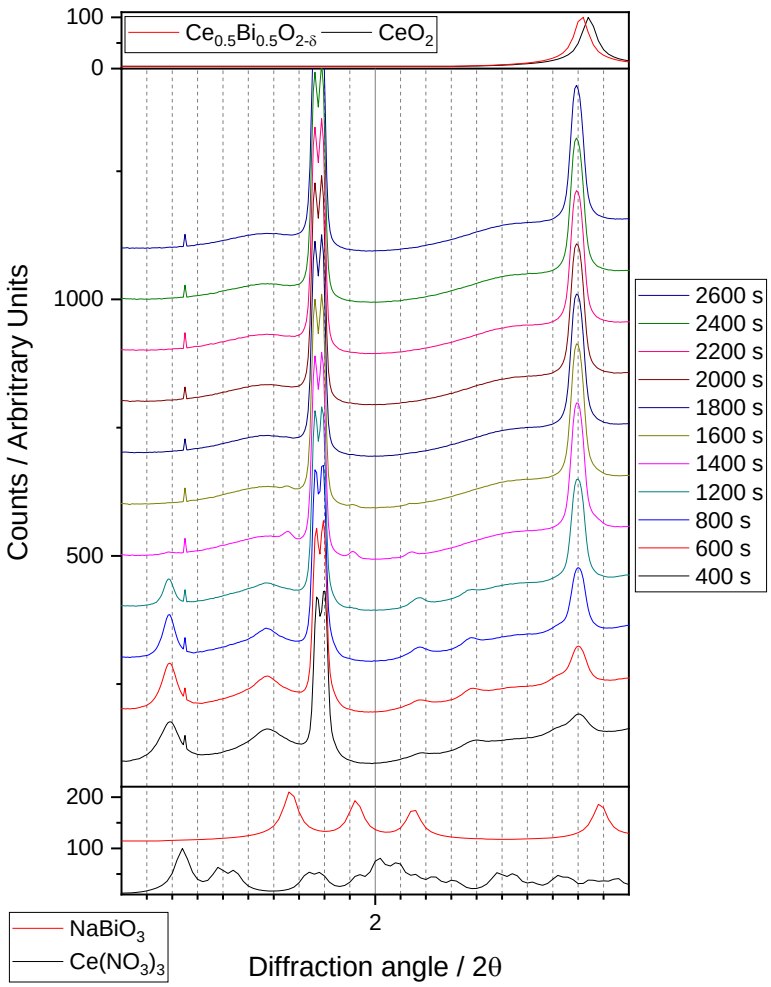

Figure 13: In situ Bragg reflections collected during the hydrothermal synthesis of $Ce_{0.5}Bi_{0.5}O_{2-\delta}$ for the reaction between $Ce(NO_3)_3$ and $NaBiO_3$ for different times at 200 °C. The results are compared against reference literature spectra for the starting reagents, intermediate phases and products. [8,11,13,14]

3.8 Conclusions

Overall the formation processes involved in the parameter sensitive hydrothermal reaction may lead to control controlled through the combination of comprehensive in situ and ex situ studies. The choice of starting reagents has implications on the reaction time to form and affects the crystallite size of the final products. The $Ce_{0.5}Bi_{0.5}O_{2-\delta}$ samples with the lower crystallite size and larger surface areas being formed from the use of Ce^{4+} starting reagents. Good agreement is observed when comparing trends from the ex situ studies with time-resolved in situ X-ray diffraction experiments. The reaction pathways leading to the formation of $Ce_{0.5}Bi_{0.5}O_{2-\delta}$ start by the dissolution of the Ce reagent, and the transformation/reduction of the Bi reagent to α-Bi_2O_3, before the incorporation into the fluorite structure. The initial stages of the reaction however are still unclear, there is evidence to suggest the CeO_2 forms

prior to the incorporation of bismuth according to the in situ XANES experiments but the results aren't definitive.

References

1. K.M.O. Jensen, C. Tyrsted, M. Bremholm and B.B. Iversen. (2014). In Situ Studies of Solvothermal Synthesis of Energy Materials. *Chemistry and Sustainability*. 7 (6), p1594-1611.
2. S.J. Moorhouse, N. Vranjes, A. Jupe, M. Drakopoulos and D. O'Hare. (2012). The Oxford-Diamond In Situ Cell for studying chemical reactions using time-resolved X-ray diffraction. *Review of Scientific Instruments*. 83, p84-101.
3. K. Maniammal, G. Madhu and V. Biju. (2017). X-ray diffraction line profile analysis of nanostructured nickel oxide: Shape factor and convolution of crystallite size and microstrain contributions. *Physica E: Low-dimensional systems and nanostructures*. 85 (85), p214-222.
4. S. Dikmen, P. Shuk and M. Greenblatt. (1998). Hydrothermal synthesis and properties of $Ce_{1-x}Bi_xO_{2-\delta}$ solid solutions. *Solid State Ionics*. 112 (3-4), p299-307.
5. G. Li, Y. Mao, L. Li, S. Feng, M. Wang and X. Yao. (1999). Solid Solubility and Transport Properties of Nanocrystalline $(CeO_2)_{1-x}(BiO_{1.5})$ by Hydrothermal Conditions. *Chemistry of Materials.* 11, p1259-1266.
6. H. Zhao, S. Feng and W. Xu. (2000). A soft chemistry route for the synthesis of nano solid electrolytes $Ce_{1-x}Bi_xO_{2-x/2}$. *Materials Research Bulletin*. 35 (14-15), p2379-2386.
7. Y.V. Frolova, D.I. Kochubey, V.V. Kriventsov, E.M. Moroz, S. Neofitides, V.A. Sadykov and D.A. Zyuzin. (2005). The influence of bismuth addition on the local structure of CeO_2. *Nuclear Instruments and Methods in Physics Research. A.* (543), p127-130.
8. K. Sardar, H.Y. Playford, R.J. Darton, E.R. Barney, A.C. Hannon, D. Thompsett, J. Fisher, R.J. Kashtiban, J. Sloan, S. Ramos, G. Cibin and R.I. Walton. (2010). Nanocrystalline Cerium-Bismuth Oxides: Synthesis, Structural Characterization, and Redox Properties. *Chemistry of Materials*. 22, p6191-6201.
9. G. Malmros. (1970). The crystal structure of alpha - Bi_2O_3. *Acta Chemica Scandinavica*. 24, p384-396.
10. F. Lazarini. (1985). Redetermination of the structure of bismuth (III) nitrate pentahydrate, $Bi(NO_3)_3$ 5 (H_2O). *Acta Crystallographica, Section C: Crystal Structure Communications*. 41, p1144-1145.
11. C. Heinrichs. (2013). Synthese und Charakterisierung wasserfreier Seltenerdmetall-Nitrate, -Acetate und -Oxyacetate. *Dissertation Koeln Universite.* p1-243.
12. T.A. Beineke and J. Delgaudio. (1968). The crystal structure of ceric ammonium nitrate. *Inorganic Chemistry*. 7, p715-721.
13. N. Kumada, N. Kinomura and A.W. Sleight. (2000). Neutron powder diffraction refinement of ilmenite-type bismuth oxides: $ABiO_3$ (A = Na, Ag). *Materials Research Bulletin*. 35, p2397-2402.
14. M. Wolcyrz and L. Kepinski. (1992). Rietveld refinement of the structure of CeOCl formed in Pd/CeO_2 catalyst: notes on the existence of a stabilized tetragonal phase of La_2O_3 in La-Pd-O system. *Journal of Solid State Chemistry*. 99, p409-413.

4. Solvothermal synthesis of lanthanide-substituted $Ce(OH)_2Cl$ and $Ce(OH)CO_3$ and their thermal decomposition to mixed-metal oxides

4.1 Introduction

Recently over the last few decades, considerable attention has focused on the synthesis of CeO_2 nanomaterials with specific dimensions and morphologies, in view of enhancing their activity and the properties of the materials for several potential applications. Whilst there have been reports of the thermal decomposition of $CeCO_3OH$ to form CeO_2 materials with unusual morphologies, (see Chapter 1) the incorporation of lanthanides into the $Ce(OH)CO_3$ structure hasn't been studied extensively. The substitution of lanthanides into or as-prepared $Ce(OH)_2Cl$ has not been previously reported. Therefore this chapter has focused on the solvothermal synthesis of trivalent lanthanide substituted cerium complexes in the form of $Ce_{1-x}Ln_x(OH)_2Cl$ and $Ce_{1-x}Ln_x(OH)CO_3$ (Ln = La, Gd, Pr and Tb), the assumption being that the 4f elements commonly exhibit the trivalent oxidation state and are known to form highly coordinated compounds as in the structures mentioned. The intent was to produce $Ce_{1-x}Ln_xO_{2-\delta}$ mixed oxides with unusual morphologies and perhaps increased homogeneity as prior to decomposition both lanthanides are in the 3+ oxidation state. Starting from the 3+ oxidation state for Pr and Tb as well may lead to the control over the oxidation state of the lanthanide by adjusting the calcination temperature. The structural characterisation of these materials and the $Ce_{1-x}Ln_xO_{2-\delta}$ samples formed by their subsequent thermal decomposition are explored. H_2-TPR is a straightforward and widely employed technique to extract information to assess the reducibility of oxide materials and was used to evaluate the synthesised lanthanide substituted ceria's.

4.2 Synthesis

4.2.1 Solvothermal synthesis of $Ce_{1-x}Ln_x(OH)_2Cl$

$CeCl_3 \cdot 7H_2O$ (Sigma-Aldrich, 99.9% purity), $LaCl_3 \cdot 7H_2O$ (Alfa Aesar, 99.9% purity), $PrCl_3 \cdot 7H_2O$ (Alfa Aesar, 99.9% purity), $GdCl_3 \cdot 7H_2O$ (Alfa Aesar, 99.9% purity) and $TbCl_3 \cdot 7H_2O$ (Alfa Aesar, 99.999% purity) powders were used as precursor materials. These powders were mixed in a stoichiometric ratio to obtain

$Ce_{1-x}Ln_x(OH)_2Cl$, varying x from 0 to 1. The level of hydration of the metal salts was determined using thermo-gravimetric analysis.

Samples of $Ce_{1-x}Ln_x(OH)_2Cl$ were prepared by solvothermal synthesis from metal salts using Teflon-lined, stainless-steel autoclaves (20 mL). In a typical synthesis, $CeCl_3$ and $LnCl_3$ (Ln = La, Pr, Gd and Tb, hydrated as noted above) with desired stoichiometric ratio (2 mmol total) were stirred in 8 mL of polyethylene glycol (Mn_{400}) for 1 h. The reaction mixtures were sealed in autoclaves and then placed in a preheated fan oven at 240 °C for 24 h, before cooling to room temperature. After the reaction, a dark brown precipitate was obtained which was recovered by suction filtration. All the solid products were washed with deionised water and dried at 70 °C overnight before further characterisation.

4.2.2 Solvothermal synthesis of $Ce_{1-x}Ln_x(OH)CO_3$

$Ce(NO_3)_3 \cdot 6H_2O$ (99.5% Alfa Aesar), $La(NO_3)_3 \cdot 6H_2O$ (99.99% Alfa Aesar), $Pr(NO_3)_3 \cdot 6H_2O$ (99.9% STREM CHEMICALS Inc), $Gd(NO_3)_3 \cdot 6H_2O$ (99.99% Alfa Aesar) and $Tb(NO_3)_3 \cdot 6H_2O$ (99.9% STREM CHEMICALS Inc) powders were used as precursor materials. These powders were mixed in a stoichiometric ratio to obtain $Ce_{1-x}Ln_x(OH)CO_3$, varying x from 0 to 0.5. The level of hydration of the metal salts was determined using thermo-gravimetric analysis.

In a typical synthesis, $Ce(NO_3)_3$ and $Ln(NO_3)_3$ (Ln = La, Pr, Gd and Tb) with desired stoichiometric ratio (2 mmol total) were stirred in 8 mL of polyethylene glycol (Mn_{200}) for 1 h. The reaction mixtures were sealed in autoclaves and then placed in a preheated fan oven at 240 °C for 24 h, before cooling to room temperature. After the reaction, a light brown precipitate was obtained which was recovered by suction filtration. All the solid products were washed with deionised water and dried at 70 °C overnight before further characterisation.

The use of a different molecular weight polyethylene glycol in this reaction is to avoid the formation of a cerium oxalate formate impurity obtained using a higher molecular weight polyethylene glycol.

4.2.3 Thermal Treatment of $Ce_{1-x}Ln_x(OH)_2Cl$ and $Ce_{1-x}Ln_x(OH)CO_3$

Mixed oxides were obtained by heating the $Ce_{1-x}Ln_x(OH)_2Cl$ and $Ce_{1-x}Ln_x(OH)CO_3$ samples in air using a muffle furnace at 10 °C min^{-1} from room temperature to 700 °C and held at this temperature for 5 h, before cooling.

4.2.4 XANES measurements

The Pr and Tb L_{III}-edge X-ray absorption data were collected on Beamline B18 at Diamond Light Source, UK. The samples were diluted with polyethylene powder and pressed into a 13 mm diameter pellets, approximately 1 mm thick. The absorption data were collected in transmission mode and the spectra were normalised using the ATHENA software package.

The Tb_4O_7 and Pr_6O_{11} reference materials were supplied by Johnson Matthey Technology Centre, UK.

4.3 $Ce(OH)_2Cl$ and $Ce(OH)CO_3$

4.3.1 Powder XRD

$Ce(OH)_2Cl$ has been prepared by solvothermal synthesis starting with $CeCl_3 \cdot 7H_2O$ as the Ce reagent. $Ce(OH)_2Cl$ is a new material not characterised before, but the X-ray pattern is similar to $La(OH)_2Cl$ so it can be used as a model for refining its crystal structure. The powder XRD pattern of $Ce(OH)_2Cl$ (Figure 32) can be indexed and the profile fitted to a monoclinic cell (space group: *P112/m*). However, the pattern of the sample made using $Ce(NO_3)_3$ as the starting reagent can be indexed to a hexagonal cell (space group: *P-62C*). This matches the unit cells of $Ce(OH)CO_3$ and $Ce(CO_3)F$ and the same results is observed when $Ce(NH_4)_2(NO_3)_6$ is used as a precursor. A satisfactory profile fit of this pattern could not be achieved due to the presence of anisotropic peak broadening, which suggests very anisotropic crystals so a single peak function cannot be used to fit the pattern.

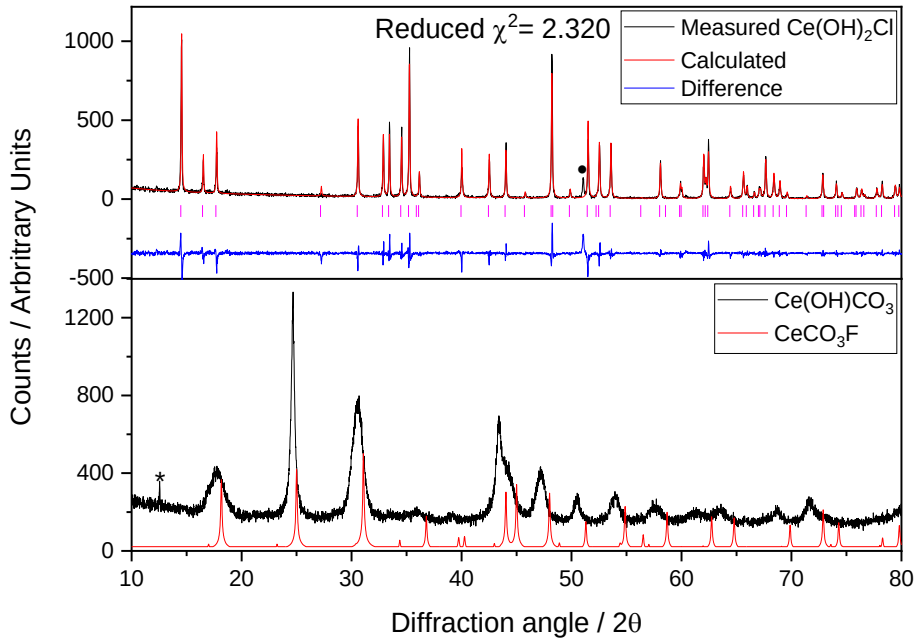

*Figure 14: XRD patterns of $Ce(OH)_2Cl$ and $CeCO_3OH$, which are compared against reference data obtained from literature. [1] (•Indicates contamination on XRD slit, *aluminium sample holder peak).*

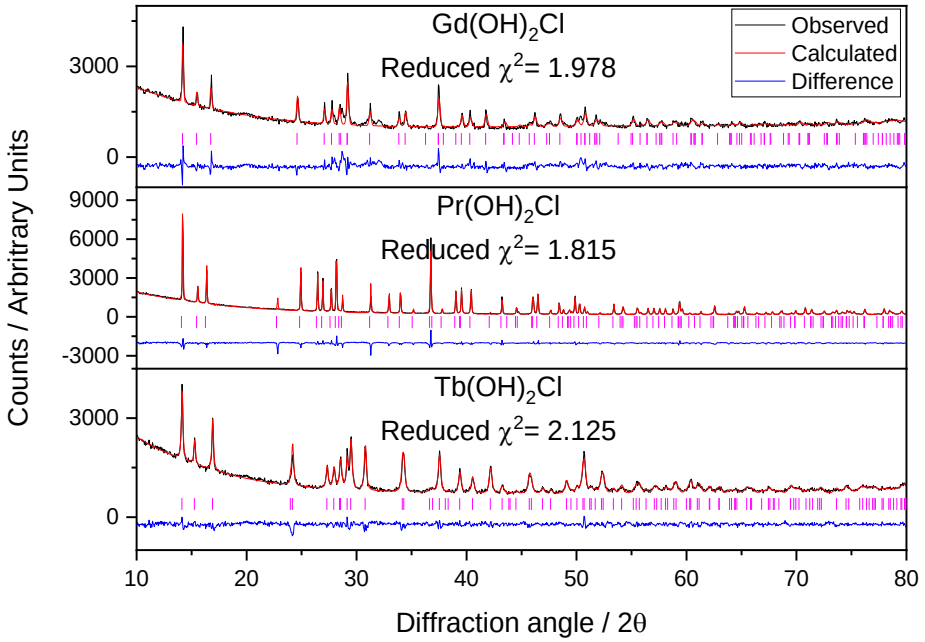

Figure 15: Le Bail fits to Powder XRD data (λ = 1.5405 Å) of $Tb(OH)_2Cl$, $Pr(OH)_2Cl$ and $Gd(OH)_2Cl$.

The powder XRD patterns of CeO_2 prepared by the thermal decomposition of $Ce(OH)_2Cl$ and $Ce(OH)CO_3$ can both be indexed and the profile fitted using the space group $Fm\bar{3}m$ with almost identical lattice parameters (Figure 34). The

crystallite size and lattice strain of the ceria powders also show little differentiation between the two samples (Table 7).

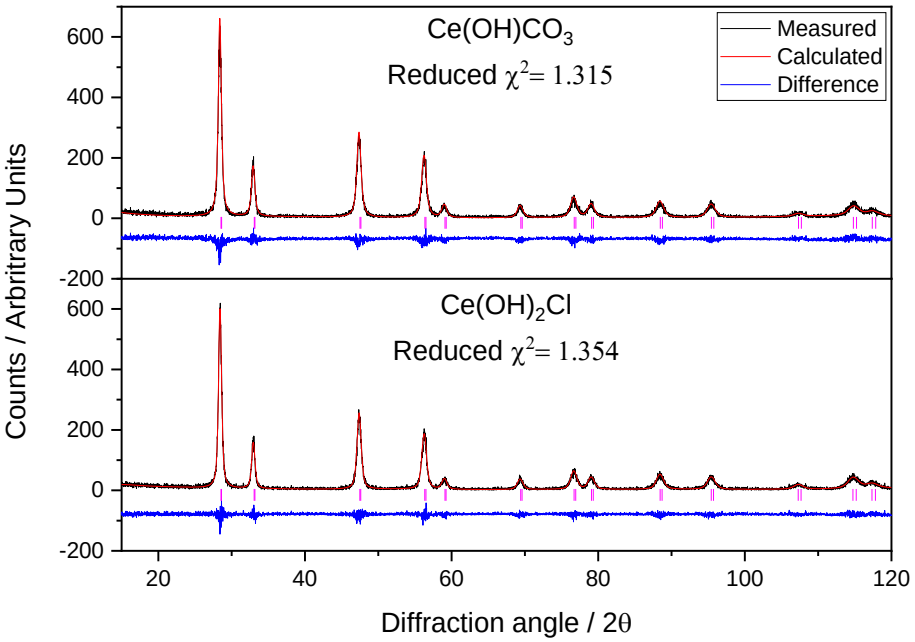

Figure 16: Le Bail fits to Powder XRD data (λ = 1.5405 Å) of $Ce(OH)_2Cl$ and $Ce(OH)CO_3$ after thermal decomposition to CeO_2.

Table 7: Results of Le Bail fitting to powder XRD data of $Ce(OH)_2Cl$ and $Ce(OH)CO_3$.

Sample	*a* (Å)	[a] Crystallite size (Å)	[b] Cε	[b] L (Å)
CeO_2 - $Ce(OH)CO_3$	5.4091 (2)	111 (23)	0.0115 (2)	225 (1)
CeO_2 - $Ce(OH)_2Cl$	5.4104 (2)	113 (23)	0.0110 (3)	223 (1)

4.3.2 Further characterisation

TGA of $Ce(OH)_2Cl$ and $Ce(OH)CO_3$ (Figure 35) under an air atmosphere both show a very sharp endothermic peak, centred at around 350 °C and 250 °C respectively. Any mass loss prior to the main mass loss can be attributed to the loss of absorbed water on the surface of the oxides or any remaining polyethylene glycol. After this the rate of mass loss decreases more slowly. At 1000 °C $Ce(OH)_2Cl$ and $Ce(OH)CO_3$ are 78.5% and 73.2% of their original mass, respectively. This difference can be explained by the simultaneous dehydroxylation and corresponding decarbonation or loss of chlorine for each sample, initiated by the oxidation of Ce^{3+}. This occurs in a single step decomposition as both products are oxidised into CeO_2, as confirmed by in situ powder XRD up to 800 °C.

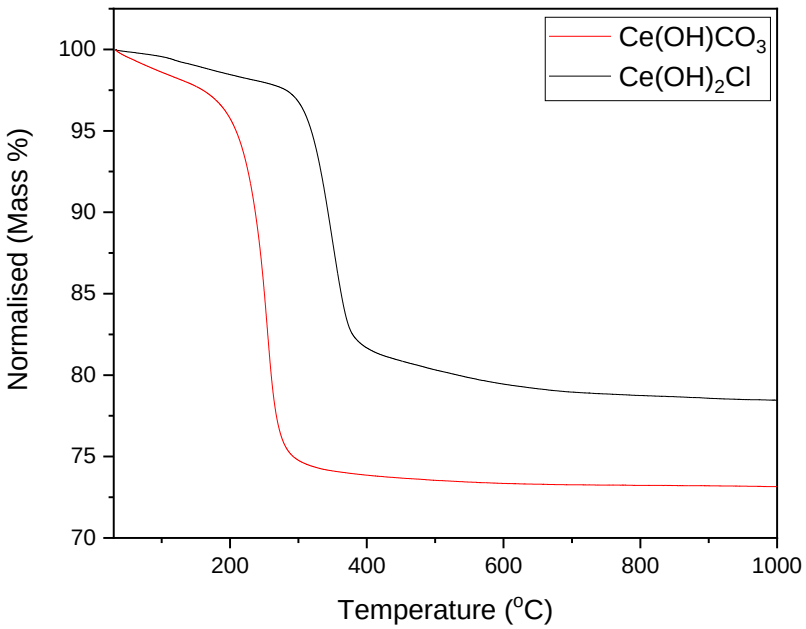

Figure 17: Thermogravimetric analysis of $Ce(OH)_2Cl$ and $Ce(OH)CO_3$.

The electron micrographs of the as-prepared $CeCO_3OH$ product (Figure 36(b)) is composed of a cluster of interwoven nanoplates compacted into oval-shaped spheres. The $Ce(OH)_2Cl$ has a similar morphology in overall shape but instead of plates it's a clusters of interwoven nanorod-shaped polyhedra (Figure 36(a)). The SEM images (Figure 36(c-d)) of the materials obtained after subsequent calcination at 700 °C of both $CeCO_3OH$ and $Ce(OH)_2Cl$ show that their structural morphologies are retained after thermal decomposition/ oxidation to CeO_2.

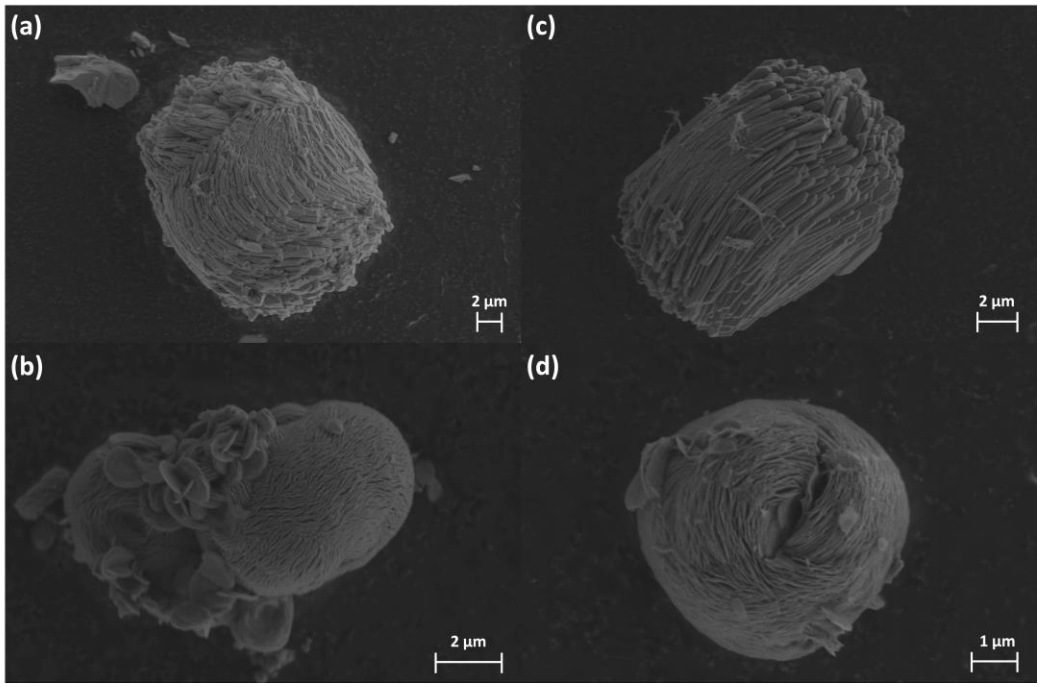

Figure 18: SEM micrographs of a) $Ce(OH)_2Cl$, b) $Ce(OH)CO_3$. The right-hand panels (c-d) correspond to the left-hand samples after thermal decomposition to $CeO_{2-\delta}$.

4.4 Lanthanum substituted ceria precursors

4.4.1 Powder XRD

As with the unsubstituted $Ce(OH)_2Cl$ the powder XRD patterns of $Ce_{1-x}La_x(OH)_2Cl$ can be indexed and the profile fitted to a monoclinic cell (space group: *P112/m*) within the range $0.1 \leq x \leq 0.2$ (Figure 37). Increasing the lanthanum content to x = 0.3 or above leads to phase segregation as when $LaCl_3$ is used solely in the solvothermal reaction the product produced is an unknown phase.

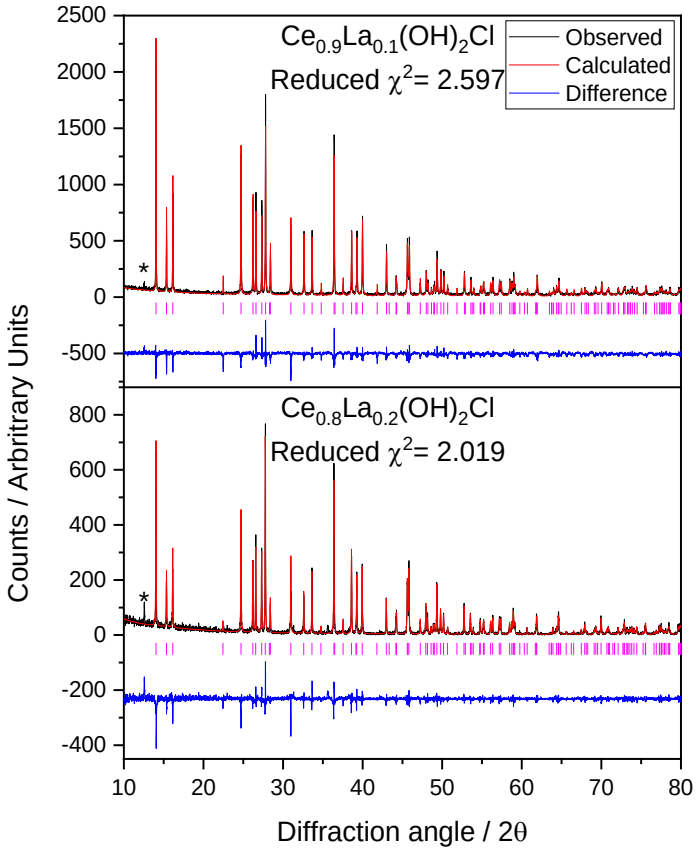

Figure 19: Le Bail fits to Powder XRD data (λ = 1.5405 Å) of $Ce_{1-x}La_x(OH)_2Cl$ ($0.1 \leq x \leq 0.2$). (contamination on XRD slit).*

Table 8: Results of Le Bail fitting to powder XRD data of $Ce_{1-x}La_x(OH)_2Cl$ ($0.1 \leq x \leq 0.2$).

Sample	*a* (Å)	*b* (Å)	*c* (Å)	β (Å)	Volume (Å^3)
$Ce_{0.9}La_{0.1}(OH)_2Cl$	6.2925 (1)	6.8802 (1)	3.95446 (7)	113.542 (1)	156.952 (3)
$Ce_{0.8}La_{0.2}(OH)_2Cl$	6.29485 (11)	6.88596 (11)	3.95854 (6)	113.585 (1)	157.254 (3)

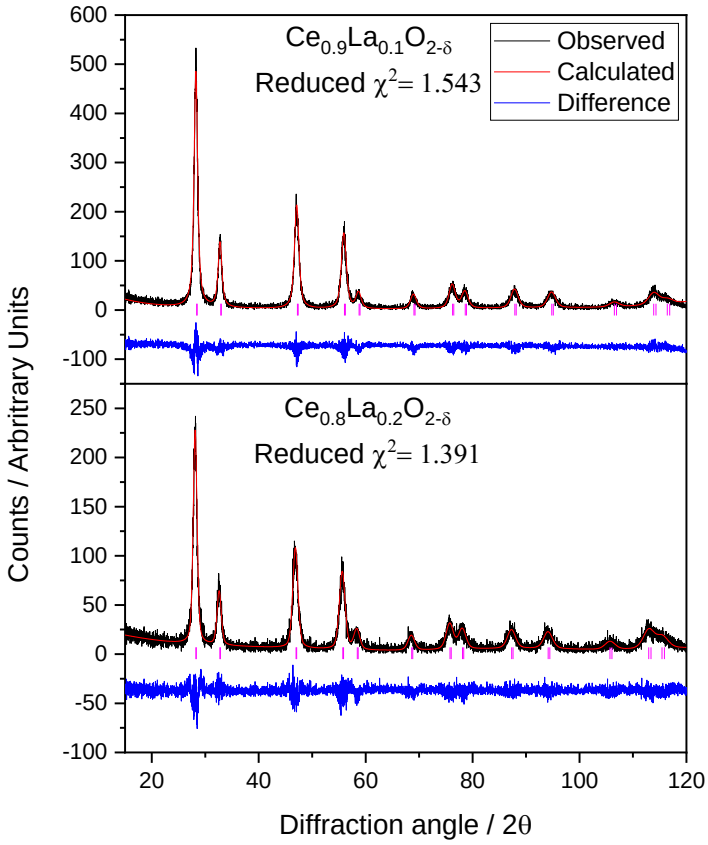

Figure 208: Le Bail fits to Powder XRD data (λ = 1.5405 Å) of $Ce_{1-x}La_xO_{2-\delta}$ (0.1 ≤ x ≤ 0.2) after thermal decomposition of $Ce_{1-x}La_x(OH)_2Cl$.

Table 9: Results of Le Bail fitting to powder XRD data of $Ce_{1-x}La_xO_{2-\delta}$ (0.1 ≤ x ≤ 0.2).

Sample	*a* (Å)	[a] Crystallite size (Å)	[b] Cε	[b] L (Å)
$Ce_{0.9}La_{0.1}O_{2-\delta}$	5.4371 (3)	78 (13)	0.01418 (6)	139 (1)
$Ce_{0.8}La_{0.2}O_{2-\delta}$	5.4664 (4)	68 (12)	0.015 (1)	113 (6)

Powder XRD patterns of $Ce_{1-x}La_xO_{2-\delta}$ prepared by thermal decomposition of $Ce_{1-x}La_x(OH)CO_3$ (Figure 39) as with CeO_2 can be indexed and the profile fitted to a cubic fluorite cell (space group $Fm\bar{3}m$) within the range $0.1 \leq x \leq 0.5$. In contrast to the lanthanum substituted $Ce(OH)_2Cl$, the $Ce(OH)CO_3$ structure is able to accommodate a higher degree of substitution up to an x value of 0.5. As x increases the Bragg peaks become broader (Figure 40) and the lattice parameter decreases linearly (Figure 41) The broadening of the Bragg peaks is likely to be caused by a reduced particle size, though crystallographic strain effects can also cause peak broadening (Table 10). As demonstrated by the increase in Williamson-Hall Cε values as more lanthanum is incorporated into the structure. The lattice expansion is

consistent with the larger atomic radius of La^{3+} compared to that of Ce^{4+} (La^{3+} and Ce^{4+} have respective ionic radii of 1.16 Å and 0.97 Å).

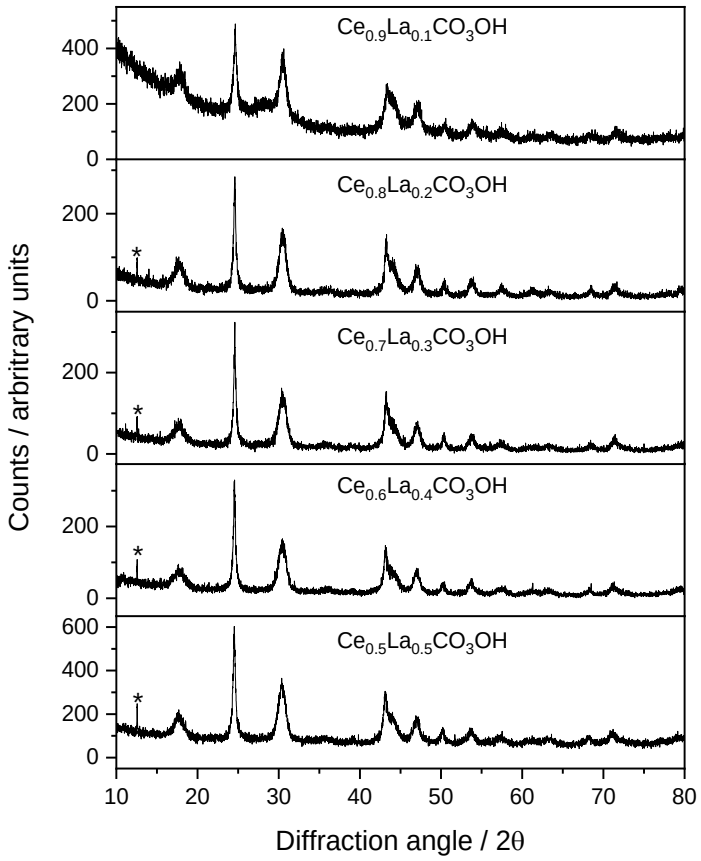

Figure 219: Powder XRD data (λ = 1.5405 Å) of $Ce_{1-x}La_x(OH)CO_3$ ($0.1 \leq x \leq 0.5$). (contamination on XRD slit).*

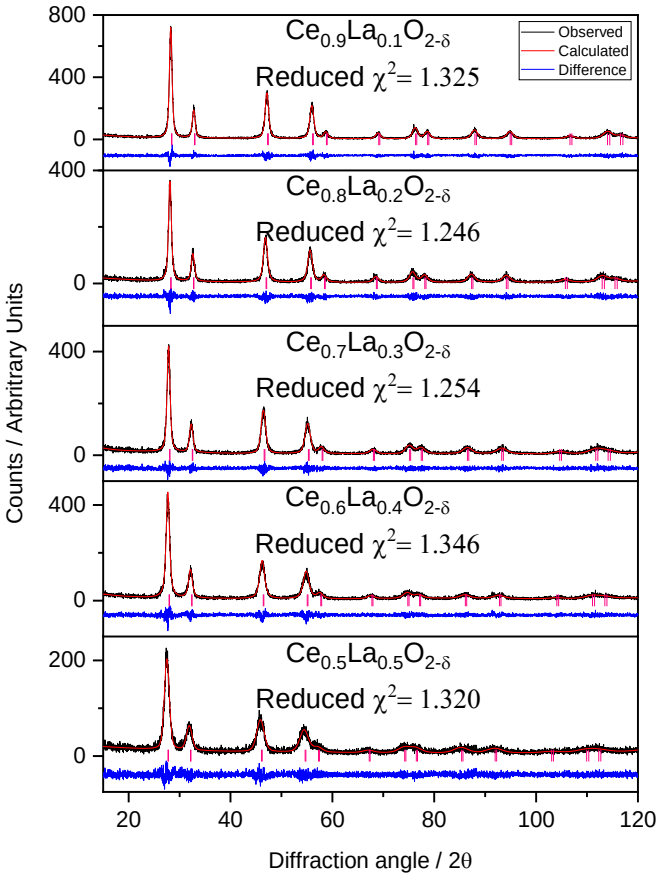

Figure 40: Le Bail fits to Powder XRD data (λ = 1.5405 Å) of $Ce_{1-x}La_xO_{2-\delta}$ ($0.1 \leq x \leq 0.5$) after thermal decomposition of $Ce_{1-x}La_x(OH)CO_3$.

Table 10: Results of Le Bail fitting to powder XRD data of $Ce_{1-x}La_xO_{2-\delta}$ ($0.1 \leq x \leq 0.2$).

Sample	*a* (Å)	[a] Crystallite size (Å)	[b] Cε	[b] L (Å)
$Ce_{0.9}La_{0.1}O_{2-\delta}$	5.4322 (2)	90 (20)	0.0146 (3)	190 (6)
$Ce_{0.8}La_{0.2}O_{2-\delta}$	5.4650 (3)	80 (19)	0.0183 (6)	184 (9)
$Ce_{0.7}La_{0.3}O_{2-\delta}$	5.5056 (3)	67 (23)	0.0326 (7)	348 (4)
$Ce_{0.6}La_{0.4}O_{2-\delta}$	5.5266 (4)	56 (23)	0.0326 (17)	248 (4)
$Ce_{0.5}La_{0.5}O_{2-\delta}$	5.5651 (7)	41 (13)	0.0496 (5)	163 (7)

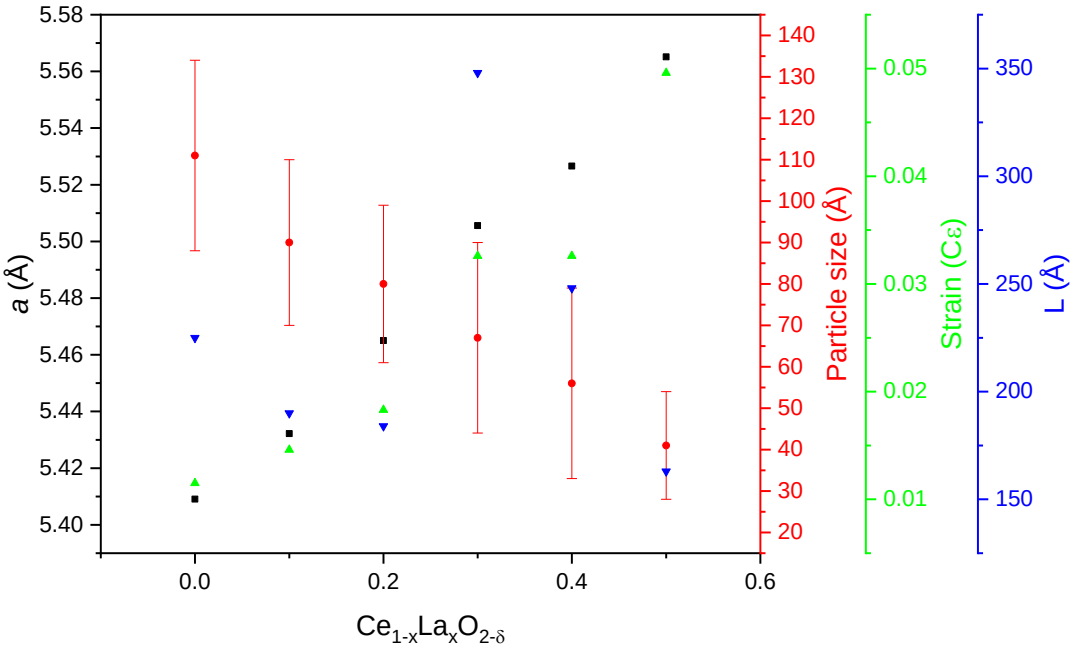

Figure 41: Lattice parameter, crystallite size, strain and L of $Ce_{1-x}La_xO_{2-\delta}$ after thermal decomposition of $Ce_{1-x}La_x(OH)_2Cl$ as a function of lanthanum substitution ($0 \leq x \leq 0.5$).

4.4.2 Further characterisation

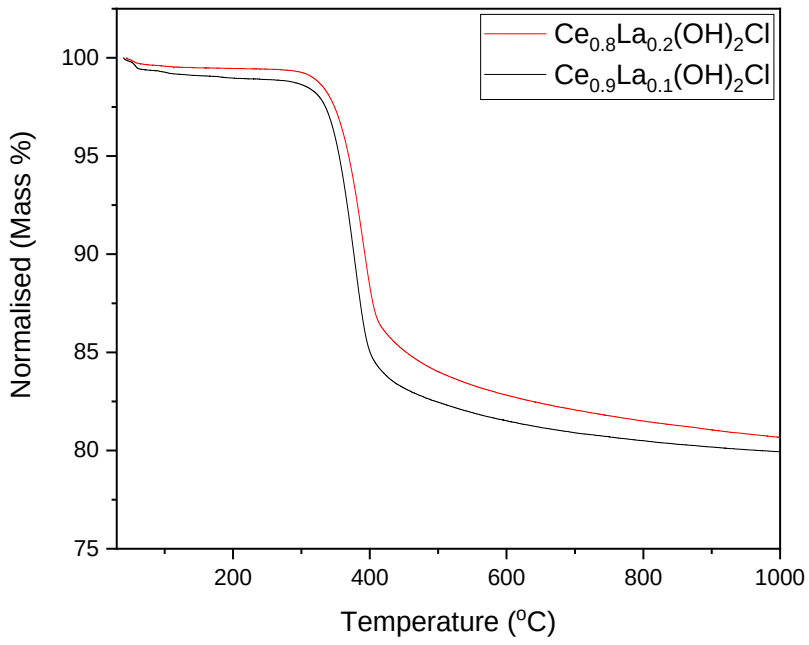

Figure 42: Thermogravimetric analysis of $Ce_{1-x}La_x(OH)_2Cl$ ($0.1 \leq x \leq 0.2$).

In the low-magnification SEM image in Figure 43(a) the morphology of $Ce_{0.9}La_{0.1}(OH)_2Cl$ can be seen clearly. The addition of lanthanum alters the morphology slightly in comparison with the unsubstituted $Ce(OH)_2Cl$. The elongated

polyhedra as previously seen have contracted and appear more like blocks. However, as with the unsubstituted $Ce(OH)_2Cl$ the calcination of the materials does not appear to change the observed morphology. The elemental compositions of the $Ce_{1-x}La_x(OH)_2Cl$ samples were determined by EDXA analysis as shown in Table 11. The elemental compositions of the products match the desired target stoichiometric ratio.

The addition of lanthanum to $Ce(OH)CO_3$ does not appear to alter the morphology in comparison to the unsubstituted cerium bis-hydroxy chloride. As with the $Ce_{1-x}La_x(OH)_2Cl$ samples calcined at 700 °C, the temperature does not transform the morphology of the particles drastically. Some pores are formed and the separation between some of the nanoplates expands in a minimal number of particles as shown in Figure 44(f). At 1000 °C, a larger quantity of particles were observed to have similar modified characteristics.

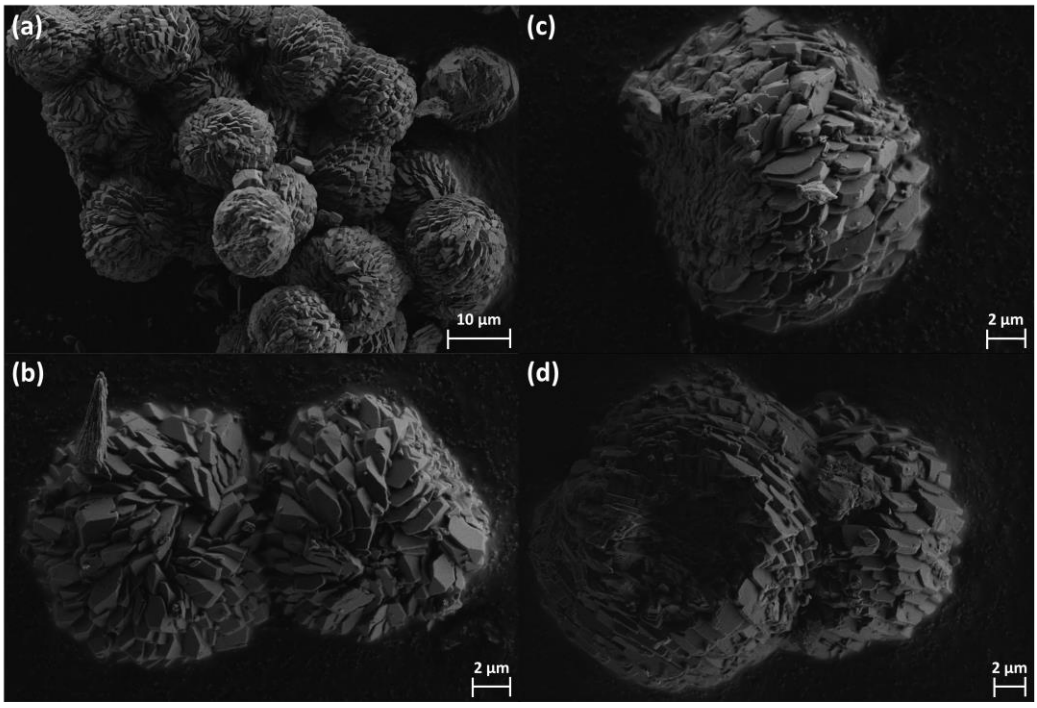

Figure 22: SEM micrographs of a) $Ce_{0.9}La_{0.1}(OH)_2Cl$, b) $Ce_{0.8}La_{0.2}(OH)_2Cl$. The right-hand panels (c-d) correspond to the left-hand samples after thermal decomposition to $Ce_{1-x}La_xO_{2-\delta}$.

Table 11: Measured values of x from SEM EDXA elemental analysis of $Ce_{1-x}La_x(OH)_2Cl$.

Sample	Atomic %		STDEV
	Ce	La	
$Ce_{0.9}La_{0.1}(OH)_2Cl$	90	10	0.4
$Ce_{0.8}La_{0.2}(OH)_2Cl$	78.6	21.4	0.7

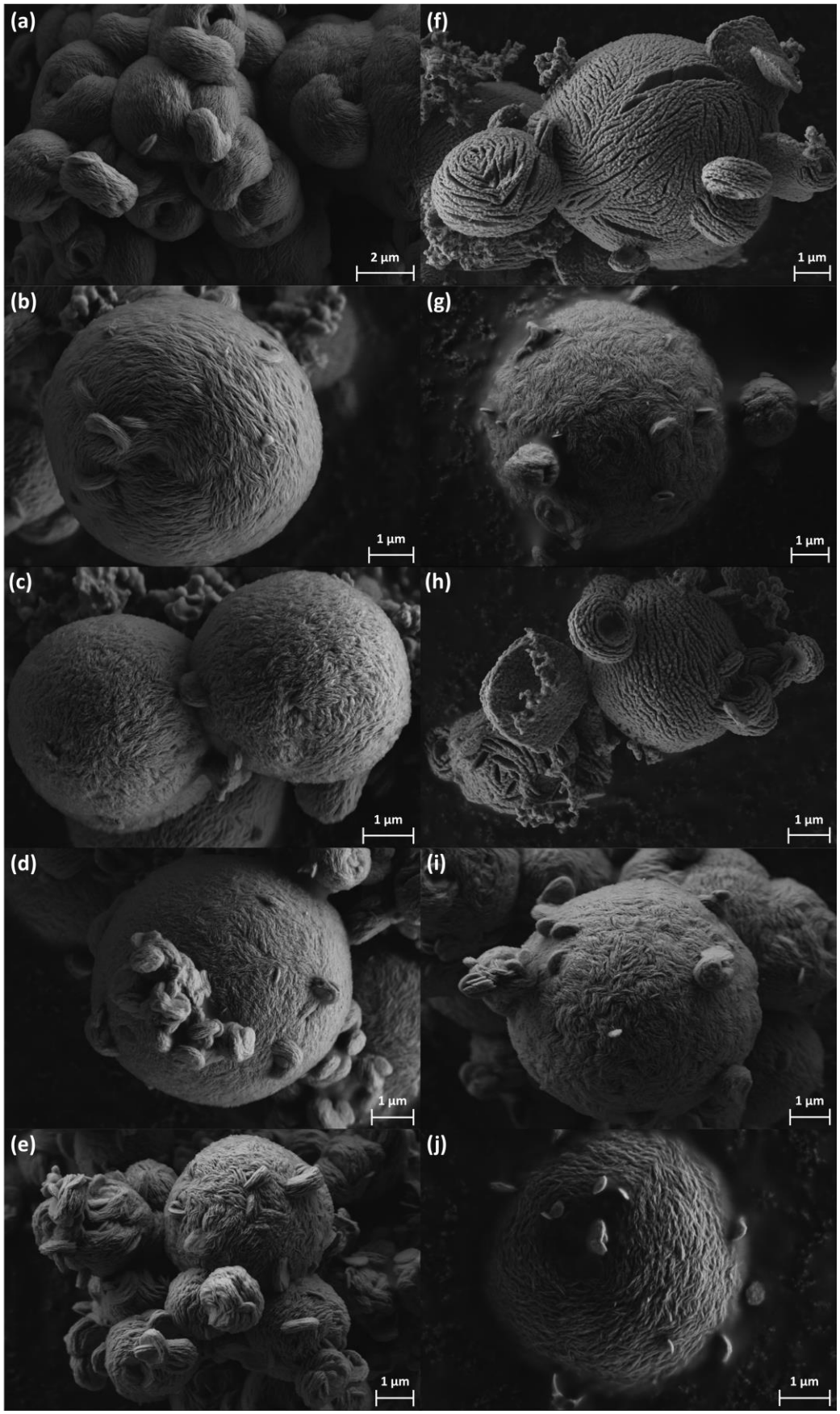

Figure 23: SEM micrographs of a) $Ce_{0.9}La_{0.1}(OH)CO_3$, b) $Ce_{0.8}La_{0.2}(OH)CO_3$, c) $Ce_{0.7}La_{0.3}(OH)CO_3$, d) $Ce_{0.6}La_{0.4}(OH)CO_3$, e) $Ce_{0.5}La_{0.5}(OH)CO_3$. The right-hand panels (f-j) correspond to left-hand samples after thermal decomposition to $Ce_{1-x}La_xO_{2-\delta}$.

Table 1: Measured values of x from SEM EDXA elemental analysis of $Ce_{1-x}La_x(OH)CO_3$.

Sample	Atomic %		STDEV
	Ce	La	
$Ce_{0.9}La_{0.1}(OH)CO_3$	91.0	9.0	1.5
$Ce_{0.8}La_{0.2}(OH)CO_3$	80.5	19.5	0.6
$Ce_{0.7}La_{0.3}(OH)CO_3$	69.7	30.3	0.9
$Ce_{0.6}La_{0.4}(OH)CO_3$	60.3	39.7	0.5
$Ce_{0.5}La_{0.5}(OH)CO_3$	48.9	51.1	1.3

4.5 Gadolinium substituted ceria precursors

4.5.1 Powder XRD

In contrast to $Ce_{1-x}La_x(OH)_2Cl$, $Ce(OH)_2Cl$ has the capability to incorporate a greater quantity of gadolinium into the monoclinic structure. Purely using $GdCl_3$ in the solvothermal reaction yields $Gd(OH)_2Cl$ (Figure 33) which provides an explanation for $Ce(OH)_2Cl$ having the capability to incorporate the increased lanthanide content. The calculated lattice parameters (*a*, *b* and *c*) for the $Ce_{1-x}Gd_x(OH)_2Cl$ samples all decrease linearly as x increases (Figure 46). Consistent with the contraction of the unit cell volume, as expected from the atomic radius of Gd^{3+} (0.938 Å) being smaller than that of Ce^{3+} (1.01 Å). Conversely when $Ce_{1-x}Gd_x(OH)_2Cl$ decomposes into $Ce_{1-x}Gd_xO_{2-\delta}$ the cell volume expands as the eight co-ordinate ionic radius of Ce^{4+} (0.97 Å) is smaller than Gd^{3+} (1.053 Å).

Contradictory to the $Ce_{1-x}La_x(OH)CO_3$, $Ce_{1-x}Gd_x(OH)CO_3$ is only capable of gadolinium substitution up to a value of x = 0.2. The powder XRD patterns of the products with substitution degrees above this are amorphous, unsurprisingly as using $Gd(NO_3)_3$ solely in the solvothermal reaction produces the same result.

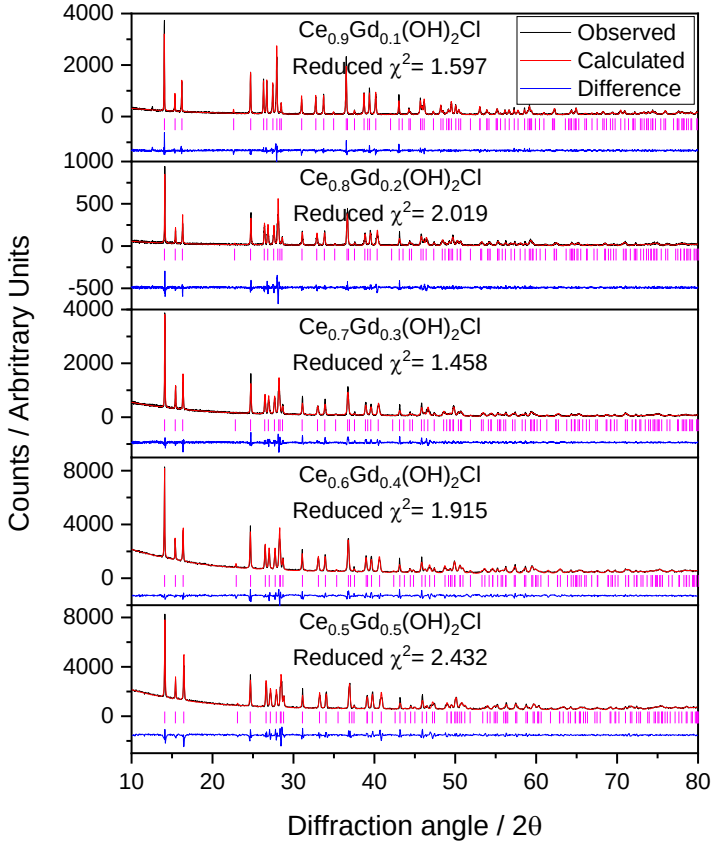

Figure 24: Le Bail fits to Powder XRD data (λ = 1.5405 Å) of $Ce_{1-x}Gd_x(OH)_2Cl$ ($0.1 \leq x \leq 0.5$).

Table 2: Results of Le Bail fitting to powder XRD data of $Ce_{1-x}Gd_x(OH)_2Cl$ ($0.1 \leq x \leq 1$).

Sample	*a* (Å)	*b* (Å)	*c* (Å)	*β* (Å)	Volume (Å^3)
$Ce_{0.9}Gd_{0.1}(OH)_2Cl$	6.27420 (14)	6.86038 (14)	3.93040 (8)	113.317 (1)	155.361 (7)
$Ce_{0.8}Gd_{0.2}(OH)_2Cl$	6.2599 (2)	6.8466 (2)	3.91150 (16)	113.139 (2)	154.157 (7)
$Ce_{0.7}Gd_{0.3}(OH)_2Cl$	6.2469 (2)	6.8328 (2)	3.89483 (14)	112.963 (2)	153.073 (7)
$Ce_{0.6}Gd_{0.4}(OH)_2Cl$	6.2330 (4)	6.8182 (7)	3.8769 (3)	112.776 (4)	151.914 (2)
$Ce_{0.5}Gd_{0.5}(OH)_2Cl$	6.2194 (4)	6.8013 (4)	3.8501 (4)	112.494 (5)	150.468 (15)

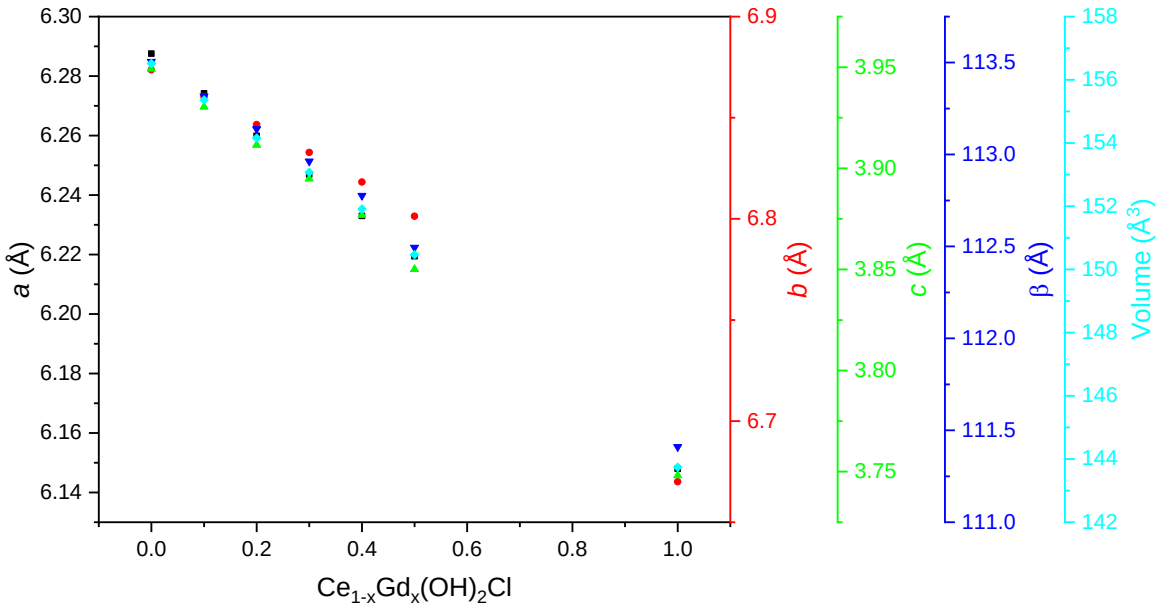

Figure 25: Lattice parameters extracted from the Le Bail fitting of the powder XRD data of $Ce_{1-x}Gd_x(OH)_2Cl$ as a function of gadolinium substitution ($0 \leq x \leq 1$).

In situ powder XRD (Figure 47) shows that upon heating to 350 °C in air, the monoclinic $Gd(OH)_2Cl$ transforms into tetragonal GdOCl with the PbFCl-type structure. Further heating causes the Bragg peaks attributed to GdOCl to begin to disappear at 750 °C and finally it converts to Gd_2O_3.

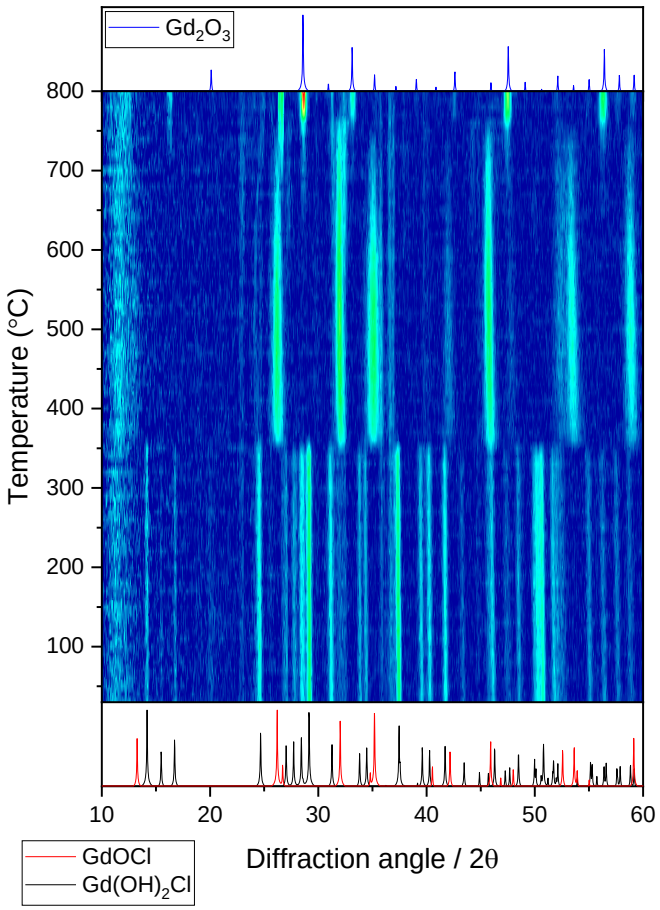

Figure 26: Contour plot of in situ powder XRD patterns of $Gd(OH)_2Cl$ heated from room temperature to 800 °C, compared against reference patterns of present phases shown above. [2-4]

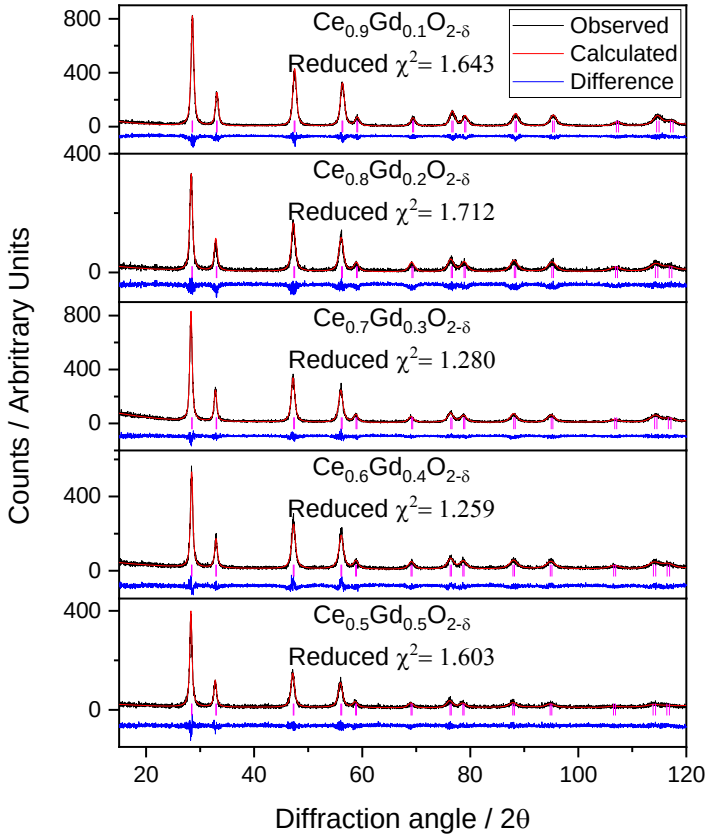

Figure 27: Le Bail fits to Powder XRD data (λ = 1.5405 Å) of $Ce_{1-x}Gd_xO_{2-\delta}$ ($0.1 \leq x \leq 0.5$) after thermal decomposition of $Ce_{1-x}Gd_x(OH)_2Cl$.

Table 3: Results of Le Bail fitting to powder XRD data of $Ce_{1-x}Gd_xO_{2-\delta}$ ($0.1 \leq x \leq 0.5$).

Sample	*a* (Å)	[a] Crystallite size (Å)	[b] Cε	[b] L (Å)
$Ce_{0.9}Gd_{0.1}O_{2-\delta}$	5.41807 (18)	97 (17)	0.0113 (3)	174 (3)
$Ce_{0.8}Gd_{0.2}O_{2-\delta}$	5.4246 (3)	92 (23)	0.0113 (3)	232 (6)
$Ce_{0.7}Gd_{0.3}O_{2-\delta}$	5.4296 (2)	91 (30)	0.0167 (2)	373 (13)
$Ce_{0.6}Gd_{0.4}O_{2-\delta}$	5.4360 (3)	84 (33)	0.0218 (2)	679 (28)
$Ce_{0.5}Gd_{0.5}O_{2-\delta}$	5.4378 (6)	89 (37)	0.02812 (13)	1240 (98)

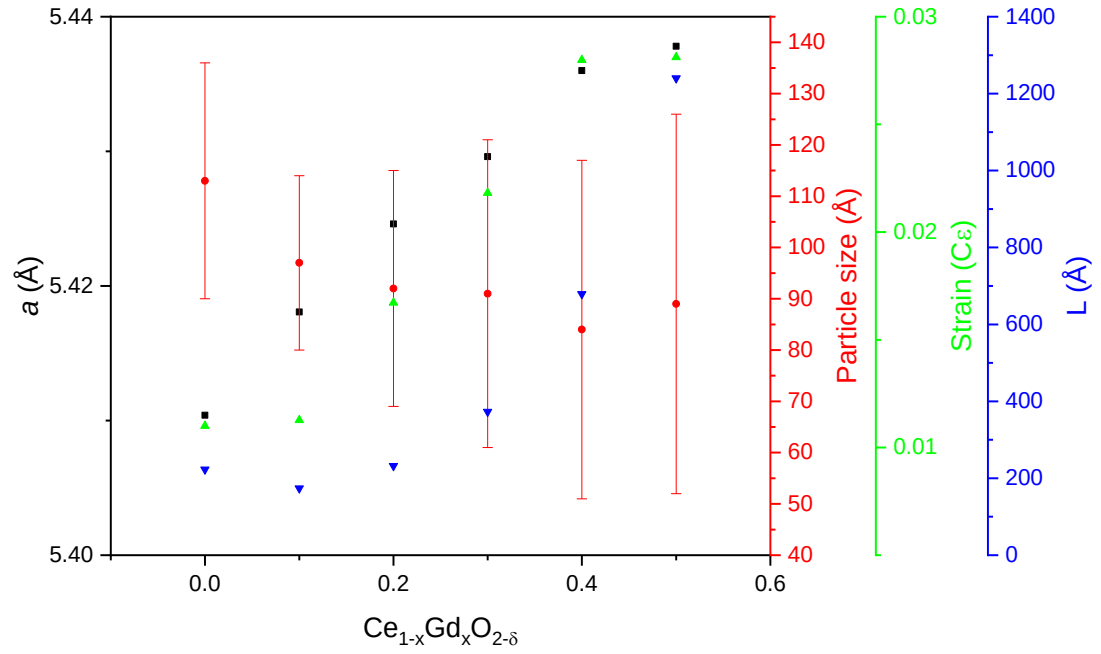

Figure 28: Lattice parameter, crystallite size, strain and L of $Ce_{1-x}Gd_xO_{2-\delta}$ after thermal decomposition of $Ce_{1-x}Gd_x(OH)_2Cl$ as a function of gadolinium substitution ($0 \leq x \leq 0.5$).

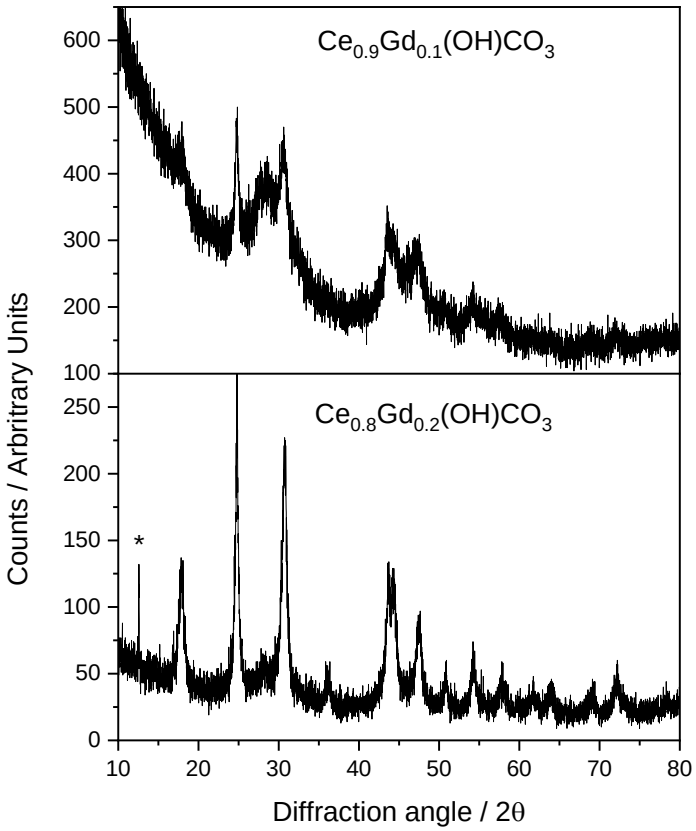

Figure 50: Powder XRD data (λ = 1.5405 Å) of $Ce_{1-x}Gd_x(OH)CO_3$ ($0.1 \leq x \leq 0.2$). (contamination on XRD slit).*

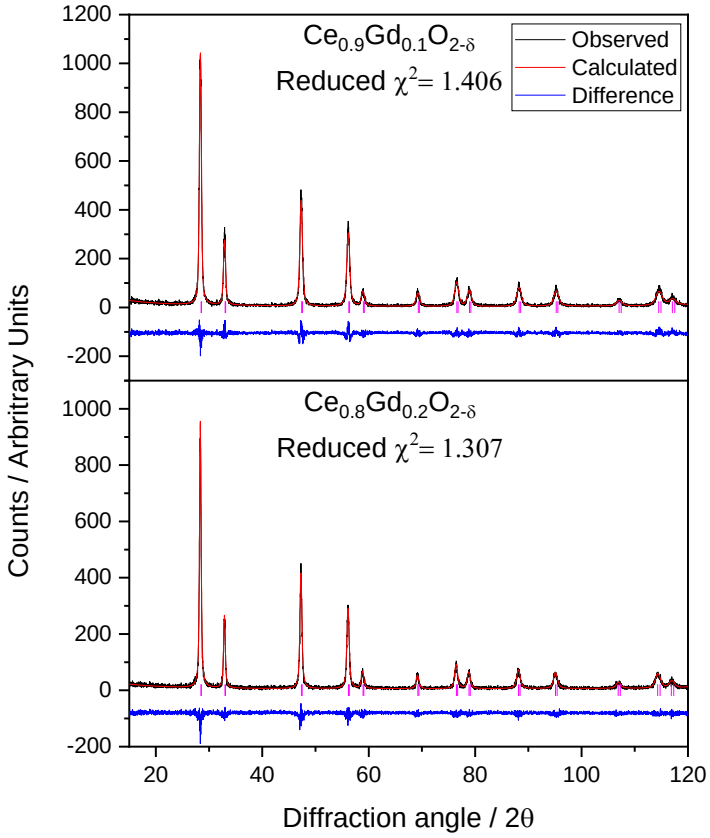

Figure 51: Le Bail fits to Powder XRD data (λ = 1.5405 Å) of $Ce_{1-x}Gd_xO_{2-\delta}$ ($0.1 \leq x \leq 0.2$) after thermal decomposition of $Ce_{1-x}Gd_x(OH)CO_3$.

Table 4: Results of Le Bail fitting to powder XRD data of $Ce_{1-x}Gd_xO_{2-\delta}$ ($0.1 \leq x \leq 0.2$).

Sample	*a* (Å)	[a] Crystallite size (Å)	[b] Cε	[b] L (Å)
$Ce_{0.9}Gd_{0.1}O_{2-\delta}$	5.41837 (14)	130 (25)	0.0096 (5)	237 (3)
$Ce_{0.8}Gd_{0.2}O_{2-\delta}$	5.42415 (13)	178 (28)	0.0054 (3)	291 (11)

4.5.2 Further Characterisation

The TGA results obtained for the $Ce_{1-x}Gd_x(OH)_2Cl$ samples show that the decomposition temperature is not significantly affected by the gadolinium content (Figure 52).

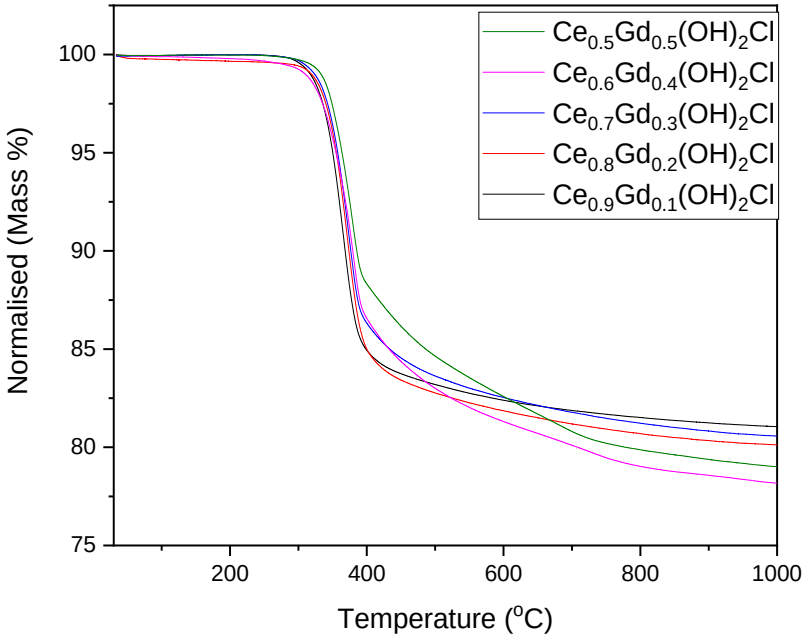

Figure 52: Thermogravimetric analysis of $Ce_{1-x}Gd_x(OH)_2Cl$ ($0.1 \leq x \leq 0.5$).

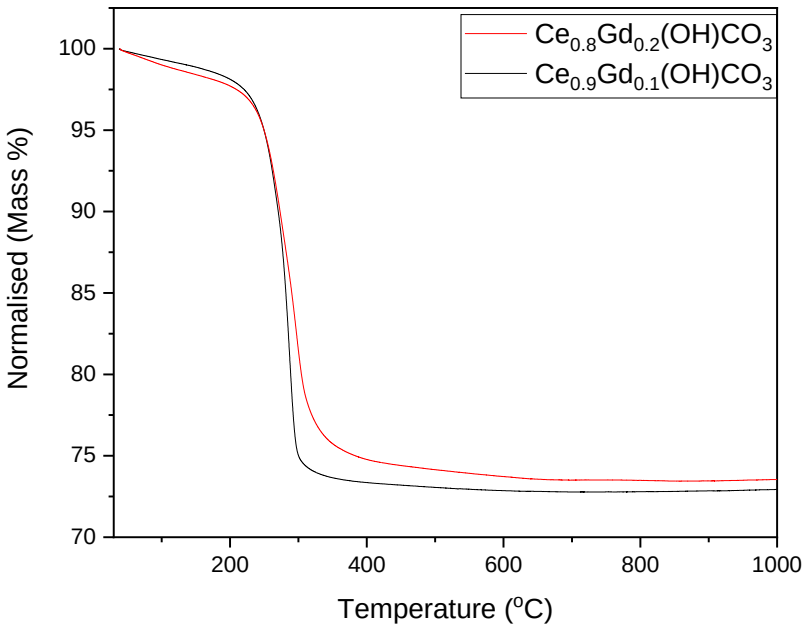

Figure 53: Thermogravimetric analysis of $Ce_{1-x}Gd_x(OH)CO_3$ ($0.1 \leq x \leq 0.2$).

The microstructures of the solvothermally prepared $Ce_{1-x}Gd_x(OH)_2Cl$ powders are shown in Figure 54. This figure reveals that the morphology of the obtained $Ce_{1-x}Gd_x(OH)_2Cl$ particles is not significantly influenced by the gadolinium content. Contrary to the minute changes the applied temperature impacts upon the

morphology of the carbonate hydroxides as previously described, the bis-hydroxy chlorides remain unaltered to a higher degree.

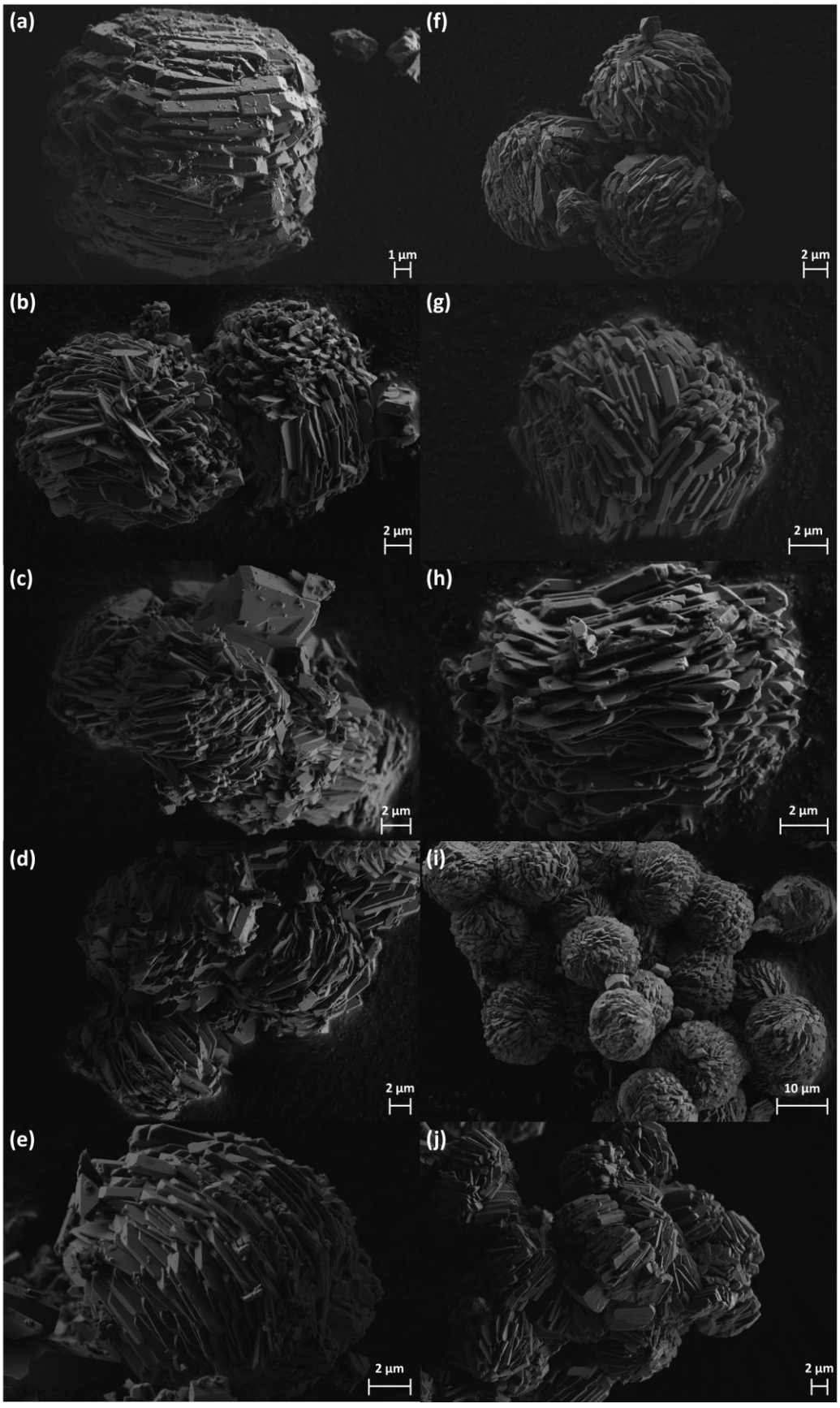

Figure 54: SEM micrographs of a) $Ce_{0.9}Gd_{0.1}(OH)_2Cl$, b) $Ce_{0.8}Gd_{0.2}(OH)_2Cl$, c) $Ce_{0.7}Gd_{0.3}(OH)_2Cl$, d) $Ce_{0.6}Gd_{0.4}(OH)_2Cl$, e) $Ce_{0.5}Gd_{0.5}(OH)_2Cl$. The right-hand panels (f-j) correspond to left-hand samples after thermal decomposition to $Ce_{1-x}Gd_xO_{2-\delta}$.

Table 56: Measured values of x from SEM EDXA elemental analysis of $Ce_{1-x}Gd_x(OH)_2Cl$.

Sample	Atomic %		STDEV
	Ce	Gd	
$Ce_{0.9}Gd_{0.1}(OH)_2Cl$	89.9	10.1	1.2
$Ce_{0.8}Gd_{0.2}(OH)_2Cl$	78.7	21.3	3.4
$Ce_{0.7}Gd_{0.3}(OH)_2Cl$	73.6	26.4	2.8
$Ce_{0.6}Gd_{0.4}(OH)_2Cl$	59.6	40.4	3.2
$Ce_{0.5}Gd_{0.5}(OH)_2Cl$	53.7	46.3	1.9

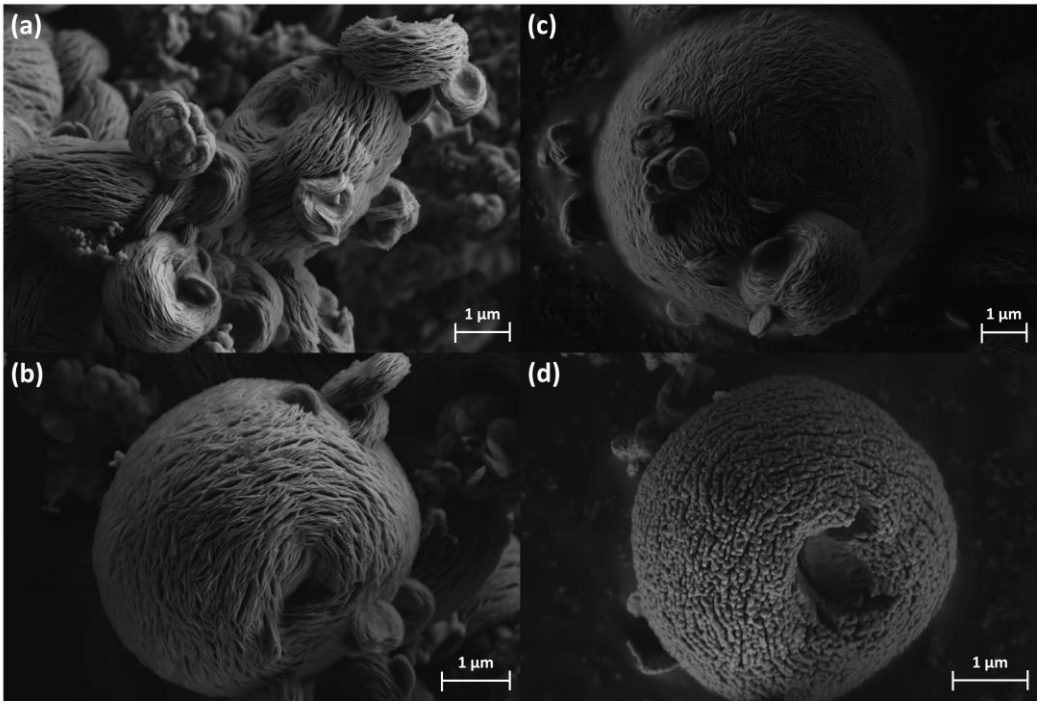

Figure 55: SEM micrographs of a) $Ce_{0.9}Gd_{0.1}(OH)CO_3$, b) $Ce_{0.8}Gd_{0.2}(OH)CO_3$. The right-hand panels (c-d) correspond to left-hand samples after thermal decomposition to $Ce_{1-x}Gd_xO_{2-\delta}$.

Table 17: Measured values of x from SEM EDXA elemental analysis of $Ce_{1-x}Gd_x(OH)CO_3$.

Sample	Atomic %		STDEV
	Ce	Gd	
$Ce_{0.9}Gd_{0.1}(OH)CO_3$	86.5	13.5	4.6
$Ce_{0.8}Gd_{0.2}(OH)CO_3$	78.7	21.3	1.7

4.6 Praseodymium substituted ceria

4.6.1 Powder XRD

Powder XRD patterns of $Ce_{1-x}Pr_x(OH)_2Cl$ can be indexed and the profile fitted to a monoclinic cell (space group: *P112/m*) within the range $0.1 \leq x \leq 0.5$ (Figure 56). Analysis of the refined lattice parameters (*a*, *b*, *c* and β) and cell volume as a function of Pr substitution (Figure 57), shows a moderately linear trend due to the smaller ionic radius of Pr^{3+} compared to Ce^{3+} (0.99 and 1.01 Å, respectively).

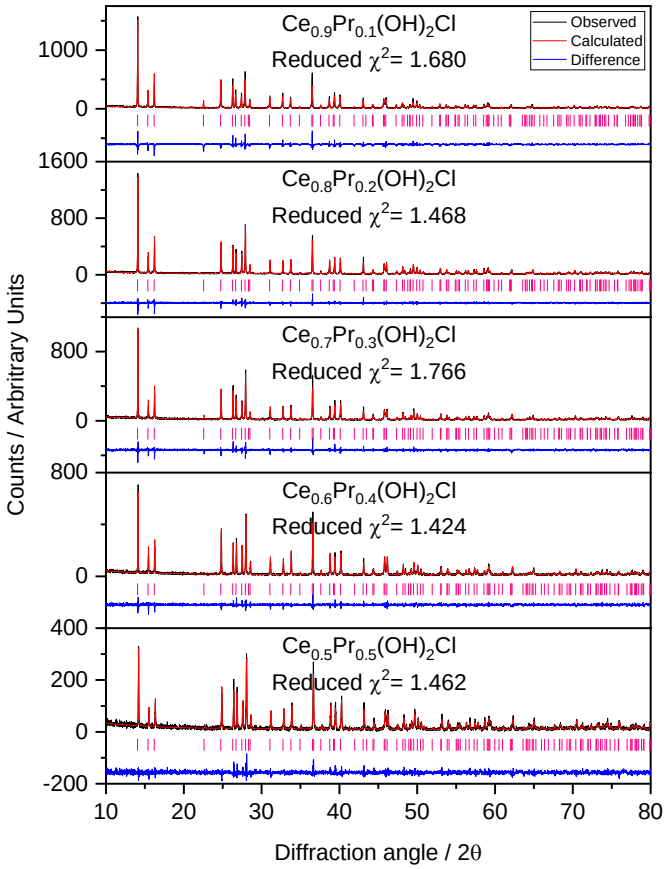

Figure 29: Le Bail fits to Powder XRD data (λ = 1.5405 Å) of $Ce_{1-x}Pr_x(OH)_2Cl$ ($0.1 \leq x \leq 0.5$).

Table 6: Results of Le Bail fitting to powder XRD data of $Ce_{1-x}Pr_x(OH)_2Cl$ ($0.1 \leq x \leq 1$).

Sample	*a* (Å)	*b* (Å)	*c* (Å)	*β* (Å)	Volume (Å^3)
$Ce_{0.9}Pr_{0.1}(OH)_2Cl$	6.2843 (2)	6.87381 (18)	3.94754 (13)	113.502 (2)	156.378 (6)
$Ce_{0.8}Pr_{0.2}(OH)_2Cl$	6.28042 (11)	6.8716 (1)	3.94320 (7)	113.491 (1)	156.070 (3)
$Ce_{0.7}Pr_{0.3}(OH)_2Cl$	6.27653 (15)	6.86907 (13)	3.93933 (9)	113.482 (1)	155.774 (4)
$Ce_{0.6}Pr_{0.4}(OH)_2Cl$	6.27272 (14)	6.86629 (13)	3.93577 (8)	113.460 (1)	155.503 (4)
$Ce_{0.5}Pr_{0.5}(OH)_2Cl$	6.2712 (2)	6.8673 (2)	3.93342 (13)	113.457 (2)	155.397 (6)
$Pr(OH)_2Cl$	6.24778 (17)	6.85337 (17)	3.9132 (1)	113.416 (2)	153.756 (5)

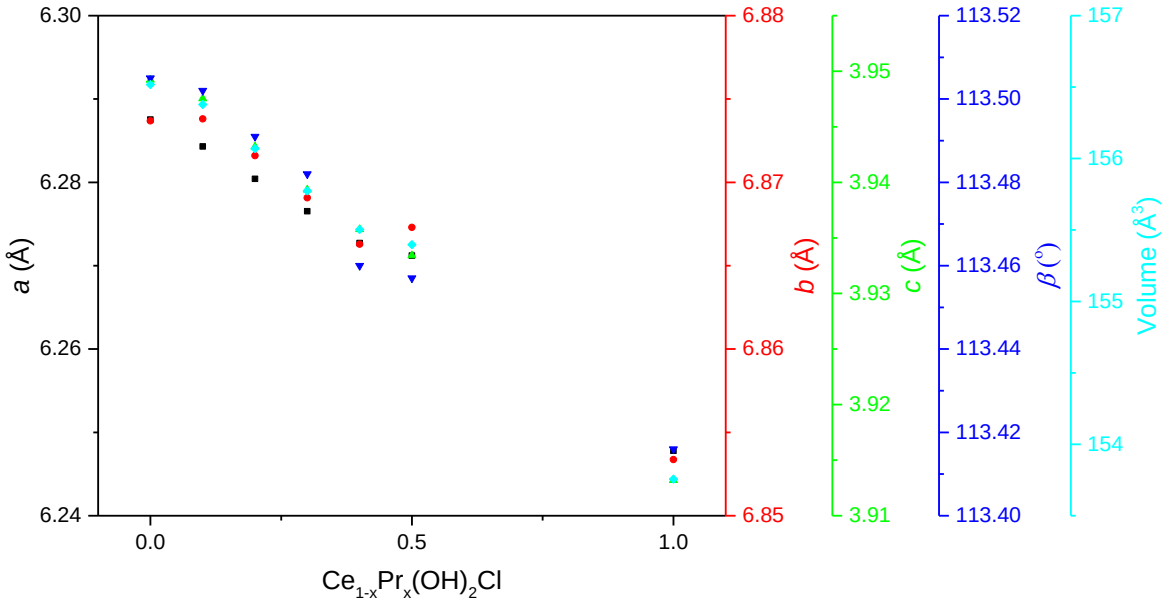

Figure 30: Geometric parameters extracted from the Le Bail fitting of the powder XRD data of $Ce_{1-x}Pr_x(OH)_2Cl$ as a function of praseodymium substitution ($0 \leq x \leq 1$).

In situ heating powder XRD in air up to 800 °C of the $Pr(OH)_2Cl$ sample again has the same transition as $Gd(OH)_2Cl$ to the oxychloride at 350 °C (Figure 58). Further heating causes the diffraction peaks of PrO_2 to emerge at 720 °C. The Bragg peaks are shifted to lower angle in comparison with the reference pattern as the praseodymium hasn't been fully converted to the 4+ oxidation state, as well as being shifted due unit cell expansion from measuring the data at high temperature.

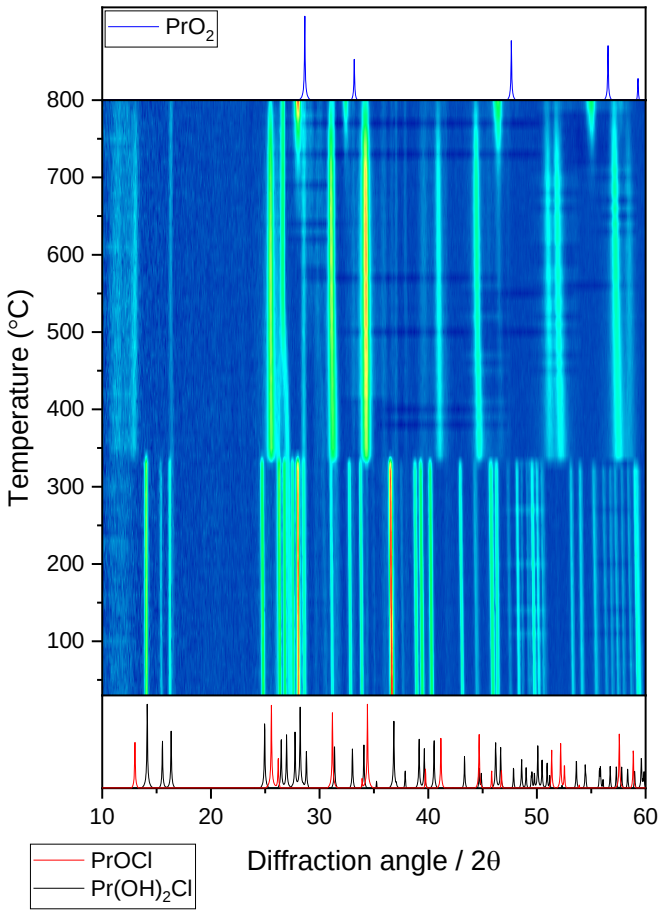

Figure 31: Contour plot of in situ powder XRD patterns of $Pr(OH)_2Cl$ heated from room temperature to 800 °C, compared against reference patterns of present phases shown above. [4-6]

Powder XRD patterns of $Ce_{1-x}Pr_xO_{2-\delta}$ prepared by the thermal decomposition of $Ce_{1-x}Pr_x(OH)_2Cl$ (Figure 59) can be indexed and the profile fitted to a cubic fluorite cell (space group: $Fm\bar{3}m$) within the range $0.1 \leq x \leq 0.5$. As x increases the lattice parameter increases until about the Pr content reaches 0.2 substitution, after which the lattice parameter decreases in the x = 0.3 to 0.5 range (Figure 60). The expected trend should be roughly linear as Pr^{4+} is marginally smaller than Ce^{4+} (0.96 and 0.97 Å, respectively). As praseodymium is a multivalent cation an explanation for this unusual trend is that the compounds contain Pr^{3+} (1.143 Å) as the major species, as it is larger than Pr^{4+}. The Pr^{3+}/Pr^{4+} ratio can give rise to non-stoichiometric phases, therefore in these Pr-substituted cerium oxides with suspected differing oxidation state ratios, different oxygen contents are possible and hence will also affect the strain values.

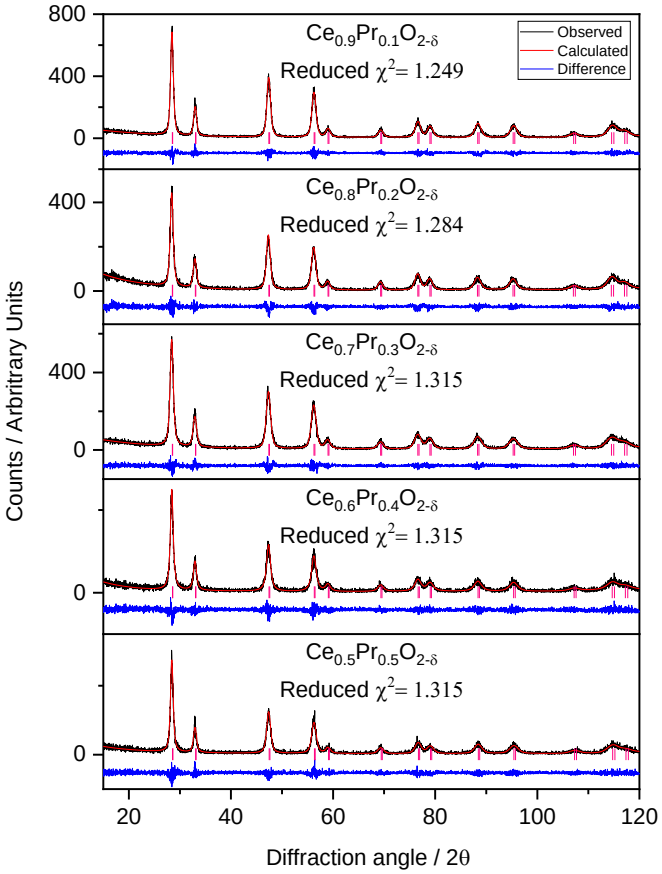

Figure 32:Le Bail fits to Powder XRD data (λ = 1.5405 Å) of $Ce_{1-x}Pr_xO_{2-\delta}$ ($0.1 \leq x \leq 0.5$) after thermal decomposition of $Ce_{1-x}Pr_x(OH)_2Cl$.

Table 7: Results of Le Bail fitting to powder XRD data of $Ce_{1-x}Pr_xO_{2-\delta}$ ($0.1 \leq x \leq 0.5$).

Sample	*a* (Å)	[a] Crystallite size (Å)	[b] Cε	[b] L (Å)
$Ce_{0.9}Pr_{0.1}O_{2-\delta}$	5.41634 (17)	89 (18)	0.0141 (3)	176 (5)
$Ce_{0.8}Pr_{0.2}O_{2-\delta}$	5.4178 (2)	77 (16)	0.0178 (3)	167 (4)
$Ce_{0.7}Pr_{0.3}O_{2-\delta}$	5.4171 (2)	74 (17)	0.0201 (1)	176 (2)
$Ce_{0.6}Pr_{0.4}O_{2-\delta}$	5.4130 (4)	78 (22)	0.0225 (6)	245 (2)
$Ce_{0.5}Pr_{0.5}O_{2-\delta}$	5.4099 (6)	82 (21)	0.01991 (12)	223 (1)

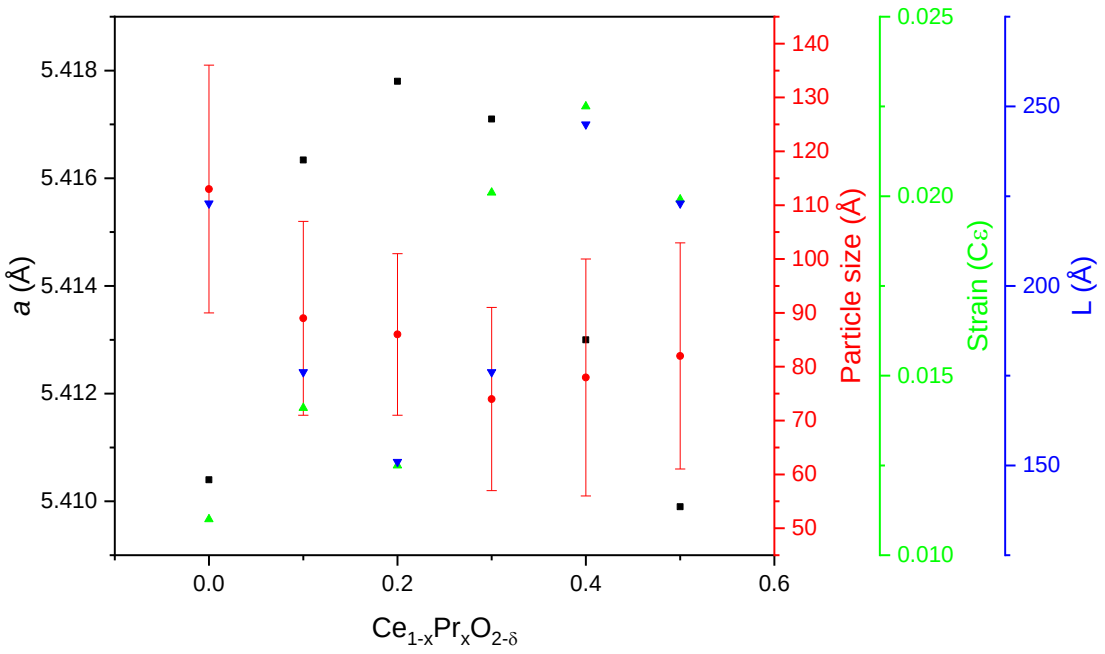

Figure 60: Lattice parameter, crystallite size, strain and L of $Ce_{1-x}Pr_xO_{2-\delta}$ after thermal decomposition of $Ce_{1-x}Pr_x(OH)_2Cl$ as a function of praseodymium substitution ($0 \leq x \leq 0.5$).

As with the $Ce_{1-x}Gd_x(OH)CO_3$, $Ce_{1-x}Pr_x(OH)CO_3$ is also only capable of a praseodymium substitution up to a value of x = 0.2 (Figure 30). Increased substitution is possible however, the reactions aren't very reproducible, so they have not been reported. The powder XRD pattern of the $Pr(NO_3)_3$ used solely in the solvothermal reaction also produces an amorphous phase.

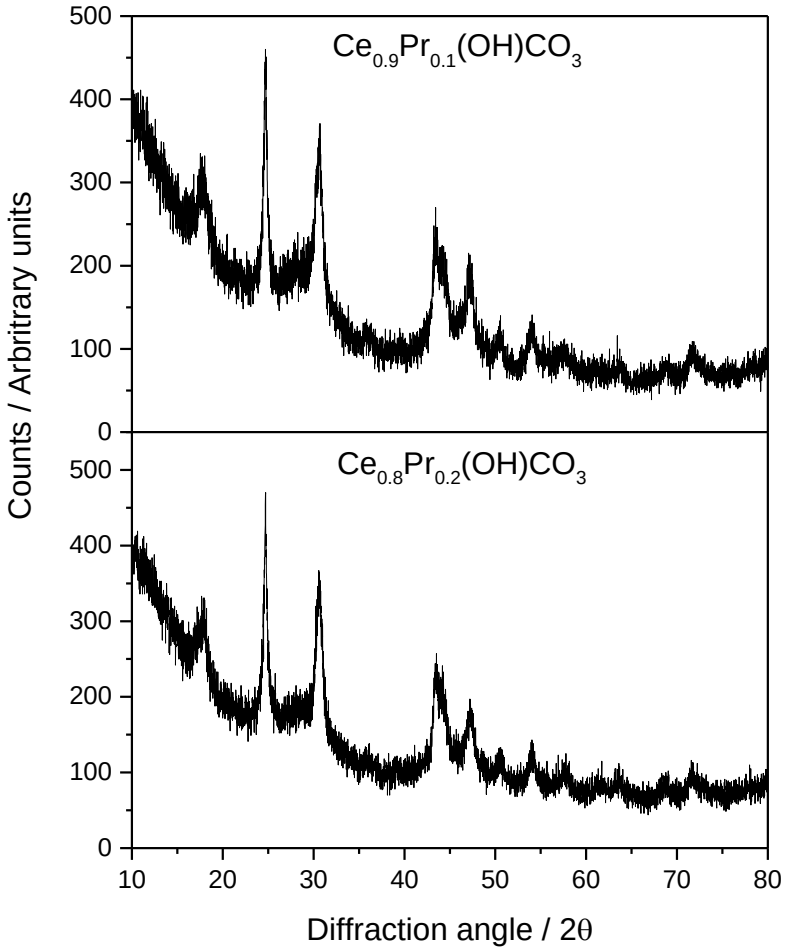

Figure 61: Powder XRD data (λ = 1.5405 Å) of $Ce_{1-x}Pr_x(OH)CO_3$ ($0.1 \leq x \leq 0.2$).

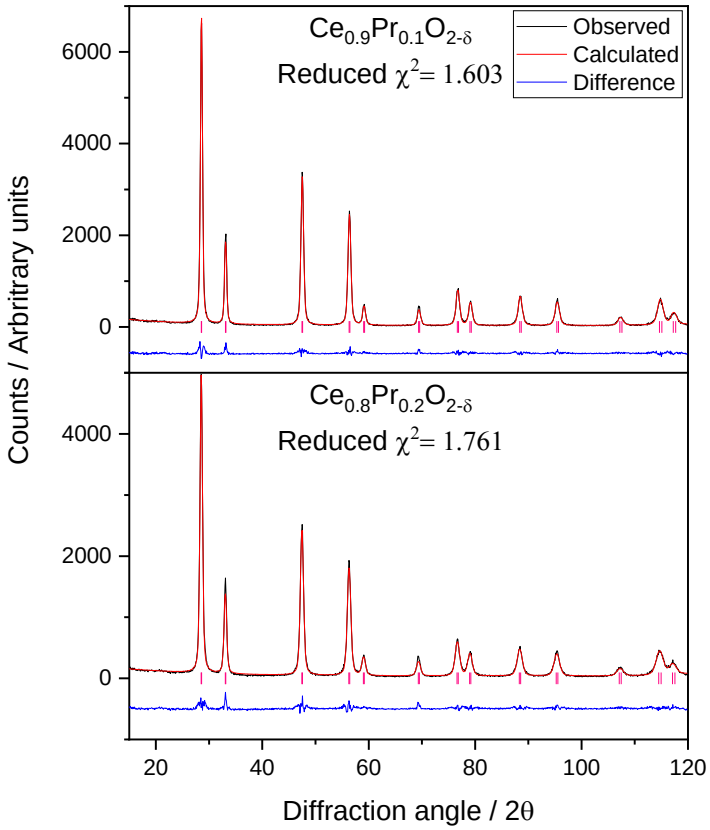

Figure 62: Le Bail fits to Powder XRD data (λ = 1.5405 Å) of $Ce_{1-x}Pr_xO_{2-\delta}$ ($0.1 \leq x \leq 0.2$) after thermal decomposition of $Ce_{1-x}Pr_x(OH)CO_3$.

Table 20: Results of Le Bail fitting to powder XRD data of $Ce_{1-x}Pr_xO_{2-\delta}$ ($0.1 \leq x \leq 0.2$).

Sample	*a* (Å)	[a] Crystallite size (Å)	[b] Cε	[b] L (Å)
$Ce_{0.9}Pr_{0.1}O_{2-\delta}$	5.4135 (2)	139 (18)	0.0053 (6)	199 (11)
$Ce_{0.8}Pr_{0.2}O_{2-\delta}$	5.41784 (19)	112 (16)	0.0077 (6)	172 (9)

The lattice parameters of the $Ce_{1-x}Pr_xO_{2-\delta}$ samples in comparison with literature values show an increased expansion of the unit cell for the same substitution values (Figure 63).

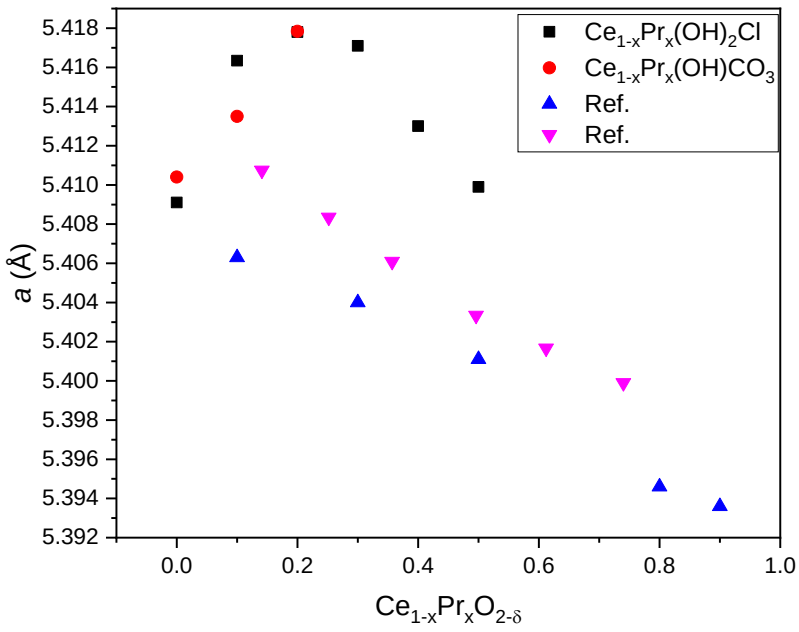

Figure 63: Qualitative comparison of lattice parameter as a function of x for the $Ce_{1-x}Pr_xO_{2-\delta}$ samples synthesised by the thermal decomposition of $Ce_{1-x}Pr_x(OH)_2Cl$ and $Ce_{1-x}Pr_x(OH)CO_3$. These results are compared against lattice parameters extracted from literature. [6-7]

4.6.2 Further Characterisation

The TGA results of the solvothermally synthesised $Ce_{1-x}Pr_x(OH)_2Cl$ ($0.1 \leq x \leq 0.5$) powders from room temperature to 1000 °C are illustrated in Figure 64. The addition of praseodymium at low substitution values (x = 0.1 or 0.2) as with $Ce(OH)_2Cl$ shows a single step decomposition trace. However, as the praseodymium content increases above these levels other decomposition steps become more prominent. These steps can be attributed to the materials undertaking the same transitions as observed in the in situ powder XRD (Figure 58). After the temperature surpasses 300 °C it is also found that the particles change colour from black to dark red.

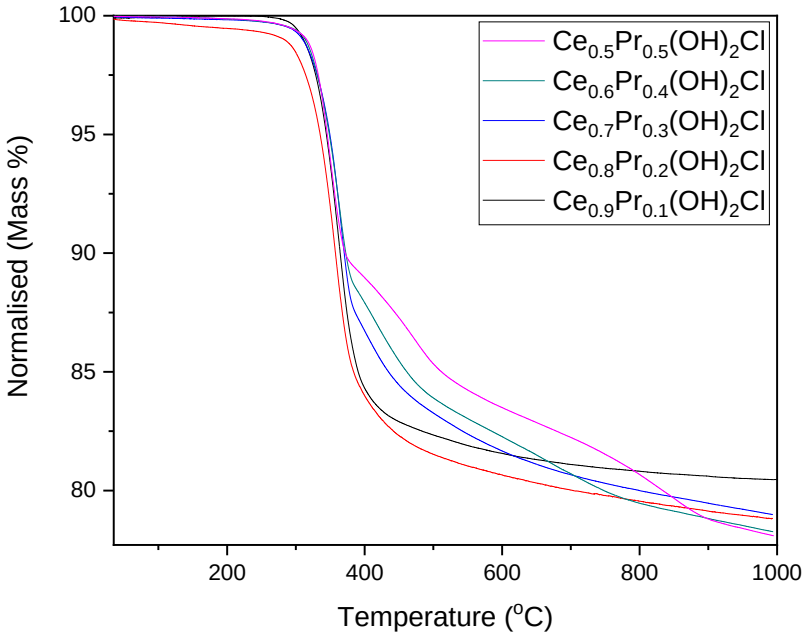

Figure 64: Thermogravimetric analysis of $Ce_{1-x}Pr_x(OH)_2Cl$ ($0.1 \leq x \leq 0.5$).

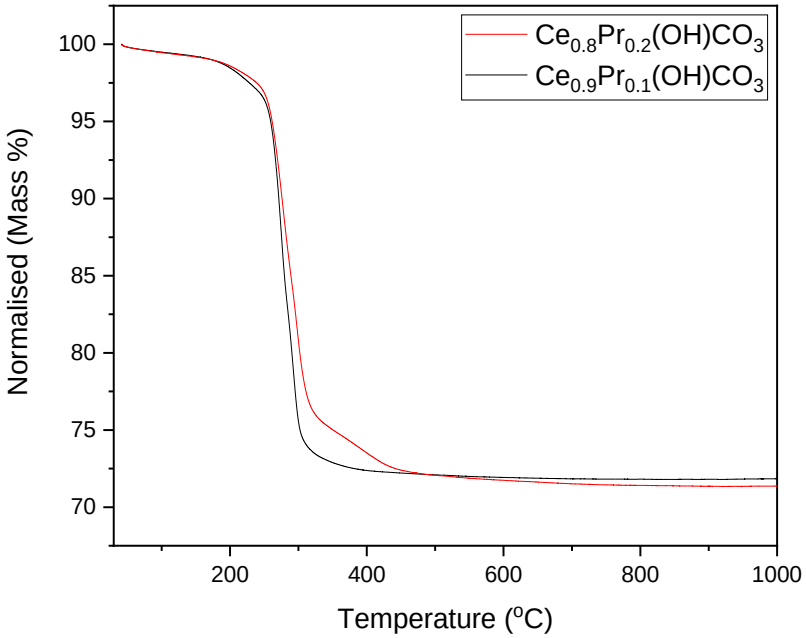

Figure 33: Thermogravimetric analysis of $Ce_{1-x}Pr_x(OH)CO_3$ ($0.1 \leq x \leq 0.2$).

Figure 66 shows the SEM micrographs of the Pr-substituted samples before ($Ce_{1-x}Pr_x(OH)_2Cl$) and after thermal decomposition to $Ce_{1-x}Pr_xO_{2-\delta}$. Herein again, the morphology isn't significantly affected by the addition of praseodymium or being

subjected to the calcination step. The elemental compositions of the $Ce_{1-x}Pr_x(OH)_2Cl$ samples were determined by EDXA analysis as shown in Table 21. The elemental compositions of the products meet the desired target stoichiometric ratio.

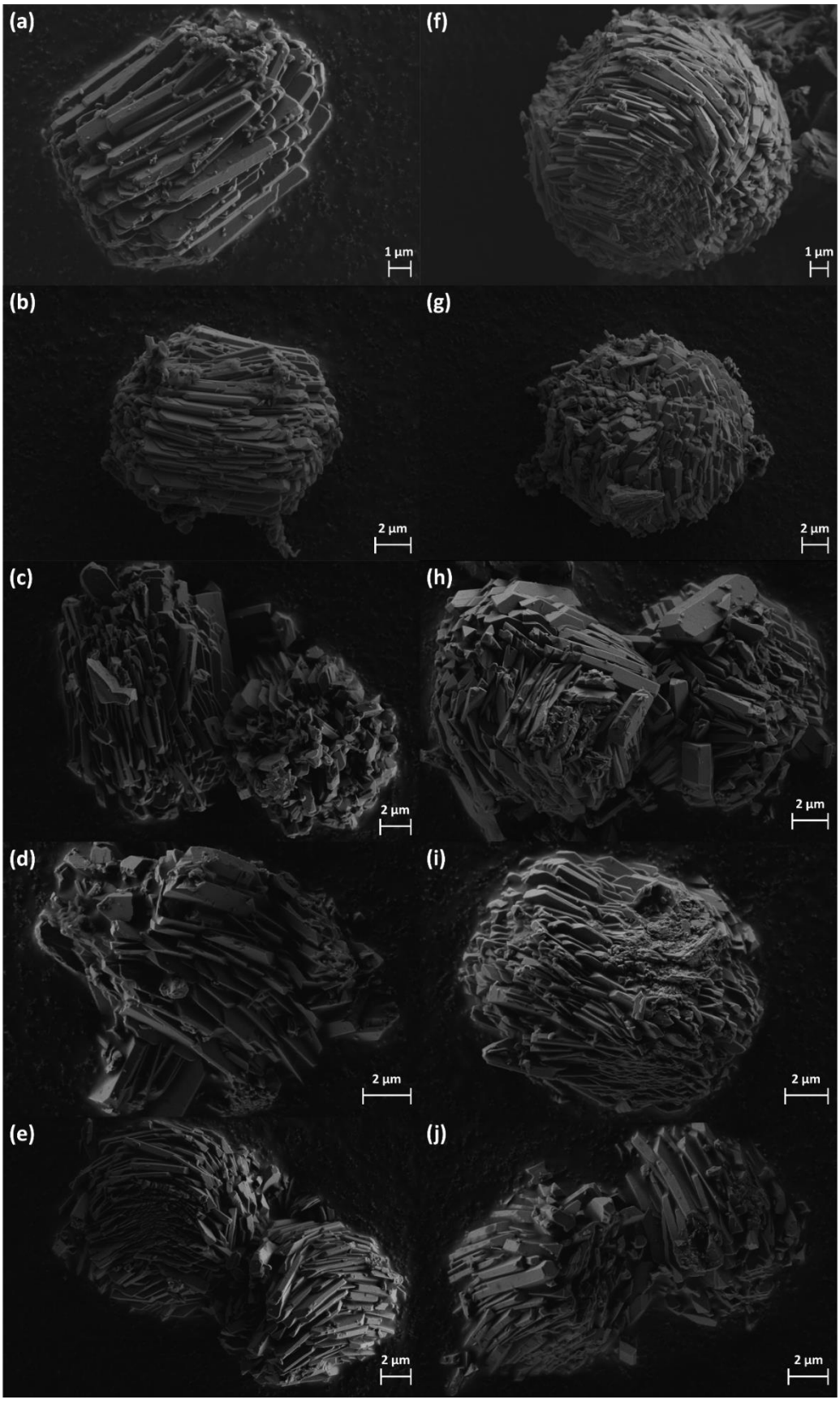

Figure 66: SEM micrographs of a) $Ce_{0.9}Pr_{0.1}(OH)_2Cl$, b) $Ce_{0.8}Pr_{0.2}(OH)_2Cl$, c) $Ce_{0.7}Pr_{0.3}(OH)_2Cl$, d) $Ce_{0.6}Pr_{0.4}(OH)_2Cl$, e) $Ce_{0.5}Pr_{0.5}(OH)_2Cl$. The right-hand panels (f-j) correspond to the left-hand samples after thermal decomposition to $Ce_{1-x}Pr_xO_{2-\delta}$.

Table 8: Measured values of x from SEM EDX elemental analysis of $Ce_{1-x}Pr_x(OH)_2Cl$.

Sample	Atomic %		STDEV
	Ce	Pr	
$Ce_{0.9}Pr_{0.1}(OH)_2Cl$	89.4	10.6	0.3
$Ce_{0.8}Pr_{0.2}(OH)_2Cl$	79.7	20.3	0.6
$Ce_{0.7}Pr_{0.3}(OH)_2Cl$	69.3	30.7	0.6
$Ce_{0.6}Pr_{0.4}(OH)_2Cl$	58.7	41.3	0.4
$Ce_{0.5}Pr_{0.5}(OH)_2Cl$	51.5	48.5	0.5

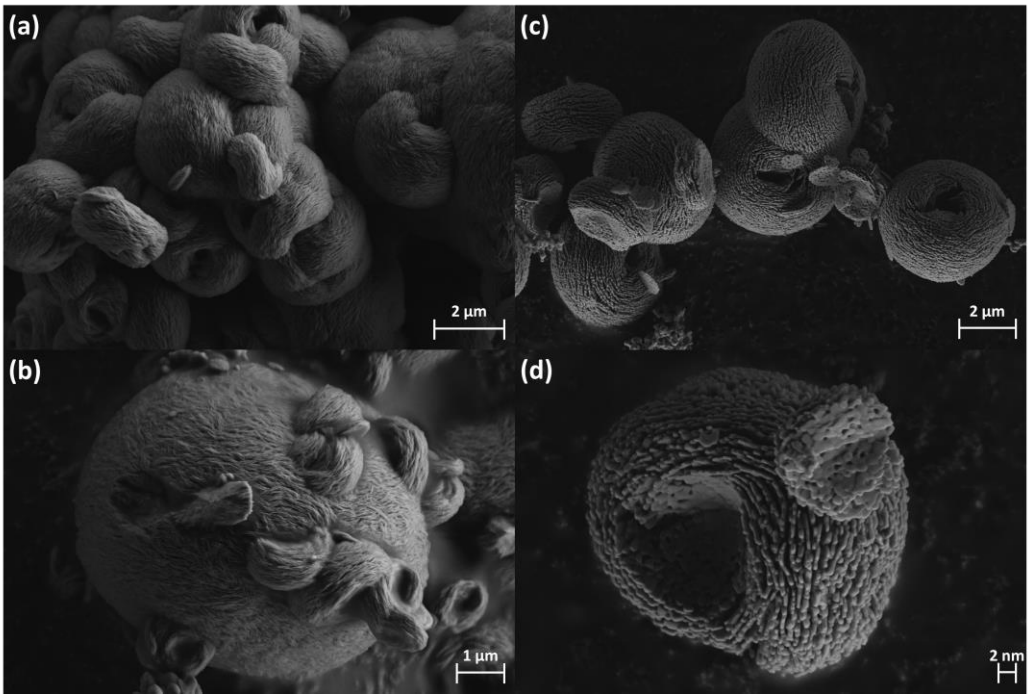

Figure 347: SEM micrographs of a) $Ce_{0.9}Pr_{0.1}(OH)CO_3$, b) $Ce_{0.8}Pr_{0.2}(OH)CO_3$. The right-hand panels (c-d) correspond to left-hand samples after thermal decomposition to $Ce_{1-x}Pr_xO_{2-\delta}$.

Table 92: Measured values of x from SEM EDXA elemental analysis of $Ce_{1-x}Pr_x(OH)CO_3$.

Sample	Atomic %		STDEV
	Ce	Pr	
$Ce_{0.9}Pr_{0.1}(OH)CO_3$	86.4	13.6	4.7
$Ce_{0.8}Pr_{0.2}(OH)CO_3$	76.7	23.3	3.6

4.7 Terbium substituted ceria

4.7.1 Powder XRD

Powder XRD patterns of $Ce_{1-x}Tb_x(OH)_2Cl$ (Figure 68) can be indexed and the profile fitted using a similar procedure applied to the Pr-substituted hydroxide chlorides (Figure 56). Analysis of the refined lattice parameters (*a*, *b*, *c* and *β*) and cell volume as a function of Tb substitution (Figure 69), shows again a moderately linear trend

due to the smaller ionic radii of Tb^{3+} compared to Ce^{3+} (0.923 and 1.01 Å, respectively).

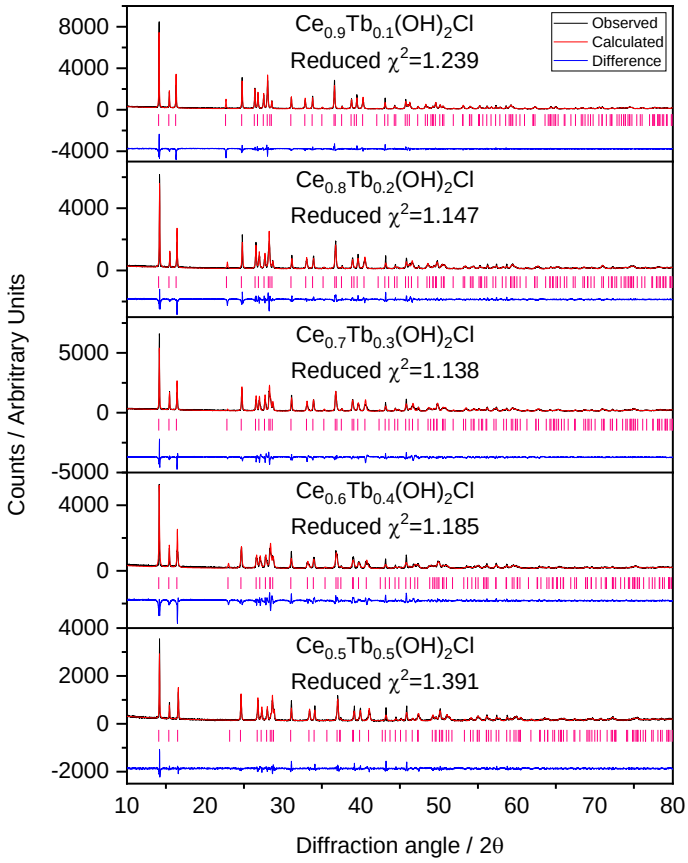

Figure 35: Le Bail fits to Powder XRD data (λ = 1.5405 Å) of $Ce_{1-x}Tb_x(OH)_2Cl$ ($0.1 \leq x \leq 0.5$).

Table 10: Results of Le Bail fitting to powder XRD data of $Ce_{1-x}Tb_x(OH)_2Cl$ ($0.1 \leq x \leq 1$).

Sample	*a* (Å)	*b* (Å)	*c* (Å)	*β* (Å)	Volume (Å^3)
$Ce_{0.9}Tb_{0.1}(OH)_2Cl$	6.2726 (3)	6.8570 (3)	3.92680 (14)	113.244 (2)	155.187 (12)
$Ce_{0.8}Tb_{0.2}(OH)_2Cl$	6.2581 (3)	6.8395 (2)	3.90568 (16)	112.976 (2)	153.910 (7)
$Ce_{0.7}Tb_{0.3}(OH)_2Cl$	6.2493 (3)	6.8259 (4)	3.89468 (17)	112.811 (2)	153.142 (15)
$Ce_{0.6}Tb_{0.4}(OH)_2Cl$	6.2401 (6)	6.8100 (8)	3.8716 (4)	112.526 (4)	151.97 (3)
$Ce_{0.5}Tb_{0.5}(OH)_2Cl$	6.2232 (2)	6.7851 (3)	3.83724 (16)	112.072 (2)	150.153 (12)
$Tb(OH)_2Cl$	6.1790 (4)	6.6749 (6)	3.7102 (3)	109.956 (6)	143.835 (14)

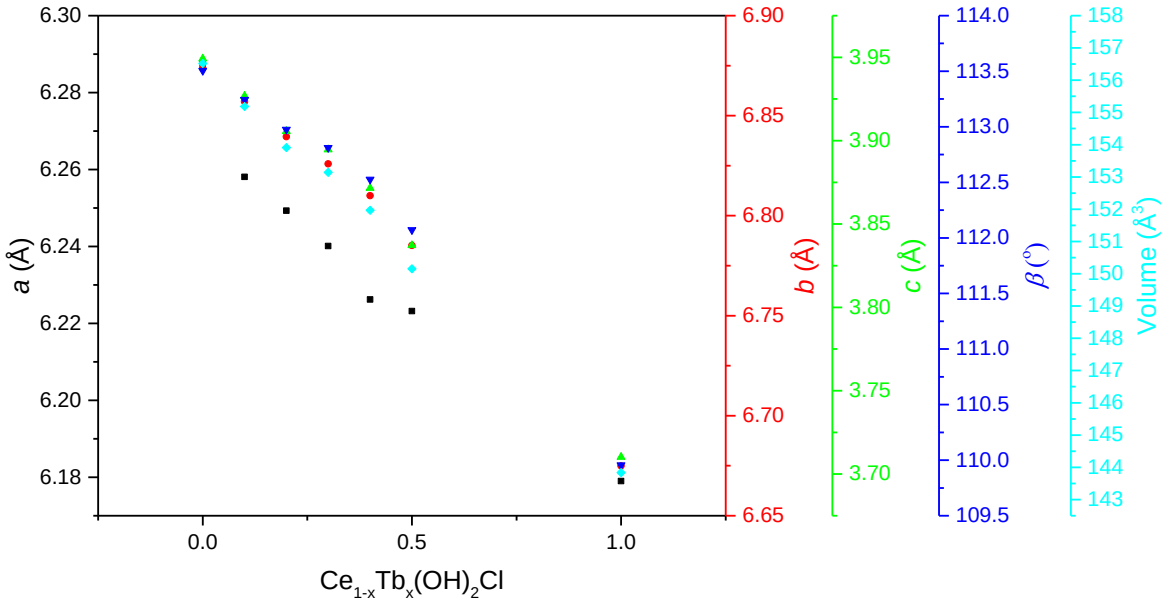

Figure 369: Geometric parameters extracted from the Le Bail fitting of the powder XRD data of $Ce_{1-x}Tb_x(OH)_2Cl$ as a function of terbium substitution ($0 \leq x \leq 1$).

Reflections attributed to TbOCl can be seen by in situ powder X-ray diffraction data of $Tb(OH)_2Cl$ in air at temperatures as low as 350 °C (Figure 70). After the temperature progresses to 550 °C, another phase transformation occurs where the TbOCl, begins to convert to Tb_2O_3.

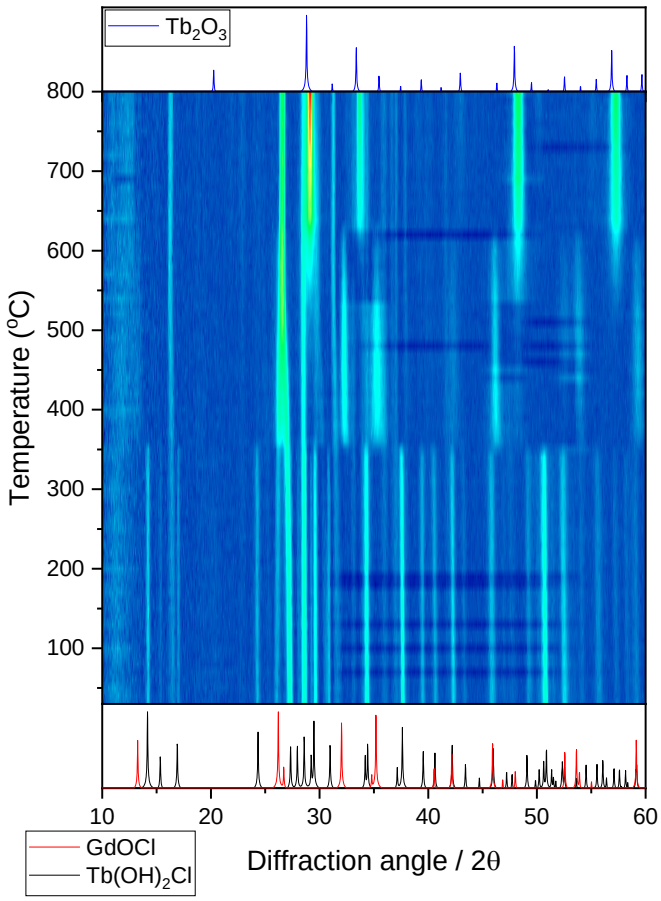

Figure 70: Contour plot of in situ powder XRD patterns of $Tb(OH)_2Cl$ heated from room temperature to 800 °C, compared against reference patterns of present phases shown above. [2,3,7]

As x increases the lattice parameter for the $Ce_{1-x}Tb_xO_{2-\delta}$ samples decreases due the contraction of the unit cell. This can be explained by the fact that the ionic radius of Tb is smaller than that of Ce, being 0.88 and 0.97 Å respectively.

The crystallite size of calcined $Ce_{0.9}Tb_{0.1}(OH)_2Cl$ was found to be 107 Å according to all the Bragg reflections across the 15 – 120 ° range using the Scherrer equation. As the terbium content increases the Bragg peaks broaden and hence the crystallite size decreases.

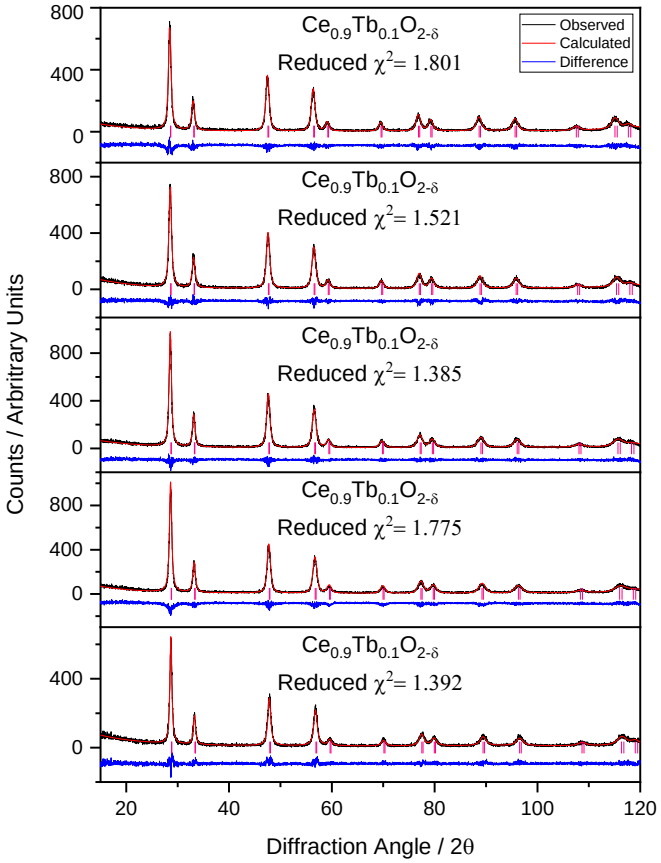

Figure 71: Le Bail fits to Powder XRD data (λ = 1.5405 Å) of $Ce_{1-x}Tb_xO_{2-\delta}$ ($0.1 \leq x \leq 0.5$) after thermal decomposition of $Ce_{1-x}Tb_x(OH)_2Cl$.

Table 11: Results of Le Bail fitting to powder XRD data of $Ce_{1-x}Tb_xO_{2-\delta}$ ($0.1 \leq x \leq 0.5$).

Sample	*a* (Å)	[a] Crystallite size (Å)	[b] Cε	[b] L (Å)
$Ce_{0.9}Tb_{0.1}O_{2-\delta}$	5.40036 (19)	107 (9)	0.0047 (5)	135 (4)
$Ce_{0.8}Tb_{0.2}O_{2-\delta}$	5.3922 (4)	106 (12)	0.0065 (5)	148 (5)
$Ce_{0.7}Tb_{0.3}O_{2-\delta}$	5.38319 (17)	95 (27)	0.01826 (6)	296 (2)
$Ce_{0.6}Tb_{0.4}O_{2-\delta}$	5.3735 (4)	88 (28)	0.0224 (2)	385 (17)
$Ce_{0.5}Tb_{0.5}O_{2-\delta}$	5.3616 (2)	78 (36)	0.01888 (4)	508 (5)

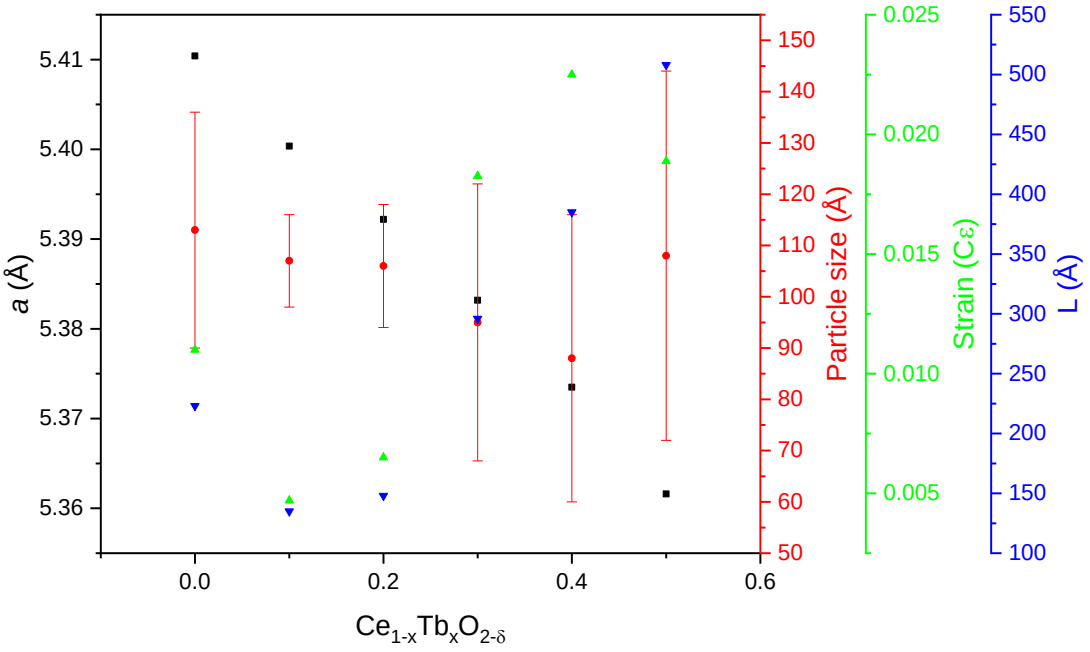

Figure 72: Lattice parameter, crystallite size, strain and L of $Ce_{1-x}Tb_xO_{2-\delta}$ after thermal decomposition of $Ce_{1-x}Tb_x(OH)_2Cl$ as a function of terbium substitution ($0 \leq x \leq 0.5$).

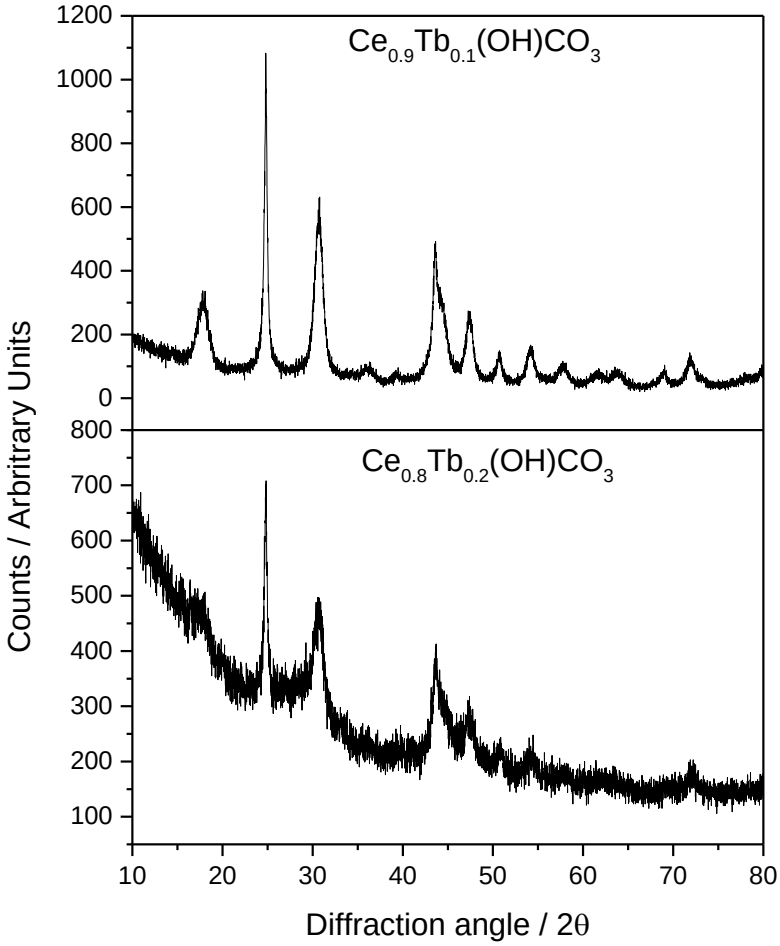

Figure 73: Powder XRD data (λ = 1.5405 Å) of $Ce_{1-x}Tb_x(OH)CO_3$ ($0.1 \leq x \leq 0.2$).

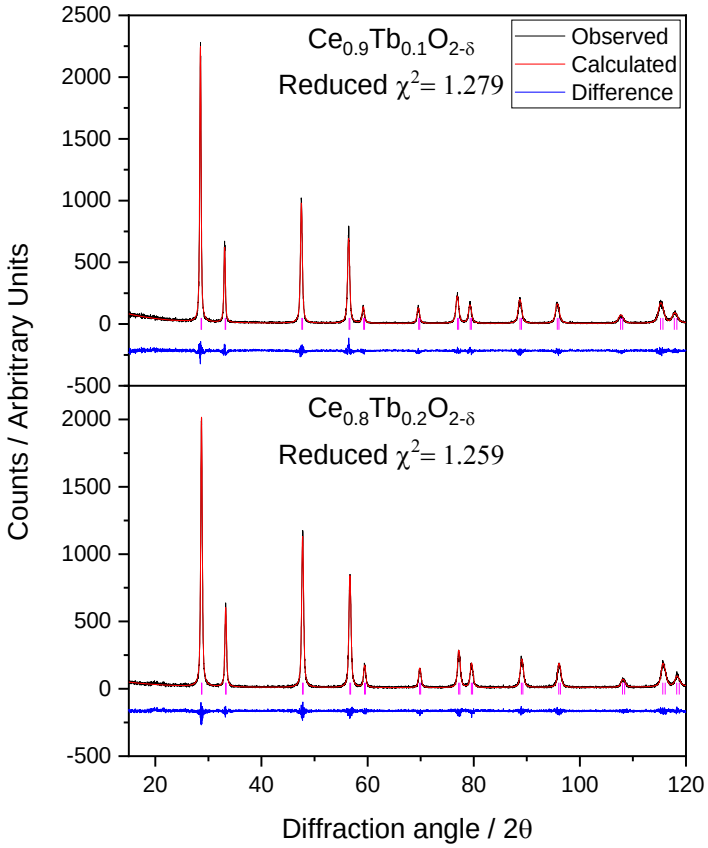

Figure 74: Le Bail fits to Powder XRD data (λ = 1.5405 Å) of $Ce_{1-x}Tb_xO_{2-\delta}$ (0.1 ≤ x ≤ 0.2) after thermal decomposition of $Ce_{1-x}Tb_x(OH)CO_3$.

Table 25: Results of Le Bail fitting to powder XRD data of $Ce_{1-x}Tb_xO_{2-\delta}$ (0.1 ≤ x ≤ 0.2).

Sample	*a* (Å)	[a] Crystallite size (Å)	[b] Cε	[b] L (Å)
$Ce_{0.9}Tb_{0.1}O_{2-\delta}$	5.39691 (7)	200 (43)	0.00658 (13)	419 (10)
$Ce_{0.8}Tb_{0.2}O_{2-\delta}$	5.38416 (7)	202 (19)	0.0027 (3)	260 (10)

The lattice parameters for the $Ce_{1-x}Tb_xO_{2-\delta}$ samples produced by the thermal decomposition of $Ce_{1-x}Tb_x(OH)_2Cl$, are larger than the values calculated for $Ce_{1-x}Tb_x(OH)CO_3$ as well as for the parameters extracted from literature. As with praseodymium, terbium is also a multivalent cation so the difference in trends between the two sets of materials can be attributed to Tb^{3+}/Tb^{4+} ratio contained within the samples. Tb^{3+} having the larger of the two ionic radii, 1.04 Å in comparison to 0.88 Å, therefore the $Ce_{1-x}Tb_x(OH)_2Cl$ samples appear to contain more Tb^{3+}.

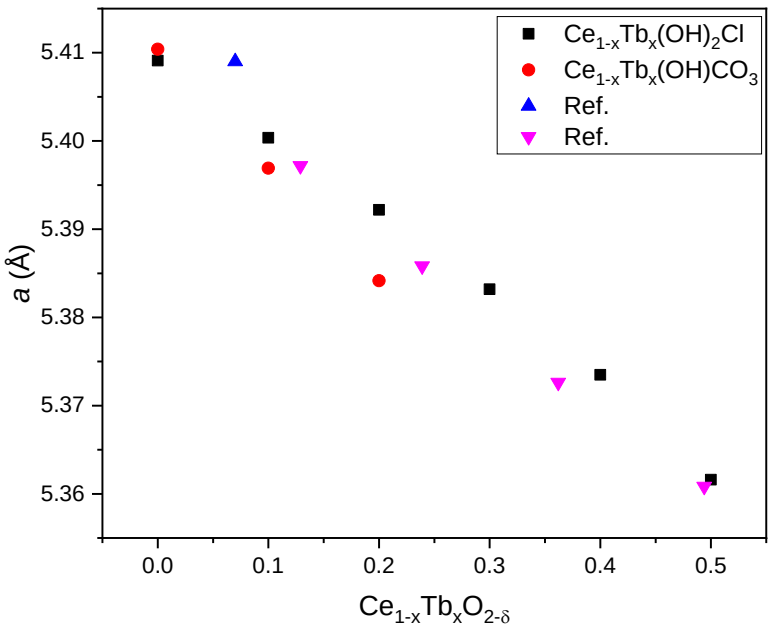

Figure 37: Qualitative comparison of lattice parameter as a function of x for the $Ce_{1-x}Tb_xO_{2-\delta}$ samples synthesised by the thermal decomposition of $Ce_{1-x}Tb_x(OH)_2Cl$ and $Ce_{1-x}Tb_x(OH)CO_3$. These results are compared against lattice parameters extracted from literature. [8-9]

4.7.2 Further characterisation

Additional characteristics of the samples were also investigated using thermogravimetric analysis. The TGA of $Ce_{1-x}Tb_x(OH)_2Cl$ ($0 \leq x \leq 0.5$) up to 1000 °C (Figure 76) shows a very sharp endothermic peak observed at around 350 °C. Increasing Tb content doesn't appear to have any significant impact of the decomposition temperature of the hydroxy chloride materials. However, the TGA traces for the $Ce_{1-x}Tb_x(OH)CO_3$ samples does impact the decomposition step increasing it to 265 and 295 °C for x = 0.1 and 0.2, respectively.

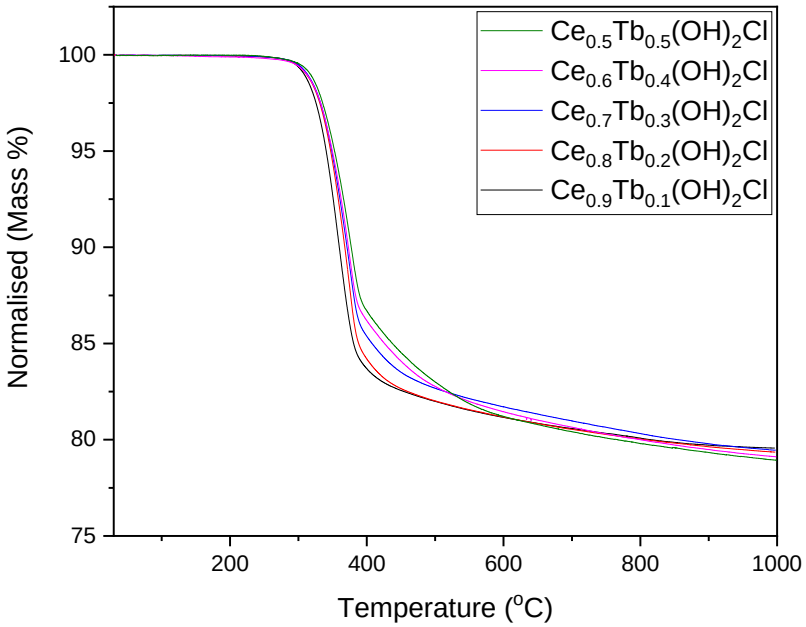

Figure 38: Thermogravimetric analysis of $Ce_{1-x}Tb_x(OH)_2Cl$ ($0.1 \leq x \leq 0.5$).

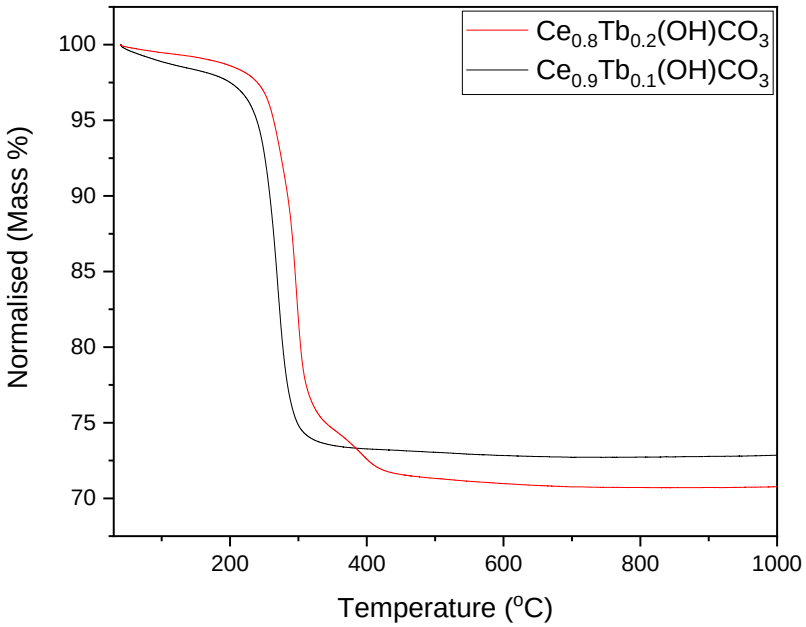

Figure 39: Thermogravimetric analysis of $Ce_{1-x}Tb_x(OH)CO_3$ ($0.1 \leq x \leq 0.2$).

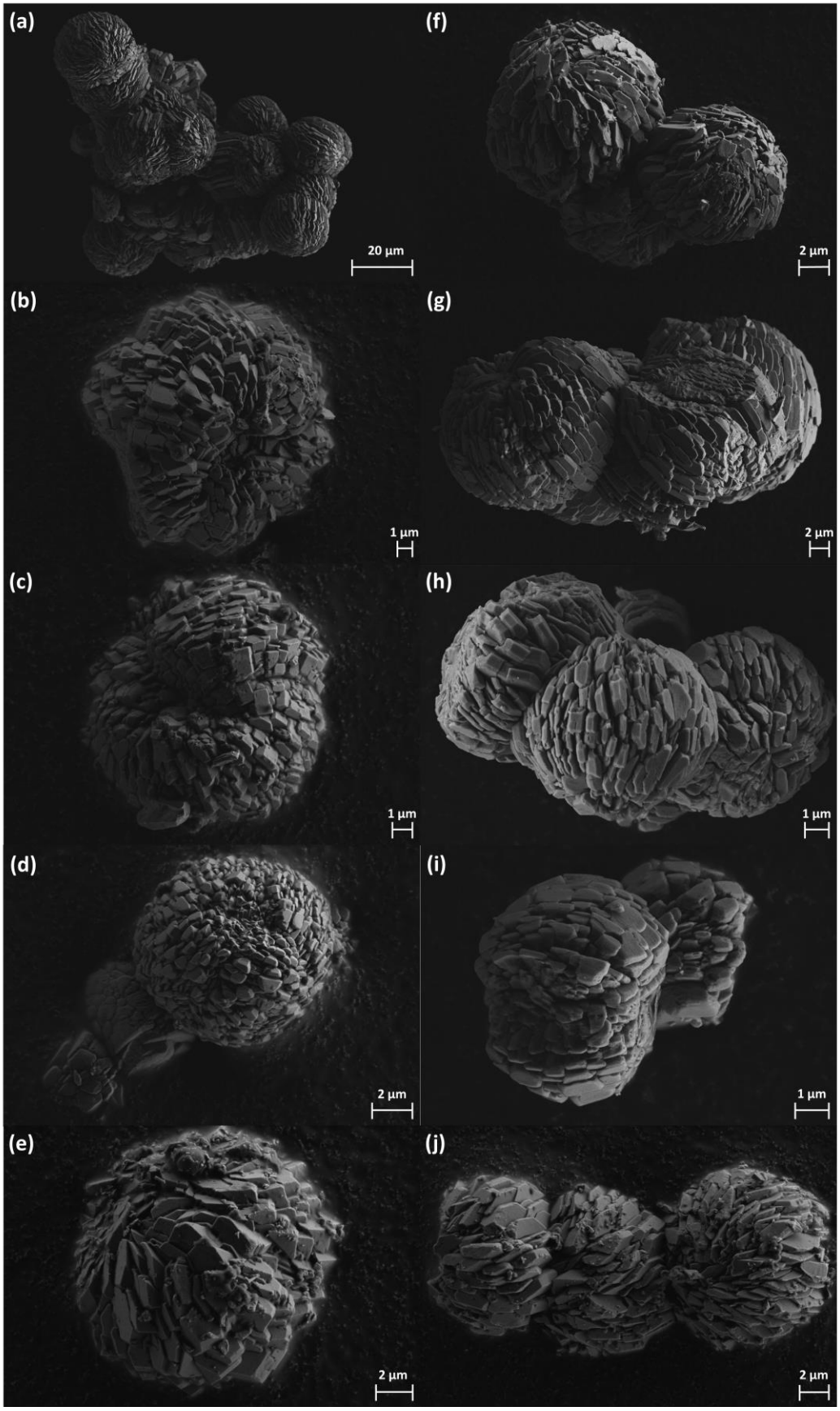

Figure 40: SEM micrographs of a) $Ce_{0.9}Tb_{0.1}(OH)_2Cl$, b) $Ce_{0.8}Tb_{0.2}(OH)_2Cl$, c) $Ce_{0.7}Tb_{0.3}(OH)_2Cl$, d) $Ce_{0.6}Tb_{0.4}(OH)_2Cl$, e) $Ce_{0.5}Tb_{0.5}(OH)_2Cl$. The right-hand panels (f-j) correspond to the left-hand samples after thermal decomposition to $Ce_{1-x}Tb_xO_{2-\delta}$.

Table 12: Measured values of x from SEM EDXA elemental analysis of $Ce_{1-x}Tb_x(OH)_2Cl$.

Sample	Atomic %		STDEV
	Ce	Tb	
$Ce_{0.9}Tb_{0.1}(OH)_2Cl$	88.6	11.4	1.5
$Ce_{0.8}Tb_{0.2}(OH)_2Cl$	78.3	21.7	2.0
$Ce_{0.7}Tb_{0.3}(OH)_2Cl$	69.5	30.5	1.8
$Ce_{0.6}Tb_{0.4}(OH)_2Cl$	58.5	41.5	2.1
$Ce_{0.5}Tb_{0.5}(OH)_2Cl$	51.8	48.2	1.4

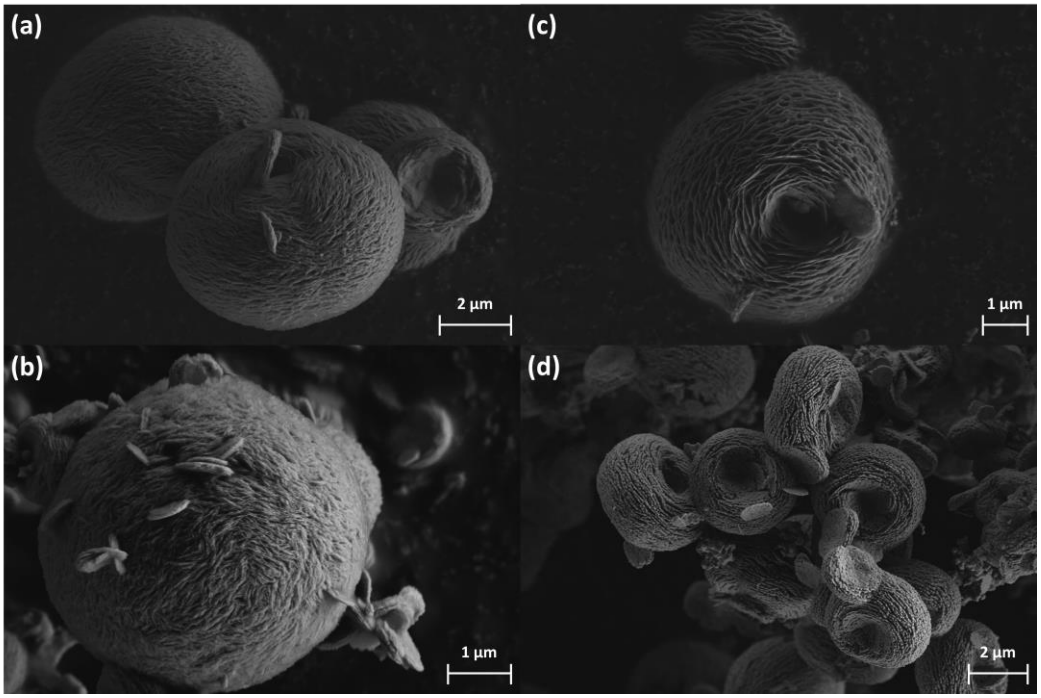

Figure 41: SEM micrographs of a) $Ce_{0.9}Tb_{0.1}(OH)CO_3$, b) $Ce_{0.8}Tb_{0.2}(OH)CO_3$. The right-hand panels (c-d) correspond to left-hand samples after thermal decomposition to $Ce_{1-x}Tb_xO_{2-\delta}$.

Table 13: Measured values of x from SEM EDXA elemental analysis of $Ce_{1-x}Tb_x(OH)CO_3$.

Sample	Atomic %		STDEV
	Ce	Tb	
$Ce_{0.9}Tb_{0.1}(OH)CO_3$	89.9	10.1	0.9
$Ce_{0.8}Tb_{0.2}(OH)CO_3$	79.4	20.6	1.5

4.8 Temperature programmed reduction (TPR)

Figure 80 shows the TPR profiles of $Ce_{0.8}Ln_{0.2}O_{2-\delta}$ prepared from the thermal decomposition of $Ce_{0.8}Ln_{0.2}(OH)_2Cl$ and $Ce_{0.8}Ln_{0.2}(OH)CO_3$ (Ln = La, Pr, Gd and Tb) up 900 °C. The reduction of the samples, irrespective of the synthesis, or the lanthanide content results in a reduction peak in the 200 – 600 °C temperature range attributed to surface reduction. A second peak is also present within the ≥ 700 °C temperature range associated with the bulk reduction of the material, pure CeO_2

being a prime example of this behaviour. A second TPR was then measured after an intermediate re-oxidation up to 600 °C under flow of 5% O_2 in He. As expected the CeO_2 samples formed from the thermal decompositions of both $Ce(OH)_2Cl$ and $Ce(OH)CO_3$ shows a diminished surface reduction after repeat H_2 reduction due to the sintering of the particles, the effect of this is seen by the surface peak being diminished and the bulk relatively larger. The results of the first H_2-TPR shows clearly that the presence of La or Gd in ceria leads to an overall decline in the total percentage of Ln reduction compared to un-substituted ceria (Table 28). The addition of Gd visually shows a slight increase in the area of the lower temperature surface reduction peak, but a large decrease in the higher temperature bulk reduction for the CeO_2 formed from the $Ce_{0.8}Gd_{0.2}(OH)_2Cl$ sample in contrast to pure ceria. The second TPR measurement for this sample show both reduction peaks shifting to lower temperature, with the surface reduction being influenced the most from 555 down to 310 °C. The CeO_2 formed from the thermal decomposition of $Ce_{0.8}Gd_{0.2}(OH)CO_3$ however suffers from a decreased area in both the surface and bulk reduction peaks. Unlike the sample from $Ce_{0.8}Gd_{0.2}(OH)_2Cl$ the second TPR profile of this sample remains unchanged from the first, with only a small increase in activity (5.6%). Visually the first TPR profiles for both $Ce_{0.8}La_{0.2}O_{2-\delta}$ samples formed from the $Ce_{0.8}La_{0.2}(OH)CO_3$ and $Ce_{0.8}La_{0.2}(OH)_2Cl$ samples show little differentiation between them. As with the $Ce_{0.8}Gd_{0.2}(OH)_2Cl$ sample the second TPR profile of the $Ce_{0.8}La_{0.2}(OH)CO_3$ sample remains unchanged from the first. The $Ce_{0.8}La_{0.2}(OH)_2Cl$ sample however, has increased surface reduction compared to the first TPR measurement and at a lower temperature (338 °C) compared to CeO_2. Typically, the incorporation of La or Gd into ceria has been reported to lower the temperature of both reduction peaks. [8-10] Whereas here it can be seen that the addition of Gd or La hinders the reduction of CeO_2 at lower temperatures before improving it. Multiple TPR measurements were conducted on the $Ce_{0.8}Gd_{0.2}O_{2-\delta}$ sample, which was originally $Ce_{0.8}Gd_{0.2}(OH)_2Cl$ (Figure 81). The TPR profiles shows that the peak associated with surface reduction follows the previously mentioned trend before the progression of the sintering process to the bulk. It is still unclear if the activation of the surface reduction speaks more towards the longevity of the catalyst or if it's due to an unknown cation migration pathway. The TPR profiles exhibits lower surface reduction temperature upon the addition of Pr or Tb which resulted in the easier reduction of Ce^{4+} to Ce^{3+} at the surface. For the first TPR

measurement the $Ce_{0.8}Pr_{0.2}O_{2-\delta}$ and $Ce_{0.8}Tb_{0.2}O_{2-\delta}$ samples contain two surface reduction peaks. This is an indication towards the surface oxygen being present in different environments, suggesting that both Tb and Pr participate towards the total observed reduction. The assumption for the calculated percentages of the Pr and Tb substituted ceria, is that the reduction is solely due to reduction of Ce^{4+}. Praseodymium and terbium however, possess the same property and hence redox capabilities of their own. However, the Gd and La cations, unlike Ce, Pr, and Tb, have only one trivalent state and hence no redox couple. The changes in the H_2-TPR profiles of these substituted materials is primarily due the replacement of the Ce^{4+} with either of the lanthanides, thereby promoting the formation of non-stoichiometric CeO_2. Supported by reports on H_2-TPR measurements on La_2O_3 which have concluded that it barely undergoes reduction and it doesn't possess any surface oxygen species. [11] The total reduction values for the Tb and Pr samples all virtually increase, and this can be explained partially by the Pr and Tb not being fully re-oxidised in 5% O_2 at 600 °C compared to the original sample calcination at 700 °C prior to the TPR measurement. Notably, the $Ce_{0.8}Tb_{0.2}O_{2-\delta}$ sample decomposed from $Ce_{0.8}Tb_{0.2}(OH)_2Cl$ has a heightened surface reduction peak intensity which shifts from 319 to 295 °C between TPR measurements. This property is an attractive quality for materials used in exhaust applications, particularly for cold start conditions. The $Ce_{0.8}Tb_{0.2}(OH)CO_3$ sample in comparison, has surface reduction peaks which emerge at higher temperatures which remain in relatively the same position during the second measurement. The TPR profiles of the $Ce_{0.8}Pr_{0.2}O_{2-\delta}$ mixed oxides show two large reduction peaks at about 450 and 540 °C, which shift to higher temperatures and have the largest Ce^{4+} reduction percentages and one of the lowest T_{max} values. The profiles however, are not atypical from other similar mixed Ce/Pr oxides. [8,9,12,13] The powder XRD measurements after the TPR/TPO measurements show no phase segregation upon repeated heating up to 900 °C (Figure 82).

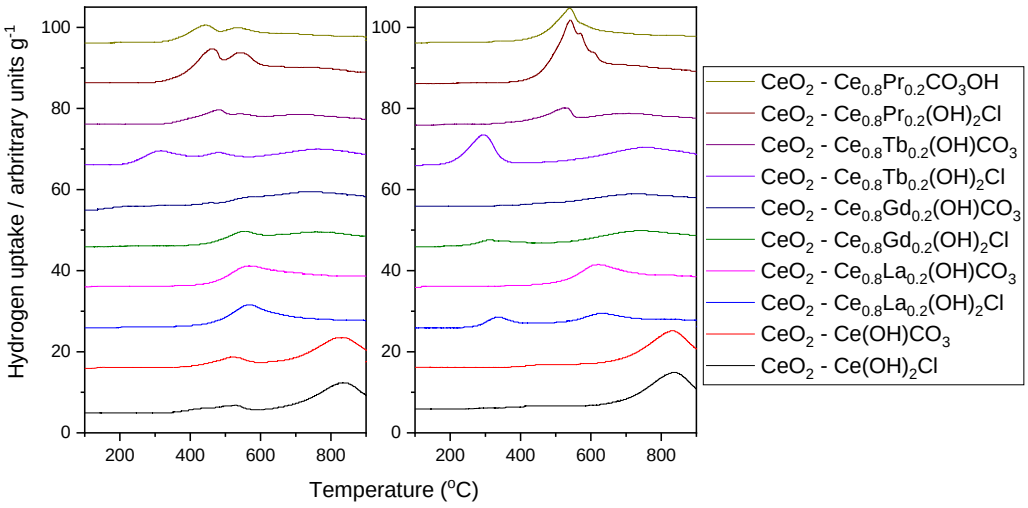

Figure 42: Sequential TPR profiles of $Ce_{1-x}Ln_x(OH)_2Cl$ and $Ce_{1-x}Ln_x(OH)CO_3$ materials after thermal decomposition to $Ce_{1-x}Ln_xO_{2-\delta}$ (with an intermediate re-oxidation (TPO) at 600 °C).

Table 148: Summary of results from TPR of CeO_2 and $Ce_{1-x}Ln_xO_{2-\delta}$ synthesised from the thermal decomposition of $Ce_{1-x}Ln_x(OH)_2Cl$ and $Ce_{1-x}Ln_x(OH)CO_3$. T_{max} corresponds to the temperature at which the maximum of H_2 uptake occurs.

Sample	First TPR	Second TPR	First TPR	Second TPR
	(Total Ln reduced / %)		T_{max} (°C)	T_{max} (°C)
CeO_2 - $Ce(OH)CO_3$	49.6	48.1	830	832
CeO_2 - $Ce(OH)_2Cl$	48.1	38.4	836	837
CeO_2 - $Ce_{0.8}La_{0.2}(OH)CO_3$	26.6	15.6	571	622
CeO_2 - $Ce_{0.8}La_{0.2}(OH)_2Cl$	20.2	36.4	569	630
CeO_2 - $Ce_{0.8}Gd_{0.2}(OH)CO_3$	16.4	22.0	745	730
CeO_2 - $Ce_{0.8}Gd_{0.2}(OH)_2Cl$	31.4	33.8	555	742
CeO_2 - $Ce_{0.8}Tb_{0.2}(OH)CO_3$	25.8	60.6	484	527
CeO_2 - $Ce_{0.8}Tb_{0.2}(OH)_2Cl$	45.6	44.6	773	295
CeO_2 - $Ce_{0.8}Pr_{0.2}(OH)CO_3$	56.0	73.8	443	540
CeO_2 - $Ce_{0.8}Pr_{0.2}(OH)_2Cl$	56.0	79.2	463	542

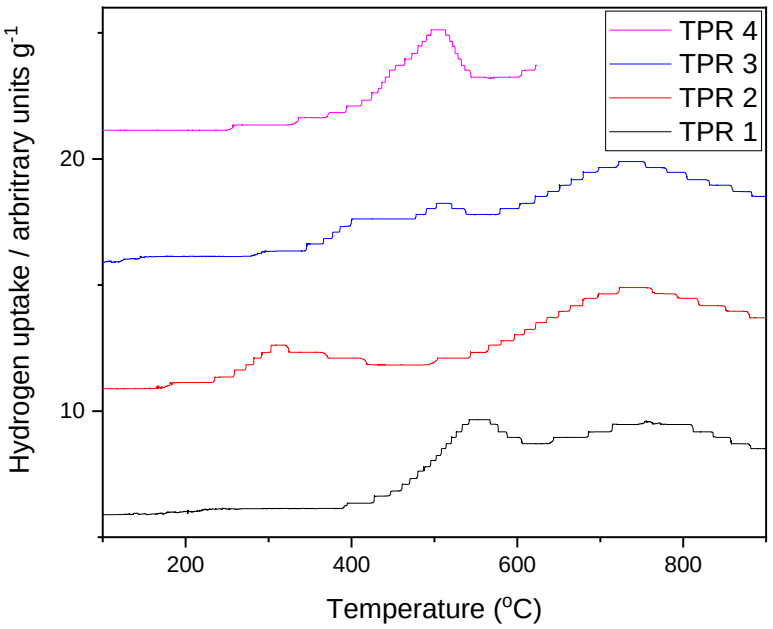

Figure 81: Sequential TPR profiles of $Ce_{0.8}Gd_{0.2}(OH)_2Cl$ after thermal decomposition to $Ce_{0.8}Gd_{0.2}O_{2-\delta}$ (with an intermediate re-oxidation (TPO) at 600 °C between each TPR measurement).

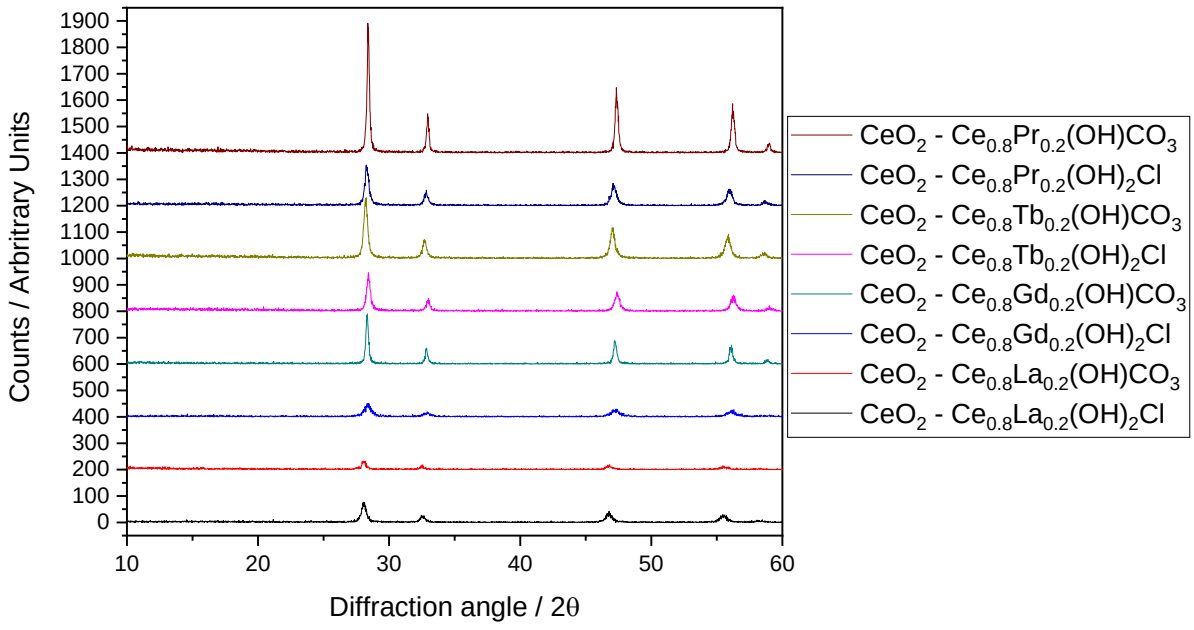

Figure 82: Powder XRD patterns of the $Ce_{1-x}Ln_xO_{2-\delta}$ samples after subjection to the TPR-TPO-TPR measurements.

4.9 X-ray absorption spectroscopy

4.9.1 Tb L_{III}-edge XANES

The choice of substituting cerium cations with terbium was motivated because the terbium ion is known to adopt the mixed valence state Tb^{3+}/Tb^{4+} in several compounds. To determine the ratio of the mixed valence state at room temperature, the calibration line was obtained using the XANES spectra of $Tb(OH)_2Cl$ and Tb_4O_7.

In this experiment, $Tb(OH)_2Cl$ was used as a Tb^{3+} standard. For the standard, the XANES spectrum exhibits one main single absorption peak which is assigned to the Tb cation being in a trivalent state (As observed typically with other lanthanide oxides). Double absorptions peaks are observed in all the rest of the cases. These two peaks arise due to the transition of a Tb $2p_{3/2}$ core electron to a mixed valence state of terbium, one Tb $4f^7$ and the higher peak Tb $4f^8L$ (L, represents a ligand hole in the O 2p orbital) both of which represent Tb^{4+} cations. A clear shift of the absorption edge to higher energies is observed upon increasing Tb substitution, indicating an increase in their valence state.

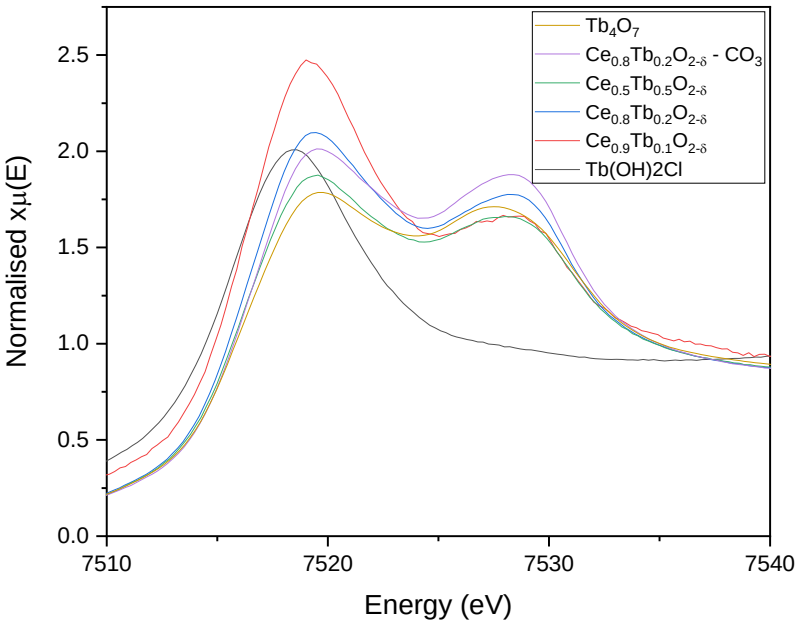

Figure 83: Normalised Tb L_{III}-edge XANES spectra of $Ce_{1-x}Tb_xO_{2-\delta}$ compared against reference compounds with known Tb oxidation states ($Tb(OH)_2Cl$ and Tb_4O_7).

The XANES comparison between the two $Ce_{0.8}Tb_{0.2}O_{2-\delta}$ samples decomposed from the $Ce_{0.8}Tb_{0.2}(OH)_2Cl$ and $Ce_{0.8}Tb_{0.2}(OH)CO_3$, shows that the sample derived from

the carbonate contains more Tb^{4+} than the other method. This observation agrees with the XRD results, the lattice parameter is smaller for the carbonate as Tb^{4+} is smaller than Tb^{3+} (0.88 and 1.04 Å, respectively).

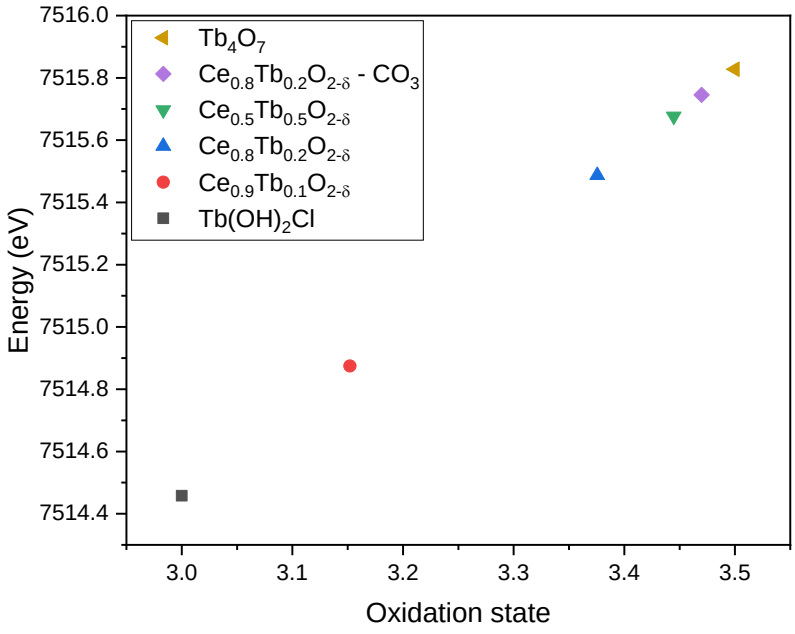

Figure 43: A plot of energy (defined at which normalised absorption = 1.0) as a function of oxidation state, extracted from a linear fit of the reference compound, to estimate the oxidation states in the $Ce_{1-x}Tb_xO_{2-\delta}$ compounds.

4.9.2 Pr L_{III}-edge XANES

In this experiment, $Pr(OH)_2Cl$ was used as a Pr^{3+} standard. For the standard, the XANES spectrum exhibits one main single absorption peak which is assigned to the Pr cation being in a trivalent state (as observed typically with other lanthanide oxides). The peak is observed due to the transition of a Pr $2p_{3/2}$ core electron to the $4f^25d$, which represents Pr^{4+} cations. Double absorptions peaks are observed in all the rest of the cases (Figure 85). These two peaks arise due to the transition of a Pr $2p_{3/2}$ core electron to a mixed valence state of praseodymium, one Pr $4f^25dL$ and the higher energy peak Pr $4f^15d$ (L, represents a ligand hole in the O $2p_{3/2}$ orbital) both of which represents Pr^{4+} cations. A clear shift of the absorption edge to higher energies is observed upon increasing Pr substitution, indicating an increase in their valence state.

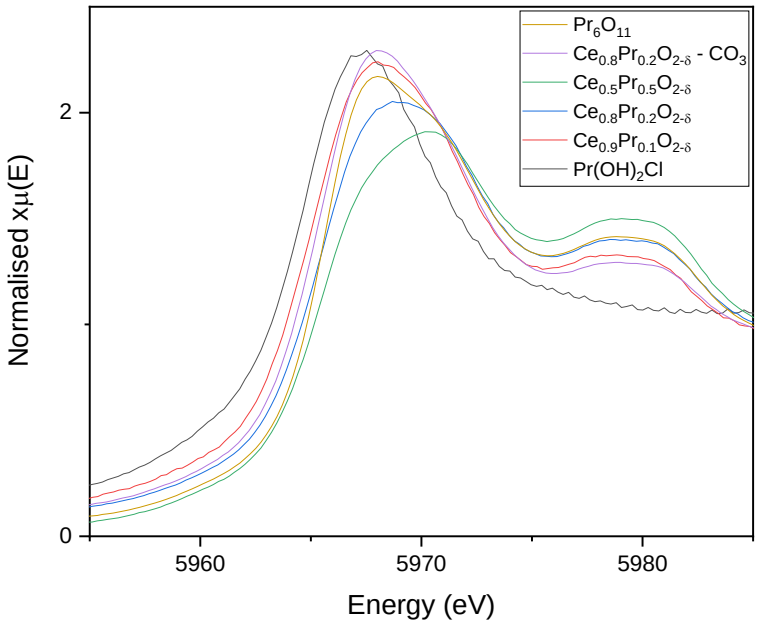

Figure 44: Normalised Pr L_{III}-edge XANES spectra of $Ce_{1-x}Pr_xO_{2-\delta}$ compared against reference compounds with known Pr oxidation states ($Pr(OH)_2Cl$ and Pr_6O_{11}).

A linear relationship between metal oxidation state and the energy shift of the absorption edge has been illustrated by Figure 86. The comparison between the two $Ce_{0.8}Pr_{0.2}O_{2-\delta}$ samples decomposed from the $Ce_{0.8}Pr_{0.2}(OH)_2Cl$ and $Ce_{0.8}Pr_{0.2}(OH)CO_3$ samples, shows that the decomposition of the hydroxy chloride sample contains more Pr^{4+}. The results deduced from the XANES spectra of the Pr-substituted ceria agreed with the results from the powder X-ray diffraction analysis. The major species of Pr in the mixed oxide is Pr^{3+} which is a larger cation than Pr^{4+} giving rise to a slight expansion of the unit cell and hence enlargement of the lattice parameter, as seen in the XRD patterns of the materials.

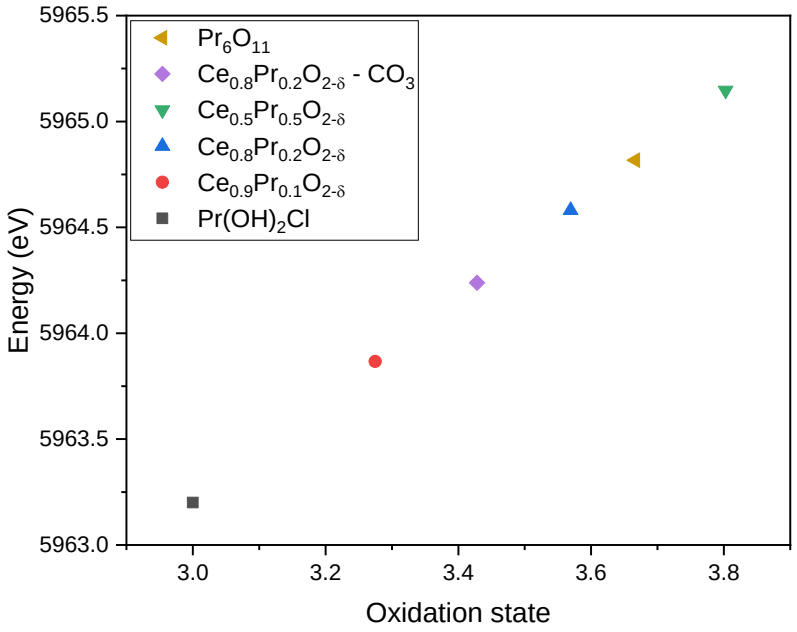

Figure 86: A plot of energy (defined at which normalised absorption = 1.0) as a function of oxidation state, extracted from a linear fit of the reference compound, to estimate the oxidation states in the $Ce_{1-x}Pr_xO_{2-\delta}$ compounds.

4.10 Conclusions

In this chapter, a solvothermal synthesis method utilizing similar conditions was used to produce an extended series of $Ce_{1-x}Ln_x(OH)_2Cl$ and $Ce_{1-x}Ln_x(OH)CO_3$ (Ln = La, Gd, Pr and Tb) materials. Simply altering the lanthanide starting reagent ($LnCl_3 \cdot nH_2O$/$Ln(NO_3)_3 \cdot nH_2O$) and the molecular weight of the polymer (Mn_{200} or Mn_{400}) yields two different structures each with their own distinct morphologies. The thermal decompositions of these materials allow for the formation of substituted cerium oxide ($Ce_{1-x}Ln_xO_{2-\delta}$) whilst retaining their unique morphologies via a novel preparation method. A detailed study of all structures was undertaken, using several techniques to prove substitution of the lanthanides has occurred. The results confirmed substitution as well as achieving the desired composition. The resulting materials were also tested to evaluate their reducibility and potential use in exhaust catalysis, by use of H_2-TPR. The outcome of these tests suggested that the $Ce_{1-x}Ln_xO_{2-\delta}$ samples formed from the decomposition of the $Ce_{1-x}Ln_x(OH)_2Cl$ generally have increased activity in comparison to the $Ce_{1-x}Ln_x(OH)CO_3$ samples. The presence of Pr or Tb leads to an increase in hydrogen uptake at lower temperatures and at an increase quantity in comparison to pure CeO_2. There is also the prospect of forming more oxygen species if the materials are fired at lower temperatures due to

the mixed oxidation states formed for the materials and the comparably easier oxidation of cerium, which occurs before the decomposition observed in the TGA (XANES confirmation). Overall these observations suggest that the substituted cerium oxides could exhibit enhanced activity in oxidizing reactions at low temperatures, but further investigation into the longevity and calcination temperature effects need to be explored to provide any definitive answers.

References

1. Y. Ni, J.M. Hughes and A.N. Mariano. (1993). The atomic arrangement of bastnaesite-(Ce),Ce(CO_3)F, and structural elements of synchysite-(Ce),roentgenite-(Ce),and parisite-(Ce). *American Mineralogist*. 78, p415-418.
2. Saiki, N. Ishizawa, N. Mizutani and M. Kato. (1985). Structural change of C-type rare earth oxides, ytterbium oxide and erbium oxide at high temperatures. *Journal of the Ceramic Association of Japan*. 93, p649-654.
3. G. Meyer and T. Schleid. (1986). Oxidchloride unter reduzierten Bedingungen: Einkristalle von NdOCl und GdOCl. *Zeitschrift fuer Anorganische und Allgemeine Chemie*. 533, p181-185.
4. R.F. Klevtsova and L.A. Glinskaya. (1969). The crystal structures of Pr$(OH)_2$Cl, Sm$(OH)_2$Cl and Gd$(OH)_2$Cl. *Zhurnal Strukturnoi Khimii*. 10, p494-497.
5. G. Brauer and H. Gradinger. (1950). Ueber heterotype Mischphasen bei Seltenerdoxyden. I. *Zeitschrift fuer Anorganische und Allgemeine Chemie.* 276, p209-226.
6. W.H. Zachariasen. (1949). Crystal Chemical Studies of the 5f-Series of Elements. XII. New Compounds Representing Known Structure Types. *Acta Crystallographica*. 2, p388-390.
7. R.A. Zehnder, D.L. Clark, B.L. Scott, R.J. Donohoe, P.D. Palmer, W.H. Runde and D.E. Hobart. (2010). Investigation of the structural properties of an extended series of lanthanide bis-hydroxychlorides Ln$(OH)_2$Cl (Ln = Nd - Lu, except Pm and Sm). *Inorganic Chemistry*. 49 (11), p4781-4790.
8. R. Chiba, H. Taguchi, T. Komatsu, H. Orui, K. Nozawa and H. Arai. (2011). High temperature properties of $Ce_{1-x}Pr_xO_{2-\delta}$ as an active layer material for SOFC cathodes. *Solid State Ionics*. 197, p42-48.
9. M. Coduri, M. Scavini, M. Brunelli, E. Pedrazzin and P. Masala. (2015). Structural characterization of Tb- and Pr-doped ceria. *Solid State Ionics*. 268, p150-155.
10. G. Groppi, C. Cristiani, L. Lietti, C. Ramella, M. Valentini and P. Forzatti. (1999). Effect of ceria on palladium supported catalysts for high temperature combustion of CH_4 under lean conditions. *Catalysis Today*. 50 (2), p399-412.
11. M.A. Malecka, L. Kepinski and W. Mista. (2008). Synthesis, structure and morphology of CeO_2 and $CeLnO_x$ mixed oxides (Ln = Pr, Tb, Lu) prepared by microemulsion method. *Journal of Alloys and Compounds*. 451 (1-2), p567-570.
12. J. Malleshappa, H. Nagabhushana, S.C. Sharma, D.V. Sunitha, N. Dhananjaya, C. Shivakumara and B.M. Nagabhushana. (2014). Self-propagating combustion synthesis and luminescent properties of nanocrystalline CeO_2: Tb (3+) (1-10 mol%) phosphors. *Journal of Alloys and Compounds*. 590, p131-139
13. M.A. Malecka, L. Kepinski and W. Mista. (2007). Structure evolution of nanocrystalline CeO_2 and $CeLnO_x$ mixed oxides (Ln = Pr, Tb, Lu) in O_2 and H_2 atmosphere and their catalytic activity in soot combustion. *Applied Catalysis B: Environmental*. 74 (3-4), p290-298.

5. Structural analysis of cerium zirconium oxides synthesised via solvothermal and precipitation methods

5.1 Introduction

In this chapter, $Ce_{1-x}Zr_xO_{2-\delta}$ (x = 0.5 or 0.8) mixed oxides were synthesised via three solution methods from alkoxides. These mixed oxides are acknowledged to be structurally complex, owing to the number of phases that can be formed from thermal treatment of the samples, often referred to in literature as t, t', t" and k. [1-2] However, they have attracted widespread interest in a number of applications, most notable for their use in automotive three-way catalysis, as a component to promote the oxygen storage capacity of the catalyst. A reduction treatment of these materials at high temperatures has shown to improve the oxygen storage/release properties, due the formation of another phase with a higher degree of Ce-Zr cationic ordering. This *k*-$Ce_2Zr_2O_8$ phase is typically prepared by the mild oxidation under atmospheric conditions of a pyrochlore-type structure, in the form of $Ce_2Zr_2O_{7+\delta}$. In general, the pyrochlore phase is formed by reducing $Ce_{0.5}Zr_{0.5}O_{2-\delta}$ at high temperatures under a flow of hydrogen. The reduction of this phase generates oxygen vacancies, which promotes cation mobility and therefore the ordering of the cationic sublattice. However, as the reduction of $Ce_{0.5}Zr_{0.5}O_{2-\delta}$ requires high temperatures (≥ 1000 °C) to form this represents a critical issue for both catalytic performance and commercial production costs. The use of hydrogen gas also poses both a fire and explosive hazard, so developing new synthetic routes to reduce these factors is key.

5.2 Synthesis

AM01 and AM01-SRMO are samples supplied by the Johnson Matthey Technology Centre, UK. The AM01 sample is a commercial $Ce_{0.5}Zr_{0.5}O_{2-\delta}$ and AM01-SRMO is the same sample subjected to a strong-reduction and mild-oxidation to form the *k*-$Ce_2Zr_2O_8$ phase.

5.2.1 Sol-gel method

Cerium 2-methoxyethoxide, 18-20% w/w in 2-methoxyethanol and zirconium n-butoxide, 80% w/w in 1-butanol were used as starting reagents. A typical procedure involves stirring the measured volumes of the alkoxide solutions together in the same centrifuge tubes (50 ml) using an analytical balance. A magnetic stirrer was placed inside the tube, sealed and placed on a stirring plate and was left to stir for a

period of 1 hour. Distilled water (~0.5 g) was measured using an analytical balance into a glass vial (20 ml) this was added dropwise using a Pasteur pipette. The mixture was left to stir for a period of 30 minutes and the centrifuge tube was placed in a centrifuge rotating at 40,000 rpm for 10 minutes. The centrifugation was repeated after washing the solid sample with fresh distilled water (2 g) twice. The solid coated centrifuge tube was air dried overnight and the solid was transferred and ground in a pestle and mortar prior to analysis.

5.2.2 Solvothermal method

Cerium 2-methoxyethoxide, 18-20% w/w in 2-methoxyethanol and zirconium n-butoxide, 80% w/w in 1-butanol were used as starting reagents. Samples of $Ce_{1-x}Zr_xO_{2-\delta}$ were prepared by solvothermal synthesis from liquid alkoxides using Teflon-lined, stainless-steel autoclaves (20 mL). In a typical synthesis, Cerium 2-methoxyethoxide and zirconium n-butoxide were measured using an analytical balance to total a desired stoichiometric ratio of 1 mmol. The reaction mixture was placed on a stirring plate and was left to stir for a period of 1 hour. The autoclaves were then sealed and placed within a preheated fan oven at 240 °C for 24 h, before cooling to room temperature. After the reaction, a dark blue/grey precipitate was obtained which was recovered by suction filtration. All the solid products were washed with deionised water and dried at 70 °C overnight before further characterization.

5.2.3 Solvothermal method (Glovebox, N_2)

The same procedure was also repeated in combination with a nitrogen filled glovebox. All the synthetic steps prior to the autoclave being placed within the oven were conducted with a glovebox, to remove the air from the headspace within the autoclave. The samples were then subjected to thermal treatment as soon as the autoclaves had cooled and were opened, without washing or filtration.

5.2.4 Thermal Treatment of $Ce_{1-x}Zr_xO_{2-\delta}$

The products recovered from the sol-gel and solvothermal synthesis were calcined in air using a muffle furnace at 10 °C min^{-1} from room temperature to 700 or 1000 °C and held at the designated temperature for 5 h, before cooling.

The $Ce_{0.5}Zr_{0.5}O_{2-\delta}$ products obtained from all three synthetic routes were also calcined within a tube furnace to various temperatures ranging between 900-1150 °C

at 10 °C min^{-1} under flow of N_2 or 5% H_2/N_2 at a flow rate of 1 ml min^{-1}. Once cooled the samples were then subject to a mild oxidation, in air at 500 °C for one hour.

5.2.5 X-ray absorption spectroscopy

The Ce L_{III}-edge and Zr K-edge X-ray absorption data was collected on Beamline B18 at Diamond Light Source, UK. The sample were diluted with polyethylene powder and pressed into a 13 mm diameter pellets, approximately 1 mm thick. The Absorption data was collected in transmission mode. The spectra were normalised using the ATHENA software package.

NIST-CeO_2, $CeCl_3$ and ZrO_2 were purchased and used as reference materials to calibrate the cerium and zirconium absorption spectra. The AM01 and AM01-SRMO reference materials were supplied by Johnson Matthey Technology Centre, UK.

5.3 $Ce_{0.5}Zr_{0.5}O_{2-\delta}$ and $Ce_{0.2}Zr_{0.8}O_{2-\delta}$ mixed oxides

5.3.1 Powder XRD

The XRD patterns of the $Ce_{0.5}Zr_{0.5}O_{2-\delta}$ and $Ce_{0.2}Zr_{0.8}O_{2-\delta}$ samples synthesised by both the solvothermal and sol-gel methods after calcination at 700 and 1000 °C in air for 5 h, are shown in Figure 87. The patterns of the powders calcined at 700 °C showed the same Bragg reflections, which shift to higher 2θ values for the Zr-rich samples. This shift is due to the contraction of the lattice which is consistent with the smaller ionic radius of Zr^{4+} (0.84 Å) compared with that of Ce^{4+} (0.97 Å). The reflections of the samples synthesised by the sol-gel method showed the most pronounced peak asymmetry, indicating a higher degree of disorder. This was further evidenced in the samples calcined at 1000 °C, by the formation of new tetragonal and monoclinic phases for the $Ce_{0.5}Zr_{0.5}O_{2-\delta}$ and $Ce_{0.2}Zr_{0.8}O_{2-\delta}$ samples respectively. The samples synthesised by the solvothermal method at 1000 °C, show less phase variation upon increasing temperature. The main difference is observed in the $Ce_{0.2}Zr_{0.8}O_{2-\delta}$ sample synthesised by the sol-gel method which was calcined at 1000 °C, which contains peaks attributed to a tetragonal phase.

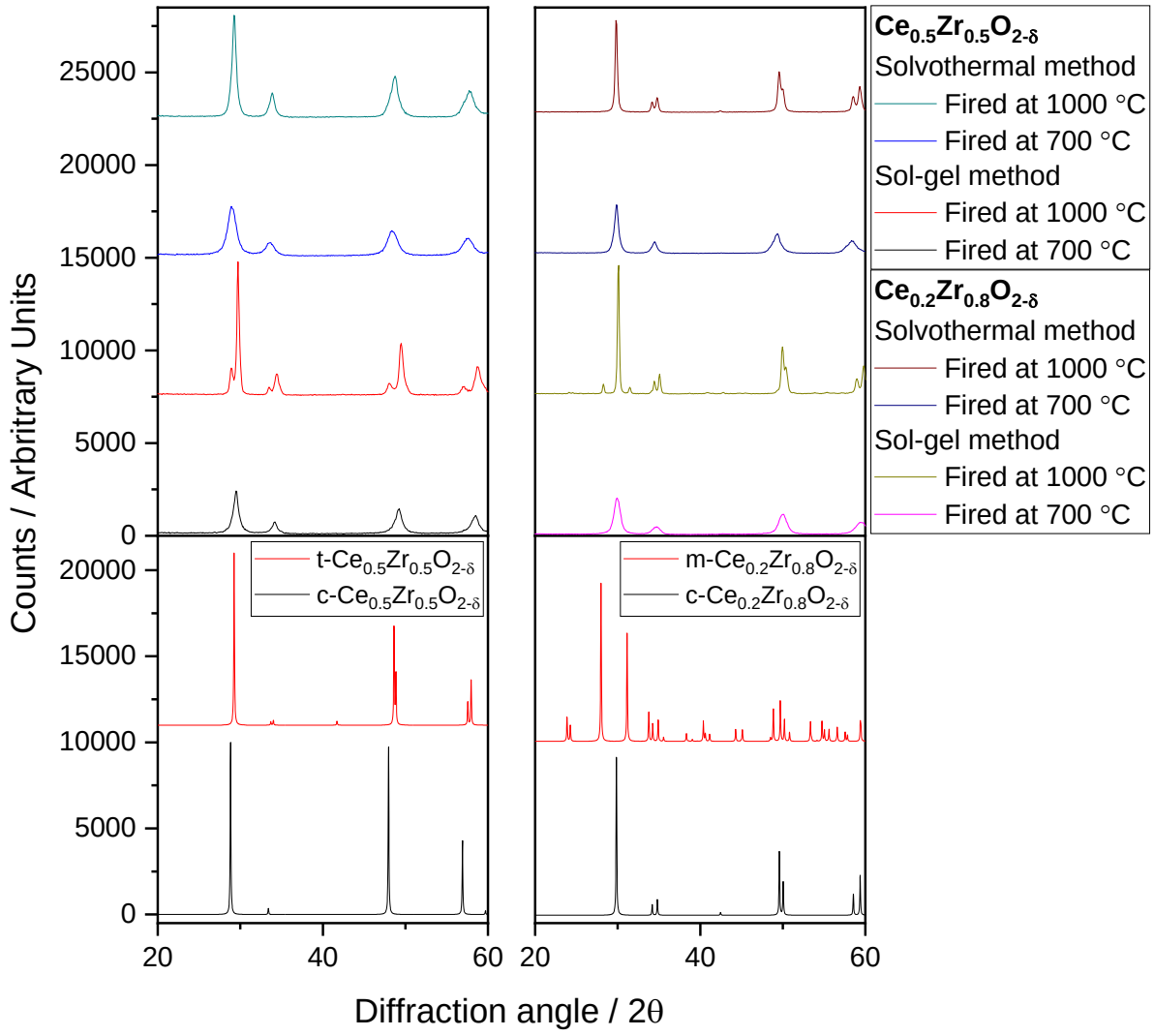

Figure 45: Powder XRD patterns of $Ce_{0.5}Zr_{0.5}O_{2-\delta}$ and $Ce_{0.2}Zr_{0.8}O_{2-\delta}$ samples calcined at various temperatures in air, synthesised via both the sol-gel and solvothermal methods, compared against reference patterns taken from literature. [3-5]

5.3.2 Raman spectroscopy

Raman spectroscopy provides information on the oxygen sublattice and hence provides complimentary information on the structure attained from XRD. Raman spectroscopy data (Figure 88) of CeO_2 shows one broad band centred at around 460-465 cm^{-1}, attributed to the F_{2g} Raman mode induced by O-Ce-O symmetric stretching vibrations characteristic of cubic ceria. The Raman spectra of the as-prepared $Ce_{0.5}Zr_{0.5}O_{2-\delta}$ and $Ce_{0.2}Zr_{0.8}O_{2-\delta}$ samples (Figure 89 and 90) in comparison show a broadening, loss of intensity, and a shift to higher wavenumbers of the F_{2g} band with increasing Zr^{4+} content. The observed shifts are caused by the contraction of the cell, from the incorporation of a smaller cation. The Ce-O bonding is longer and weaker than the Zr-O bond, hence the increased Zr^{4+} content creates a distortion

of the ceria lattice. The $Ce_{0.2}Zr_{0.8}O_{2-\delta}$ samples calcined at 700 °C and prepared via both the solvothermal and sol-gel methods exhibit multiple extra Raman bands at ca. 260, 320, and 630 cm^{-1}, characteristic of tetragonal-ZrO_2 which has six Raman-active modes of symmetry ($A_{1g} + 3E_g + 2B_{1g}$). [6] The $Ce_{0.2}Zr_{0.8}O_{2-\delta}$ synthesised by the sol-gel method and calcined at 1000 °C contains a doublet of Raman bands at ca. 170-190 cm^{-1}, which is characteristic of monoclinic ZrO_2 (Figure 88).

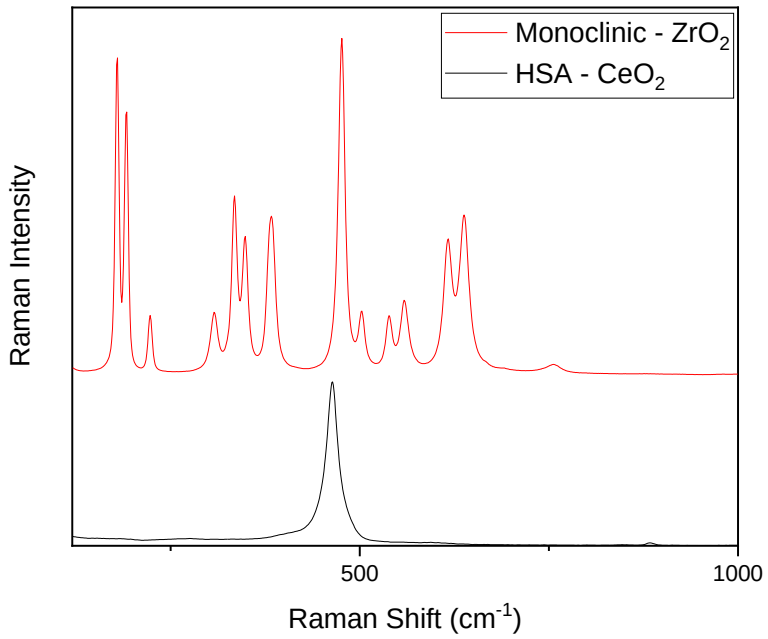

Figure 88: Raman spectra of reference materials (m-ZrO_2 and CeO_2).

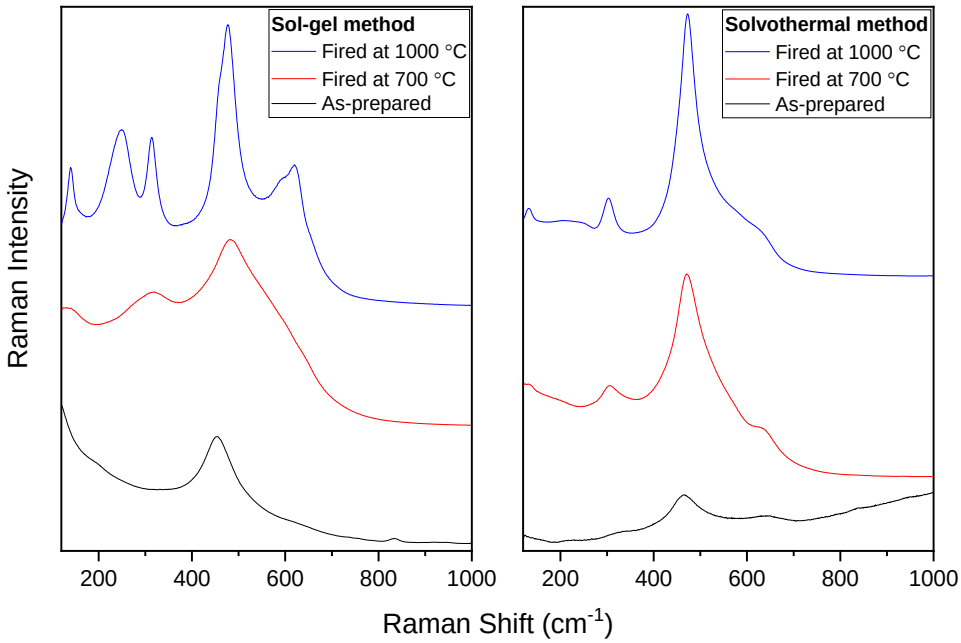

Figure 46: Raman spectra of the $Ce_{0.5}Zr_{0.5}O_{2-\delta}$ samples calcined at various temperatures in air, synthesised via both the sol-gel and solvothermal methods.

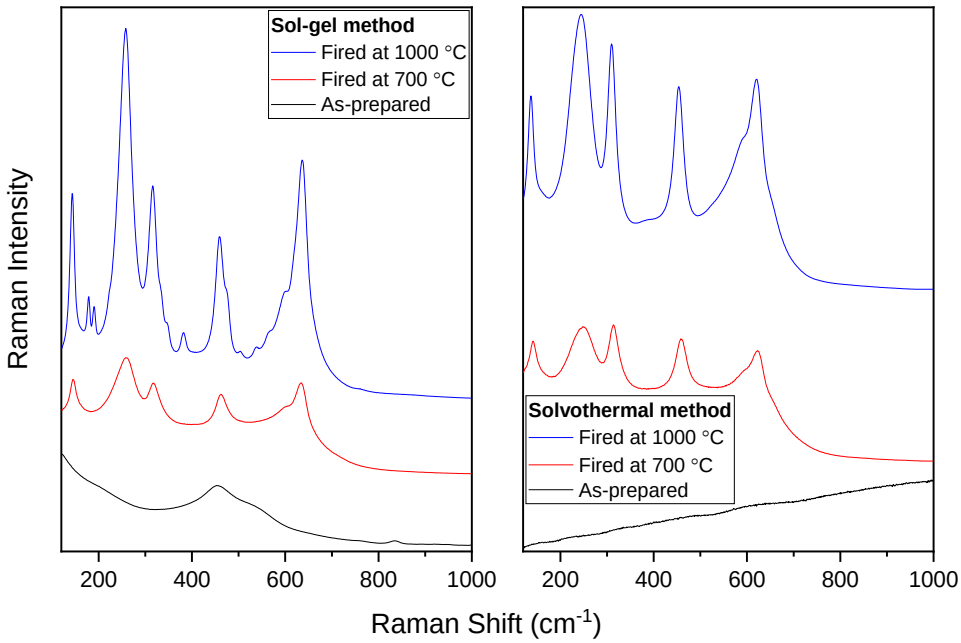

Figure 90: Raman spectra of the $Ce_{0.2}Zr_{0.8}O_{2-\delta}$ samples calcined at various temperatures in air, synthesised via both the sol-gel and solvothermal methods.

5.4 X-ray absorption spectroscopy (XAS)

5.4.1 Ce L_{III}-edge XANES

The Ce L_{III}-edge XANES presented in Figure 91 shows that the as-prepared materials synthesised by the sol-gel method have the same profile as NIST-CeO_2. For these samples it means that the oxidation state of cerium is Ce^{4+}. The as-prepared materials synthesised by the solvothermal method however show a shift of the edge position to lower energy, and a double peak feature which indicates that the materials contain more Ce^{3+}. The starting reagent (cerium 2-methoxy ethoxide) contains cerium in the +4 oxidation state, therefore the reduction of the Ce^{4+} in the solvothermal reaction occurs as the alcohols act as a reducing agent. A linear relationship between cerium oxidation state and the energy shift of the absorption edge has been illustrated by Figure 92. Both the $Ce_{0.5}Zr_{0.5}O_{2-\delta}$ and $Ce_{0.2}Zr_{0.8}O_{2-\delta}$ samples synthesised by the solvothermal method show that approximately 50% of the cerium has been reduced after the applied procedure. All of the other calcined samples contained cerium in the +4 oxidation state.

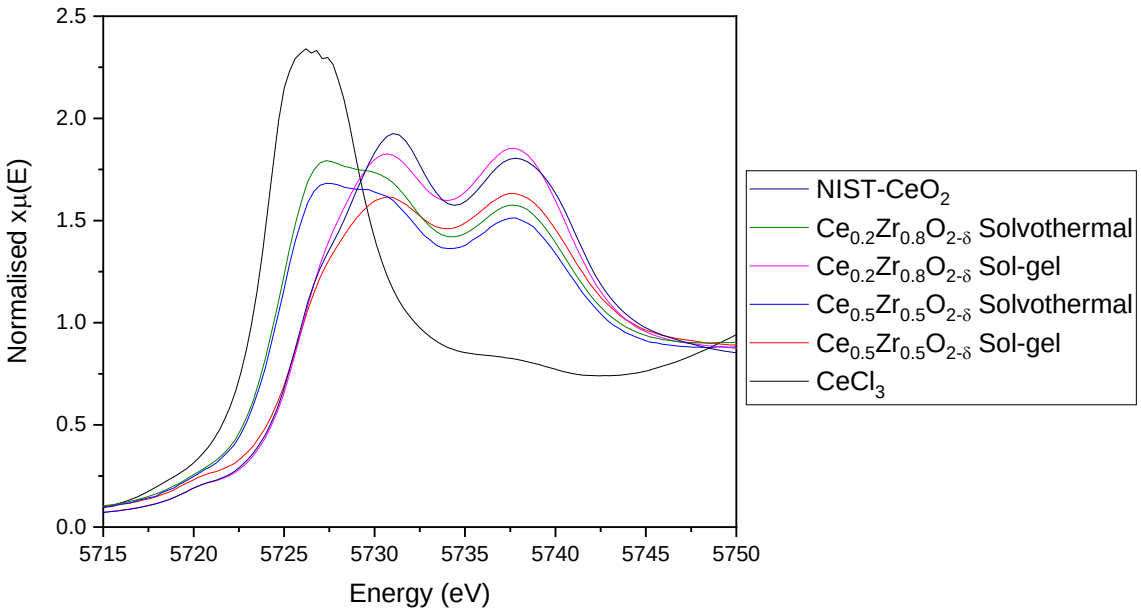

Figure 91: Normalised Ce L_{III}-edge XANES spectra of the as-prepared $Ce_{1-x}Zr_xO_{2-\delta}$ compared against reference compounds with known Ce oxidation states ($CeCl_3$ and NIST-CeO_2).

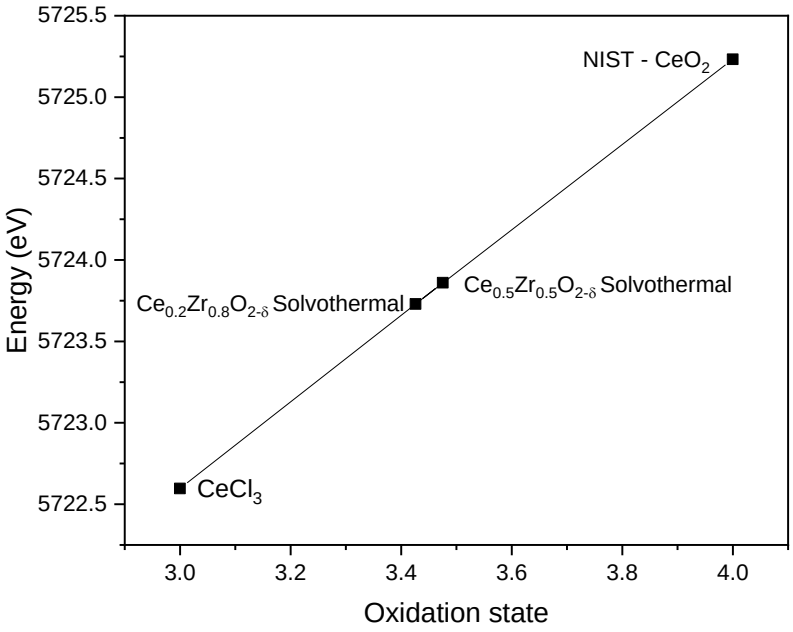

Figure 92: A plot of energy (defined at which normalised absorption = 1.0) as a function of oxidation state, extracted from a linear fit of the reference compounds, to estimate the Ce oxidation states in the $Ce_{1-x}Zr_xO_{2-\delta}$ compounds.

5.4.1 Zr K-edge XANES

Contrary to cerium, zirconium's oxidation state remains as Zr^{4+}, irrespective of oxygen uptake/release as shown by the unaltered Zr K-edge energy position. Some structural information can be determined from the inspection of the Zr K-edge XANES spectra (Figure 93), which shows slight variations on the pre-edge (A) and near-edge (B) absorption regions. The pre-edge absorption region is sensitive to the Zr-O geometry and can be assigned to the 1s → 4d transition. This transition is affected by the extent of mixing of the d and p orbitals and is more prominent for materials with a greater centrosymmetric distortion. The pre-edge feature for the AM01 samples is particularly more prominent than the other samples in the XANES comparison. For the near-edge region, the distinguishable feature is the splitting of the main peak. The asymmetric peak intensity ratio between the edge peak and peak B, is more pronounced for AM01-SRMO which again is correlated to the symmetry of the Zr-O local co-ordination. The intensity difference between the two becoming more apparent for a more centrosymmetric site. The samples prepared via the sol-gel method having the lowest peak intensity ratio of the samples resembling more like the ZrO_2 profile.

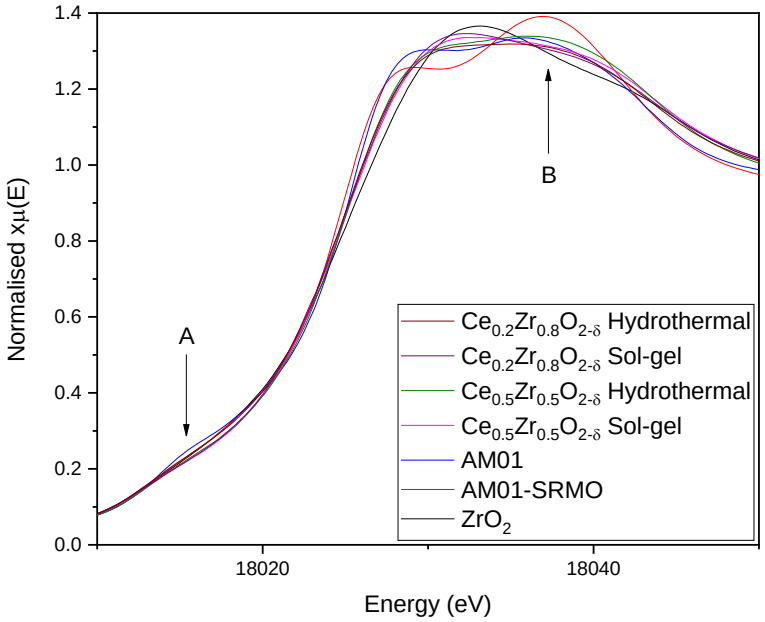

Figure 473: Normalised Zr K-edge XANES spectra of $Ce_{1-x}Zr_xO_{2-\delta}$ compared against reference compounds (ZrO_2, AM01 and AM01-SRMO).

5.5 *k*-$Ce_2Zr_2O_8$ mixed oxide

5.5.1 Powder XRD

The powder XRD pattern (Figure 94) of the reference *k*-$Ce_2Zr_2O_8$ (Space group: $P2_13$) consist of the structural Bragg peaks for fluorite type structure as well as reflections that are assigned to the ordered arrangement of Ce^{3+} and Zr^{4+} cations along the (1,1,0) direction. The AM01-SRMO sample and the AM01 sample heated to 1150 °C under flow of 5% H_2/N_2 can both be indexed to this phase. However, the XRD pattern of the AM01 sample heated to 1150 °C under flow of N_2 reveals that the *k*-$Ce_2Zr_2O_8$ phase doesn't form under these conditions, instead there are additional Bragg reflections attributed to a new tetragonal phase.

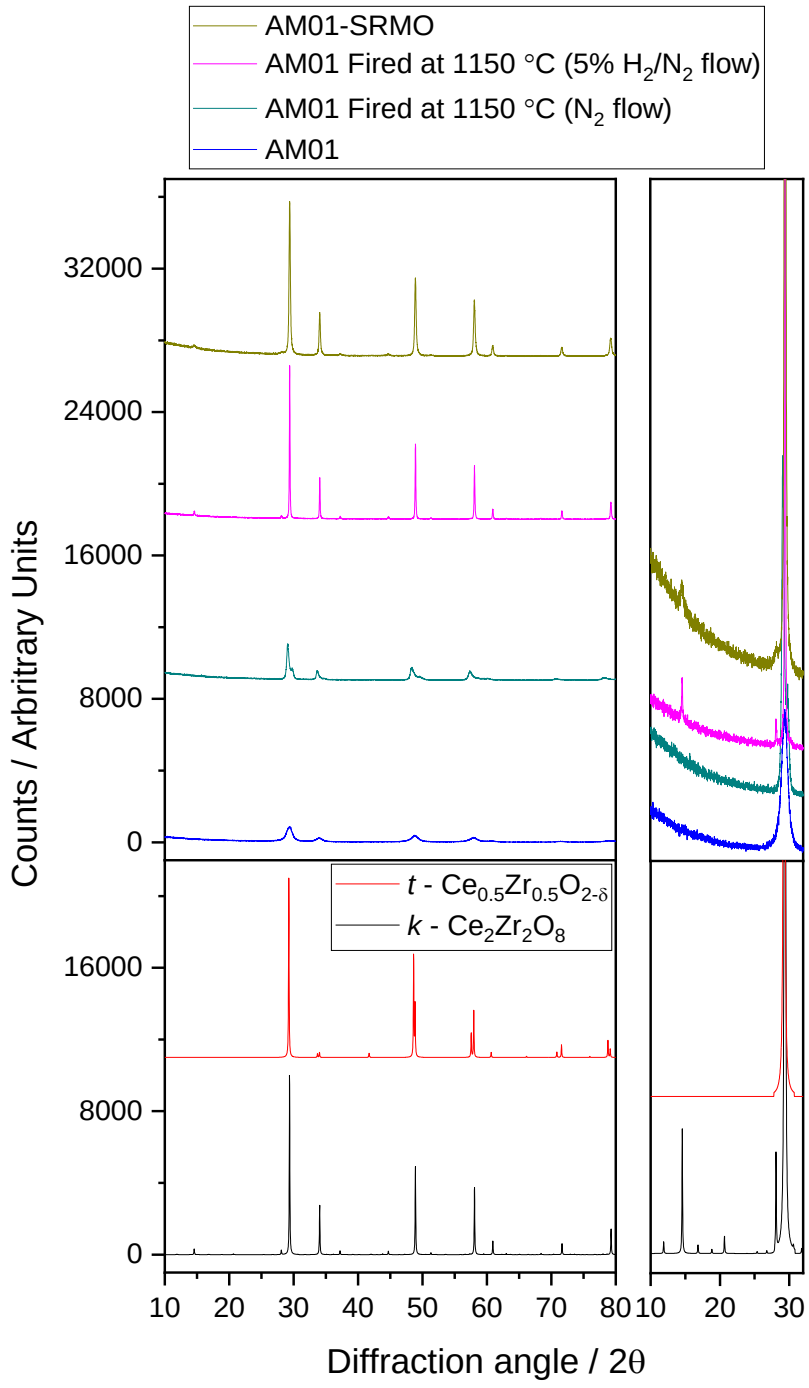

Figure 48: Powder XRD patterns of AM01 reference materials calcined at various temperature under different gas flows, compared against reference patterns taken from literature. [5,7]

Figure 95 shows the powder XRD patterns of the $Ce_{0.5}Zr_{0.5}O_{2-\delta}$ samples synthesised via three different methods at 1150 °C under flow of either H_2 or 5% H_2/N_2 gas. Contrary to the commercial AM01 sample all three methods can form the ordered *k*-$Ce_2Zr_2O_8$ phase under N_2.

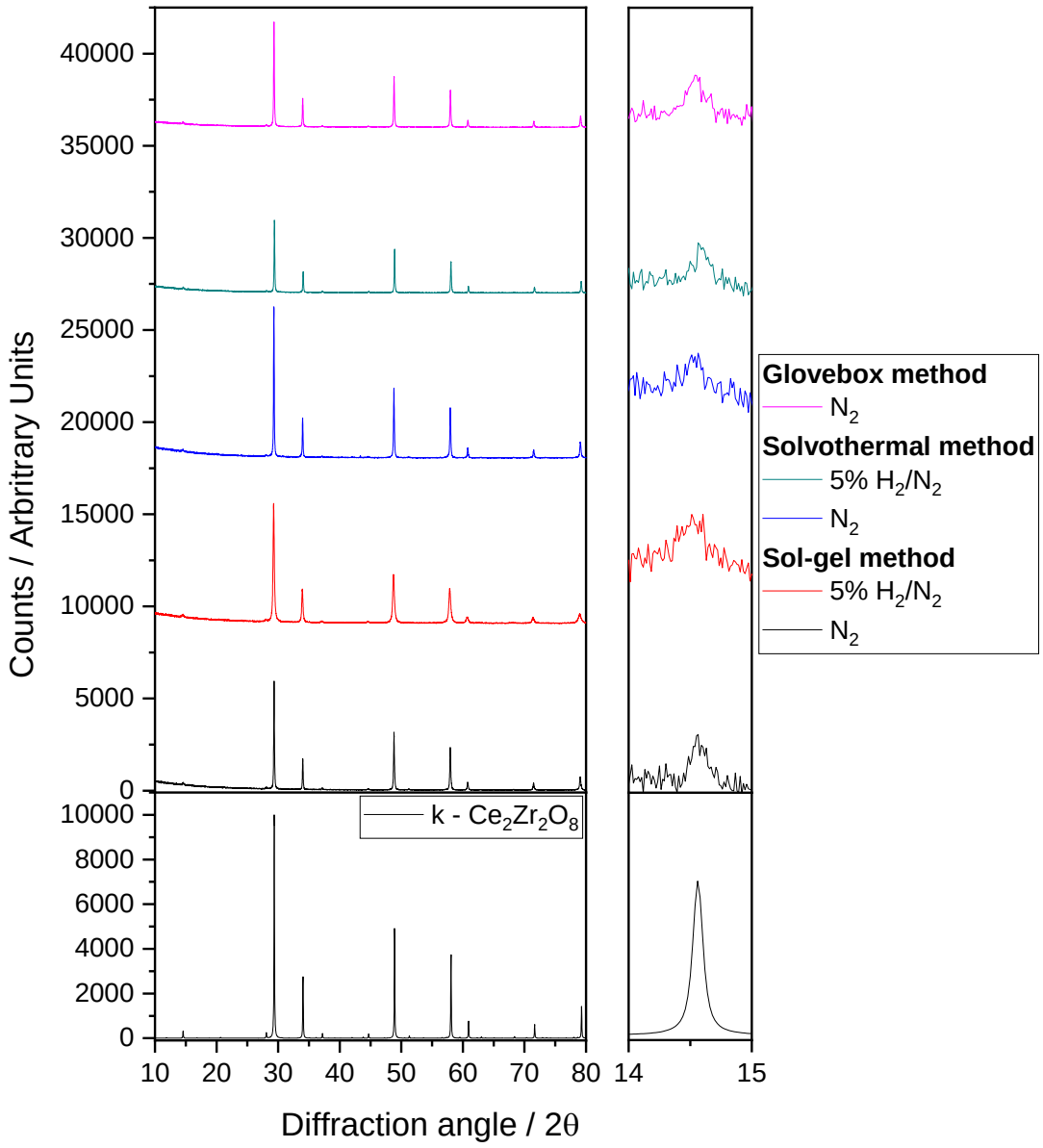

Figure 95: Powder XRD patterns of $Ce_{0.5}Zr_{0.5}O_{2-\delta}$ calcined at 1150 °C under different gas flows, synthesised by all three synthesis methods and compared against a reference k-$Ce_2Zr_2O_8$ pattern. [7]

The sol-gel synthesis route to form the *k*-$Ce_2Zr_2O_8$ phase was repeated and the reduction temperature was decreased to observe if the phase could be formed at lower temperatures. The powder XRD patterns shown in Figure 96. show that as the reduction temperature is lowered the Bragg peaks become broader and the reflections attributed to the *k*-$Ce_2Zr_2O_8$ phase are no longer visible.

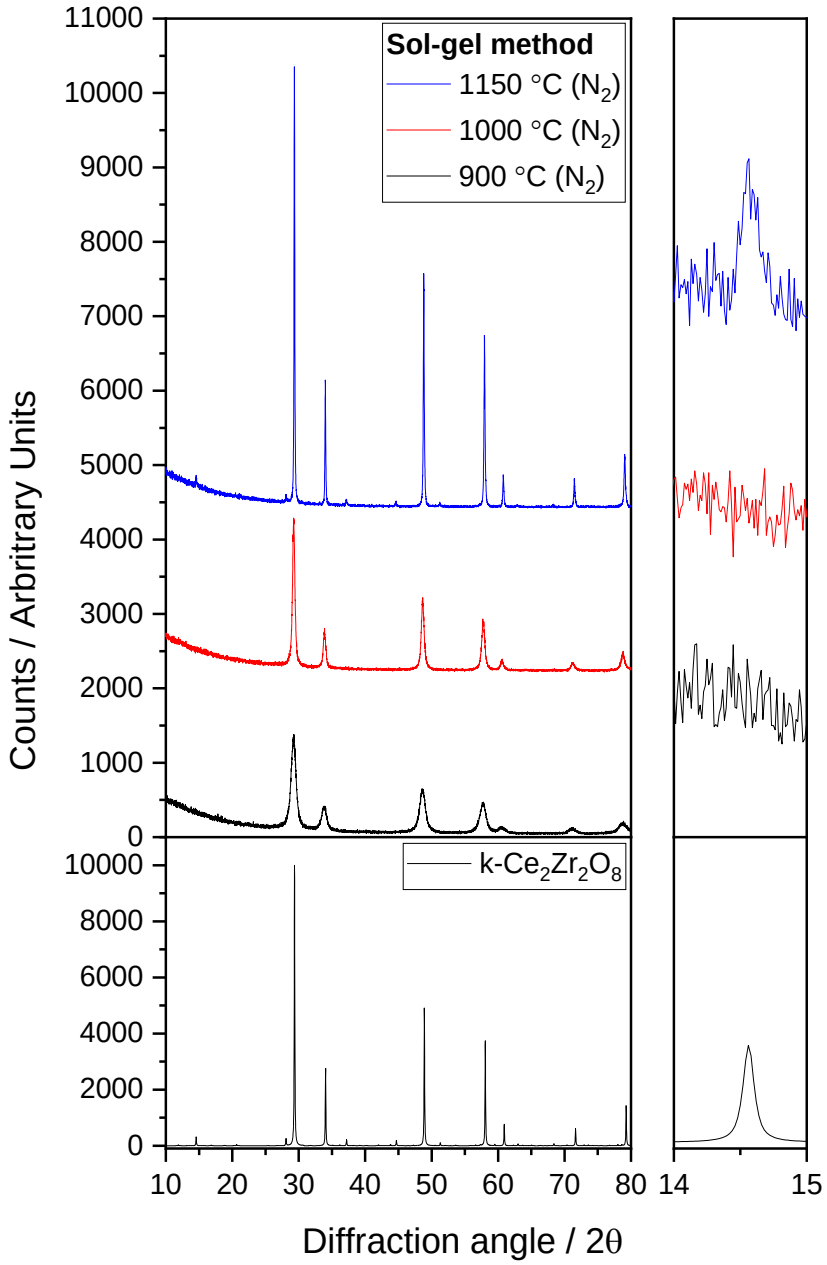

Figure 96: Powder XRD patterns of $Ce_{0.5}Zr_{0.5}O_{2-\delta}$ samples calcined at various temperatures under flow of N_2, synthesised via the sol-gel method and compared against a reference k-$Ce_2Zr_2O_8$ pattern. [7]

The glovebox method was chosen as the synthetic route of choice over the conventional solvothermal method as Conducting the solvothermal reaction within a glovebox, removes the air from the autoclave, thought to enable further reduction of the Ce^{4+} cations. Hence, reducing the temperature required to form the *k*-$Ce_2Zr_2O_8$ phase as a larger quantity of the cerium cations would already be present as Ce^{3+}. The same alterations in temperature were applied as with the sol-gel method and the powder XRD patterns of the results are shown in Figure 97. At a reduction

temperature of 1000 °C, the presence of the reflections associated with the *k*-$Ce_2Zr_2O_8$ phase are visible. At 900 °C, however close inspection does suggest the possibility of the presence of the characteristic peaks, but they're very weak with respect to the noise so the assignment is somewhat inconclusive.

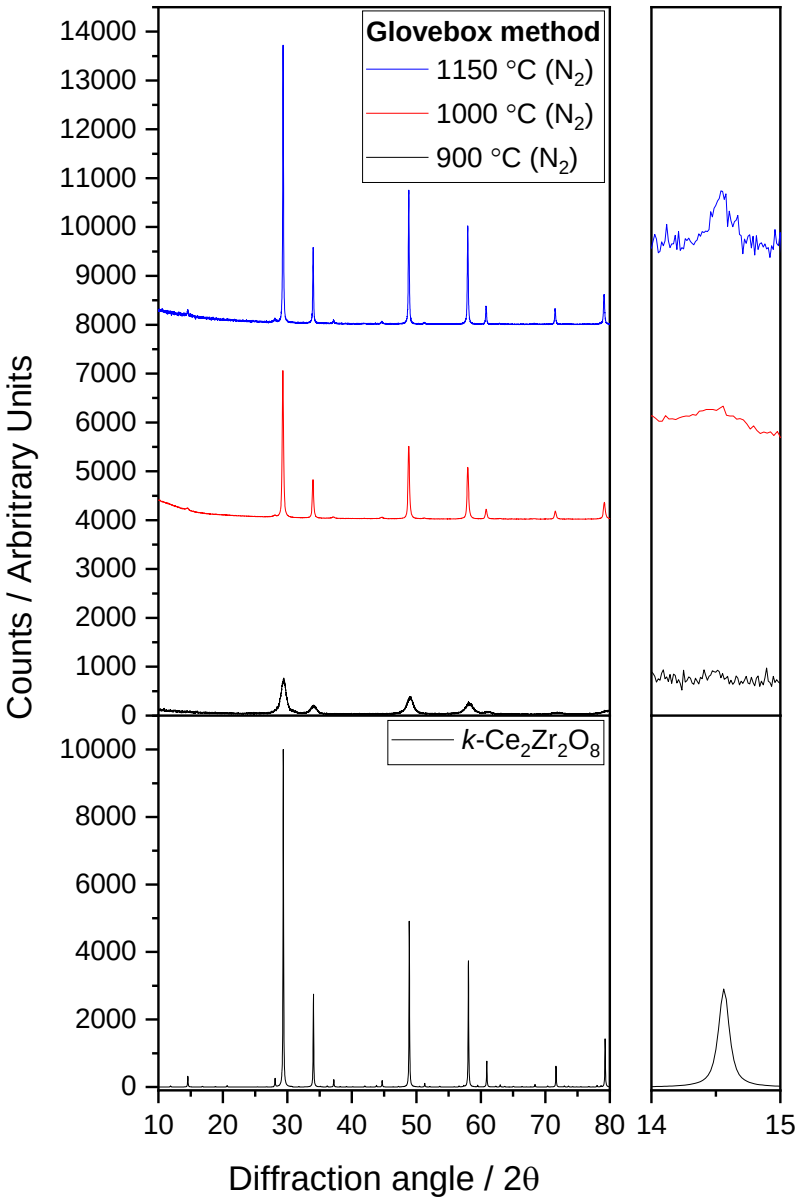

Figure 49: Powder XRD patterns of $Ce_{0.5}Zr_{0.5}O_{2-\delta}$ samples calcined at various temperatures under flow of N_2, synthesised via the glovebox method and compared against a reference k-$Ce_2Zr_2O_8$ pattern. [7]

The in situ powder XRD experiment (Figure 98) shows that the re-oxidation treatment plays a key role in the ordering of the cationic lattice. As the temperature increases on this sample previously re-oxidised at 500 °C, the intensity of Bragg peaks attributed to the cationic order decrease. Thus, severe or prolonged oxidation

leads to the formation of an oxide with a random distribution of Ce-Zr in the sublattice. In contrast using an insufficient oxidation temperature will result in the formation of a product containing a large quantity of Ce^{3+}, indicated by the samples greenish hue.

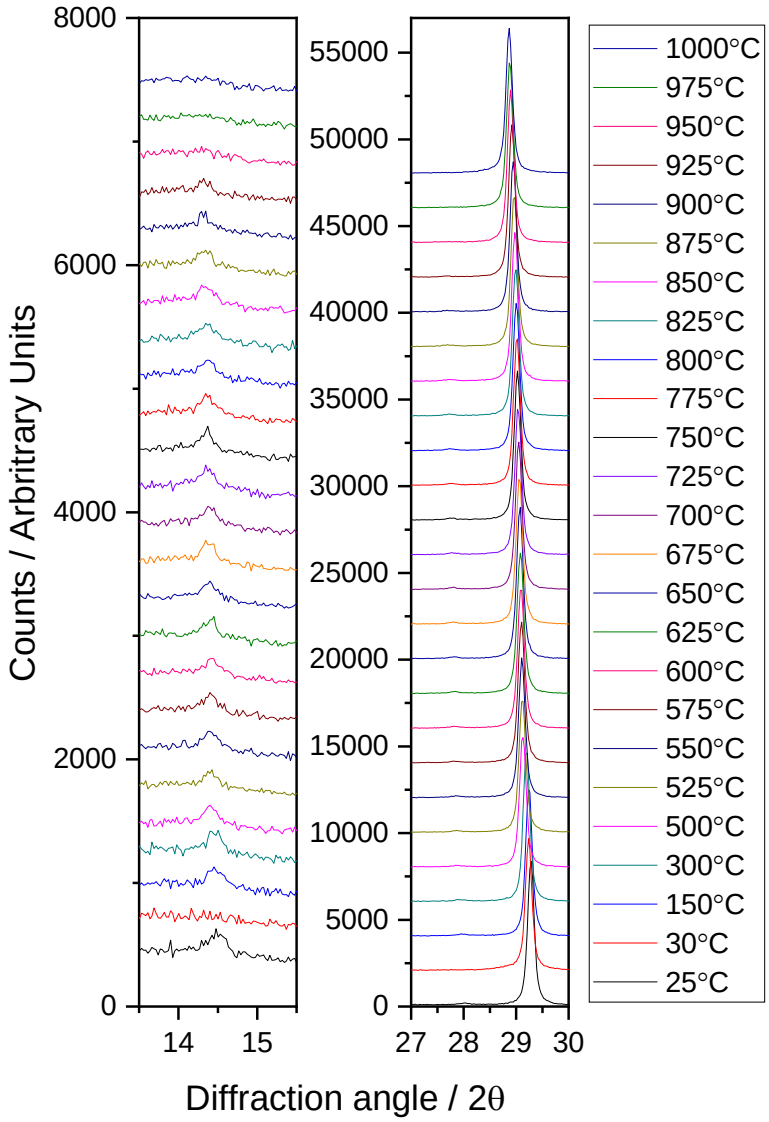

Figure 50: In situ powder XRD heating experiment of k-$Ce_2Zr_2O_8$ in air a) (1,1,1) peak b) (3,1,1) and (2,2,2) peak respectively.

5.5.2 Raman spectroscopy

The Raman spectrum of the *k*-$Ce_2Zr_2O_8$ phase changes dramatically in comparison to the previous Raman spectra, with an observed large number of Raman bands due to the lower symmetry of the kappa-phase. The Raman spectra of the AM01 samples

(Figure 99) corresponds well with the results obtained by XRD, in that the AM01 sample fired under N_2 contains more bands attributed to the tetragonal structure.

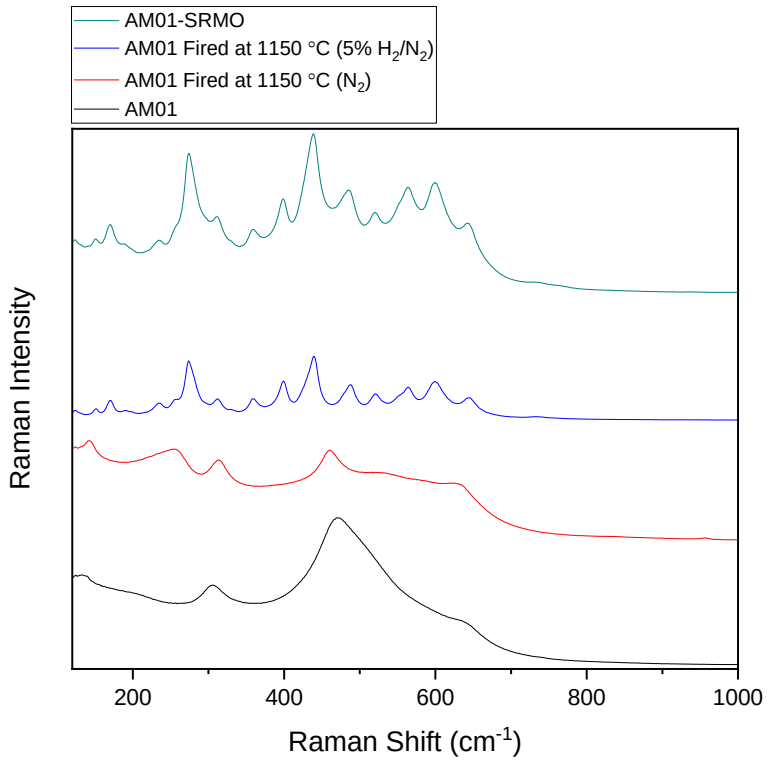

Figure 99: Raman spectra of AM01 reference materials calcined at various temperatures under different gas flows.

Figure 100 shows the Raman spectra of the $Ce_{0.5}Zr_{0.5}O_{2-\delta}$ samples synthesised via three different methods at 1150 °C under flow of either H_2 or 5% H_2/N_2 gas. Comparing the glovebox and solvothermal methods calcined under nitrogen, revealed the Raman bands for the glovebox method appear to be more well-defined. The sample fired under 5% H_2/N_2 exhibiting the largest spectral separations of the Raman bands which correlates to the sample contain less structural disorder. The sol-gel method however, appears to become more disordered under flow of 5% H_2/N_2.

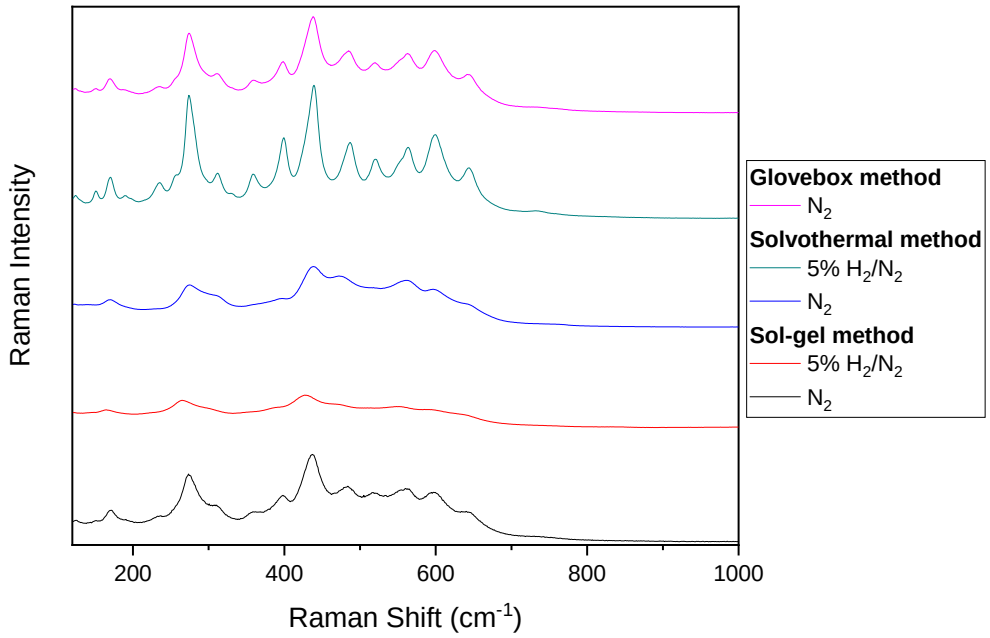

Figure 100: Raman spectra of the $Ce_{0.5}Zr_{0.5}O_{2-\delta}$ samples calcined at 1150 °C, under different gas flows, synthesised by all three synthetic methods.

5.6. Temperature programmed reduction/oxidation (TPR/TPO)

The TPR measurements (Figure 101) indicates how the reduction profiles are influenced by the choice of thermal treatment. Notably the AM01 and solvothermal method samples calcined under flow of 5% H_2/N_2, have similar TPR profiles for the first measurement, with a slightly lower T_{max} value for the solvothermal method. The main difference between the two samples occurs during the second TPR measurement where the solvothermal method sample's reduction peak shifts to lower temperature (393 °C) and reaches nearly 100% reduction. Whereas the AM01 sample shows little variation from the first. The solvothermal method sample calcined at the same temperature under N_2, exhibits the same change in T_{max} reduction values. The total percentage of reduction however is similar to the $Ce_{0.5}Zr_{0.5}O_{2-\delta}$ samples fired in air, and the peaks themselves are very broad. For the sample fired in air for both synthesis methods, shows for the first TPR that the increased calcination temperature (1000 °C) lessens the total reduction percentage. The AM01 sample is calcined at 500 °C in air, therefore the difference between all measurements can presumably attributed to sintering.

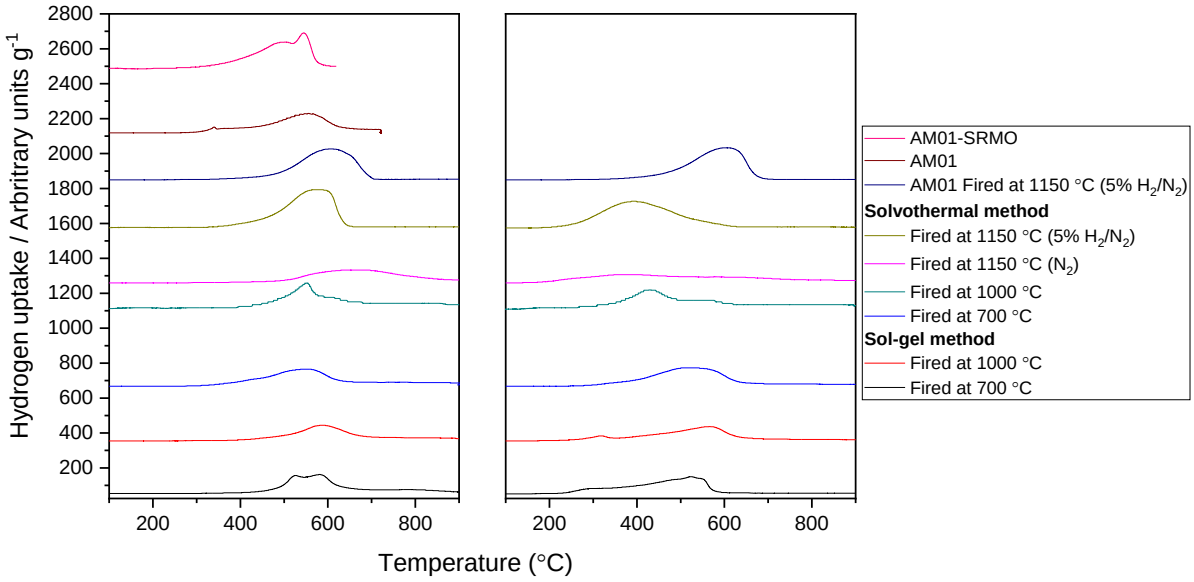

Figure 51: Sequential TPR profiles of the AM01 reference materials and the $Ce_{0.5}Zr_{0.5}O_{2-\delta}$ samples calcined at various temperatures under flow of air unless otherwise stated, synthesised via both the sol-gel and solvothermal methods (with an intermediate re-oxidation (TPO) at 600 °C).

Table 29: Summary of results from TPR of the AM01 reference materials and the $Ce_{0.5}Zr_{0.5}O_{2-\delta}$ samples calcined at various temperatures under flow of air unless otherwise stated, synthesised via both the sol-gel and solvothermal methods. T_{max} corresponds to the temperature at which the maximum of H_2 uptake occurs.

Sample	First TPR (Total Ce^{4+} reduced / %)	Second TPR (Total Ce^{4+} reduced / %)	First TPR T_{max} (°C)	Second TPR T_{max} (°C)
AM01-SRMO	86	N/A	545	N/A
AM01	70	N/A	553	N/A
AM01 Fired at 1150 °C (5% H_2/N_2)	86	89	607	604
Solvothermal method				
Fired at 1150 °C (5% H_2/N_2)	92	98	576	393
Fired at 1150 °C (N_2)	65	65	665	380
Fired at 1000 °C	49	52	552	430
Fired at 700 °C	66	69	550	523
Sol-gel method				
Fired at 1000 °C	52	64	587	436
Fired at 700 °C	59	59	581	524

5.7 Conclusions

In conclusion three methods using alkoxide starting reagents have successfully been able to synthesis the ordered *k*-$Ce_2Zr_2O_8$ phase without the use of reducing gases. Presumably due to the homogeneous mixing of the Ce-Zr cations in the liquid phase for the sol-gel method. For the solvothermal methods, the incorporation of a larger

quantity of Ce^{3+} cations, 'pre-reduces' the sample compared with conventional synthesis which aids that method in the formation of the *k*-$Ce_2Zr_2O_8$ phase at lower temperature in comparison to the sol-gel method.

References

1. M. Yashima, H. Arashi, M. Kakihana and M. Yoshimura. (1994). Raman scattering study of cubic-tetragonal phase transition in $Zr_{1-x}Ce_xO_2$ solid solution. *Journal of the American Ceramic Society*. 77 (4), p1067-1071.
2. S. Otsuka-Yao-Matsuo, T. Omata, N. Izu and H. Kishimoto. (1998). Oxygen Release Behavior of $CeZrO_4$ Powders and Appearance of New Compounds k and t*. *Journal of Solid State Chemistry*. 138, p47-54.
3. V.P. Kolko, D.A. Zyuzin, V.A. Sadykov, V.V. Kriventsov and E.M. Moroz. (2007). Structure of the mixed oxides $Me_x(Ce_{0.5}Zr_{0.5})_{1-x}O_y$ (Me= Gd, Pr). *Glass Physics and Chemistry*. 33 (4), p335-339.
4. R. Jimenez, W. Bucheli, A. Varez and J. Sanz. (2011). Humidity related low temperature conductivity hysteresis of $Ce_{1-x}Zr_xO_2$. *Fuel Cells.* 11 (5), p642-653.
5. A. Varez, E. Garcia-Gonzalez, J. Jolly and J. Sanz. (2007). Structural characterization of $Ce_{1-x}Zr_xO_2$. *Journal of the European Ceramic Society*. 27, p3677-3682.
6. S. Urban, P. Dolcet, M. Moller, L. Chen, P.J. Klar, I. Djerdj, S. Gross, B.M. Smarsly and H. Over. (2016). Synthesis and full characterization of the phase-pure pyrochlore $Ce_2Zr_2O_7$ and the κ-$Ce_2Zr_2O_8$ phases. *Applied Catalysis B: Environmental*. 197, p23-34.
7. H. Kishimoto, T. Omata, S. Otsuka-Yao-Matsuo, K. Ueda, H. Hosono and H. Kawazoe. (2000). Crystal structure of metastable kappa-($CeZrO_4$) phase possessing an order arrangement of Ce and Zr ions. *Journal of Alloys and Compounds*. 312, p94-103.

6. Exploratory synthesis of new cerium oxide materials

6.1 Cerium aluminium oxides

6.1.1 Introduction

In this chapter, the aim was to explore using solvothermal chemistry to prepare new forms of ceria or new cerium oxides. The first target was substitution of aluminium into cerium dioxide via hydrothermal synthesis, in the targeted form of $Ce_{1-x}Al_xO_{2-\delta}$. There are lots of papers about incorporating trivalent cations in ceria to introduce oxide defects, and these are usually lanthanides. It would be interesting to include much smaller trivalent cations so to distort the structure and hence introduce more strain that may lead to enhanced oxide ion diffusion. Hydrothermal synthesis has already been used to introduce unusual metal cations into ceria, so this may provide a method to include small cations such as Al^{3+}. A study of the materials was undertaken using several techniques to determine the local environment of the Al. Furthermore, the redox and thermal properties of the oxides were explored under varying levels of Al substitutions and humidity conditions, to determine any influences from the presence of aluminium.

6.1.2 Hydrothermal synthesis

Aluminium nitrate nonahydrate ($Al(NO_3)_3 \cdot 9H_2O$, 1.2 mmol) and cerium nitrate hexahydrate ($Ce(NO_3)_3 \cdot 6H_2O$, 2.8 mmol) were used as starting reagents. Both precursors were ground with a pestle and mortar and measured using an analytical balance and transferred into a Teflon autoclave liner (20 ml). Sodium hydroxide (10 M, 8 ml) was measured and was transferred into the Teflon liner. A magnetic stirrer was placed inside the liner, which was covered with a lid and placed on a stirring plate and was left to stir for a period of 3 hours. This was followed by sealing the Teflon liner in a steel autoclave and transferring it into a pre-heated oven set at 240 °C for 96 hours. The mixture was filtered using a Büchner funnel and flask under vacuum pump suction. The solid was placed within a drying oven (70 °C) overnight and ground in a pestle and mortar prior to analysis.

The above procedure was repeated using quantities totalling 4 mmol of the cerium and aluminium nitrates according to desired target ratios, to produce $Ce_{1-x}Al_xO_{2-\delta}$ ($0 \leq x \leq 0.5$) as the final product.

6.1.2.1 Humidity controlled conditions

$Ce_{0.7}Al_{0.3}O_{2-\delta}$ samples were synthesised using the hydrothermal method as described in section 6.1.2, and then subjected to the following listed conditions prior to analysis. Preliminary characterisation suggested that the Al may be on the surface of the materials and hence influenced by the surrounding conditions, so the aim to investigate the effect of humidity.

6.1.2.1.1 Fresh sample

The cerium aluminium oxide reaction was timed to complete the reaction the day before the TPR analysis and stored in a glass vial (10 ml).

6.1.2.1.2 Dry sample

Calcium oxide (CaO, 2 g) was transferred into a centrifuge tube (50 ml) and a fresh sample of cerium aluminium oxide was suspended over the solid within the tube in a glass vial (5 ml) and sealed.

6.1.2.1.3 50% Humidity

Magnesium nitrate ($Mg(NO_3)_2 \cdot 9H_2O$, 2 g) was transferred into a centrifuge tube (50 ml) a small quantity of distilled water was added to form a slurry in order to create a saturated salt solution. Cerium aluminium oxide was suspended over the salt solution within the tube in a glass vial (5 ml) and tube was then sealed.

6.1.2.1.4 90% Humidity

The same procedure as described in section 6.1.2.3 was applied using potassium sulfate (K_2SO_4, 2 g) as the salt.

6.1.2.1.5 Aged sample

The cerium aluminium oxide reaction was timed to complete the reaction the 5 days prior to the TPR analysis and stored in a glass vial (10 ml).

6.1.3 Powder XRD

The powder XRD patterns of $Ce_{1-x}Al_xO_{2-\delta}$ can be indexed and the profile fitted to a cubic fluorite cell (space group: $Fm\bar{3}m$) within the range $0.1 \leq x \leq 0.5$. The XRD patterns show that the lattice parameter of all five of the samples don't show any trend upon increasing Al content (Figure 102). This suggests that Al hasn't been substituted for Ce, as the ionic radius range of Al^{3+} (0.39 – 0.535 Å) is nearly half

the size of Ce^{4+} (0.97 Å) so the expected trend would be a larger contraction of the ceria lattice.

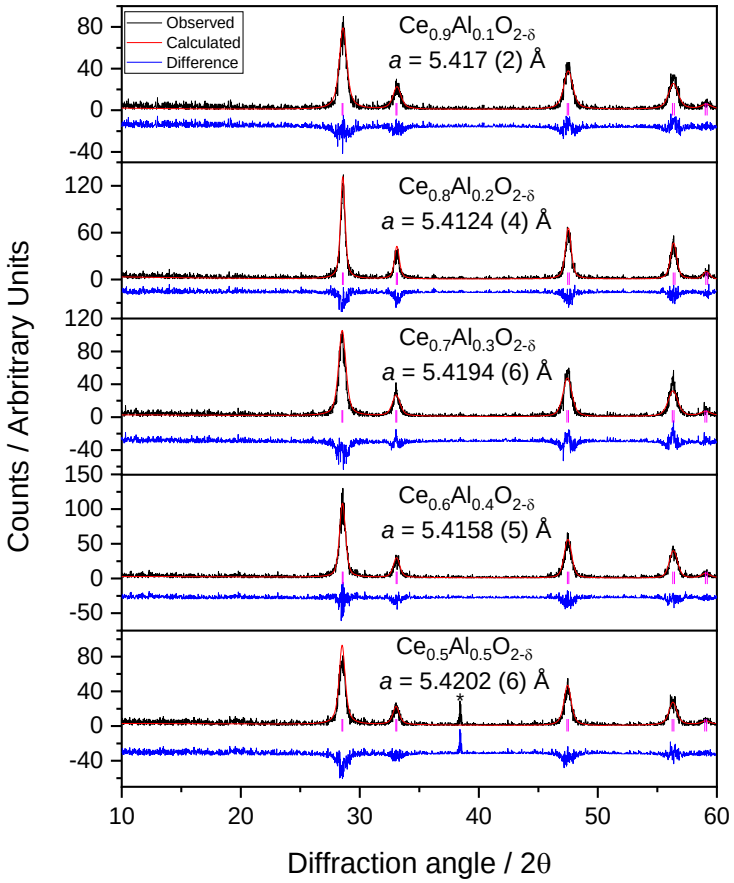

*Figure 102: Le Bail fits to Powder XRD data (λ = 1.5405 Å) of $Ce_{1-x}Al_xO_{2-\delta}$ ($0.1 \leq x \leq 0.5$). (*Indicates aluminium sample holder peaks).*

6.1.4 Further characterisation

^{27}Al solid-state NMR is a useful tool for analysing the local co-ordination of aluminium as the chemical sift of ^{27}Al is sensitive to the aluminium's geometry. The majority of observable nuclei is constituted by nuclides with a spin of least a half, and aluminium a spin of $I = 5/2$. ^{27}Al solid-state NMR was used to determine the presence of aluminium and the local environment of the aluminium present. The interaction of the quadrupole moment with the electronic surroundings of the nucleus tends to dominate the NMR spectrum, because of the strong overlap between the various resonances, since it's usually the second largest interaction after the fundamental Zeeman interaction. The NMR spectra for the $Ce_{0.8}Al_{0.2}O_{2-\delta}$ sample

(Figure 103(a)) contains aluminium co-ordinated in multiple co-ordination states (AlO_4, AlO_5 and AlO_6). The acquisition of the NMR spectra required an extended period of time to collect, also implying that the target aluminium content was not achieved. Repeating the NMR spectral acquisition (Figure 103(b)) after one months' time showed that the aluminium co-ordination changed to be predominantly pentavalent (32 ppm) with a distribution of quadrupolar broadening parameters and a small quantity of hexavalent aluminium (-2 ppm). The powder XRD pattern remained unchanged however, suggesting that the aluminium is mobile or easily hydratable and has not been incorporated in the ceria lattice.

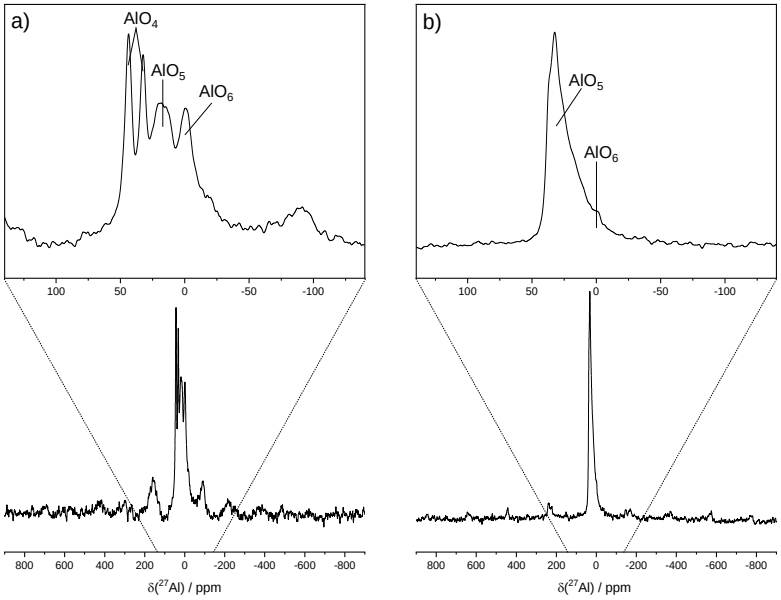

Figure 103: ^{27}Al solid-state nuclear magnetic resonance spectrum of $Ce_{0.8}Al_{0.2}O_{2-\delta}$ a) sample as-made b) the same sample left in air for a period of one months' time.

The ^{27}Al solid-state NMR was repeated using a $Ce_{0.5}Al_{0.5}O_{2-\delta}$ sample (Figure 104(a)) as it was expected to contain more Al. The NMR spectra, contrary to the $Ce_{0.8}Al_{0.2}O_{2-\delta}$ sample contains pentavalent aluminium in two states, one more crystalline than the other. After this NMR acquisition of the sample was conducted and finished the sample was placed inside a glovebox for 57 days. The NMR spectra of the same sample was re-measured (Figure 104(b)) and again as above the aluminium geometry changed, providing further evidence of its surface mobility.

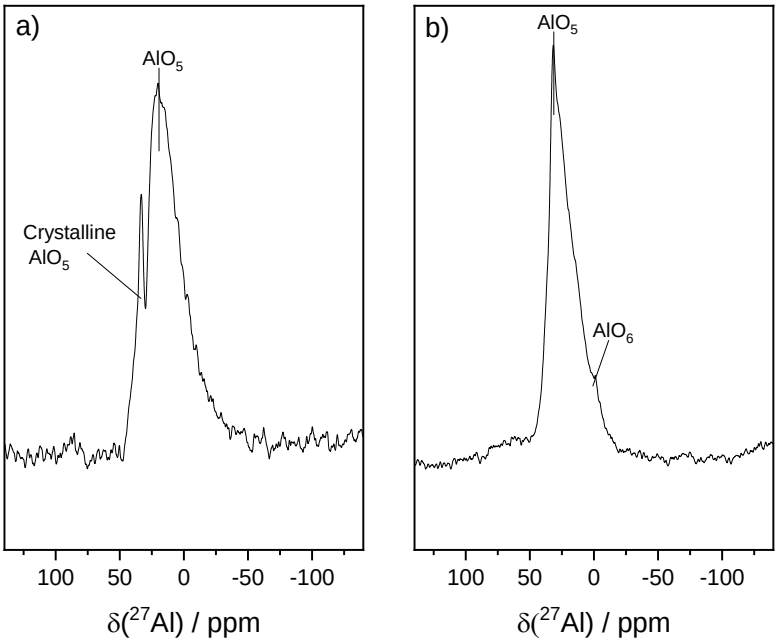

Figure 52: ^{27}Al solid-state nuclear magnetic resonance spectrum of $Ce_{0.5}Al_{0.5}O_{2-\delta}$ a) sample as-made b) the same sample left under N_2 within a glovebox for a period of 57 days.

The Raman spectra (Figure 105) of HSA (high surface area) CeO_2 shows one broad band centred at around 460-465 cm^{-1}, attributed to the F_{2g} Raman mode induced by O-Ce-O symmetric stretching vibrations characteristic of cubic ceria. The $Ce_{0.7}Al_{0.3}O_{2-\delta}$ samples show no displacement in the Raman shift upon the addition of aluminium, again suggesting that the aluminium hasn't been incorporated into the ceria lattice, as this lattice mode is sensitive to any defects/disorder present in the oxygen sublattice.

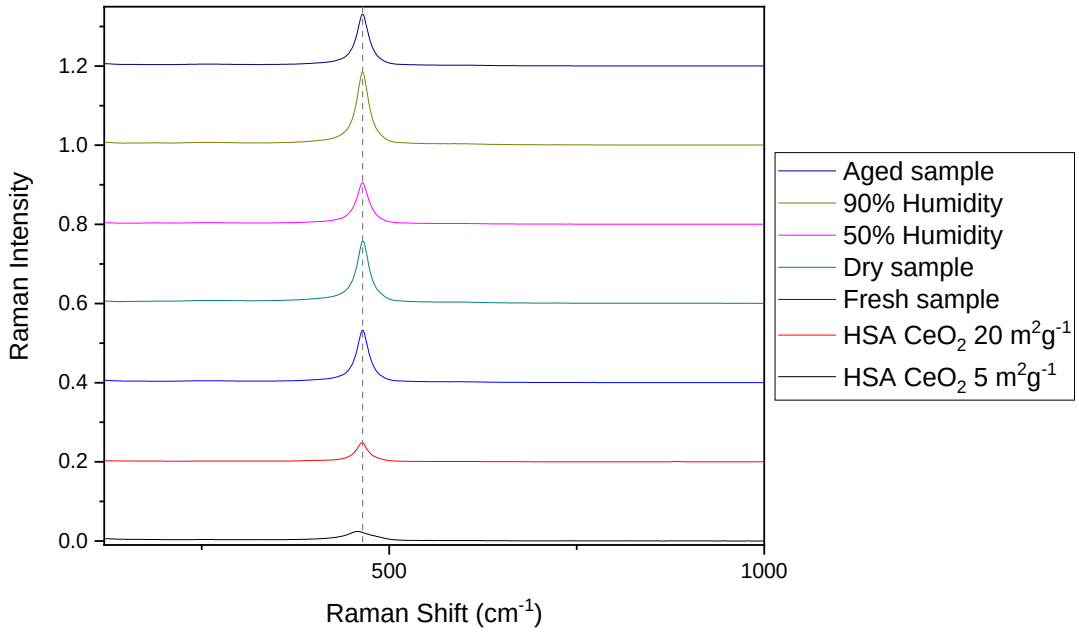

Figure 53: Raman spectra of reference HSA CeO_2 materials compared against the $Ce_{0.7}Al_{0.3}O_{2-\delta}$ samples subjected to varying levels of humidity's.

6.1.5 Temperature programmed reduction/oxidation (TPR/TPO)

Temperature programmed reduction measurements were conducted on a series of $Ce_{1-x}Al_xO_{2-\delta}$ ($0 \leq x \leq 0.5$) samples (Figure 106) to evaluate any surface redox properties the materials might have due to the presence of the aluminium on the surface. In comparison to the CeO_2 produced by a conventional method, the aluminium samples showed improved catalytic activity attributed to the surface reduction of the materials. The aged samples in comparison with the fresh samples, showed a second lower temperature surface reduction peak at 350 °C.

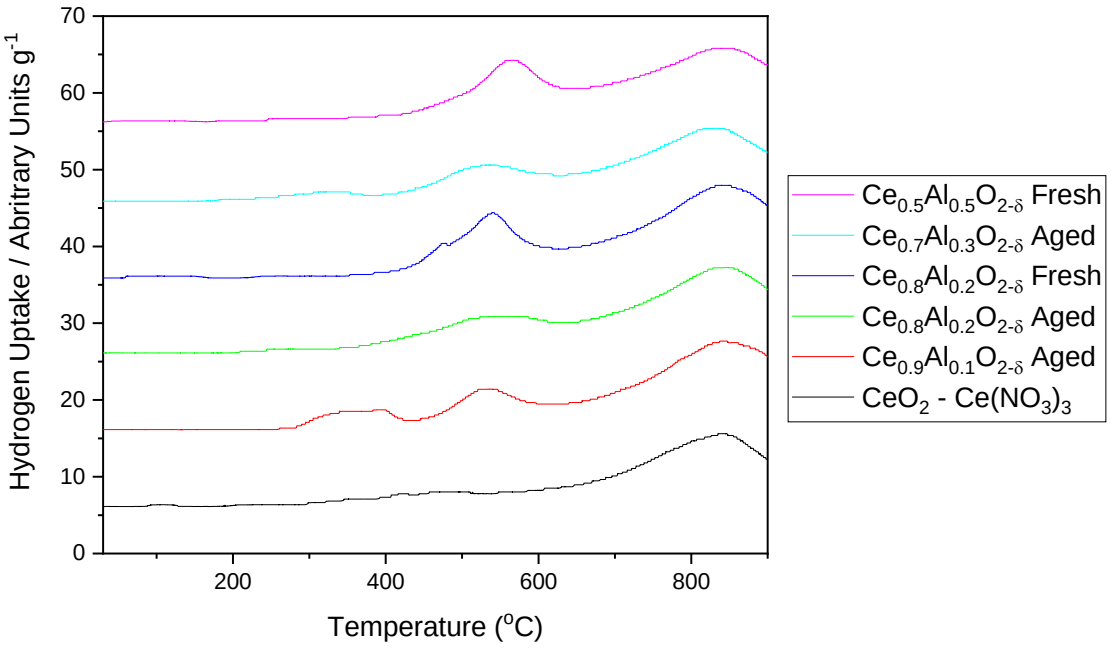

Figure 54: Temperature programmed reduction spectrum of $Ce_{1-x}Al_xO_{2-\delta}$ ($0 \leq x \leq 0.5$).

Temperature programmed reduction measurements were conducted on a series of $Ce_{0.7}Al_{0.3}O_{2-\delta}$ samples (Figure 107) subjected to different humidity conditions. The first TPR measurement for all the sets of data was limited to 600 °C to assess whether increased surface reduction could be re-activated for cycling if the materials were sintered at high temperatures (900 °C). The first TPR measurements (Figure 107) on the cerium aluminium oxides have a relatively large surface reduction at less than 600 °C in comparison to pure CeO_2.The freshly prepared samples show a lower temperature surface reduction (~400 °C) than the samples subjected to longer and higher levels of humidity. After the second reduction cycle it can be observed that a minimal amount of the surface reduction is still retained. This is probably due to the sintering of the ceria particles, and hence the addition of aluminium does not dramatically increase the stability of ceria at high temperatures. However, exposing the samples to different conditions changes their first TPR profiles, which is consistent with the solid-state NMR that suggests mobile and/or hydratable Al at the surface.

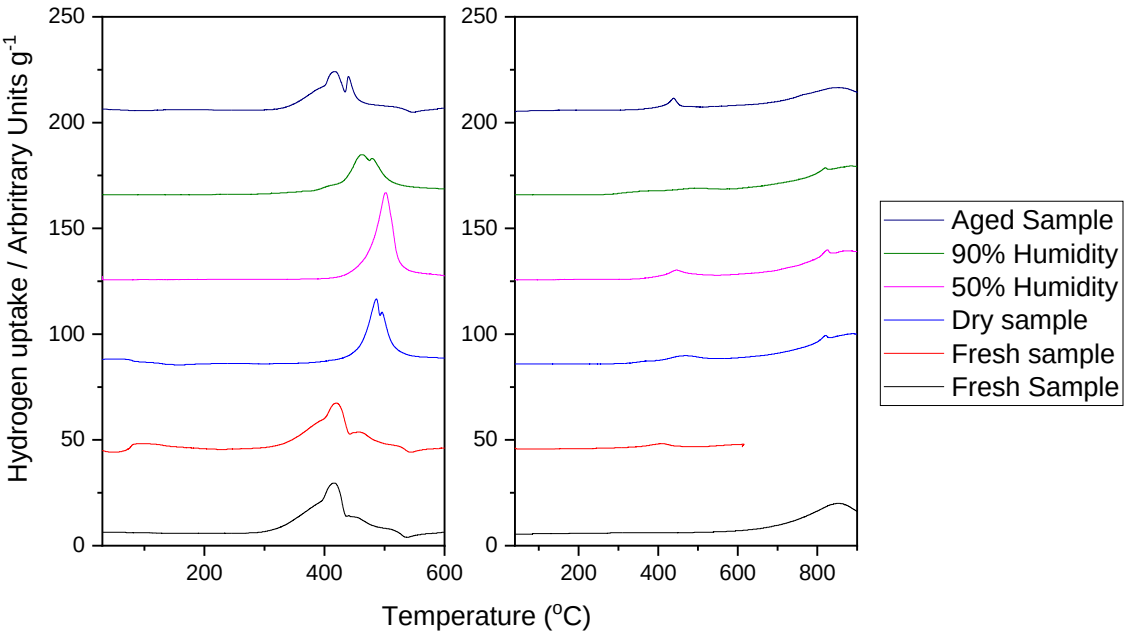

Figure 55: Sequential TPR profiles of $Ce_{0.7}Al_{0.3}O_{2-\delta}$ subjected to varied controlled humidity's (with an intermediate re-oxidation (TPO) at 600 °C).

6.1.6 Conclusions

In this section it has been shown that the substitution of aluminium into the CeO_2 fluorite structure is not possible by a hydrothermal method that has been used for other metal substitutions. The aluminium is however present in a small quantity on the surface of the materials. Changes in atmospheric moisture enables transitions in aluminium co-ordination to transpire as confirmed by ^{27}Al solid state NMR. These changes in humidity levels and hence aluminium co-ordination has a direct result on the materials measured TPR profiles, increasing the surface reduction of CeO_2. Unfortunately, the increased surface reduction is lost after repeat measurements.

6.2 Black ceria

6.2.1 Introduction

This section's focal point is not on the incorporation of other metal cations, but purely on the colour of the products formed from using an ethyl acetate: H_2O mixture in a solvothermal reaction. Typically, CeO_2 is pale yellow/white in colour, however it is shown here that under certain reaction conditions the colour of the product is dark blue/black. Similar types of materials have been synthesised recently in the form of $TiO_{2-\delta}$ by creating surface oxygen vacancies and/or defects via either chemical reduction, [1-2] H_2 reduction [3-4] and hydrothermally. [5] These materials

have shown to possess improved photocatalytic activity which is a desirable property for applications such as H_2 water splitting.

6.2.2 Solvothermal synthesis

Cerium nitrate hexahydrate ($Ce(NO_3)_3 \cdot 6H_2O$, 2 mmol) was ground with a pestle and mortar and weighed using an analytical balance and transferred into a Teflon liner (20 ml). A 50% v/v mixed solution (8 ml) of water and ethyl acetate was measured using a measuring cylinder (10 ml) and was transferred into the Teflon liner. A magnetic stirrer was placed inside the liner and was left to stir for a period of 3 hours. This was followed by sealing the Teflon liner in a steel autoclave and transferring it into a pre-heated oven set at 240 °C for 96 hours. The mixture was filtered using a centrifuge tube (50 ml) in combination with a centrifuge rotating at 40,000 rpm for 10 minutes. The centrifugation was repeated after washing the solid sample with fresh distilled water (30 ml) twice. The solid coated centrifuge tube was placed within a drying oven (70 °C) overnight and the solid was transferred and ground in a pestle and mortar prior to analysis.

6.2.3 Solvothermal control reactions

The same solvothermal synthesis as described in section 6.2.2 was applied using gallium nitrate hydrate ($Ga(NO_3)_3 \cdot nH_2O$, 2 mmol) or titanium isopropoxide ($Ti[OCH(CH_3)_2]_4$, 2 mmol) in place of cerium nitrate.

6.2.3 Powder XRD

The solvothermal reaction of cerium nitrate in an ethyl acetate – water (50:50) mixture produces a dark blue/ black coloured highly crystalline sample of CeO_2 confirmed by XRD. The dark colour could be due to the presence of Ce^{3+} and/or organics on the surface of the particles. Another possibility is carbonate incorporation as reported by others for TiO_2 [6] which changes the band gap and gives the material a dark colour. The interesting aspect of this material is the colour as usually ceria has a yellow/white appearance.

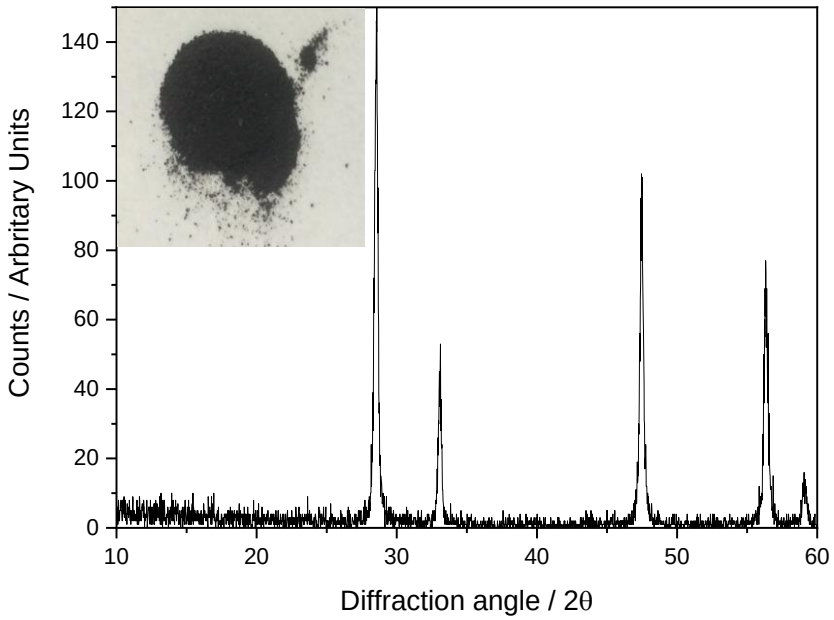

Figure 568: Powder XRD pattern of CeO_2 formed from the solvothermal synthesis in ethyl acetate: H_2O and the photograph of the material produced.

Control reactions were conducted to investigate if same phenomenon occurred within other metal oxides that are known to have a white/pale colour. As mentioned in section 6.2.1 TiO_2 can be adopt non-stoichiometry and can adsorb carbonate species but applying this synthetic procedure to titanium isopropoxide produces anatase with an observed yellow colour.

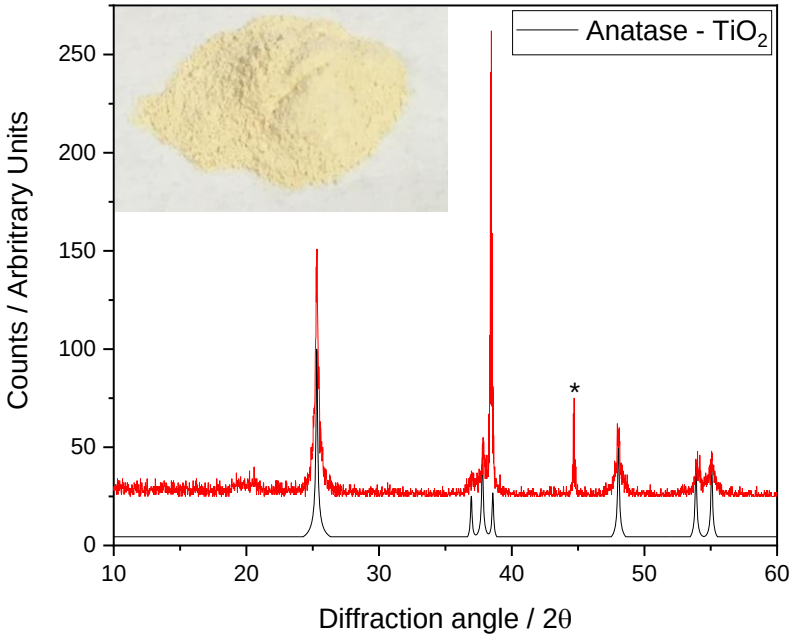

Figure 57: Powder XRD pattern of TiO_2 formed from the solvothermal synthesis in ethyl acetate: H_2O and the photograph of the material produced. The powder pattern is compared against one taken from literature. [7] *(*Indicates aluminium sample holder peaks).*

The solvothermal reaction of gallium nitrate in an ethyl acetate – water (50:50) mixture produces a white coloured crystalline sample of monoclinic β-Ga_2O_3 confirmed by XRD. β-Ga_2O_3 is the most stable of the gallium oxide polymorphs (α-, γ-, δ-, and ε-Ga_2O_3), all of which can be ultimately transformed into β-Ga_2O_3 through calcination. [8] The formation of this polymorph under solvothermal conditions, is another interesting use of these experimental parameters.

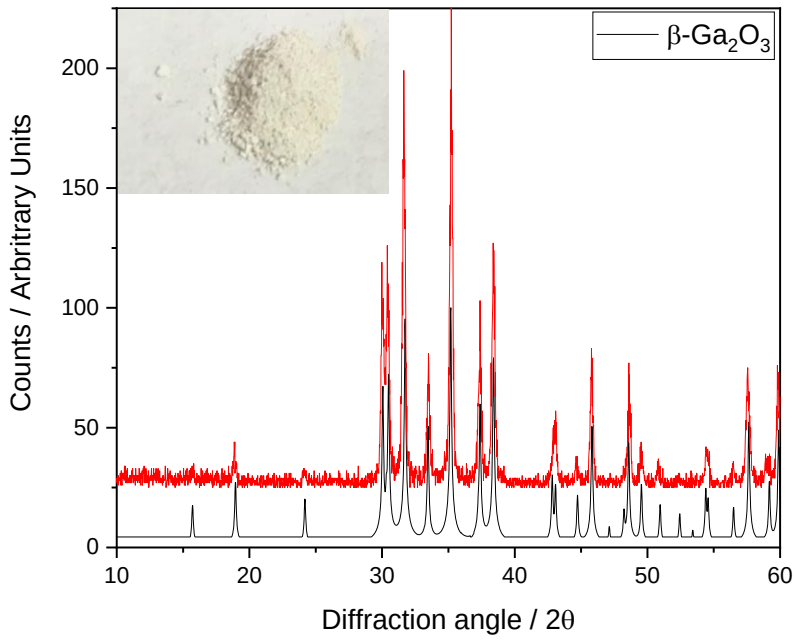

Figure 58: Powder XRD pattern of β-Ga_2O_3 formed from the solvothermal synthesis in ethyl acetate: H_2O and the photograph of the material produced. The measured powder pattern is compared against one taken from literature. [9]

6.2.4 Further characterisation

The FT-IR spectra of ethyl acetate contains characteristic bands at ca. 1732 cm^{-1} (C = O stretch), and at 1042 and 1233 cm^{-1} for the C – O stretches. The FT-IR spectra comparison of black ceria against CeO_2 (Figure 111) shows that the black ceria sample does contain extra stretching vibrations in comparison to the conventionally synthesised ceria. The most prominently band being observed at ca. 1071 cm^{-1}, possibly suggesting the preservation of the C – O stretch.

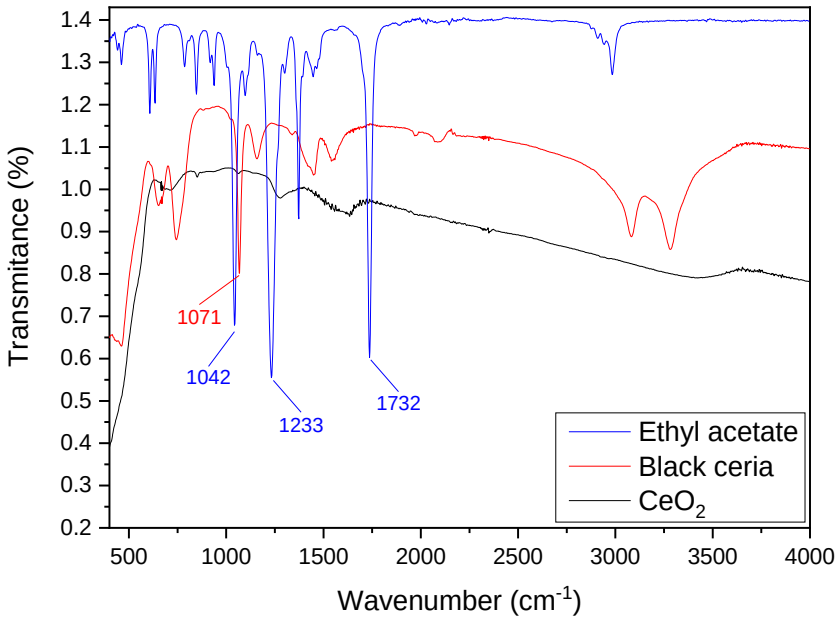

Figure 59: FT-IR spectrum of black compared against CeO_2 and ethyl acetate.

The TGA spectra of the black ceria (Figure 112) shows a 3.3% greater mass loss than CeO_2 and doesn't plateau up to 1000 °C. The increased mass difference between samples suggests that more surface absorbents are being desorbed suggesting the black colour is due to surface organics. This is further emphasised by the fact that the black colour is lost upon heating to higher temperatures.

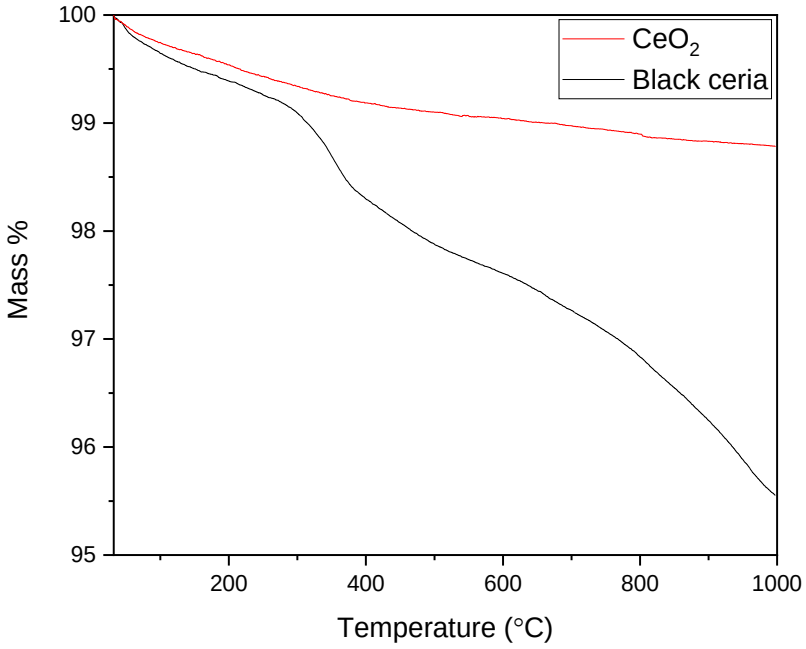

Figure 60: Thermogravimetric analysis of CeO_2 and black ceria.

The TEM micrograph of the black ceria sample (Figure 113) shows that morphology of the material is cuboidal, with sizes ranging in the 10-100 nm region.

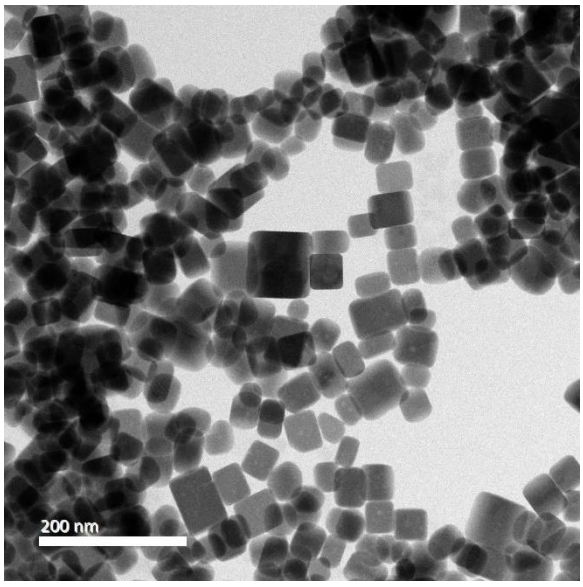

Figure 61: TEM micrograph of the black ceria sample.

6.2.5 X-ray absorption spectroscopy (XAS)

6.2.5.1 CeL_{III}-edge XANES

The comparison of the XANES spectrum of black ceria (Figure 114) with the Ce reference compounds shows that the material contains cerium predominantly +4 oxidation state. Therefore, the black/blue colour of the material isn't due to the presence of large amounts of Ce^{3+}, for example, on the surface as confirmed by XPS.

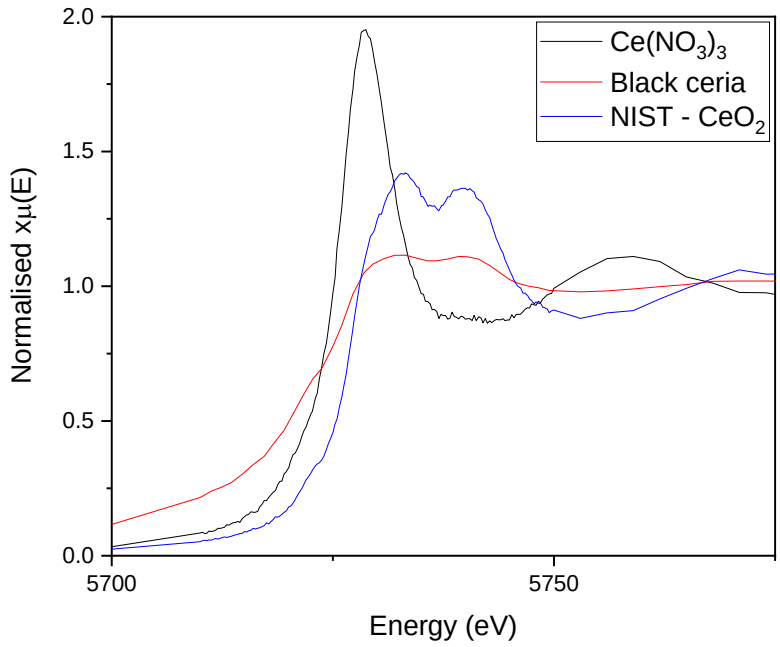

Figure 62: Normalised Ce L_{III}-edge XANES spectra of black ceria compared against reference compounds with known Ce oxidation states ($Ce(NO_3)_3$ and NIST-CeO_2).

6.2.6 Temperature programmed reduction/oxidation (TPR/TPO)

The temperature programmed oxidation of the black ceria (Figure 115) shows a large consumption of oxygen between 180 – 420 °C. The uptake is larger than the calibration peak of 1 ml min^{-1} suggesting that there is a substantial desorption of the organic species from the surface of the material.

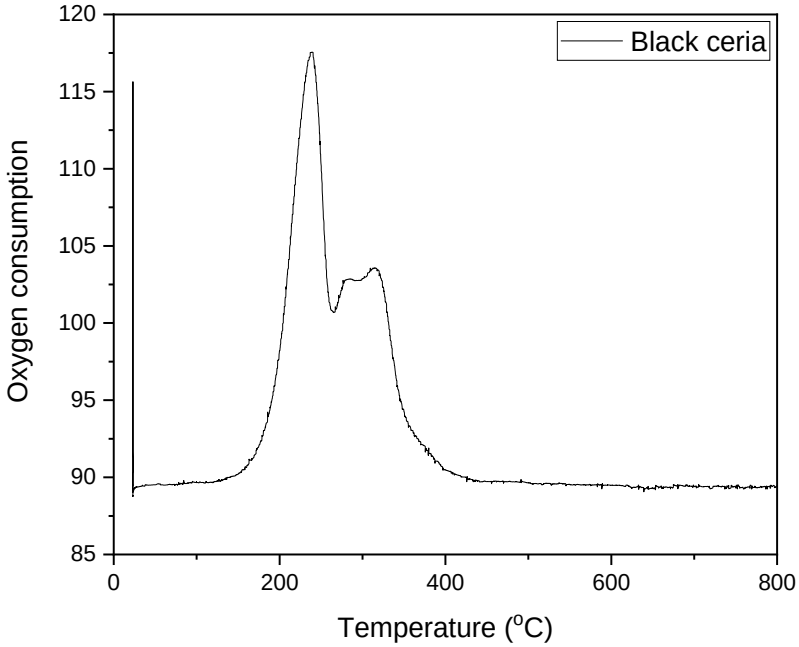

Figure 63: Temperature programmed oxidation of black ceria.

6.2.7 Conclusion

In this chapter a novel solvothermal approach was developed for forming an atypical, darkly coloured ceria sample. Ce L_{III}-edge XANES confirmed that the black colour was not due the presence of Ce^{3+} within the sample inducing non-stoichiometry ($CeO_{2-\delta}$). The TPO and FT-IR measurements provide evidence towards to the black colour of the materials being attributed to surface absorbed organics.

References

1. X. Zou, J. Liu, J. Su, F. Zuo, J. Chen and P. Feng. (2013). Facile Synthesis of Thermal- and Photostable Titania with Paramagnetic Oxygen Vacancies for Visible-Light Photocatalysis. *Chemistry – A European Journal*. 19 (8), p2866-2873.
2. S. Tominaka, Y. Tsujimoto, Y. Matsushits and K. Yamaura. (2011). Synthesis of Nanostructured Reduced Titanium Oxide: Crystal Structure Transformation Maintaining Nanomorphology. *Nanomaterials*. 50, p7418-7421.
3. X. Liu, S. Gao, H. Xu, Z. Lou, W. Wang, B. Huang and Y. Dai. (2013). Green synthetic approach for Ti^{3+} self-doped TiO_{2-x} nanoparticles with efficient visible light photocatalytic activity. *Nanoscale*. 5, p1870-1875.
4. A. Naldoni, M. Allieta, S. Santangelo, M. Marelli, F. Fabbri, S. Cappelli, C.L. Bianchi, R. Psaro and V.D. Santo. (2012). Effect of Nature and Location of Defects on Bandgap Narrowing in Black TiO_2 Nanoparticles. *Journal of the American Chemical Society*. 134 (18), p7600-7603.

5. H. Lu, B. Zhao, R. Pan, J. Yao, J. Qiu, L. Luo and Y. Liu. (2014). Safe and facile hydrogenation of commercial Degussa P25 at room temperature with enhanced photocatalytic activity. *Royal Society of Chemistry Advances*. 4, p1128-1132.
6. S. Chen, Y. Xiao, Y. Wang, Z. Hu, H. Zhao and W. Xie. (2018). A Facile Approach to Prepare Black TiO_2 with Oxygen Vacancy for Enhancing Photocatalytic Activity. *Nanomaterials*. 8 (4), p245-261.
7. S. Geller. (1960). Crystal Structure of β-Ga_2O_3. *The journal of Chemical Physics*. 33 (3), p676-684.
8. R. Roy, V.G. Hill and E.F. Osborn. (1952). Polymorphism of Ga_2O_3 and the system Ga_2O_3-H_2O. *Journal of the American Chemical Society*. 74 (3), p719-722.
9. M. Horn, C.F. Schewerdtfeger and E.P. Meagher. (1972). Refinement of the structure of anatase at several temperatures. *Zeitschrift für Kristallographie*. 136, p273-281.
10. B. Liu, L. Liu, X. Lang, H. Wang, X. Lou and E.S. Aydil. (2014). Doping high-surface-area mesoporous TiO_2 microspheres with carbonate for visible light hydrogen production. *Energy and Environmental Science*. 7, p2592-2597.

7. Overall conclusions and future work

The previous four chapters have discussed the substitution of Ce for various other cations via novel synthetic routes. The chapters focus on the characterisation of the materials and the subsequent catalytic property testing of selected materials. The study illustrates the impact and influence the starting reagents and preparative techniques have on the structure and characteristics of the resultant mixed metal oxides.

7.1 Understanding the crystallisation mechanisms involved in the synthesis of cerium bismuth oxides

Four different $Ce_{0.5}Bi_{0.5}O_{2-\delta}$ samples were hydrothermally synthesised from a combination of starting reagents with different oxidation states. The choice of starting reagents has implications on the reaction time to form and affects the crystallite size of the final products. The $Ce_{0.5}Bi_{0.5}O_{2-\delta}$ samples with the lower crystallite size and larger surface areas were derived from the use of $Ce(NH_4)_2(NO_3)_6$. It was recognized that the cubic structure of $Ce_{0.5}Bi_{0.5}O_{2-\delta}$ was formed via the formation of α-Bi_2O_3 before the inclusion into CeO_2. Further X-ray diffraction measurements using the Oxford-Diamond in situ cell (ODISC) at different reaction temperatures and concentrations. In order to perform additional Rietveld refinements to study the transformation kinetics of the starting reagents into the final crystalline mixed oxides.

7.2 Solvothermal synthesis of lanthanide-substituted $Ce(OH)_2Cl$ and $Ce(OH)CO_3$ and their thermal decomposition to mixed-metal oxides

The solvothermal reaction of $CeCl_3$ in PEG yields a previously unreported material. Collecting high resolution X-ray diffraction data at a synchrotron of the $Ce(OH)_2Cl$ and also the synthesised $Ce(OH)CO_3$ sample would be advantageous in refining the structures. Solvothermal synthesis of an extended series of $Ce_{1-x}Ln_x(OH)_2Cl$ and $Ce_{1-x}Ln_x(OH)CO_3$ (Ln = La, Gd, Pr and Tb) materials was achieved by simply altering the lanthanide starting reagent ($LnCl_3 \cdot nH_2O$/$Ln(NO_3)_3 \cdot nH_2O$) and the molecular weight of the polymer (Mn_{200} or Mn_{400}). Lanthanide substitution of up to 50% was achieved for each lanthanide apart from lanthanum, high resolution X-ray diffraction data would aid in indexing the pure sample produced from $LaCl_3$ in PEG. The thermal decompositions of the mixed materials allow for the formation of lanthanide substituted cerium oxide ($Ce_{1-x}Ln_xO_{2-\delta}$) with unique morphologies. XANES revealed that the thermal decomposition of $Ce_{1-x}Ln_x(OH)_2Cl$ (Ln = Pr and Tb) at 700 °C produces oxides that contain both +4 and +3 oxidation states of the substituted lanthanide. Probing different calcination temperatures and subsequent XANES and TPR measurements on the Pr and Tb samples would be beneficial to look at how controllable and the effects of a larger quantity of Ln^{3+} has on the reducibility of the materials.

7.3 Structural analysis of cerium zirconium oxides synthesised via solvothermal and precipitation methods

Three methods using alkoxide starting reagents have successfully been able to synthesise the ordered k-$Ce_2Zr_2O_8$ phase without the use of reducing gases. XANES measurements revealed that the solvothermal method of synthesis produces materials that contain a larger quantity of Ce^{3+}. Removing the oxygen from the autoclave by performing the reaction in the glovebox is presumed to permit further reduction of cerium, hence enabling the formation of the pyrochlore phase at lower calcination temperatures. Conducting further XANES measurements would be advantageous as it would provide information about the differences in cerium oxidation states between the two solvothermal methods. The recorded Raman spectra and X-ray diffraction patterns show that both the sol-gel and solvothermal methods can synthesise the ordered k-$Ce_2Zr_2O_8$ phase under N_2 contrary to AM01 which phase segregates. The speculation proposed for the solvothermal methods is that it ‘pre-

reduces' the cerium cations thereby eliminating the requirement for the H_2 reduction step in the conventional method. The formation of the k-$Ce_2Zr_2O_8$ phase using the sol-gel method is speculated to be from greater homogeneity of the Ce-Zr cations due to the mixing in the liquid state, and hence reducing the sample under 5% H_2/N_2 has an adverse effect on the cationic ordering in comparison to under N_2. In order to better understand the structural differences between the kappa and pyrochlore phase produced via each synthesis method, high-resolution electron microscopy and compositional analysis would be beneficial techniques to implement. The techniques will help to develop a bettering understanding of the disorder-order transition in the cation sublattice of these oxides in correlation to the synthesis method utilized. Other further work would include reperforming the synthesise using other alkoxide starting reagents to identify any markable difference in structure or calcination temperature required to reduce the Ce-Zr oxide to the pyrochlore phase under N_2 gas. Research into the synthesis of the alkoxide starting reagents from scratch also would serve to affect commercial viability as the cost of buying pre-made alkoxides is expensive.

7.4 Exploratory synthesis of new cerium oxide materials

The substitution of aluminium into the CeO_2 fluorite structure was not found to be possible via the tested hydrothermal methods discussed in the chapter. The aluminium was discovered to be present in a small quantity on the surface of the materials. Performing ICP-OES on the aluminium samples would determine how much aluminium is present on the surface of the materials.

A novel solvothermal approach was developed for forming an atypical, darkly coloured ceria sample. Performing ICP-OES on the black ceria sample would aid in the identification of the apparent surface absorbed organics. Testing the photocatalytic activity of the black ceria sample under visible light irradiation, would assess the material for any commercial applications.

8. Appendix

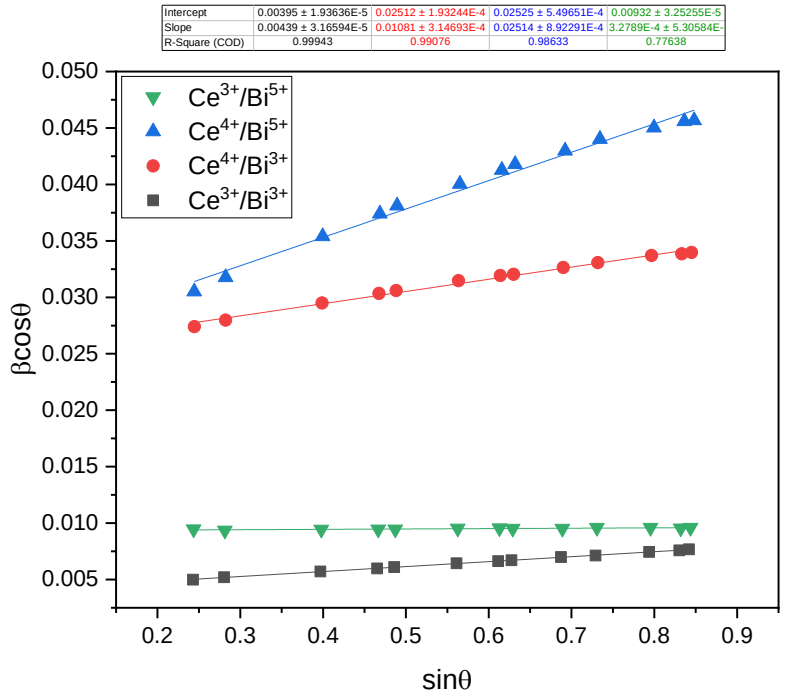

Figure 6416: Williamson-Hall plot of the $Ce_{0.5}Bi_{0.5}O_{2-\delta}$ samples as-prepared at 240°C for 96 hours.

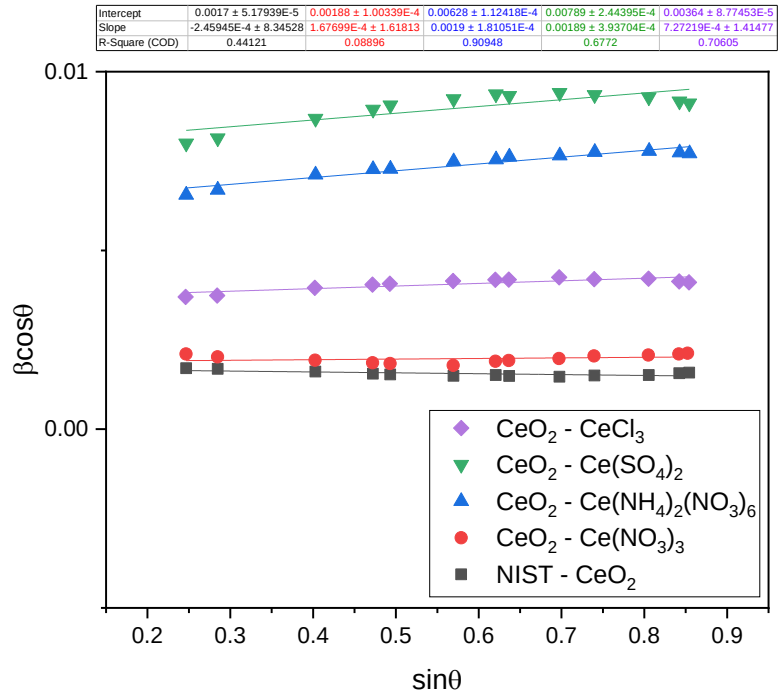

Figure 117: Williamson-Hall plot of the CeO_2 samples as-prepared at 240°C for 96 hours.

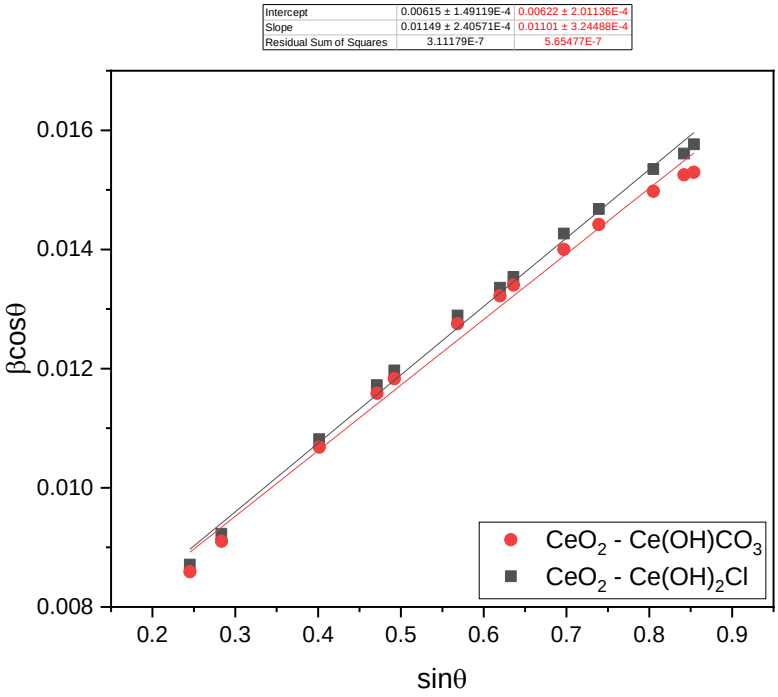

Figure 118: Williamson-Hall plot of the $Ce(OH)_2Cl$ and $Ce(OH)CO_3$ after thermal decomposition to CeO_2.

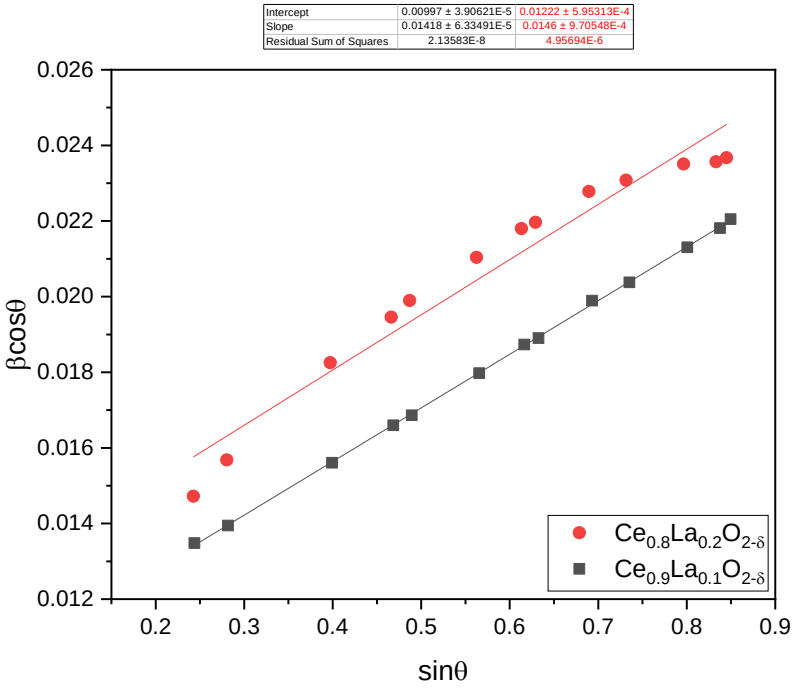

Figure 119: Williamson-Hall plot of the $Ce_{1-x}La_xO_{2-\delta}$ ($0.1 \leq x \leq 0.2$) samples after thermal decomposition of $Ce_{1-x}La_x(OH)_2Cl$.

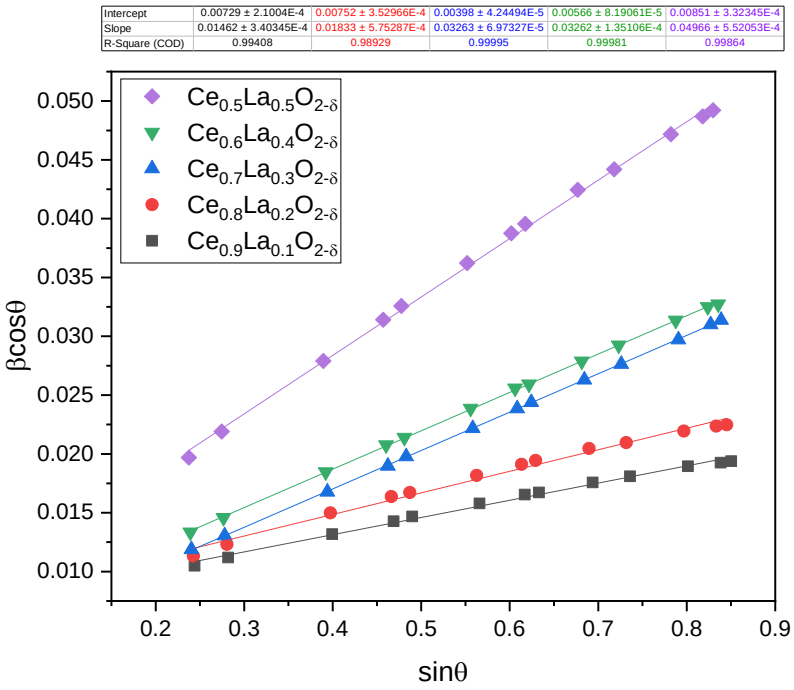

Figure 120: Williamson-Hall plot of the $Ce_{1-x}La_xO_{2-\delta}$ ($0.1 \leq x \leq 0.5$) samples after thermal decomposition of $Ce_{1-x}La_x(OH)CO_3$.

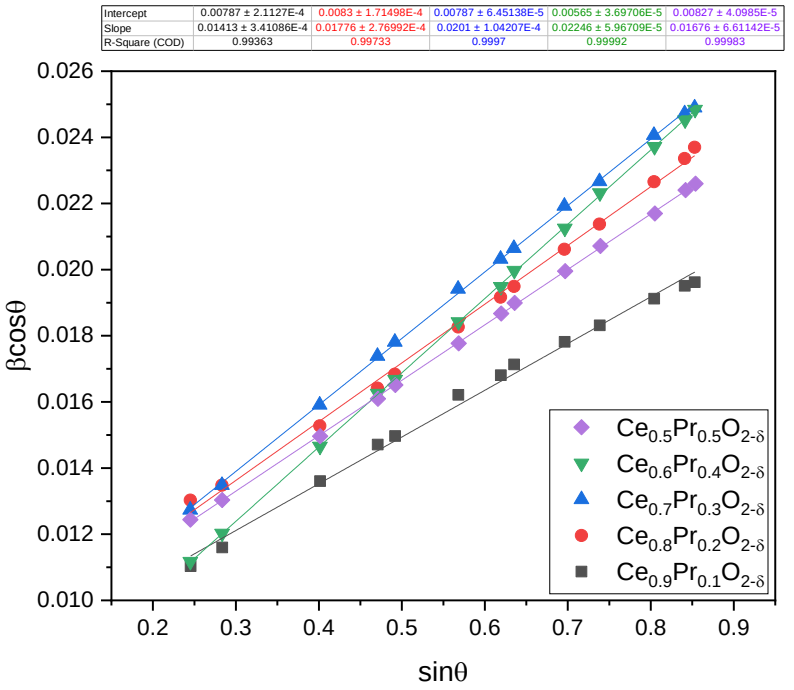

Figure 121: Williamson-Hall plot of the $Ce_{1-x}Pr_xO_{2-\delta}$ ($0.1 \leq x \leq 0.5$) samples after thermal decomposition of $Ce_{1-x}Pr_x(OH)_2Cl$.

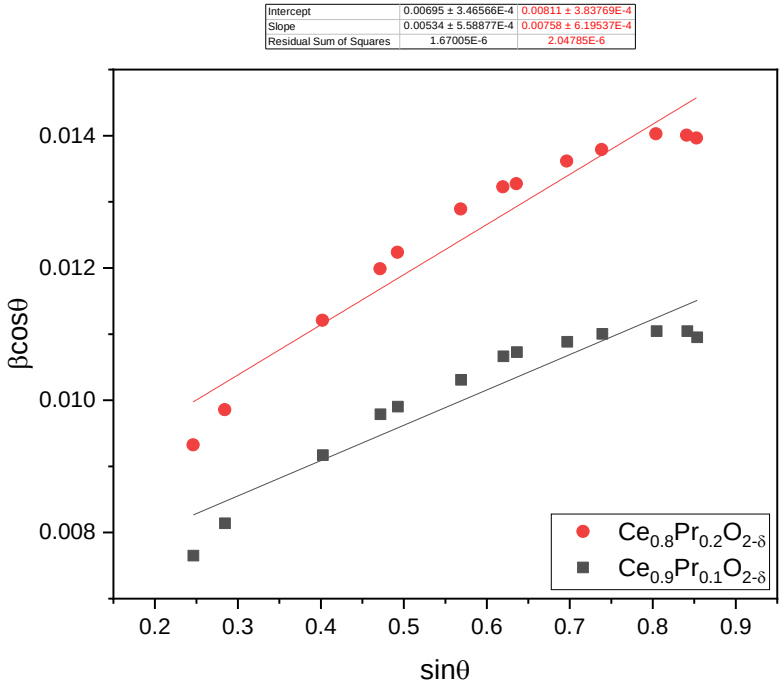

Figure 122: Williamson-Hall plot of the $Ce_{1-x}Pr_xO_{2-\delta}$ ($0.1 \leq x \leq 0.2$) samples after thermal decomposition of $Ce_{1-x}Pr_x(OH)CO_3$.

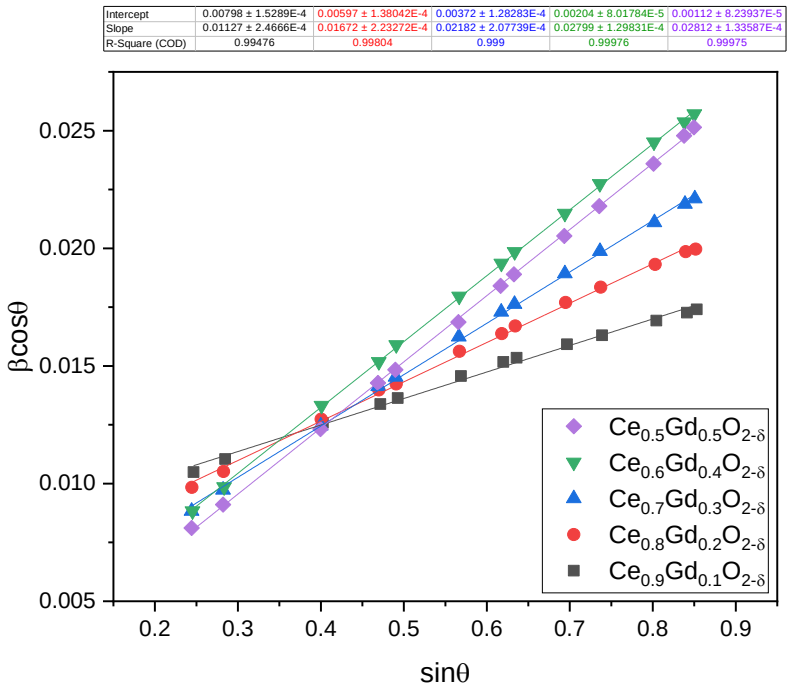

Figure 123: Williamson-Hall plot of the $Ce_{1-x}Gd_xO_{2-\delta}$ ($0.1 \leq x \leq 0.5$) samples after thermal decomposition of $Ce_{1-x}Gd_x(OH)_2Cl$.

Intercept	0.00798 ± 1.5289E-4	0.00476 ± 1.67693E-4
Slope	0.01127 ± 2.4666E-4	0.00544 ± 2.71224E-4
Residual Sum of Squares	3.24615E-7	3.93069E-7

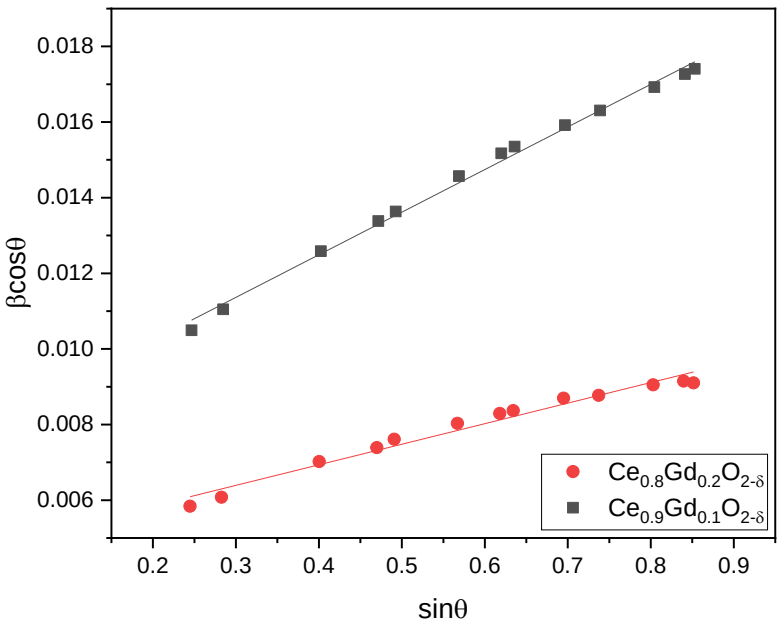

Figure 124: Williamson-Hall plot of the $Ce_{1-x}Gd_xO_{2-\delta}$ ($0.1 \leq x \leq 0.2$) samples after thermal decomposition of $Ce_{1-x}Gd_x(OH)CO_3$.

Intercept	0.0103 ± 3.20644E-4	0.00934 ± 2.77484E-4	0.00468 ± 3.59749E-5	0.0036 ± 1.49671E-4	0.00273 ± 2.65121E-5
Slope	0.00474 ± 5.16367E-4	0.00653 ± 4.46021E-4	0.01826 ± 5.77452E-5	0.0224 ± 2.39796E-4	0.01888 ± 4.23968E-5
R-Square (COD)	0.88469	0.9512	0.99989	0.99874	0.99994

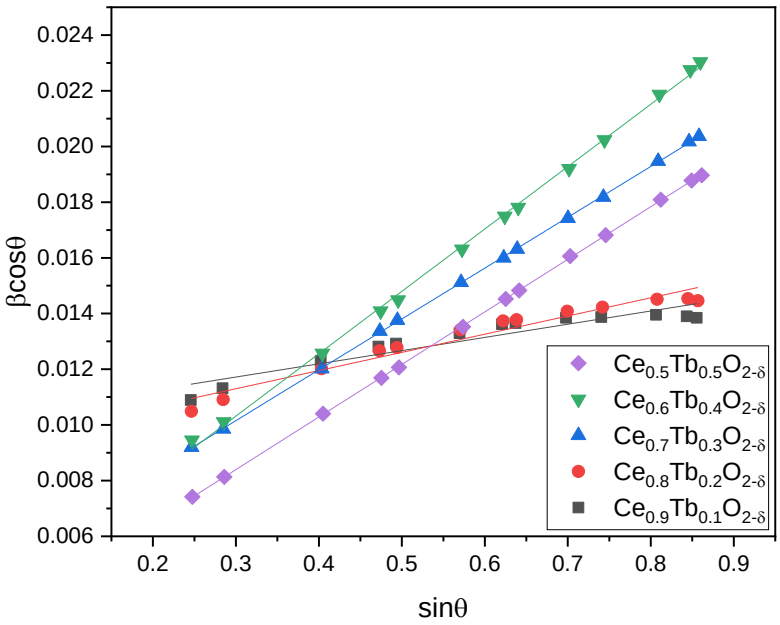

Figure 125: Williamson-Hall plot of the $Ce_{1-x}Tb_xO_{2-\delta}$ ($0.1 \leq x \leq 0.5$) samples after thermal decomposition of $Ce_{1-x}Tb_x(OH)_2Cl$.

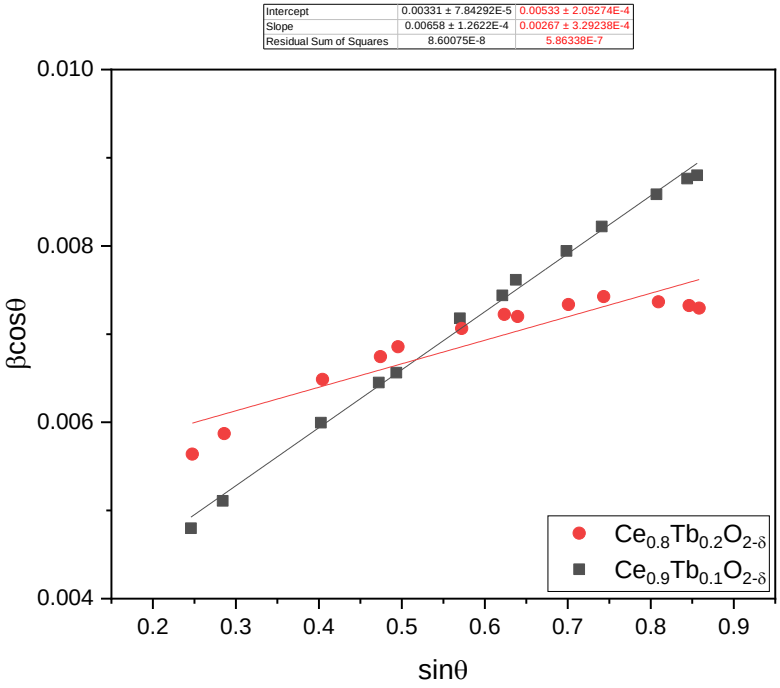

Figure 126: Williamson-Hall plot of the $Ce_{1-x}Tb_xO_{2-\delta}$ ($0.1 \leq x \leq 0.2$) samples after thermal decomposition of $Ce_{1-x}Tb_x(OH)CO_3$.